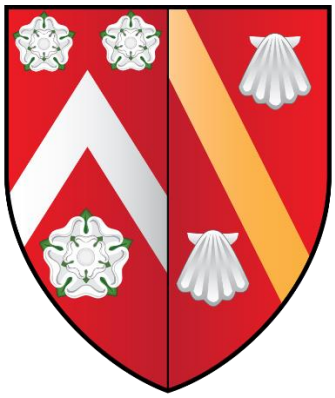
Supramolecular Halogen Bonding and Photo-Responsive Transmembrane Anion Transporters

Laura E. Bickerton

Wadham College, University of Oxford





A thesis submitted for the degree of Doctor of Philosophy

Chemistry Research Laboratory

Trinity Term 2022

Supramolecular Halogen Bonding and Photo-responsive Transmembrane Anion Transporters

Laura E. Bickerton, Wadham College, University of Oxford

Supervisors: Professor Matthew Langton and Professor Paul Beer

Abstract of thesis submitted for the degree of Doctor of Philosophy, Trinity Term 2022

This thesis describes the design, synthesis and testing of novel anion host architectures which exploit hydrogen, halogen, and chalcogen bonding for the purpose of selective and stimuli-responsive anion transport across lipid bilayer membranes.

Chapter 1 introduces the field of anion supramolecular chemistry, with particular focus on areas of relevance to this thesis, namely transmembrane anion transport.

Chapter 2 describes the design, synthesis and testing of monodentate halogen and hydrogen bonding anion transporters.

Chapter 3 describes the design, synthesis and testing of bidentate halogen and chalcogen bonding anion transporters with non-protonophoric activity and carriers with higher denticity.

Chapter 4 describes the design, synthesis and testing of photo-caged, stimuli-responsive anion transporters

Chapter 5 describes the experimental procedures used within this research and details the characterisation of compounds presented in Chapters 2–4.

Chapter 6 summarises and concludes this thesis.

The **Appendix** holds all the original data for the ^{1}H NMR titration experiments and the anion transport assays.

Acknowledgements

Firstly, I would like to thank my supervisors Professor Matthew Langton and Professor Paul Beer. They both took a chance on me and I will always be grateful for the great opportunity I had to work in their groups. I have loved my time in Oxford and their great mentorship, guidance and support has been instrumental in my success so far. I am honoured to be Professor Matthew Langton's first DPhil student and I wish all the best to those who follow.

My time in the Langton and Beer groups has been an amazing experience primarily because of the great people I met along the way. The first person I met in the group was Zongyao Zhang followed by Vihanga Munasinghe and then Heike Kuhn. It has been great to go on this journey together, particularly with Heike who has a natural talent for gift giving and being a very supportive friend.

I would like to thank Olivia Knapp for being a ray of sunshine to work with, providing endless lab banter and excellent friendship. Thanks to Dr Jessica Pancholi, your incredible support and advice is much appreciated and often needed. Thanks to Dr Edward 'TJ' Mitchell, Dr Richard Tse and Dr Jane Liew for fun times on our trip to Italy for ISMSC 2019. Thanks to Dr Andrew Docker, I have appreciated all of your help, support and collaborations. Thanks to Dr Xiaobo Shang for being a kind and positive person to work with, I hope to visit you in China very soon! Thanks to Dr Robert Hein for being a great friend, you inspire me to ask more questions in group meetings and I hope to continue playing board games with you. Dr Aaron Scott, thank you for being such a great person to work next to in the lab. Thanks to Toby Johnson for always trying to make people smile and Jamie Wilmore for being a very chatty person to work with and buying all the coffee!

Thanks to Dr Krzysztof Bąk, I appreciate all the pep-talks and I am sure there will be many more needed throughout my post-doctoral position. You have helped me endlessly throughout my PhD and I am very grateful to have you. Additionally, I have learned a lot from my fruitful collaborations with Professor Fernanda Duarte and Dr Alistair Sterling and I look forward to working with them in the future.

Finally, to everyone in the Beer and Langton groups, Adam Beecroft, Aidan Kerckhoffs, Andrew Taylor, Arya Arun, Charlie Simms, Dr Grace Turner, Dr Harry Klein, Hui Min Tay, Isi Moss, Kelly Britton, Dr Luiza Bondila, Shaun Gartland, Dr Tim Barendt and Dr Valentine Bunchuay, you have all been a pleasure to work with and I am going to miss you all a lot. Thanks to my mentor Dr Jonathan Foster and my women in supramolecular chemistry (WISC) mentees Pip, Claire and Olivia.

During my time in Oxford I was fortunate enough to live with great housemates and friends; Catriona Rooney, Sabrina Wang, Jack Holland, Bertie Ansell, Megan Stoker, I loved our nights around the fire pit and watching the Great British Bake Off.

I would like to thank my friends outside of Oxford: Christina and Tom Maycliffe, Zoe Dunn, Helena Short, Ruth Foster, Sophie Bolton, Bryony Davies and Grace Kimber for always being there for me. Thanks to my brothers, Thomas and Edward, and my grandparents, Ann and Alan, for your unconditional love and support. Finally, I would like to thank my parents, Richard and Jacqueline, this would not have been possible without you both.

L.E.B

Previously Published Work

Some of the work described in this thesis has already been published:
"Controlling Transmembrane Ion Transport via Photo-regulated Carrier Mobility"
Bickerton, Laura E.; Langton, Matthew J.; ***Chem. Sci.*** 2022.

"Highly Active Halogen Bonding and Chalcogen Bonding Chloride Transporters with Non-Protonophoric Activity"
Bickerton, Laura E.; Docker, Andrew; Sterling, Alistair J.; Kuhn, Heike; Beer, Paul D.; Duarte, Fernanda; Langton, Matthew J.; ***Chem. - A Eur. J.***, 2021, **27**, 11738–11745.

"Transmembrane anion transport mediated by halogen bonding and hydrogen bonding triazole anionophores"
Bickerton, Laura E.; Sterling, Alistair J.; Beer, Paul D.; Duarte, Fernanda; Langton, Matthew J.; ***Chem. Sci.*** 2020, **11**, 4722-4729.

Review Article:
"Supramolecular chemistry in lipid bilayer membranes"
Bickerton, Laura E.; Johnson, Toby G.; Kerckhoffs, Aidan; Langton, Matthew J.; ***Chem. Sci.,*** 2021, **12**, 11252–11274.

Oral Presentations

"Supramolecular Halogen and Chalcogen Bonding Anion Transporters"
1st Women in Supramolecular Chemistry (WISC) workshop, Sept 2021, University of Cagliari, Italy. 15-minute oral presentation funded by the Royal Society of Chemistry-Biological and Medicinal Chemistry Sector International Travel Prize (£1500).

International Symposium on SupraBiomolecular Systems, 3-minute flash talk, May 2021, Online.

"Halogen Bonding Anionophores"
Invited inaugural talk, RSC Macrocyclic and Supramolecular Chemistry Early Career Symposium, Aug 2020, Online.

Poster Presentations

"Non-protonophoric Halogen and Chalcogen Bonding Anion Transporters"
Rigaku outstanding poster prize awarded at the RSC Macrocyclic and Supramolecular Chemistry Meeting, Dec 2021, Online.

International Symposium on Macrocyclic and Supramolecular Chemistry, July 2021, online.

"Halogen Bonding Transmembrane Anion Transporters"
Royal Society of Chemistry Macrocyclic and Supramolecular Chemistry Meeting, Dec 2020, online.

International Symposium on Macrocyclic and Supramolecular Chemistry, Aug 2020, online.

Chemical Science outstanding poster prize RSC Macrocyclic and Supramolecular Chemistry Meeting, Dec 2019, University of Kent.

RSC Dalton Division Southern Regional Meeting, Sept 2019, University of Oxford.

Glossary of Abbreviations

δ	chemical shift
Δ	change in (a physical quantity)
λ	wavelength
µ	micro
+ve	positive
-ve	negative
Å	Ångström
A^-	anion
Ac	acetyl
AMT	active metal template
aq.	aqueous
Ar*H*	aryl proton
ATP	adenosine triphosphate
a.u.	arbitrary units
Boc	*tert*-butoxycarbonyl (protecting group)
br.	broad
Bu	butyl
cat.	catalytic
CF	5(6)-carboxyfluorescein;
conc.	concentrated
CuAAC	Cu(I)-catalysed azide-alkyne cycloaddition
°C	degrees Celsius
d	deuterated
d	doublet
dd	doublet of doublets
DBU	1,8-diazabicyclo[5.4.0]undec-7ene
DCM	dichloromethane
DMAP	4-dimethylaminopyridine
DMF	*N*,*N*-Dimethylformamide
DMSO	dimethylsulfoxide
DNA	deoxyribonucleic acid
DPPC	1,2-dipalmitoyl-sn-glycero-3-phosphocholine
EDC·HCl	N-(3-dimethylaminopropyl)-N'-ethylcarbodiimide hydrochloride
EDTA	ethylenediaminetetraacetic acid
eq.	equivalent
ESI-MS	electrospray ionisation mass spectrometry
ESP	electrostatic surface potentials
Et	ethyl

et al.	*et alia*
EYPG	egg-yolk phosphatidylglycerol
FCCP	carbonyl cyanide-*p*-trifluoromethoxyphenylhydrazone;
g	gram
h	hour(s)
HB	hydrogen bonding
HEPES	*N*-(2-hydroxyethyl)piperazine-*N*'-(2-ethanesulfonic acid)
HOBt	hydroxybenzotriazole
HOESY	heteronuclear overhauser effect spectroscopy
HPTS	8-hydroxy-1,3,6-pyrenetrisulfonate
HRMS	high resolution mass spectrometry
Hz	hertz
IUPAC	international Union of Pure and Applied Chemistry
J	coupling constant
K	kelvin
K_a	association constant
KF	potassium fluoride
KOH	potassium hydroxide
L	litre
LUVs	large unilamellar vesicles
m	metre, milli or multiplet
M	molar concentration
Me	methyl
MeCN	acetonitrile
MeOH	methanol
MIM	mechanically interlocked molecule
min(s)	minute(s)
mol	mole
Ms	methanesulfonyl
MS	mass spectrometry
m/z	mass-to-charge ratio
NMR	nuclear magnetic resonance spectroscopy
OAc	acetate
p	para
Ph	phenyl
pH	$-\log_{10}[H^+]$
pK_a	$-\log_{10} K_a$ (in this case, K_a is the acid dissociation constant)
POPC	1-palmitoyl-2-oleoyl-sn-glycero-3-phosphocholine
POPG	1-palmitoyl-2-oleoyl-sn-glycero-3-phospho-(1'-rac-glycerol) 16:0-18:1 PG
ppm	parts per million
Pr	propyl

q	quartet
quin.	quintet
RNA	ribonucleic acid
rt	room temperature
s	singlet or seconds
sat.	saturated
sep.	septet
t	triplet
t	tertiary alkyl group*, tert*-alkyl
TBA	tetrabutylammonium
TBTA	tris[(1-benzyl-1*H*-1,2,3-triazol-4-yl)methyl]amine
TFA	trifluoroacetic acid
THF	tetrahydrofuran
TLC	thin layer chromatography
Ts	toluenesulfonyl
UV-Vis	ultraviolet-visible
VT	variable temperature
X	halogen atom
XB	halogen bonding
V_{max}	electrostatic potential surface maxima

Table of Contents

Chapter 1 Introduction 1

1.1 Anion Supramolecular Chemistry 1

1.1.1 Anion Recognition 1

1.2 Transmembrane Anion Transport 4

1.2.1 Naturally Occurring Transmembrane Ion Transporters 6

1.3 Anion Transport Assays 9

1.3.1 Fluorescence-Based Kinetic Ion Transport Assays 10

1.3.2 Ion-Selective Electrode Assays 14

1.4 Abiotic Receptors for Transmembrane Transport 14

1.4.1 Hydrogen Bonding Receptors for Anion Transport 15

1.4.2 Alternative Intermolecular Interactions for Anion Transport 26

1.4.3 Stimuli Responsive Anion Transporters 35

1.5 Project Aims 43

1.6 References 44

Chapter 2 Acyclic Halogen and Hydrogen Bonding Anion Transporters 54

2.1 Introduction 54

2.1.1 Chapter Aims 57

2.2 Synthesis 58

2.2.1 Anion Recognition 62

2.3 Anion Transport Activity 63

2.3.1 The HPTS Assay 63

2.4 Anion Transport Mechanistic Studies 72

2.4.1 Mobile Carrier Mechanism 72

2.4.2 Mediation of Anion Specific Transport 75

2.5 Anion Selectivity 78

2.5.1 Chloride Over Hydroxide Selectivity 78

2.5.2 Halide Selectivity 81

2.6 Computational Rational 84

2.7 Chapter Conclusions 88

2.8 References 90

Chapter 3 Multidentate Chalcogen, Halogen and Hydrogen Bonding Anion Transporters with Non-Protonophoric Activity 94

3.1 Introduction 94

3.1.1 Chapter Aims 100

3.2 Synthesis 101

3.2.1 Solid State Analysis 106

3.2.2 Anion Recognition 108

3.3 Anion Transport 113

3.3.1 Initial Transport Activity 113

3.3.2 The NMDG Assay 116

3.4 Computational Chemistry 121

3.5 Chapter Conclusions 126

3.6 References 128

Chapter 4 Stimuli Responsive Anion Transporters 133

4.1 Introduction 133

4.1.1 Chapter Aims 138

4.2 Design of Anchored Photo-Caged Transporters 139

4.3 Synthesis of Mobile Carriers 140

4.3.1 Anion Recognition 142

4.4 Transport Activity of Mobile Carriers 144

4.4.1 The HPTS Assay 144

4.4.2 Control Experiments 145

4.5 Synthesis of *ortho*-Nitrobenzyl Photo-Cleavable Carriers 146

4.5.1 Synthesis of Stimuli-Responsive Anchored Transporter (AT4.4) 148

4.5.2 Synthesis of Stimuli-Responsive Anchored Transporter (AT4.6) 149

4.6 Photocleavage Experiments 150

4.7 Photo-controlled Ion Transport Experiments 154

4.7.1 The HPTS Assay 154

4.7.2 Mechanistic Investigations 159

4.8 Coumarin Photolabile Linker 161

4.8.1 Synthesis of Coumarin Linkered Anchored Transporter AT4.7 163

4.9 Chapter Conclusions 166

4.10 References 167

Chapter 5 Experimental 170

5.1 General Remarks 170

5.1.1 Experimental Methods 170

5.1.2 Solvents, Reactants and Reagents 170

5.2 Synthetic Procedures 171

5.2.1 Synthesis of Novel Compounds for Chapter 2 171

5.2.2 Synthesis of Novel Compounds for Chapter 3 185

5.2.3 Synthesis of Novel Compounds for Chapter 4 193

5.3 Single Crystal X-Ray Diffraction Experiments 207

5.4 ^{1}H NMR Titration Experiments 209

5.5 Anion Transport Experiments 210

5.5.1 Vesicle Preparation 210
5.5.2 The HPTS Assay[27,28] 210
5.5.3 Transport Mechanism Studies 213
5.5.4 Transport Selectivity Studies 215

5.6 Computational Chemistry 218
5.6.1 Chapter 2 218
5.6.2 Chapter 3 219

5.7 References 220

Chapter 6 Thesis Conclusions 224

Appendices 227

CHAPTER 1

Chapter 1 Introduction

1.1 Anion Supramolecular Chemistry

Supramolecular chemistry is defined as '*chemistry beyond the molecule*' and although an incredibly broad field, it focuses primarily on the weak non-covalent interactions that promote self-assembly of molecules in order to generate functional supramolecular systems. From the first Nobel prize in this area awarded in 1987, to the second awarded in 2016, supramolecular chemistry has gained great momentum and become a well-established chemical discipline in its own right. Supramolecular chemistry in lipid membranes in particular takes inspiration from the collective work of Cram,[1] Lehn,[2] and Pedersen,[3] who pioneered structure-specific host-guest chemistry research, and the work of Sauvage,[4] Stoddart,[5] and Feringa,[6] for their development of molecular machines capable of completing complex tasks, in order to create new membrane-bound supramolecular systems which function as biomimetic receptors, sensors and transporters.

1.1.1 Anion Recognition

Anions are implicated in many biological, industrial and environmental processes. Within nature the primary applications of membrane-bound biological machines include ion transport, signalling and molecular sensing. Importantly, the poly-anions DNA and RNA hold all the genetic information and are therefore responsible for the function of all known organisms. Even the amino acids encoded for by DNA can all behave as monovalent anions in some environments. Alongside this, the phosphate rich ATP and ADP serve as the currency for intracellular energy transfer and thus determine the life of the organism. In the human body alone there are over 400 genes which encode for ion channels.[7] Mutations and

mis-regulation of ion channels can lead to life-altering disorders described as channelopathies, these include Bartter syndrome, Best disease, and cystic fibrosis (CF).[8] Additionally, anions are prevalent in the environment we live in, from chloride in the oceans to sulphates in acid rain.[9] As a result of their importance, anions already feature in many medical interventions including fluoride to prevent tooth decay,[10] and as the *in vivo* products of prodrugs.[11] The applications of binding anions in aqueous media are vast, ranging from organocatalysis,[12] to the separation and remediation of harmful anions in the environment from industrial or radioactive waste and transmembrane anion transport for channelopathy and cancer treatment.[13,14]

However, significant challenges remain which need to be overcome when designing novel anion receptors. When attempting anion recognition, receptors need to have high levels of anion affinity *and* selectivity in order to be suitable for real-world applications. Anions present themselves in many geometries and sizes which increases the difficulty of artificial receptor design and synthetic accessibility. Whilst cations are predominantly spherical, anions can adopt various geometries including spherical (such as the halides), linear (azide), bent (nitrite), trigonal-planar (carbonate, nitrate), tetrahedral (phosphate, sulphate) and octahedral (hexafluorophosphate) (**Figure 1.1**). As a result, this creates an opportunity to design receptors which have a preorganised binding pocket tuned for a particular anion.

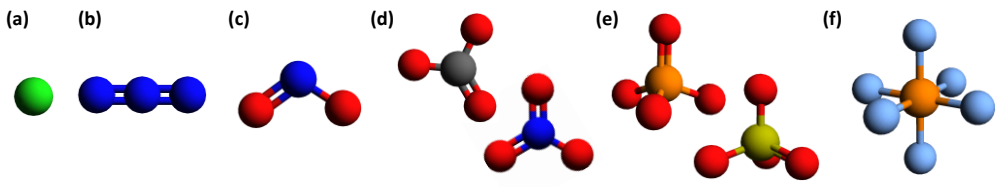


Figure 1.1. (a) Spherical chloride, (b) linear azide, (c) bent nitrite, (d) trigonal-planar carbonate (left) and nitrate (right), (e) tetrahedral phosphate (left) and sulphate (right) and (f) octahedral hexafluorophosphate.

An additional challenge to account for is the dependency anions have on the pH of their surroundings. Anions, and certain receptors, exist under multiple protonation equilibria and they have the ability to lose and gain protons depending on the pH. Therefore, binding anions in solution must occur within this restrictive "pH window" in which the anion is deprotonated whilst the receptor remains protonated.[15]

For example, the biologically relevant anion bicarbonate is implicated in many bodily processes, however, probing bicarbonate binding and transmembrane transport is inherently challenging due to its many equilibria and interconversion between bicarbonate, carbonic acid, and carbon dioxide. In order to overcome this, these properties must be exploited to generate selective binding conditions for specific applications. As previously eluded to, receptors also fall victim to this restrictive pH window. Thiosquaramide motifs, for instance, are deprotonated at a pH values greater than 7 and thus are unable to bind and be exploited for transport applications.[16] However, at pH 4 the receptor is protonated and the transmembrane transport activity is restored, thus highlighting the pH dependence of anion recognition.

Solvation is another a key obstacle to anion recognition in aqueous media.[17] Firstly, most functional organic supramolecular systems are not water soluble, and secondly, anions themselves are heavily solvated in aqueous media and so possess very high dehydration penalties. These large free energies of solvation associated with anions are related to the Hofmeister series of anion hydrophobicity; with increasing charge density of the anions, the strength of hydration increases and lipophilicity decreases (**Figure 1.2**).[18] Thus, to bind strongly hydrated anions in aqueous media, the receptor needs to bind with sufficient affinity to overcome these penalties.[19]

In addition, how a supramolecule assembles specifically in aqueous media is often determined by the hydrophobic effect. In nature this drives protein folding and in supramolecular chemistry the hydrophobic effect can significantly influence the self-assembly of the molecules, thus impacting the arrangement of bond donors and their ability as receptors.[15]

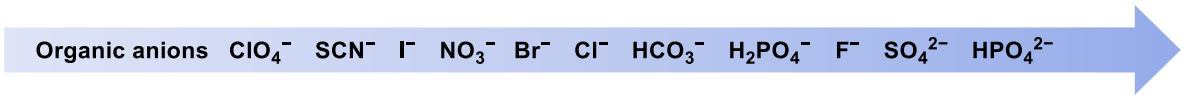


Figure 1.2. The Hofmeister series of anion hydrophobicity in order of increasing hydration.[18]

1.2 Transmembrane Anion Transport

The highly complex, life-facilitating reactions occurring in living organisms require cellular compartmentalisation, which is achieved by lipid bilayer membranes. These membranes physically segregate the chemical environments either side of the bilayer, and are essential for many cellular processes, such as photosynthesis.[20,21] Hydrophobic molecules are able to cross the bilayer by simple diffusion but hydrophilic ions are membrane impermeable and thus require the actions of a selective membrane channel, pump or carrier which work to provide a hydrophilic pathway for the ion.[22] These integrated and peripheral membrane proteins allow ion transport, whilst maintaining the osmotic balance between the intra and extravesicular environments. Transport activity is governed by environmental changes which stimulate or inhibit the action of the membrane proteins.

The transported ions can cross the bilayer via one of three mechanisms shown in **Figure 1.3**. Uniport is the transport of a molecule or ion through the membrane without known coupling to the transport of any other molecule or ion.[23] This transport is often termed facilitated diffusion, in which integral membrane proteins called uniporters aid the

transport of molecules or ions down their concentration gradient. Due to the specificity of the uniporters, the rate of transport of a particular species is limited by the number of transporters within the membrane capable of its transport, hence, the transport rate is governed by the magnitude of the ion concentration gradient and the concentration of uniporters in the membrane.

Co-transport encompasses the symport and antiport transport mechanisms and involves the simultaneous transport of more than one ion or small molecule. It is often termed secondary active transport because the movement of the first species against its concentration gradient relies on the movement of a second species down its concentration gradient.[24] Antiporters typically transport two ions of the same charge in opposite directions in relation to each other. The transport mechanism adopted by a membrane channel or mobile carrier is different depending on the ion being transported and the function needed to be accomplished.

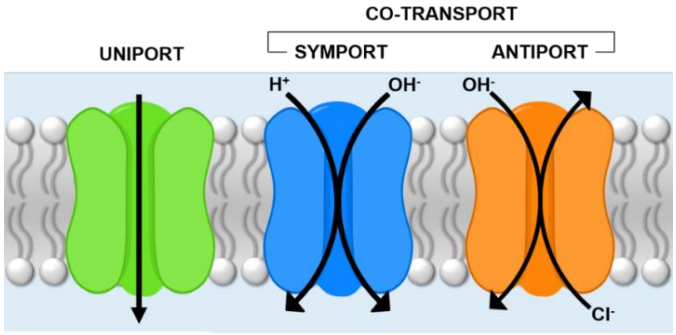


Figure 1.3. Mechanisms of transport across a lipid bilayer.

1.2.1 Naturally Occurring Transmembrane Ion Transporters

1.2.1.1 Pumps

The synthesis of ATP involves many highly sophisticated membrane-spanning biological machines including membrane pumps called ATPases. These pumps use energy to fuel their action and drive proton transport across a lipid membrane against their concentration gradient. Membrane pumps and channels work together in many instances, in this example the protons flow through the channel compartment of ATP synthase providing the energy to generate ATP.[25]

1.2.1.2 Channels

Membrane channels create a pore across the lipid bilayer to allow ions to flow from one side to the other *via* passive transport or facilitated diffusion.[25] They are highly sophisticated structures with high ion specificity. One ubiquitous example of this is the potassium ion channel (**Figure 1.4a**).[25] The conformation of the channel is such that potassium can enter while solvated, but must transiently lose its associated water molecules whilst travelling through the narrowest part of the channel. Selectivity is achieved through the favorable interactions between potassium and the carbonyls of the amino acids lining the pore of the so-called selectivity filter, which compensate for the dehydration penalty (**Figure 1.4b**). This channel cannot overcome the dehydration penalty associated with sodium thus selectivity for potassium is achieved.

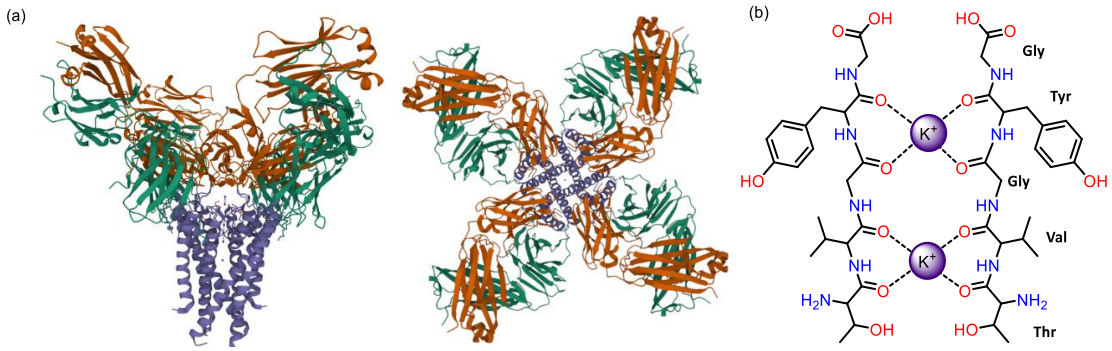


Figure 1.4. (a) A crystal structure of the potassium ion channel taken from the protein data bank (1K4C).[26] (b) a schematic of the interactions between potassium and the amino acids lining the channel in the selectivity filter.

The Na-K-Cl symporters are an example of protein-based symporters within the human body. They function to maintain electroneutrality by transporting sodium and potassium along with two chloride ions.[27] Bartter syndrome is caused by mutations to the NKCC2 symporters found in the kidneys, with symptoms including life-threatening dehydration and a high concentration of urinary potassium and chloride among many others. Despite dietary supplements and a couple of pharmaceutical drugs used to alleviate the symptoms, there are no direct treatments and it requires the patient to live under medical surveillance.[28] There is therefore a pressing need to create synthetic carriers or channels that can be administered to patients to treat these channelopathies.[7,29]

1.2.1.3 Mobile Carriers

Mobile ion carriers are small lipid soluble molecules which can reversibly bind ions to transport them across lipid bilayer membranes.[30] Although structurally simpler when compared to channels and pumps are much rarer in the human genome. Bacterial examples are much more common. Valinomycin is an example of a neutral mobile carrier capable of transporting potassium cations across lipid bilayers via a uniport mechanism.[31] Its ester

carbonyl groups point inwards to form an octahedral complex with its cationic guest, which is sufficiently hydrophobic to cross the bilayer. Valinomycin is highly selective for potassium over other monovalent cations (**Figure 1.5a**). The stability constants for K^+ and Na^+ valinomycin complexes were determined in organic solvent mixtures and valinomycin bound K^+ more strongly in all solvents, with stability constants almost 10^4 times greater than those calculated for the valinomycin-Na^+ complex.[32] While valinomycin can still bind and transport sodium, it is this innate binding selectivity that allows for K^+-specific transport.[33]

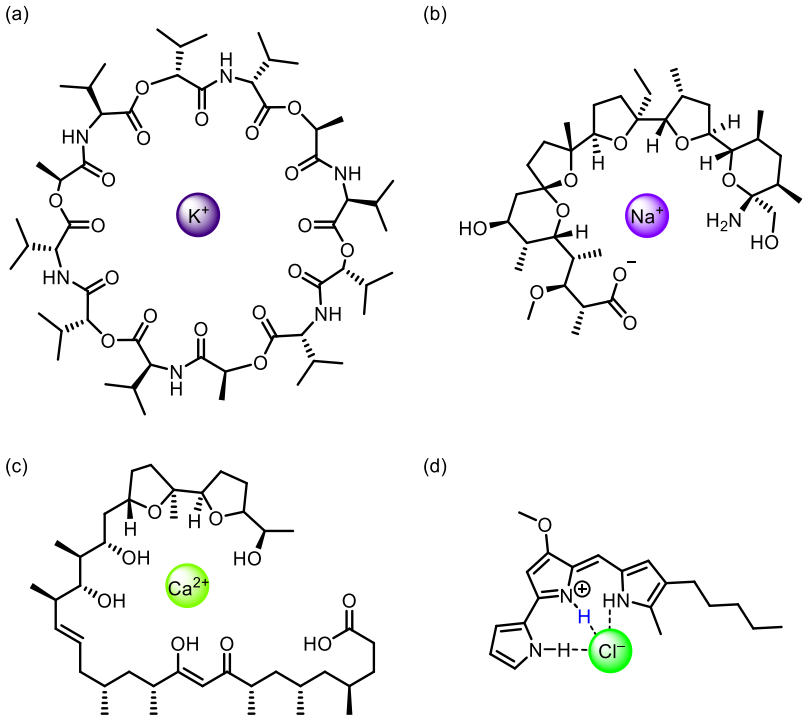


Figure 1.5. Mobile carriers; (a) valinomycin, (b) monensin, (c) ionomycin and (d) prodigiosin.

Unlike macrocyclic valinomycin, monensin is an acyclic carboxylate ionophore (**Figure 1.5b**). It is naturally produced by *streptomyces cinnamonensis* and facilitates Na^+/H^+ antiport. When antiport occurs for ions of the same electrical charge, such as in the case of

monensin, transport does not affect the membrane potential of a cell because the transport purely relies on the concentration gradients of the species in question.

Divalent cations also have vehicles for transmembrane translocation. Ionomycin and calcimycin are both examples of calcium transporters which bind calcium cations in a 1:1 stoichiometry with high specificity (**Figure 1.5c**).[34,35,36] Like monensin these acyclic carriers form a chelating ring around their guest via head to tail hydrogen bonding interactions. Prodigiosin on the other hand is a smaller acyclic H^+/Cl^- symporter produced by strains of *Serratia* and *Streptomyces* (**Figure 1.5d**).[37] It is one of the rare examples of a mobile carrier in nature where an anion is involved in the transport mechanism. This particular carrier is reported to uncouple lysosomal vacuolar-type H^+-ATPase by reversing lysosomal acidification.[38] An influx of protons through the H^+-ATPase pump normally maintains the acidic environment of the lysosomal lumen but upon the addition of prodigiosin the pH rises rapidly. The action of prodigiosin is reliant on Cl^- transport, it is postulated that the proton appended to the pyrrolium cation forms an intermolecular hydrogen bond with Cl^- which is reinforced by the surrounding N–H hydrogen bond donors.

1.3 Anion Transport Assays

In order for synthetic anion transporters to be suitable for their proposed function they must work via the mechanism of the biological transporter they intend to mimic. This section will discuss how the transport of anions is probed *in vitro* and will provide the context when discussing synthetic examples of anion transporters later on in this introduction.

The transport ability and mechanism of synthetic anion carriers is often investigated with a series of kinetic assays using large unilamellar vesicles (LUVs), which are typically

around 100-200 nm in diameter, using a fluorescent probe or an ion-selective electrode, depending on the ion-transport process of interest.[39]

1.3.1 Fluorescence-Based Kinetic Ion Transport Assays

1.3.1.1 The HPTS Assay[40]

The so-called HPTS assay is one of the most widely used transport experiments due to its ease of set up and application. It employs 8-hydroxypyrene-1,3,6-trisulfonic acid trisodium salt (HPTS) as an internal fluorescent pH probe to monitor the dissipation of a pH gradient across the lipid bilayer (**Figure 1.6**).[16,41] The LUVs are suspended in a buffer solution with matched osmotic pressure either side of the bilayer. A pH gradient is generated by a base pulse (e.g. NaOH) at the start of the assay and the dissipation of this gradient via Cl^-/OH^- or Na^+/H^+ antiport, or H^+/Cl^- symport, is monitored. Once the carrier is added the time-dependent change in fluorescence intensity (λ_{em} = 510 nm) can be monitored simultaneously at λ_{ex} = 405 nm (acidic form of HPTS) and λ_{ex} = 460 nm (basic form) which allows for ratiometric analysis. Addition of a detergent to lyse the vesicles allows calibration of the assay to 100% transport (complete gradient dissipation). The assay can then be repeated at multiple concentrations for each carrier under investigation.

The carriers in question can be incorporated into the bilayer when the vesicles are prepared, or added externally in a water-miscible organic solvent which allows for convenient and rapid screening of many host species at various concentrations. The HPTS assay is highly versatile and can be used to study cation and anion transport; ion exchange of the internal and external salt solutions allows for investigations into the host transporter's cation or anion selectivity.

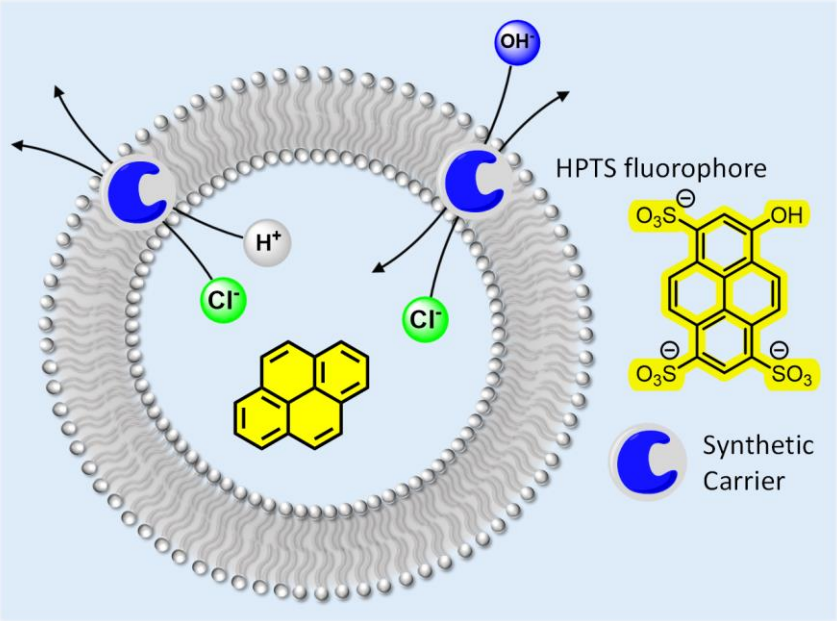


Figure 1.6. HPTS assay mechanism and structure of the HPTS dye.

1.3.1.2 The Lucigenin Assay

The lucigenin (LG) assay is comparable to the HPTS assay in its ubiquity and ease of application. Lucigenin is a water-soluble fluorescent dye which can be quenched by anions (**Figure 1.7**). It is most commonly used to monitor chloride/nitrate antiport transport processes, exploiting the quenching of the lucigenin by Cl^-, however Bąk et al have expanded the scope of the assay to probe the transport of oxyanions including some common drugs, metabolites and nucleotides.[42] The vesicles are synthesised with an internal and external $NaNO_3$ HEPES buffer, and then the sodium salt of the chosen anion and the carrier can be added. Here, it is the addition of an anion gradient which drives the transporter to facilitate transport.

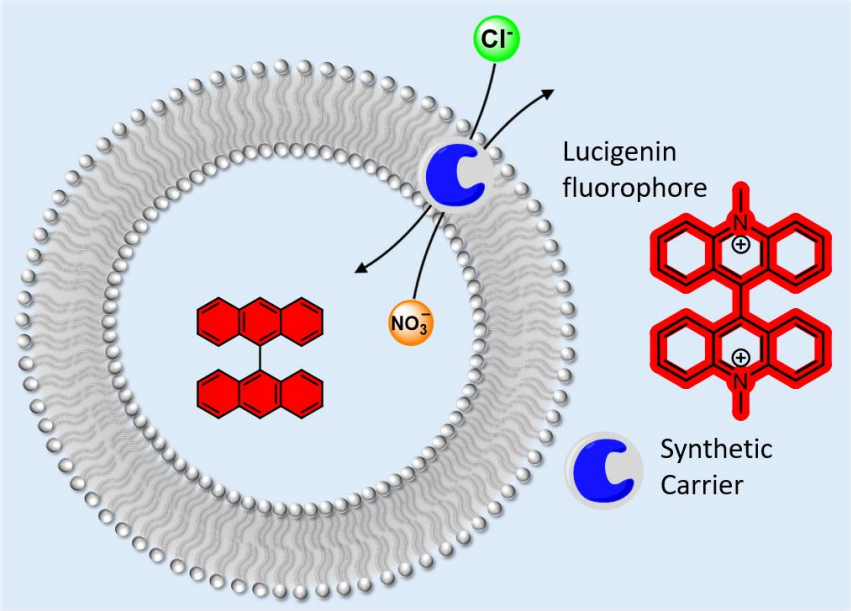


Figure 1.7. The lucigenin Cl^-/NO_3^- antiport assay.

1.3.1.3 Alternative Fluorescent Probes

To probe the transport of other ions some less commonly used fluorescent dyes have been used in kinetic assays with LUVs. These include calcein to probe calcium transport (**Figure 1.8a**), SPQ (6-methoxy-*N*-(3-sulfopropyl)quinolinium) for chloride (**Figure 1.8b**), the voltage-sensitive safranin O (**Figure 1.8c**), and lastly ANTS/DPX which are often loaded into the vesicles together and their efflux upon addition of transporter is monitored (**Figure 1.8d**). These dyes fit the criteria needed by those used for probing ion transport: soluble in aqueous conditions at the pH of the assay (typically pH 7), membrane impermeable, and specific to a particular ionic species such that its response can be used as a direct measurement of transport.

The development of new assays and fluorescent dyes for investigating transport is an important area of current research and can be used to advance this field. For example, a recent breakthrough was made in the direct measurement of bicarbonate transport by

Valkenier, Butler and co-workers with a europium complex capable of selectively detecting changes in the intravesicular carbonate concentration (**Figure 1.8e**).[43]

Although not the primary focus of this thesis, cation transport is a newly growing area with examples of metal cation transporters including those for Zn(II)[44] and Cu(II)[45,46] emerging. Valkenier and co-workers demonstrated the first example of a mobile carrier for Cu(I) cations mediated by bis-imidazole-functionalised calix[4]arenes.[47] To quantify Cu(I) transport, the authors developed a new assay in LUVs in which the fluorescent dye bathocuproine disulphonate (BCS) was encapsulated within the vesicles (**Figure 1.8f**). Transport of Cu(I) across the vesicle membrane (added as Cu(II) in the presence of a reducing agent) is reported by fluorescence quenching of BCS, due to complexation of Cu(I) in a 2:1 receptor:cation stoichiometry.

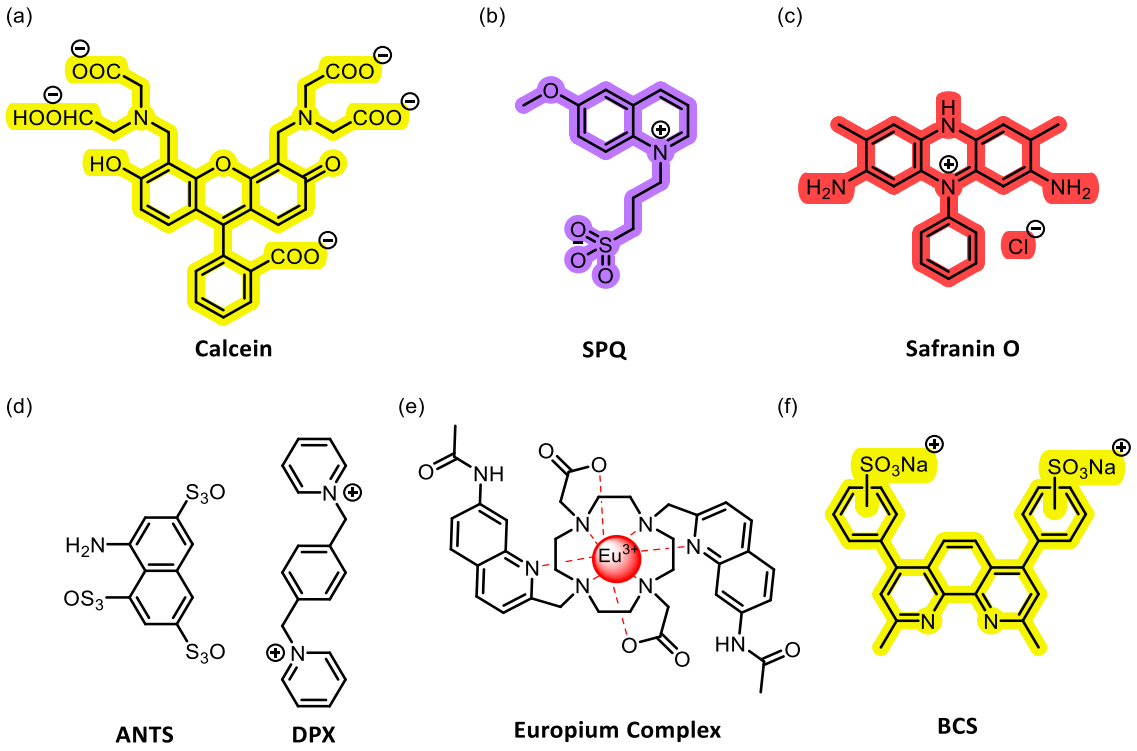


Figure 1.8. Alternative fluorescent dyes for probing anion transport.[39,43,47]

1.3.2 Ion-Selective Electrode Assays

These experiments allow for the elucidation of transport without the use of fluorescent dyes. They are often a more direct approach to probing transport since the electrode can be specific for a particular ion. Another advantage is that it avoids any disruptive interactions between the test ionophore and the more typical fluorescent dyes. When an external stimulus such as light is being used to control transport activity, ion-selective electrode transport experiments allow transport to be monitored without interference between the in-situ irradiation and the detector of a fluorometer.[39,48]

1.4 Abiotic Receptors for Transmembrane Transport

Supramolecular chemists are often inspired by highly sophisticated biological molecular machinery when attempting to create biomimetic synthetic architectures.[49] A wide variety of intermolecular interactions may be incorporated into anion transporters to investigate the relationship between host-guest binding affinity and transport efficiency; including electrostatic interactions, hydrogen bonding, anion-π interactions and sigma hole interactions (**Figure 1.9**).[21,22,50] Host-guest binding affinity has a large influence on anion transport ability.[51] Binding needs to be sufficiently strong enough such that the carrier can recognise and bind the anion in the aqueous phase/at the membrane interface, prior to traversing across the bilayer, but not too strong such that release on the other side is inhibited.[52]

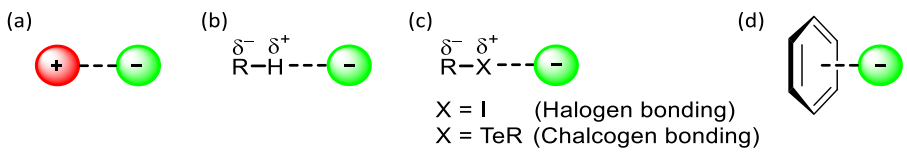


Figure 1.9. An overview of the intermolecular interactions that will be discussed. (a) Electrostatic interaction, (b) Hydrogen Bonding, (c) Halogen Bonding, (d) Anion-π interactions.

Due to the negatively charged nature of anions, positively charged receptors have consequently been widely explored for anion binding particularly in aqueous solution, such as those including quaternary ammonium- or pyridinium-based motifs.[53] However, charged receptors make poor transporters due to their low lipophilicity and thus poor membrane partitioning ability.[20] Ion-ion interactions alone are also not used for anion transport because despite being relatively strong, they are not directional and therefore they are often used to supplement the more directional ion-dipole interactions such as hydrogen and halogen bonding.[49]

1.4.1 Hydrogen Bonding Receptors for Anion Transport

Hydrogen Bonds (HB) are ubiquitous in nature; this powerful ion-dipole interaction is integral to intra- and inter-molecular recognition. When a hydrogen atom is bound to a relatively electronegative atom (e.g., O, C, N) it becomes polarised (**Figure 1.9b**). This induced electro-positivity on the hydrogen allows it to interact with an electronegative atom such as an anion. These interactions underpin protein folding, structure and therefore function among many other applications within biology, and as a result are used extensively in the development of functional supramolecular structures.

The simplest hydrogen bonding motif commonly used for developing anion transporters are the urea and thiourea groups due to their solubility in aqueous media. With lower pK_a values, thioureas are the stronger acid when compared to ureas and thus display increased hydrogen bonding abilities.[54]

Davis and co-workers used these simple anion binding motifs to pioneer investigations into the relationship between structure and activity. They presented a series of steroidal cholapod transporters each with either two urea (**Figure 1.10a**) or thiourea

(**Figure 1.10b**) anion binding motifs and thus four possible hydrogen bonds.[55] They periodically changed the substituents, and analysis of the structure-activity relationship data revealed a general trend of increasing anion binding potency with increased the transport activity. Although initially anticipating successful transport with analogous cationic receptors (**Figure 1.10c**), this was not the case and despite the overall transport complex being electroneutral, host protonation proved to be hugely detrimental to activity.

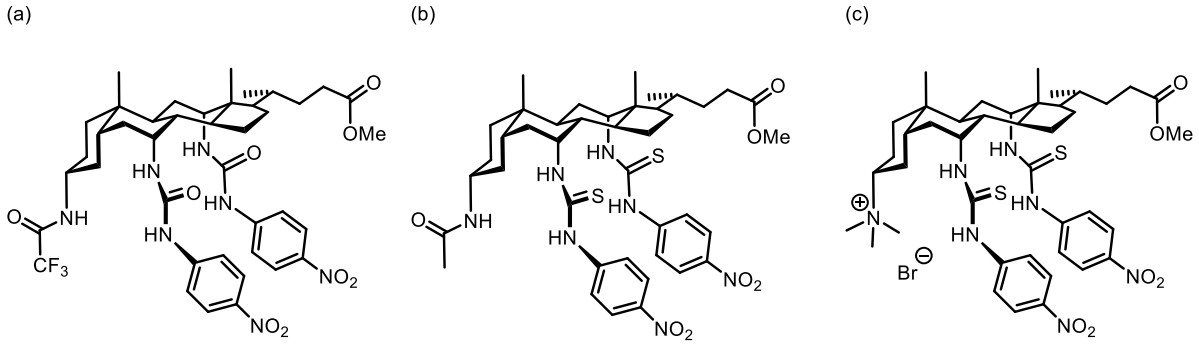


Figure 1.10. Steroidal cholapod transporters.[55]

Later, Gale and co-workers developed upon this further with the synthesis of twenty-two 1-hexyl-3-phenylpolythiourea transporter analogues in order to perform quantitative structure-activity relationship (QSAR) analysis.[51] For this family of thiourea carriers, a linear relationship between Hammett constant values and binding affinity for chloride was reported. The carriers with a trifluoromethyl group (**Figure 1.11a**), and a nitro group (**Figure 1.11b**), proved to have the best transport activity with EC_{50} values of 0.44 and 0.45 mol% (transporter to lipid) owing to their high Hammett constants and strong Cl^- binding affinity. In comparison, carriers such as those with the addition of keto or ester substituents (**Figure 1.11c**), which are less electron withdrawing, resulted in reduced transport activity. This indicates that increasing the electronegativity of the substituents in

close proximity to the hydrogen bond donor generally has a positive effect on membrane transport ability.

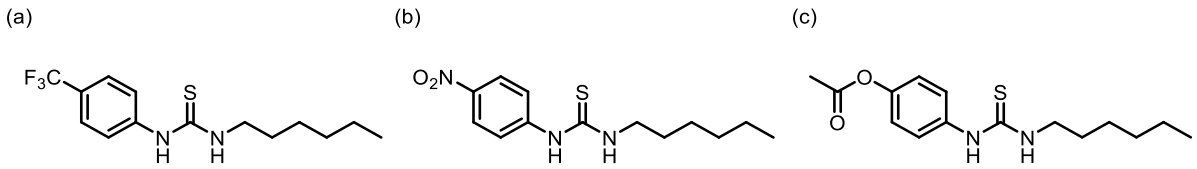


Figure 1.11. 1-hexyl-3-phenylpolyurea transporters.[51]

The impact of carrier size and lipophilicity on the way in which mobile carriers translocate and rotate within membrane is not yet fully understood. For transmembrane transport purposes, carriers need to be sufficiently lipophilic to partition into lipid bilayer, yet not too hydrophobic, so that the carrier can avoid inactivity caused by precipitation or high affinity for the hydrophobic environment of the bilayer. The most widely used measure of lipophilicity is the partition coefficient, P, of a molecule between an aqueous and lipophilic phase, usually octanol and water, typically represented by logP. The lower the logP value, the more hydrophilic the molecule is and the higher the affinity it has for the aqueous phase. A very high value represents a hydrophobic molecule, corresponding to a significantly higher concentration of the compound in the lipid phase.

Felix, Davis and co-workers created a series of dithioureidodecalin carriers with increasing lengths of alkyl chains and HB urea motifs for mediating anion transport.[56] They used the lucigenin Cl^-/NO_3^- assay combined with molecular dynamics simulations to show that by increasing the size and lipophilicity of the carrier the transport rate can be tuned. The smallest, and thus the least lipophilic carrier (**Figure 1.12a**), could rotate very quickly rotate within the bilayer due to its size, however transport was slow because it could not

partition easily through the hydrophilic heads of the lipid bilayer. In contrast, the largest carrier with a 10-carbon chain was the most lipophilic (**Figure 1.12c**), and therefore could easily partition into the bilayer, but due to its large size, rotation within the membrane and delivery of the anion to the other side of the membrane was suppressed. As depicted in **Figure 1.12**, they hypothesize that the carrier must flip during the transport mechanism to deliver the ion from one side to the other of the membrane. Thus, carriers need to be small enough to turn with in the bilayer and deliver the anion to the other side whilst balancing lipophilicity such that it can penetrate into the bilayer (**Figure 1.12b**).

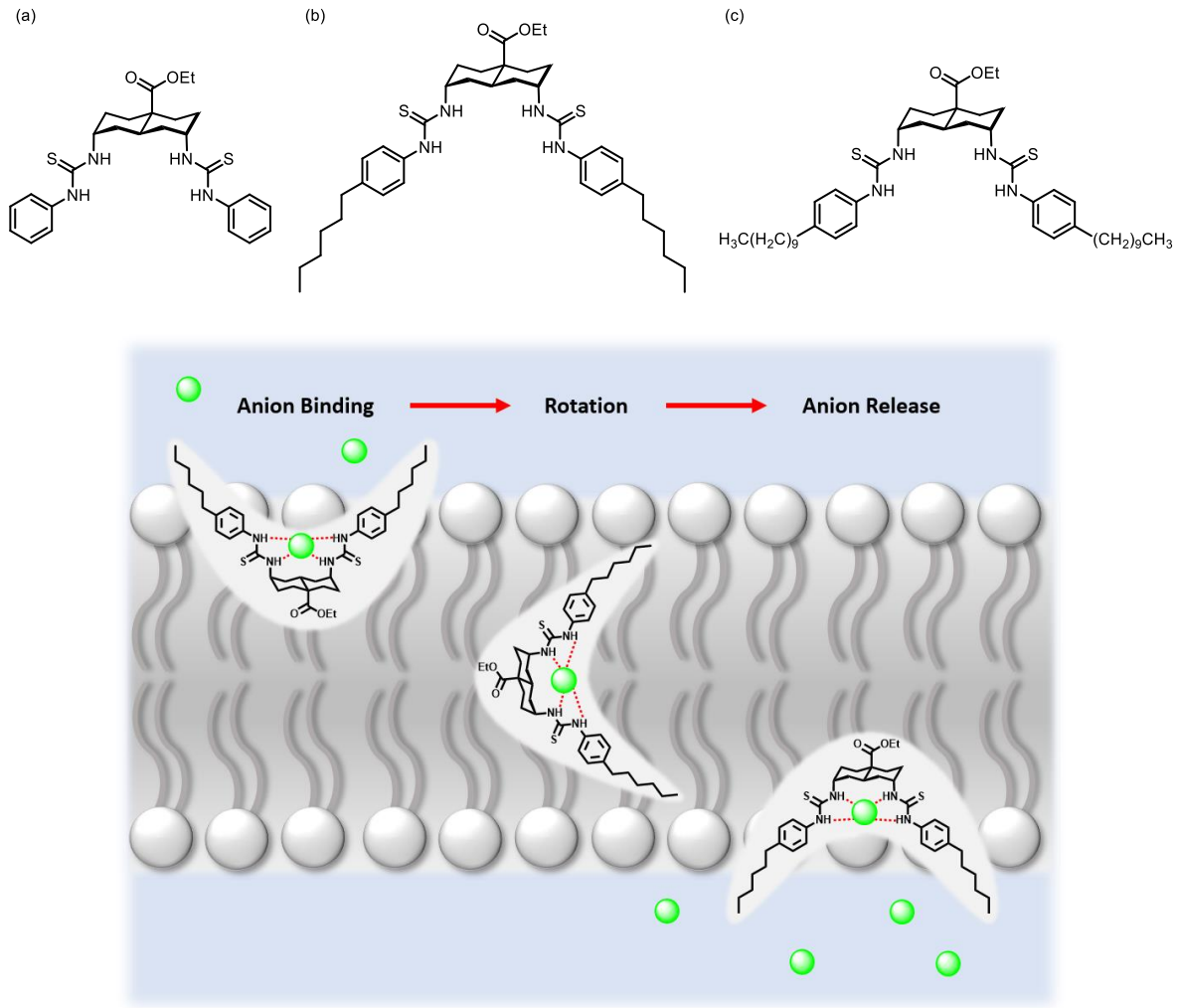


Figure 1.12. A series of dithioureidodecalin carriers and a carrier rotation across the bilayer.[56]

In a similar study, Quesada and co-workers reported a series of tamjamine derived anion transporters with a bipyrrole–enamine moiety for anion recognition and transport (**Figure 1.13**).[57] Alkylation of an amine group with alkyl chains of increasing length from a single methyl group up to long carbon chains (**Figure 1.13a/b**) enabled them to investigate the effect of cLogP on the initial chloride efflux ($\%s^{-1}$) and explore the effect of lipophilicity on transport activity. This analysis revealed a parabolic relationship between chloride transport and lipophilicity, providing support for the results found by Davis and co-workers. The authors concluded that the optimum logP value to be 4.2 for this family of compounds.

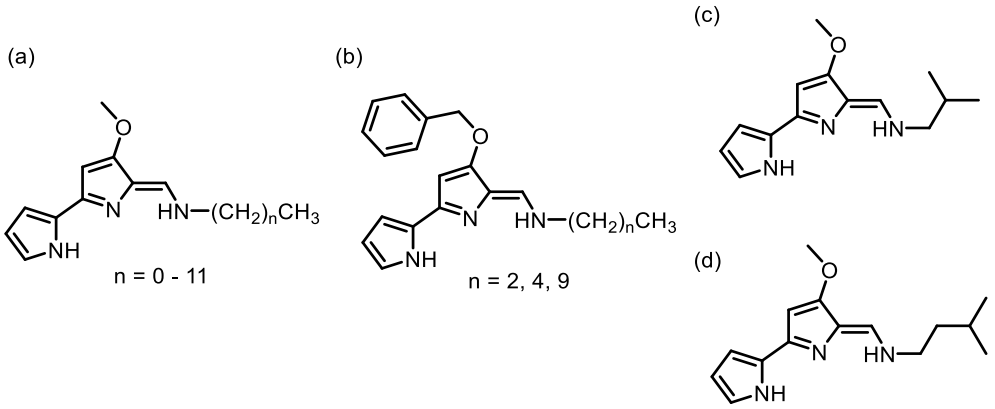


Figure 1.13. Tamjamine derived anion transporters with a bipyrrole–enamine moiety for anion recognition and transport.[57]

Squaramide and thiosquaramide HB motifs are comparable bidentate H-bond donors to urea motifs. Again, there are two hydrogen bond donors per motif for anion recognition, however, squaramides are more acidic due to their aromatic character, making them typically more potent anion receptors.[58] This has been shown to have a positive impact on transport ability and activity. The first example of squaramide anion transporters was reported by Gale and co-workers in 2012.[59] They tested a series of compounds using an

ion selective electrode (ISE) assay to monitor Cl^-/NO_3^- and Cl^-/HCO_3^- antiport mechanisms. They found that three of their squaramide carriers (**Figure 1.14a-c**) were nearly one order of magnitude more active than analogous thiourea and urea-based transporters. Increased fluorination was also linked to increased transport activity relating to their increased lipophilicity and Hammett constants. The authors highlighted the advantage of using squaramides to increase transport activity without significantly increasing the lipophilicity which could be detrimental.

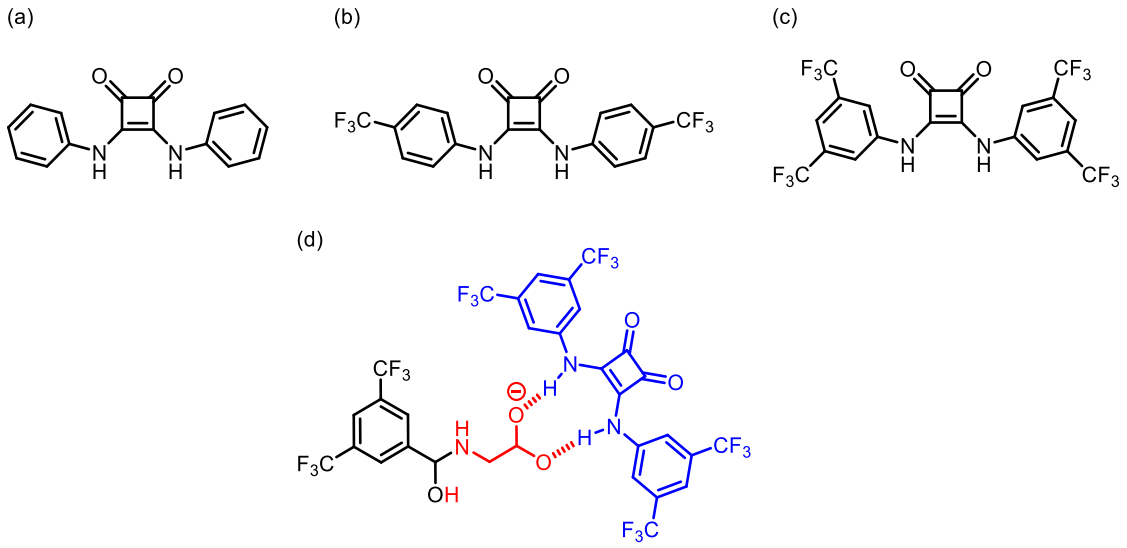


Figure 1.14. (a-c) Squaramides as potent transmembrane anion transporters.[59] (d) Glycine transporter.[60]

The same group also demonstrated that a squaramide could be used to transport amino acids (**Figure 1.14d**). Glycine transport was facilitated by the squaramide anionophore which formed hydrogen bonds with the glycine carboxylate motifs, and hemi-aminal formation between the amino acid amine and a simple electron deficient aldehyde within the membrane.[60] In this study, amino acid transport was examined using a ^{13}C NMR assay with ^{13}C-enriched glycine, and fluorescence assays in which the transported amino acid could bind to intracellular calcein, displacing bound Cu(II) and triggering an increase in

fluorescence which could be monitored over time. Control experiments show the necessity of both the squaramide and the aldehyde for effective glycine transport.

Most synthetic carriers reported to date are synthesised with a goal to facilitate chloride transport. Surprisingly, examples of anion carriers capable of mediating oxyanion transport are comparatively rare, perhaps due in part to a historic lack of suitable assays like ion-pair transporter systems, or the complexity of studying the transport of species that can exist in multiple protonation states. The most recent example of oxyanion transport was presented by Caltagirone and co-workers who show how the squaramide motif can be supplemented with additional hydrogen bond donors to increase the denticity of the structure and support oxyanion transport (**Figure 1.15**).[61] They reported five squaramide receptors bearing aromatic substituents with various heteroatoms providing additional hydrogen bonds to the parent squaramide. Caltagirone and co-workers tested the receptor's binding and transport capabilities with a wide variety of anions and oxyanions via the HPTS assay, ^{1}H NMR spectroscopy and UV-vis. The parent squaramide (**Figure 1.15a**) shows considerably weaker guest binding in all cases when compared to carriers which possess additional indole moieties (**Figure 1.15b**). This illustrates how supplementing the architecture with additional HB donors can induce cooperative binding that enhances host-guest binding strength. They proposed that additional HB motifs can act as an alternative to incorporating electron withdrawing units to increase binding potency and transport ability.

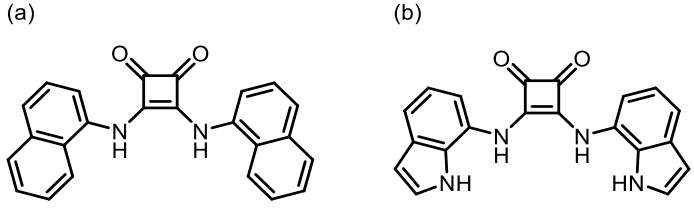


Figure 1.15. Oxoanion transport mediated by squaramides.[61]

Multidentate HB carriers for oxyanion transport have also been presented in the form of 1,8-diamidocarbazoles by Chmielewski and co-workers (**Figure 1.16**).[62] They reported a series of readily accessible bis-amide derivatives of 1,8-diamidocarbazoles (**Figure 1.16a**) and 3,6-dichloro-1,8-diamidocarbazoles (**Figure 1.16b**), which proved to be tuneable 'turn-on' fluorescence sensors for $H_2PO_4^-$ and AcO^-, and potent transmembrane transporters of chloride. The group then evaluated the transport ability of thioamide analogues (**Figure 1.16c**) and reported superior binding ability and transport activity of the 1,8-di(thioamido)carbazoles when compared to the diamidocarbazoles.[63] The thioamide carbazole derivative was shown to be effective for the transport of various biologically relevant oxyanions such as aspirin and pyruvate.[42] As a result of their study, Chmielewski and co-workers proposed that replacing amides with thioamides would become a useful tool for supramolecular chemists to create carriers with improved anion transport efficiency.

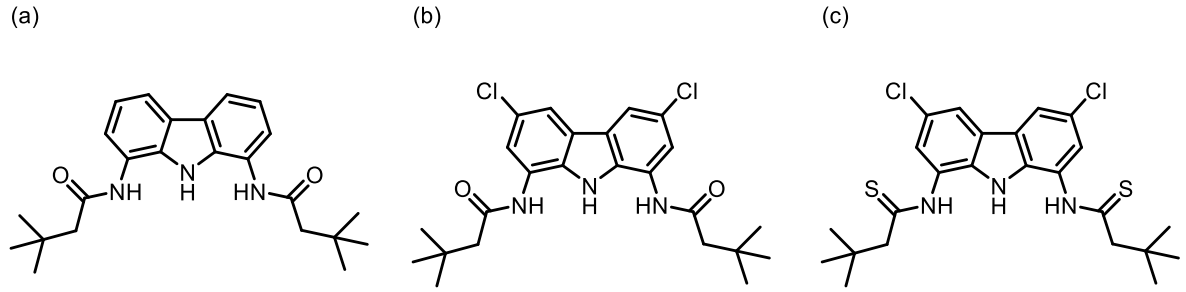


Figure 1.16. (a/b) Carbazole-based anion transporters.[42,62,63] (c) Thioamide carbazole-based anion transporter.[64]

Kinbara and co-workers pioneered the use of multi-block amphiphiles as ion channels,[65] and have more recently reported a related imidazolium derivative, which acts as a mobile anion carrier (**Figure 1.17**).[66] The structure consists of an

imidazolinium anion binding site, positioned between diphenylacetylene units appended with non-ionic, hydrophilic octa(ethylene glycol) chains. The anionophore mediates selective nitrate transport, with an observed selectivity trend of NO_3^- > ClO_4^- > Cl^- > Br^- > I^-. This example highlights the significant diversity among supramolecular architectures capable of facilitating anion transport.

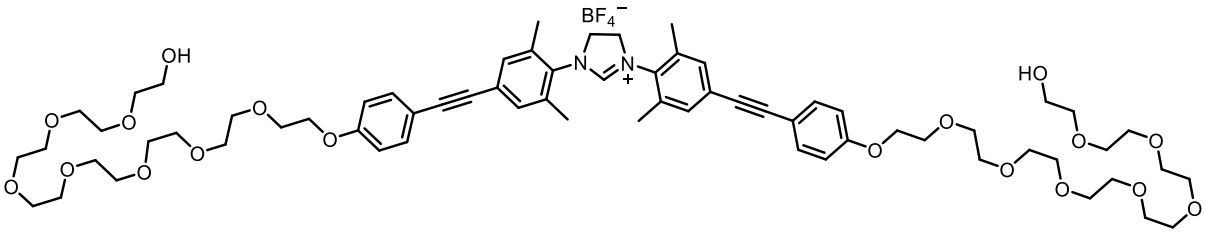


Figure 1.17. Imidazolium mobile anion carrier.[66]

1.4.1.1 Hydrogen Bonding Receptors for Ion-Pair Transport

Although described earlier as a simple acyclic HB motif for anion transport, the thiourea binding motif has also been incorporated into a more sophisticated preorganised receptor for ion-pair transport. Ion-pair transporters remain rare in the literature despite being highly desirable for biomimetic applications.[67–69] This is primarily due to the difficulties not only in binding both an anion and cation, but also in the elucidation of ion-pair binding and transport mechanisms with the current techniques available. The first example of an ion-pair transporter was reported by Smith and co-workers in 2003, who demonstrated that sodium and potassium chloride could be transported as a contact ion-pair by a macrobicycle (**Figure 1.18a**). It features a diaza-18-crown-6 motif for cation binding and an isophthalamide hydrogen bond donor for simultaneous chloride binding.[68]

Valkenier and co-workers have more recently reported a calix[6]arene tris-thiourea derivative capable of transporting organic ion-pairs (**Figure 1.18b**).[70] The transporter comprises of a calix[6]arene cavity for propylammonium binding and three pendant urea or thiourea motifs for anion binding. Transport assays were conducted using variations of the lucigenin assay, and they demonstrated that the transport of chloride was dependant on, and only occurred in the presence of, a propylammonium cation via the transport of the ion-pair.

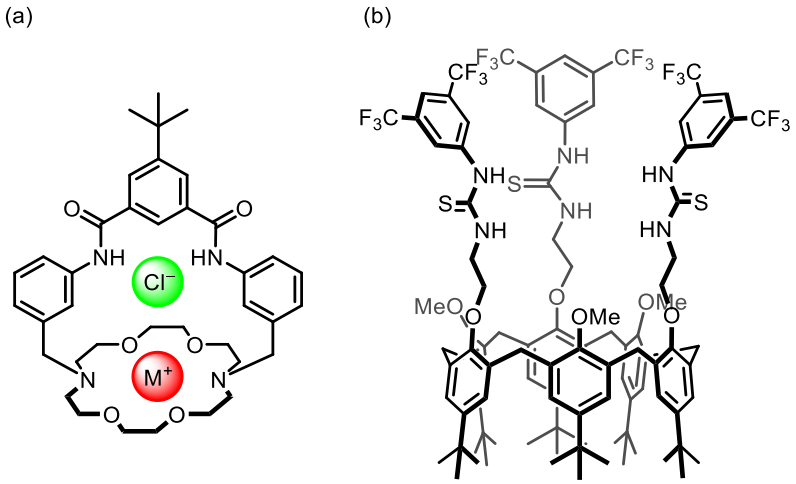


Figure 1.18. (a) Macrobicycle ion pair transporter with diaza-18-crown-6 motif for Na^+ and K^+ binding and an isophthalamide HB donor for Cl^- binding.[68] (b) Calix[6]arene tris-thiourea derivative capable of transporting organic ion-pairs.[70]

1.4.1.2 Anion Selectivity with HB receptors

$Cl^- > OH^-$ selectivity is critical for applications such as treatment of channelopathies, to avoid the toxic dissipation of cellular pH gradients. However, it is difficult to maintain high transport activity and achieve high anion selectivity. Whilst it is possible to tune the host-guest binding strength, lipophilicity and thus transport activity of HB receptors, acyclic analogues such as thioureas have no intrinsic $Cl^- > OH^-$ selectivity.[71] The first strategy used

to achieve anion selectivity is to maximise preorganisation and geometric complementarity between the transporter and guest anion. Davis and co-workers reported macrocyclic derivatives (**Figure 1.19b**) of their previous cholapod mobile carriers (**Figure 1.19a**),[55] which were capable of encapsulating the anion in a preoganised binding pocket. This enabled enhanced selectivity for chloride over nitrate by a factor of up to 2.5 relative to their acyclic cholapod analogues.[72] In addition, the cholaphanes were also more active than their acyclic counterparts and exhibited very high chloride over hydroxide selectivity (~100 fold) which is described as non-protonophoric activty.[71]

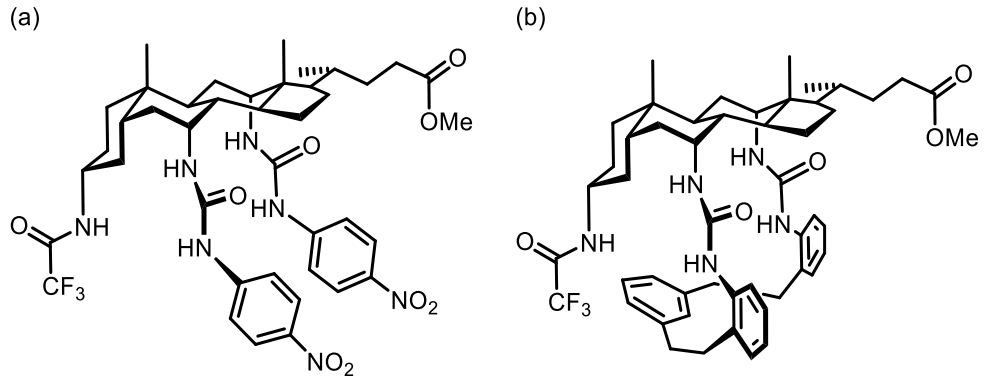


Figure 1.19. (a) Steroidal acyclic cholapod.[55] (b) macrocyclic cholaphane.[72]

1.4.2 Alternative Intermolecular Interactions for Anion Transport

Although, numerous artificial anion transporters have been reported in the literature, the vast majority of them suffer from poor selectivity, which limits their real-life application, such as replacing the functionality of faulty chloride channels in cystic fibrosis. Achieving both chloride selectivity *and* high transport activity is intrinsically difficult with acyclic HB receptors, yet these are the most ubiquitous abiotic anionophores in the literature to date. The use of non-classical intermolecular interactions for mediating anion transport, including C–H hydrogen bonding,[73] anion–π,[74] and sigma hole interactions,[50] have emerged as effective alternatives to polar acidic hydrogen bonding motifs. The following section will discuss promising examples of alternative interactions in the context of anion transport.

1.4.2.1 Anion-π Interactions

Whilst cation-π interactions are well-established within the literature,[75,76] anion-π interactions have been mostly overlooked, likely due to their counterintuitive nature and expectation of repulsive interaction. These primarily electrostatic interactions arise between an electron deficient aromatic system and an anion.[77,78] Whilst these interactions cannot compete with hydrogen bonds and sigma hole interactions in terms of strength, their neutrality and ease of introduction into anion recognition architectures has allowed anion-π interactions to have an increasing range of application in catalysis, sensing and transmembrane transport.[78]

The use of these exotic non-covalent interactions for membrane transport was pioneered by Matile and co-workers who reported the first examples of membrane transport mediated via anion-π interactions, in the form of anion–π slides, and ditopic mobile ion transporter systems.[59,79,64] They first incorporated electron deficient oligo(*p*-

phenylene)-*N,N*-naphthalenediimide (O-NDI) units into a membrane spanning membrane scaffold (**Figure 1.20a**). Later, they created a similar structure with oligo(*p*-phenylene)-*N,N*-perylenediimide (O-PDI) units. Both of these membrane-spanning supramolecules acted as slides for anions to cross the bilayer by 'hopping' from one NDI/PDI unit to another.

Since it was experimentally challenging to assess the complete role of the anion–π interactions in the transport process, the group adapted their NDI rigid rods into a series of NDI monomers which behaved as mobile anion transporters (**Figure 1.20b/c**).[81] Anion transport activity was determined using the HPTS, LG and CF fluorescent assays resulting in modest activities in the low µM range. They also achieved an unusual anti-Hofmeister selectivity trend of $Cl^- > Br^- > I^-$. After assessment of the carriers' selectivity towards oxyanions ($NO_3^- > ClO_4^- > SO_4^{2-} > AcO^-$) they reported the molecules' potential applications towards selective nitrate transport.

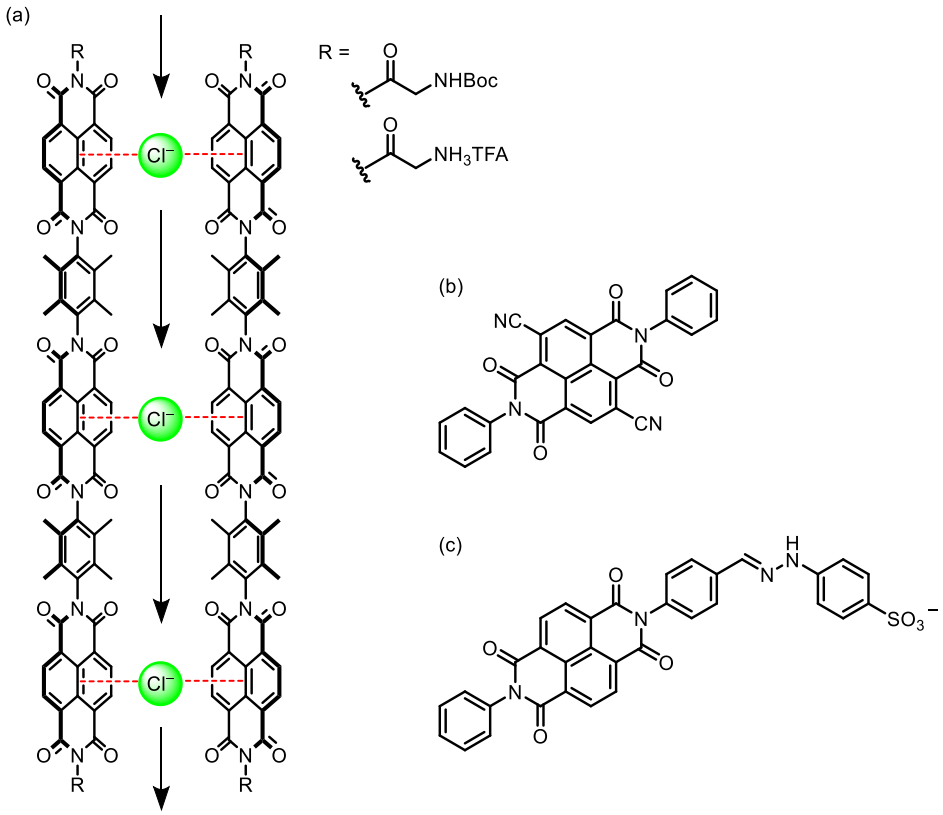


Figure 1.20. (a) Anion–π slide. (b/c) NDI mobile transporters.[81]

1.4.2.2 Sigma Hole Interactions

Sigma hole interactions are the non-covalent attraction between an electrophilic region (σ-hole) on an electron-deficient halogen or chalcogen atom (the bond donor), and a nucleophilic region of a Lewis base (the bond acceptor).[82] These interactions are associated with σ* orbitals on the halogen or chalcogen bond donor, and originate from anisotropic distribution of electron density which leads to a highly localized area of positive electrostatic surface potential on the heavier elements, known as the sigma hole (**Figure 1.21**). Sigma hole interactions have strict linear directionality; the σ holes are located on the extension of one of the covalent bonds to the atom, with the R-X···Anion bond angle near to 180° (where X represents the sigma-hole bond donor, **Figure 1.9**, **Page 14**).[83] The magnitude of the σ-hole increases with the electron deficiency and polarizability of the atom and can be enhanced by electron withdrawing substituents (**Figure 1.21**). The most effective halogen bond (XB) and chalcogen bond (ChB), donors are therefore associated with iodine and tellurium respectively.[84]

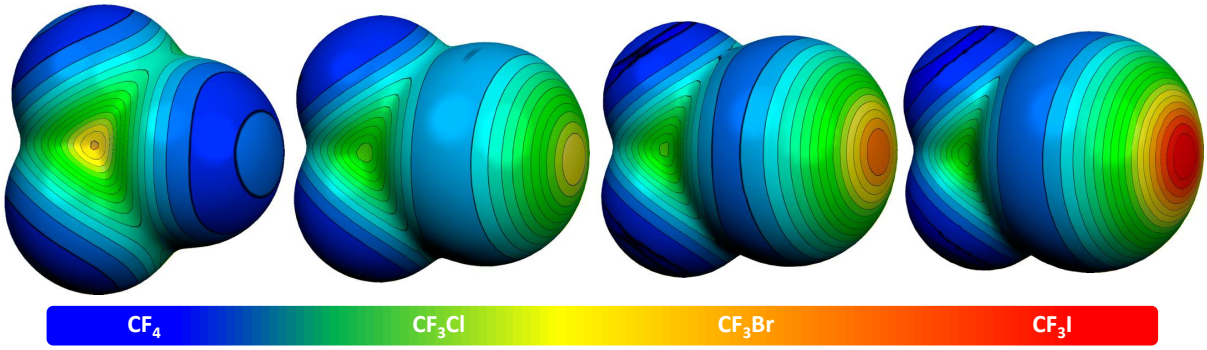


Figure 1.21. Molecular electrostatic potentials, in Hartrees, at the 0.001 e/bohr^3 isodensity surfaces of CF_4, CF_3Cl, CF_3Br and CF_3I. Red represents increasing region of positive potential.[84] Adapted with permission from reference [84] Copyright © Springer-Verlag 2006.

The nature of these interactions is still under investigation but the bonding contributions include electrostatic effects, charge transfer, polarization, and dispersion forces. These interactions are studied primarily in the solid state, but there has been great interest around halogen bonding anion recognition in solution due to the increased strength, directionality, and potential selectivity compared to hydrogen bonding systems.[85] This research has been pioneered primarily by the Taylor and Beer groups. In 2010, Taylor and co-workers presented a series of multidentate halogen bonding receptors for anion recognition (**Figure 1.22**).[86] Importantly, their neutral iodoperfluoroarene tripodal receptor bound strongly and selectively to chloride over the other halides and anionic species (K_a = 1.9 x 10^4 M^{-1} in acetone-d_6).

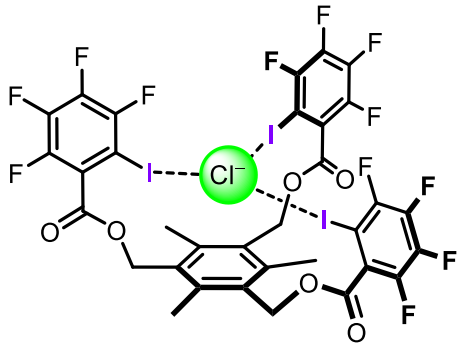


Figure 1.22. Tridentate halogen bonding receptor for anion recognition in solution.[86]

In the same year, Beer and co-workers reported the first example of halogen bond assisted [2]rotaxane formation through bromide anion-templated synthesis (**Figure 1.23a**).[87] The incorporation of halogens into the cavity of this interlocked structure greatly improved anion recognition capabilities. More recently, they reported a [2]rotaxane (**Figure 1.23b**), which was made water soluble with β-cyclodextrin stoppers, and could bind iodide with two orders of magnitude higher affinity that its HB analogue in pure water.[88] These key early

studies confirmed the viability of selective anion recognition and sensing with halogen bonding in aqueous media.

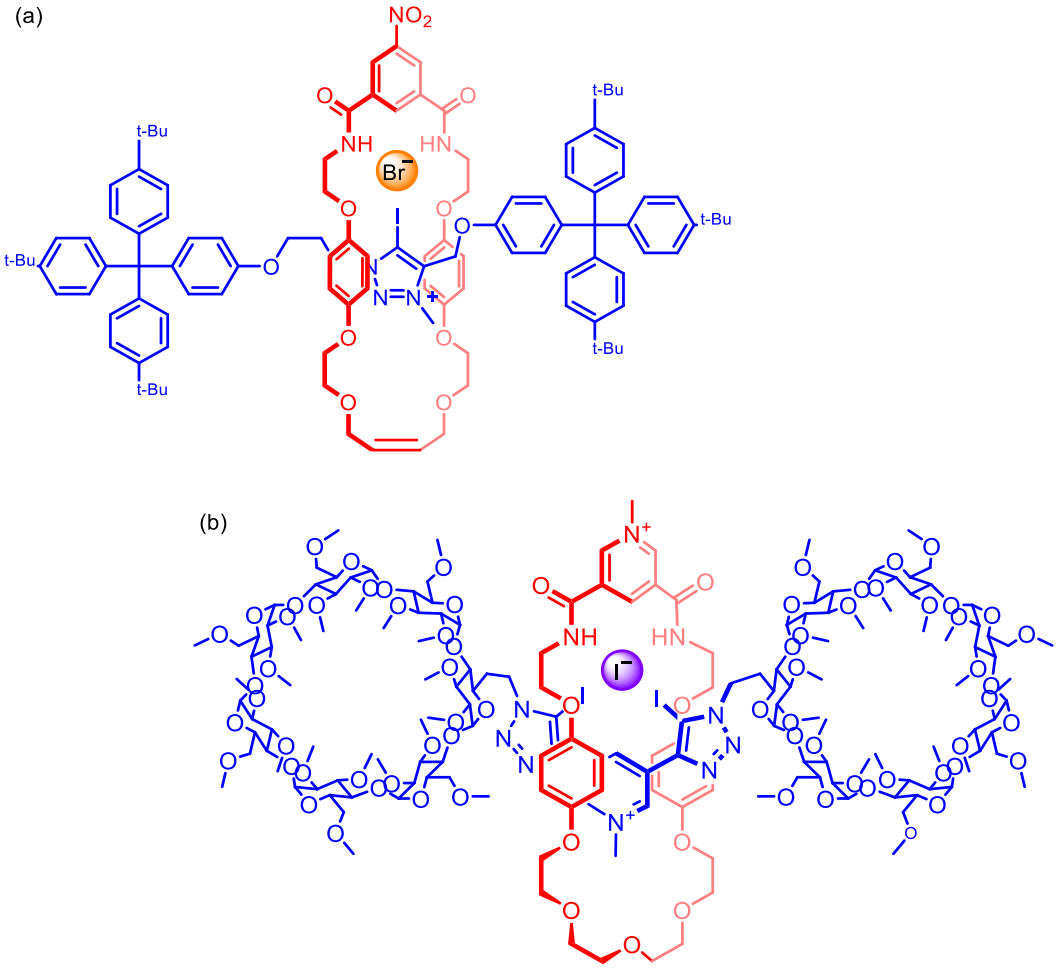


Figure 1.23. (a) XB templated [2]rotaxane.[87] (b) XB water soluble [2]rotaxane.[88]

Advantageously, sigma hole interactions are typically more hydrophobic than polar NH or OH hydrogen bond donors which is advantageous for membrane uptake. An additional consequence is that they are less inclined to promote detrimental transporter aggregation within the membrane.[73] Sigma hole interactions are currently under exploited within medicinal and biological chemistry, but it is anticipated that incorporation of XB and ChB interactions into anion transporters may improve both selectivity and binding strength (and hence transport activity).

There are currently only a handful of XB anion transporter examples known to date, ranging from macrocyclic structures to small molecules and channels.[89,90] Building upon their NDI-based mobile carriers, Matile and co-workers established that they could mediate transport with a series of ditopic anion-π and halogen bonding mobile transporters (**Figure 1.24a-c**), albeit with low activity (EC_{50} values up to 25 μM in the HPTS assay).[74]

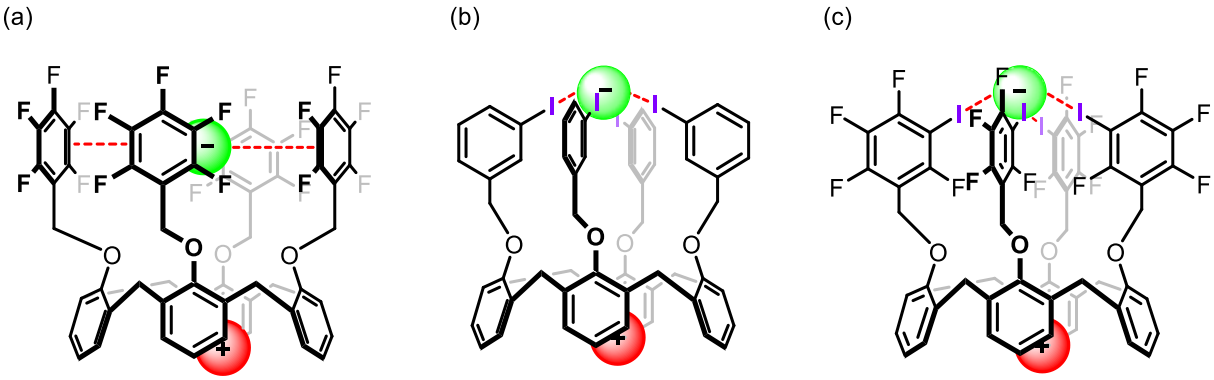


Figure 1.24. (a) Calix[4]arenes for anion-π. (b/c) halogen bonding anion transport. [74]

Within hydrogen bonding systems, reducing the size and sophistication of the transporters generally leads to inactivity or lack of selectivity.[91,92] However, Matile and co-workers established that even simple commercially available halogenated perfluoroalkanes and arenes could facilitate anion transport across membranes, including gaseous iodo-perfluoromethane (**Figure 1.25a**).[41] The halogen bonding transporters not only showed appreciable transport activity, but also some chloride selectivity. The electron withdrawing nature of the fluorine atoms increased the potency of the halogen bond donor, thus increasing the strength of anion binding. For example, perfluorination of hexyl iodide lowered the EC_{50} value from 2 mM (**Figure 1.25c**) to 3.1 μM (**Figure 1.25d**), corresponding to

an increase in transport activity. This was the first example of tuning the binding ability of halogen bonding in the context of increasing transport activity.

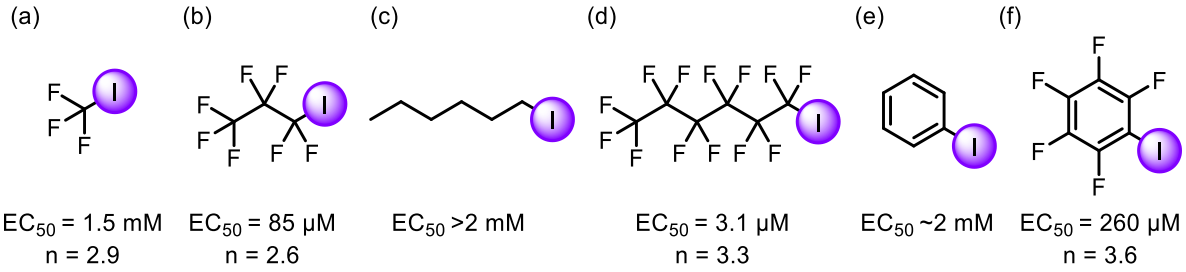


Figure 1.25. Halogenated perfluoroalkanes and arenes for anion transport across membranes.[41]

Since this example, more sophisticated XB structures have been reported. For example, Zeng and co-workers decorated a membrane-spanning chloride anion channel decorated with halogen bond donors and reported EC_{50} values as low as 3.6 μM in the HPTS assay.[93] In addition, Wang and co-workers presented a series of XB macrocyclic transporter systems, which also mediated chloride transport with low micromolar (**Figure 1.26**).[94]

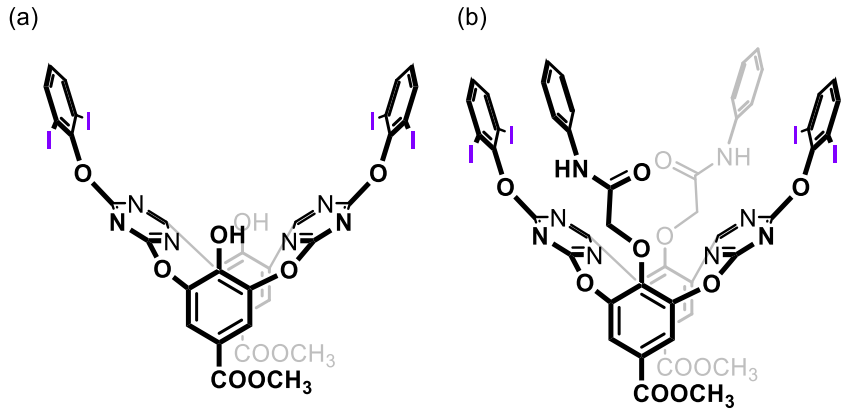


Figure 1.26. Halogen bonding macrocycles.[94]

1.4.2.3 Chalcogen and Pnictogen Bonding Receptors for Anion Transport

As previously discussed, the chalcogens have the ability to form two sigma-hole interactions per atom, as opposed to just one found in halogen bonding derivatives.[95] However, examples in the context of anion binding, and transport in particular, are rare. In a similar fashion, the pnictogens (group 15) can form up to three bonding interactions. These exotic interactions first arose in the context of anion transport when Matile and co-workers compared the transport activity of a family of electron deficient halogen, chalcogen and pnictogen bonding receptors (**Figure 1.27**).[96] They found that the tellurium-centred chalcogen bonding carriers (**Figure 1.27b**), were highly active in comparison to their halogen bonding analogues (**Figure 1.27a**), which is likely attributed to the presence of two sigma-hole donors and the proximity of the two π-acidic perfluoro benzene surfaces for secondary anion–π interactions. On the other hand, they found that the larger tris(perfluorophenyl)stibane pnictogen bonding receptor (**Figure 1.27c**) damaged the integrity of the vesicles by forming membrane-disruptive supramolecular amphiphiles.

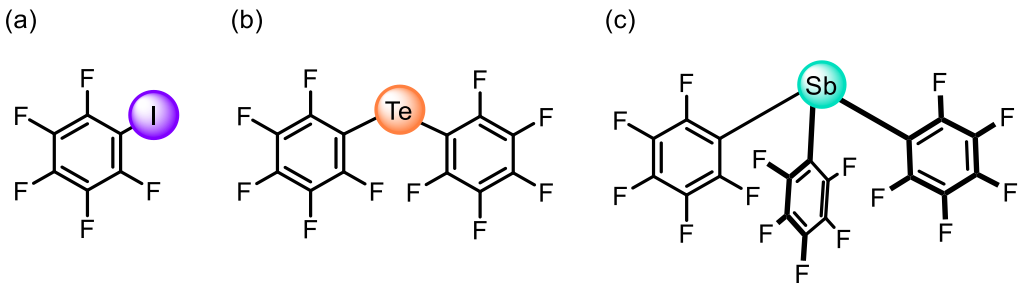


Figure 1.27. Electron deficient (a) halogen, (b) chalcogen and (c) pnictogen bonding anionophores.[96]

This research led the way for future incorporations of ChB and PnB into anion transporters. Gabbai and co-workers designed and synthesised the diaryltellurides Mes(C_6F_5)Te and (C_6F_5)$_2$Te, and demonstrated that their transport activity could be

enhanced by oxidative methylation to form $[Mes(C_6F_5)TeMe]^+$ and $[(C_6F_5)_2TeMe]^+$, (**Figure 1.28,** (a) and (b) respectively).[97] They hypothesised that this enhancement is triggered by the lowering of the energy of the tellurium-centred σ* orbitals and deepening of the associated sigma-holes, leading to increased Lewis acidity and potency of the chalcogen bond donor.

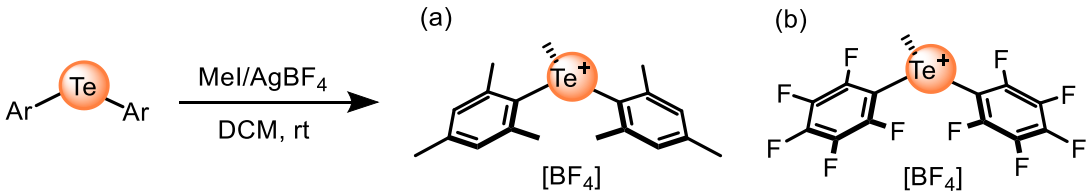


Figure 1.28. The oxidisation products (a) and (b), synthesised from their parent diaryltellurides.[97]

Gabbai and co-workers have also introduced a variety of other main-group elements for anion transport, including pnictogenium cations and phosphonium boranes.[98] In this work the ability of tetraaryl-stibonium and tetraaryl-bismuthonium cations (**Figure 1.29**) to transport fluoride anions was assessed not only in LUVs but also in human erythrocytes cells.[98] There was existing precedent for the ability of phosphonium cations to cross the lipid bilayer and interact with mitochondria,[99] but these were not suitable for anion transport because they lacked Lewis acidic donor sites. As a result, this led to the development of the tetraaryl-stibonium and tetraaryl-bismuthonium cations which act as pnictogen bond donors. Using a fluoride selective electrode, they determined that the most hydrophobic tetraaryl-stibonium carriers, had the highest activity, followed by the analogous bismuth cations. Not only do these cations have advantageous increased lipophilicity, they are known to form a covalent

bond with fluoride anions which may explain their selectivity towards this halide (**Figure 1.29**).

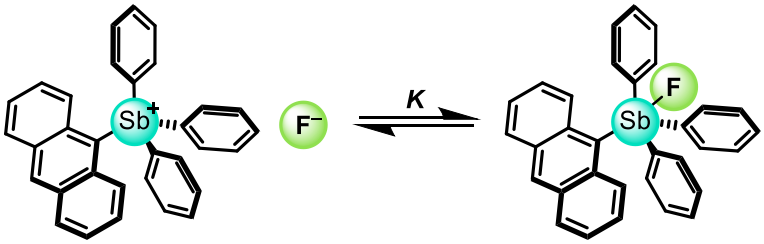


Figure 1.29. Pnictogenium anionophore and the binding equilibrium that occurs with fluoride.[98]

1.4.3 Stimuli Responsive Anion Transporters

In nature, transmembrane ion channels, pumps and carriers are responsive to changes in their environment, whether this be chemical or physical.[25] For example, rhodopsins respond to light to regulate transmembrane ion currents.[100] These membrane proteins are studied for applications within optogenetics, therapeutic drugs and emerging biotechnologies.[101,102] There are two classes of rhodopsins, the first being microbial, which act as gated pumps, sensors or channels; and the second act as photoreceptors in the eyes of vertebrates and invertebrates.[100] One commonality between the two classes is that they are both controlled by the isomerisation of the photo-responsive chromophore retinal, upon photon absorption. Bacteriorhodopsin is a membrane pump found in archaea built from several membrane-spanning alpha helices predominantly comprising of non-polar amino acids.[25] When illuminated with light, retinal isomerises from the *cis* to *trans* isomer which allows protons to be pumped across the membrane to generate a proton gradient which in turn drives ATP synthesis.

Many transmembrane transport systems are ligand or voltage-gated and thus, respond to their chemical environment. The voltage-gated potassium channels are an example of channels which respond to changes in the membrane's potential.[25] In order to open and close, they rely on the movement of a transmembrane-voltage-sensitive paddle, known as the S4 domain, which contains multiple permanently charged arginine residues.[103,104] When open, potassium flows down its concentration gradient to return the cell to its resting state during action potentials.

To date, man-made transmembrane systems pale in comparison to the elegance and functionality displayed by the biological machinery.[105] To match their complexity, and function, the potential of dynamic systems working in the out-of-equilibria regime using chemical fuel, photons or other potential gradients to perform work continuously needs to be harnessed.[106] Gaining spatio-temporal control over abiotic components is integral to meeting this challenge. There are ways in which this could be achieved with the use of external stimuli.[107]

1.4.3.1 Restricting Movement and Self-Assembly

Gaining control over the ability of the mobile ion carrier can be used as a mechanism in which to control the transport process. Jeong and co-workers reported a urea-based procarrier which was unable to partition into the bilayer due to caging with hydrophilic stoppers, including a carboxylic acid or polar sugar (**Figure 1.30**).[108] Only once this stopper was cleaved by enzymes was the carrier free to perform transmembrane transport via a mobile carrier mechanism.

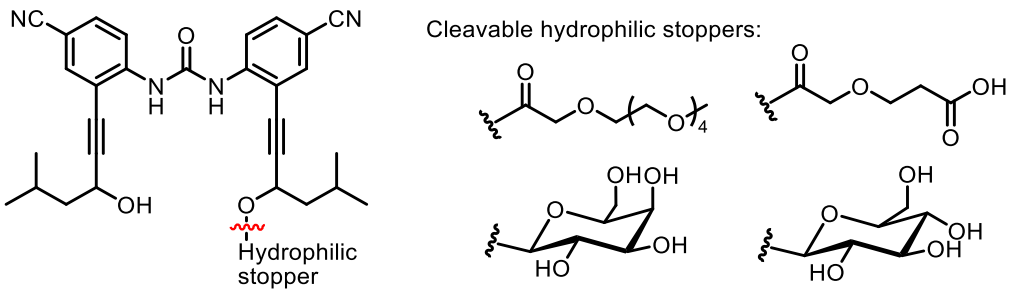


Figure 1.30. Urea-based procarrier and the hydrophilic tails for caging.[108]

In a similar fashion, Manna and co-workers reported a water soluble sulfonium-based procarrier (**Figure 1.31a**), again with removable hydrophilic groups that rendered it unable to perform anion transport.[109] The carrier could then be activated by three different stimuli; 365 nm UV light, reduction with glutathione (GSH) or in the presence of reactive oxygen species (ROS). Once activated (**Figure 1.31b**), the carrier could selectively transport chloride, dissipating a pH gradient and leading to cell death. This is of particular importance since cancer cells over produce ROS and GSH, thus this carrier may be suited to applications within targeted cancer therapy.

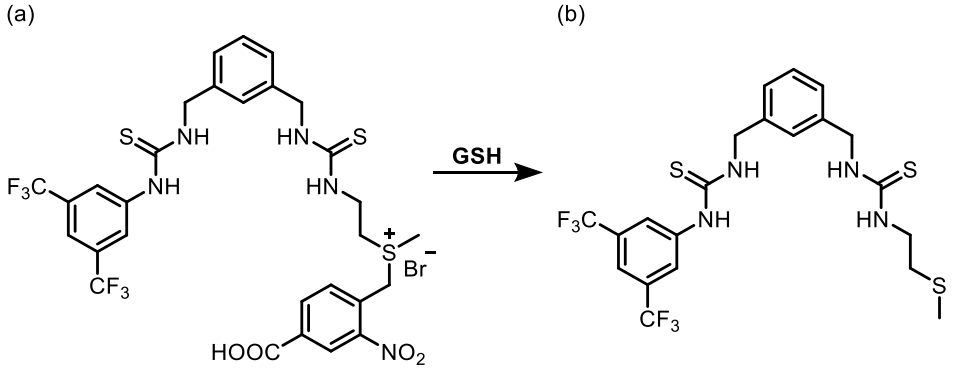


Figure 1.31. (a) Water soluble sulfonium-based procarrier and its transport-active analogue (b).[109]

In a related approach, Gabbai and co-workers reported an inactive dicationic hydrophilic stibonium/sulfonium procarrier,[110] which upon fast reduction of the sulfonium moiety to the corresponding thioether with glutathione, generates a lipophilic mono-cationic carrier suitable for transmembrane chloride transport via pnictogen bonding. The observations made by Gabbai and co-workers based on this example and previous examples demonstrate that there is potential to control the redox states of main group elements as a means to control the properties of chalcogen bond donors.

Inhibiting channel self-assembly has been a popular approach when controlling channel-mediated transport. One such example was presented by Talukdar and co-workers, who prepared a 2,4-nitrobenzenesulfonyl (DNS) protected 2-hydroxy isophthalamide which cannot facilitate transport as a monomer unit (**Figure 1.32**).[111] Upon the addition of glutathione, the DNS group is cleaved off exposing the hydroxyl group and engenders channel self-assembly. This membrane spanning channel was capable of M^+/X^- antiport and causing apoptosis in LUVs and MCF-7 cancer cells.

Since esterase enzymes are also overexpressed in cancer cells, Talukdar and co-workers adapted this approached to generate esterase-responsive channels.[112] They used methyl pivalate as a caging group for their original isophthalamide monomer which could be removed with the addition of esterase enzymes.[112] After activation and self-assembly they observed both apoptosis and disruption of autophagy indicating the potential applications in cancer treatment.[113]

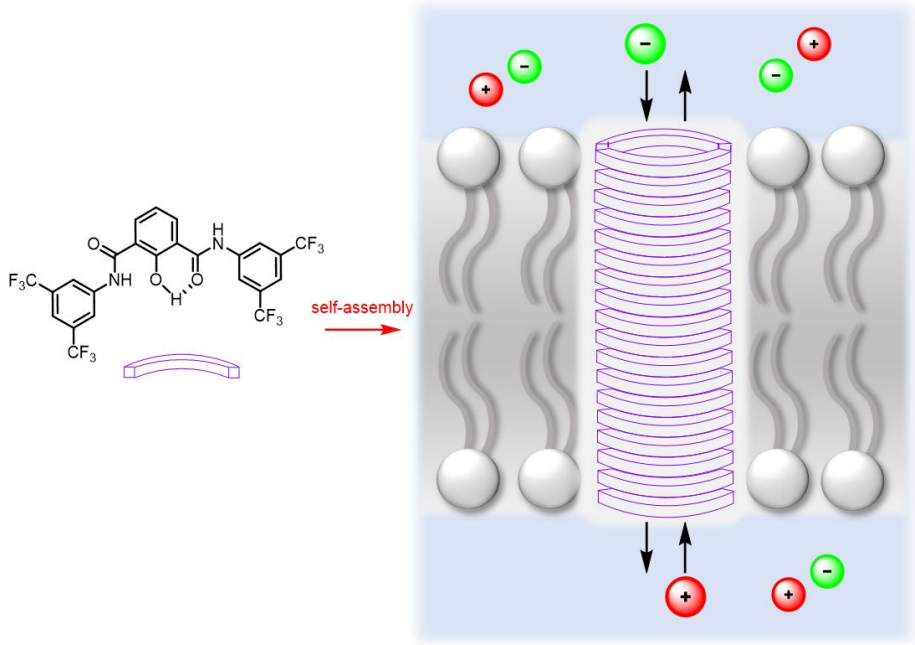


Figure 1.32. Isophthalamide monomer and its self-assembly into a membrane spanning channel.[111–113]

In an alternative approach, Zhu, Liu and co-workers used competitive metal cation binding to control channel formation and transmembrane transport.[114] They designed an artificial phenanthroline derivative which assembled into a helical channel via intermolecular π-π interactions and intramolecular H-bonds. This channel supports cation transport across LUVs with a selectivity trend of $Cs^+ > Rb^+ > K^+ > Na^+ > Li^+$, however, in the presence of Cu(I), the single helix converts into an intertwined double helix thus blocking the cavity and switching off transport. This process could be reversed by the addition of ammonia to remove the Cu(I) and re-generate the original active single helical channel.

More recently, Clayden, Cockroft, Webb and co-workers developed a foldamer in which transport could be activated with the addition of Cu(II) (**Figure 1.33**).[115] In the presence of copper chloride, their octameric α-aminoisobutyric acid foldamer unit assembled into dimer using head-to-tail hydrogen bonding with a membrane-

spanning pore throughout the centre for anion transport. They reported a 5- to 8-fold increase in transport activity in comparison to the monomers. This activity could then be switched off with the addition of EDTA to remove the Cu(II) from the complex and dismantled the helical channel.

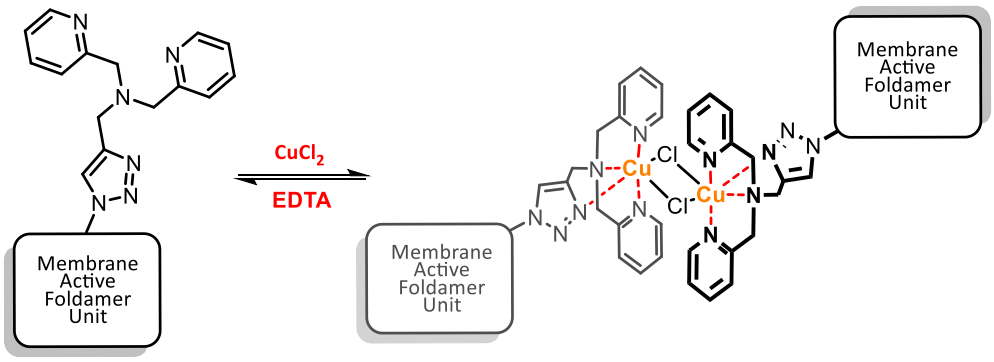


Figure 1.33. Foldamer monomer and formation membrane-spanning pore in the presence of copper chloride.[115]

1.4.3.2 Restricting the Binding Site

An alternative method of "caging" a mobile carrier is by blocking or restricting the binding site such that anion recognition is prevented until the cage is removed by an external stimulus. Gale and co-workers have used gold to block the binding site of a bis-imidazole-based anion transporter (**Figure 1.34a**).[116] When coordinated to Au(III), the carrier was not able to facilitate transport, gold decomplexation upon addition of a reducing agent such as glutathione uncaged the binding site and activated the transporter (**Figure 1.34b**).

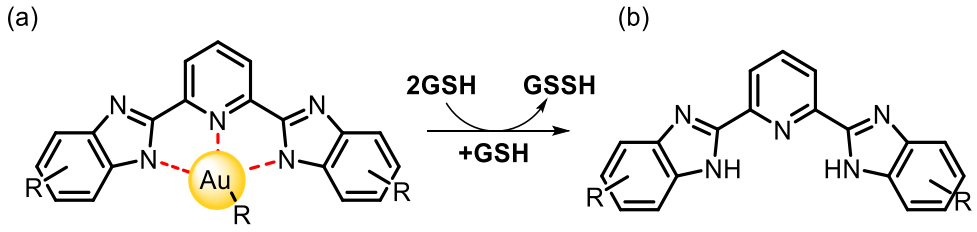


Figure 1.34. Stimuli-responsive bis-imidazole-based anion transporter.[116]

1.4.3.3 Photoswitches

The use of photoswitches to control host-guest binding ability and transport activity has gained recent popularity. The first example of a photoswitchable azobenzene-based transporter came from Jeong and co-workers.[117] They conjugated urea or thiourea motifs either side of an azobenzene photoswitch, such that strong anion binding could only occur when in the *cis* conformation via cooperative H-bond coordination. For all carriers in the series, they found that the *trans* isomers could not facilitate transport, in-situ irradiation with 365 nm UV light yielded the transport-active *cis* isomer.

Kerckhoffs and Langton then built on this foundation and presented azobenzenes appended with squaramide anion binding motifs (**Figure 1.35**).[48] In this example, they avoided the use of bio-incompatible UV light for isomerisation, by using red shifted photoswitches that could be switched between the inactive *trans* isomer and transport-active *cis* isomer using biocompatible red light. A chloride selective electrode was used to measure the chloride efflux whilst performing *in-situ* photo-isomerisation of the carrier in the membrane to illustrate the reversibility of the system.

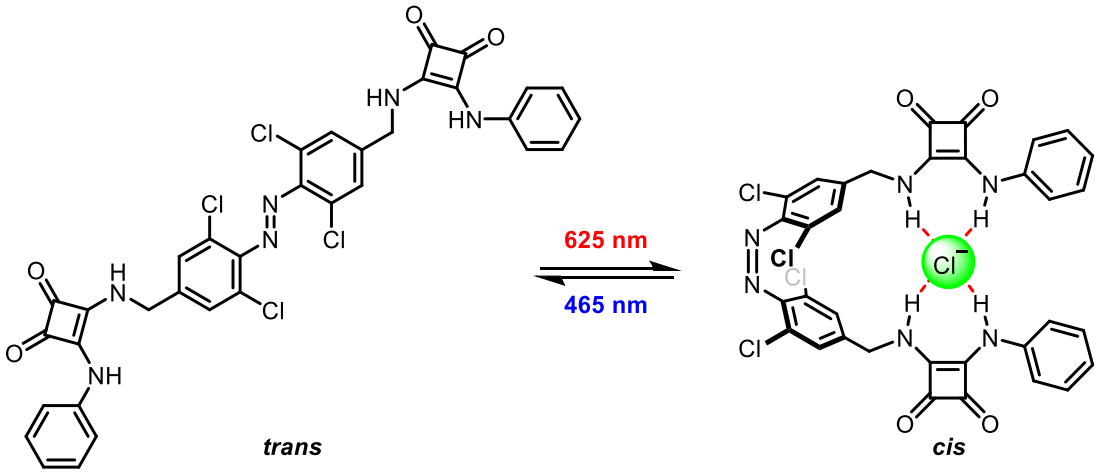


Figure 1.35. Photo-switchable squaramide anion transporter.[48]

Other photoswitches have since been employed for anion transport purposes. Gale, Feringa and co-workers have incorporated a stiff-stilbene photo-switch into a thiourea based reversible carrier scaffold.[11-7] They controlled activity by switching transport on with 365 nm UV light and off with 385 nm light. Most recently, Talukdar and co-workers presented anion transmembrane transport controlled by a phenyl-hydrazone photo-switch (**Figure 1.36**).[119] Unlike previous examples, transport was off in the *cis* conformation due to intramolecular hydrogen bonding blocking the anion receptor binding site. The transporter could be switched into the *trans* isomer activating transport with the addition of acid. The carrier could be switched into the 'off' *cis* isomer with 365 nm light, although reversible switching was not shown in the membrane.

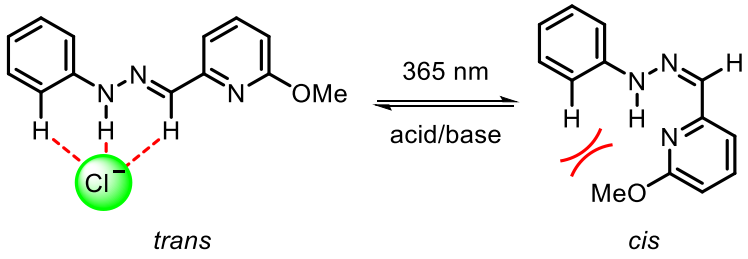


Figure 1.36. Photo-switchable phenyl-hydrazone transporter.[119]

1.5 Project Aims

The aims of this project are to develop mobile carriers which function as effective anion transporters across lipid bilayer membranes with an ultimate goal of developing carriers that are selective for chloride and stimuli-responsive. Hydrogen, halogen and chalcogen bonding will be exploited to bind the anionic guest species, and the anion transport activity and selectivity will be investigated. The aim is then to explore the effect of multidentate systems on membrane transport efficiency and selectivity. Novel approaches to controlling ion transport using light will also be investigated.

Chapter 2 describes the design, synthesis and testing of readily accessible monodentate halogen and hydrogen bonding receptors for anion transport applications.

Chapter 3 describes the design, synthesis and testing of bidentate halogen and chalcogen bonding anion receptors with a pre-organised binding cavity capable of encapsulating the anion and providing a hydrophilic pathway across the bilayer for the anion. Detailed investigations into the non-protonophoric activity of these carriers will also be presented.

Chapter 4 describes the design, synthesis and testing of a photo-caged, stimuli responsive anion transporter and introduces a novel approach of controlling anion transport by tethering the anion carrier to the lipid bilayer. It explores the use of photo-protecting groups, such as *o*-nitrobenzyl and coumarin, as photo-labile linkers between the mobile carriers and the membrane anchoring groups. The mechanism and kinetics of photocleavage in and ex situ will also be explored.

Chapter 5 outlines the experimental procedures undertaken throughout this research and *Chapter 6* summarises and concludes this thesis.

1.6 References

1 D. J. Cram, *Angew. Chem. Int. Ed. Engl.*, 1988, **27**, 1009–1020.

2 J.-M. Lehn, *Angew. Chem. Int. Ed. Engl.*, 1988, **27**, 89–112.

3 C. J. Pedersen, *Angew. Chem. Int. Ed. Engl.*, 1988, **27**, 1021–1027.

4 J.-P. Sauvage, *Angew. Chem. Int. Ed.*, 2017, **56**, 11080–11093.

5 J. F. Stoddart, *Angew. Chem. Int. Ed.*, 2017, **56**, 11094–11125.

6 B. L. Feringa, *Angew. Chem. Int. Ed.*, 2017, **56**, 11060–11078.

7 P. Imbrici, A. Liantonio, G. M. Camerino, M. De Bellis, C. Camerino, A. Mele, A. Giustino, S. Pierno, A. De Luca, D. Tricarico, J.-F. Desaphy and D. Conte, *Front. Pharmacol.*, 2016, **7**, 121.

8 J.-B. Kim, *Korean J. Pediatr.*, 2014, **57**, 1–18.

9 S. G. Chang, D. Littlejohn and K. Y. Hu, *Science*, 1987, **237**, 756–758.

10 E. Medjedovic, S. Medjedovic, D. Deljo and A. Sukalo, *Mater. Sociomed.*, 2015, **27**, 395–398.

11 A. J. Wiemer and D. F. Wiemer, *Top. Curr. Chem.*, 2015, **360**, 115–160.

12 F. Dressler and P. R. Schreiner, *Anion-Binding Catal.*, 2022, 1–77.

13 N. H. Evans and P. D. Beer, *Angew. Chem. Int. Ed.*, 2014, **53**, 11716–11754.

14 N. Busschaert, C. Caltagirone, W. Van Rossom and P. A. Gale, *Chem. Rev.*, 2015, **115**, 8038–8155.

15 P. D. Beer and P. A. Gale, *Angew. Chem. Int. Ed.*, 2001, **40**, 486–516.

16 N. Busschaert, R. B. P. Elmes, D. D. Czech, X. Wu, I. L. Kirby, E. M. Peck, K. D. Hendzel, S. K. Shaw, B. Chan, B. D. Smith, K. A. Jolliffe and P. A. Gale, *Chem. Sci.*, 2014, **5**, 3617–3626.

17 Y. Liu, A. Sengupta, K. Raghavachari and A. H. Flood, *Chem*, 2017, **3**, 411–427.

18 P. Jungwirth, *J. Phys. Chem. Lett.*, 2013, **4**, 4258–4259.

19 M. J. Langton, C. J. Serpell and P. D. Beer, *Angew. Chem. Int. Ed.*, 2016, **55**, 1974–1987.

20 P. Walter, B. Alberts, A. Johnson, J. Lewis, M. Raff and K. Roberts, *Molecular Biology of the Cell*, Garland, 4th Ed., 2002.

21 L. E. Bickerton, T. G. Johnson, A. Kerckhoffs and M. J. Langton, *Chem. Sci.*, 2021, **12**, 11252–11274.

22 J. T. Davis, O. Okunola and R. Quesada, *Chem. Soc. Rev.*, 2010, **39**, 3843–3862.

23 H. Lodish, A. Berk, S. L. Zipursky, P. Matsudaira, D. Baltimore and J. Darnell, in *Molecular Biology of the Cell*, ed. W. H. Freeman, Fourth Edi., 2002, pp. Uniporter-Catalyzed Transport.

24 H. Lodish, A. Berk, S. L. Zipursky, P. Matsudaira, D. Baltimore and J. Darnell, in *Molecular Biology of the Cell*, ed. W. H. Freeman, Fourth Edi., 2002, pp. Cotransport by Symporters and Antiporters.

25 G. G. Jeremy M. Berg, Lubert Stryer, John Tymoczko, *Biochemistry*, W.H. Freeman;, Ninth Edit., 2019.

26 Y. Zhou, J. H. Morais-Cabral, A. Kaufman and R. Mackinnon, *Nature*, 2001, **414**, 43–48.

27 M. Haas and B. 3rd Forbush, *J. Bioenerg. Biomembr.*, 1998, **30**, 161–172.

28 T. da S. Cunha and I. P. Heilberg, *Int. J. Nephrol. Renovasc. Dis.*, 2018, **11**, 291–301.

29 H. Li, H. Valkenier, A. G. Thorne, C. M. Dias, J. A. Cooper, M. Kieffer, N. Busschaert, P. A. Gale, D. N. Sheppard and A. P. Davis, *Chem. Sci.*, 2019, **10**, 9663–9672.

30 J. C. Freedman, in *Cell Physiology Source Book*, ed. N. Sperelakis, Fourth Edi., Academic Press, San Diego, 2012, ch. 4, pp. 61–66.

31 C. Moore and B. C. Pressman, *Biochem. Biophys. Res. Commun.*, 1964, **15**, 562–567.

32 M. C. Rose and R. W. Henkens, *Biochim. Biophys. Acta*, 1974, **372**, 425–435.

33 P. Läuger, *Science*, 1972, **178**, 24–30.

34 C. M. Liu and T. E. Hermann, *J. Biol. Chem.*, 1978, **253**, 5892–5894.

35 W. L. Erdahl, C. J. Chapman, R. W. Taylor and D. R. Pfeiffer, *Biophys. J.*, 1994, **66**, 1678–1693.

36 P. W. Reed and H. A. Lardy, *J. Biol. Chem.*, 1972, **247**, 6970–6977.

37 T. Sato, H. Konno, Y. Tanaka, T. Kataoka, K. Nagai, H. H. Wasserman and S. Ohkuma, *J. Biol. Chem.*, 1998, **273**, 21455–21462.

38 S. Ohkuma, T. Sato, M. Okamoto, H. Matsuya, K. Arai, T. Kataoka, K. Nagai and H. H. Wasserman, *Biochem. J.*, 1998, **334**, 731–741.

39 S. Matile and N. Sakai, *Anal. Methods Supramol. Chem.*, 2012, 711–742.

40 A. M. Gilchrist, P. Wang, I. Carreira-Barral, D. Alonso-Carrillo, X. Wu, R. Quesada and P. A. Gale, *Supramol. Chem.*, 2021, 1–20.

41 A. V. Jentzsch, D. Emery, J. Mareda, S. K. Nayak, P. Metrangolo, G. Resnati, N. Sakai and S. Matile, *Nat. Commun.*, 2012, **3**, 905.

42 K. M. Bak, B. van Kolck, K. Maslowska-Jarzyna, P. Papadopoulou, A. Kros and M. J. Chmielewski, *Chem. Commun.*, 2020, **56**, 4910–4913.

43 L. Martínez-Crespo, S. H. Hewitt, N. A. De Simone, V. Šindelář, A. P. Davis, S. Butler and H. Valkenier, *Chem. Eur. J.*, 2021, **27**, 7367–7375.

44 D. Magda, P. Lecane, Z. Wang, W. Hu, P. Thiemann, X. Ma, P. K. Dranchak, X. Wang, V. Lynch, W. Wei, V. Csokai, J. G. Hacia and J. L. Sessler, *Cancer Res.*, 2008, **68**, 5318–5325.

45 S. M. Kaiser and B. I. Escher, *Environ. Sci. Technol.*, 2006, **40**, 1784–1791.

46 S. Tardito, I. Bassanetti, C. Bignardi, L. Elviri, M. Tegoni, C. Mucchino, O. Bussolati, R. Franchi-Gazzola and L. Marchiò, *J. Am. Chem. Soc.*, 2011, **133**, 6235–6242.

47 N. Renier, O. Reinaud, I. Jabin and H. Valkenier, *Chem. Commun.*, 2020, **56**, 8206–8209.

48 A. Kerckhoffs and M. J. Langton, *Chem. Sci.*, 2020, **11**, 6325–6331.

49 J. W. Steed and J. L. Atwood, *Supramolecular Chemistry: Second Edition*, 2009.

50 D. A. Decato, E. A. John, O. B. Berryman, M. S. Taylor, A. Docker, P. D. Beer, L. Turunen, M. Erdélyi, S. Wilcox, W. Herrebout, M. Erdelyi, A. Vargas Jentzsch, S. Matile, J. J. Koenig, M. Breugst, R. L. Sutar, C. Fave, B. Schöllhorn, P. S. Ho, D. M. Anderson, K. T. Mahmudov, V. A. Aliyeva, M. F. C. Guedes da Silva and A. J. L. Pombeiro, *Halogen Bonding in Solution*, 2021.

51 N. Busschaert, S. J. Bradberry, M. Wenzel, C. J. E. Haynes, J. R. Hiscock, I. L. Kirby, L. E. Karagiannidis, S. J. Moore, N. J. Wells, J. Herniman, G. J. Langley, P. N. Horton, M. E. Light, I. Marques, P. J. Costa, V. Félix, J. G. Frey and P. A. Gale, *Chem. Sci.*, 2013, **4**, 3036–3045.

52 X. Wu, A. M. Gilchrist and P. A. Gale, *Chem*, 2020, **6**, 1296–1309.

53 N. L. Kilah and P. D. Beer, eds. P. A. Gale and W. Dehaen, Springer Berlin Heidelberg, Berlin, Heidelberg, 2010, pp. 301–340.

54 P. A. Gale, J. T. Davis and R. Quesada, *Chem. Soc. Rev.*, 2017, **46**, 2497–2519.

55 B. A. McNally, A. V. Koulov, T. N. Lambert, B. D. Smith, J. B. Joos, A. L. Sisson, J. P. Clare, V. Sgarlata, L. W. Judd, G. Magro and A. P. Davis, *Chem. Eur. J.*, 2008, **14**, 9599–9606.

56 S. J. Edwards, I. Marques, C. M. Dias, R. A. Tromans, N. R. Lees, V. Félix, H. Valkenier and A. P. Davis, *Chem. – A Eur. J.*, 2016, **22**, 2004–2011.

57 V. Saggiomo, S. Otto, I. Marques, V. Félix, T. Torroba and R. Quesada, *Chem. Commun.*, 2012, **48**, 5274–5276.

58 R. I. Storer, C. Aciro and L. H. Jones, *Chem. Soc. Rev.*, 2011, **40**, 2330–2346.

59 N. Busschaert, I. L. Kirby, S. Young, S. J. Coles, P. N. Horton, M. E. Light and P. A. Gale, *Angew. Chem. Int. Ed.*, 2012, **51**, 4426–4430.

60 X. Wu, N. Busschaert, N. J. Wells, Y. B. Jiang and P. A. Gale, *J. Am. Chem. Soc.*, 2015, **137**, 1476–1484.

61 G. Picci, M. Kubicki, A. Garau, V. Lippolis, R. Mocci, A. Porcheddu, R. Quesada, P. C. Ricci, M. A. Scorciapino and C. Caltagirone, *Chem. Commun.*, 2020, **56**, 11066–11069.

62 K. M. Bąk, K. Chabuda, H. Montes, R. Quesada and M. J. Chmielewski, *Org. Biomol. Chem.*, 2018, **16**, 5188–5196.

63 R. Pomorski, M. García-Valverde, R. Quesada and M. J. Chmielewski, *RSC Adv.*, 2021, **11**, 12249–12253.

64 P. Wang, X. Wu and P. A. Gale, *Supramol. Chem.*, 2021, **33**, 143–149.

65 T. Muraoka, T. Shima, T. Hamada, M. Morita, M. Takagi, K. V. Tabata, H. Noji and K. Kinbara, *J. Am. Chem. Soc.*, 2012, **134**, 19788–19794.

66 M. Mori, K. Sato, T. Ekimoto, S. Okumura, M. Ikeguchi, K. V. Tabata, H. Noji and K. Kinbara, *Chem. Asian J.*, 2021, **16**, 147–157.

67 P. A. Gale, C. C. Tong, C. J. E. Haynes, O. Adeosun, D. E. Gross, E. Karnas, E. M. Sedenberg, R. Quesada and J. L. Sessler, 2010, 3240–3241.

68 A. V Koulov, J. M. Mahoney and B. D. Smith, *Org. Biomol. Chem.*, 2003, **1**, 27–29.

69 J. H. Lee, J. H. Lee, Y. R. Choi, P. Kang, M.-G. Choi and K.-S. Jeong, *J. Org. Chem.*, 2014, **79**, 6403–6409.

70 G. Grauwels, H. Valkenier, A. P. Davis, I. Jabin and K. Bartik, *Angew. Chem. Int. Ed.*, 2019, **58**, 6921–6925.

71 X. Wu, L. W. Judd, E. N. W. Howe, A. M. Withecombe, V. Soto-Cerrato, H. Li, N. Busschaert, H. Valkenier, R. Pérez-Tomás, D. N. Sheppard, Y. B. Jiang, A. P. Davis and P. A. Gale, *Chem*, 2016, **1**, 127–146.

72 L. W. Judd and A. P. Davis, *Chem. Commun.*, 2010, **46**, 2227–2229.

73 M. Lisbjerg, H. Valkenier, B. M. Jessen, H. Al-Kerdi, A. P. Davis and M. Pittelkow, *J. Am. Chem. Soc.*, 2015, **137**, 4948–4951.

74 A. Vargas Jentzsch, D. Emery, J. Mareda, P. Metrangolo, G. Resnati and S. Matile,

Angew. Chem. Int. Ed., 2011, **50**, 11675–11678.

75 D. A. Dougherty, *Acc. Chem. Res.*, 2013, **46**, 885–893.

76 A. S. Mahadevi and G. N. Sastry, *Chem. Rev.*, 2013, **113**, 2100–2138.

77 P. Gamez, T. J. Mooibroek, S. J. Teat and J. A. N. Reedijk, *Acc. Chem. Res.*, 2007, **40**, 435–444.

78 D. X. Wang and M. X. Wang, *Acc. Chem. Res.*, 2020, **53**, 1364–1380.

79 S. Bhosale, A. L. Sisson, P. Talukdar, A. Fürstanberg, N. Banetji, E. Vauthey, G. Bollot, J. Mareda, C. Röger, F. Würthner, N. Sakai and S. Matile, *Science*, 2006, **313**, 84–86.

80 A. Perez-Velasco, V. Gorteau and S. Matile, *Angew. Chem. Int. Ed.*, 2008, **47**, 921–923.

81 R. E. Dawson, A. Hennig, D. P. Weimann, D. Emery, V. Ravikumar, J. Montenegro, T. Takeuchi, S. Gabutti, M. Mayor, J. Mareda, C. A. Schalley and S. Matile, *Nat. Chem.*, 2010, **2**, 533–538.

82 G. R. Desiraju, P. S. Ho, L. Kloo, A. C. Legon, R. Marquardt, P. Metrangolo, P. Politzer, G. Resnati and K. Rissanen, *Pure Appl. Chem.*, 2013, 85, 1711.

83 A. Brown and P. D. Beer, *Chem. Commun.*, 2016, **52**, 8645–8658.

84 T. Clark, M. Hennemann, J. S. Murray and P. Politzer, *J. Mol. Model.*, 2007, **13**, 291–296.

85 J. Y. C. Lim and P. D. Beer, *Chem*, 2018, **4**, 731–783.

86 M. G. Sarwar, B. Dragisic, S. Sagoo and M. S. Taylor, *Angew. Chem. Int. Ed.*, 2010, **49**, 1674–1677.

87 N. L. Kilah, M. D. Wise, C. J. Serpell, A. L. Thompson, N. G. White, K. E. Christensen and P. D. Beer, *J. Am. Chem. Soc.*, 2010, **132**, 11893–11895.

88 M. J. Langton, S. W. Robinson, I. Marques, V. Félix and P. D. Beer, *Nat. Chem.*, 2014, **6**, 1039–1043.

89 A. V. Jentzsch and S. Matile, eds. P. Metrangolo and G. Resnati, Springer International Publishing, Cham, 2015, pp. 205–239.

90 A. Vargas Jentzsch and S. Matile, *Halogen Bond. Solut.*, 2021, 195–231.

91 S. Matile, A. Vargas Jentzsch, J. Montenegro and A. Fin, *Chem. Soc. Rev.*, 2011, **40**, 2453–2474.

92 A. P. Davis, D. N. Sheppard and B. D. Smith, *Chem. Soc. Rev.*, 2007, **36**, 348–357.

93 C. Ren, X. Ding, A. Roy, J. Shen, S. Zhou, F. Chen, S. F. Yau Li, H. Ren, Y. Y. Yang and H. Zeng, *Chem. Sci.*, 2018, **9**, 4044–4051.

94 W. L. Huang, X. D. Wang, S. Li, R. Zhang, Y. F. Ao, J. Tang, Q. Q. Wang and D. X. Wang, *J. Org. Chem.*, 2019, **84**, 8859–8869.

95 L. Vogel, P. Wonner and S. M. Huber, *Angew. Chem. Int. Ed.*, 2019, **58**, 1880–1891.

96 L. M. Lee, M. Tsemperouli, A. I. Poblador-Bahamonde, S. Benz, N. Sakai, K. Sugihara and S. Matile, *J. Am. Chem. Soc.*, 2019, **141**, 810–814.

97 B. Zhou and F. P. Gabbaï, *Chem. Sci.*, 2020, **11**, 7495–7500.

98 G. Park, D. J. Brock, J.-P. Pellois and F. P. Gabbaï, *Chem*, 2019, **5**, 2215–2227.

99 S. R. A. J., P. C. M., G. A. M. and M. M. P., *Proc. Natl. Acad. Sci.*, 2003, **100**, 5407–5412.

100 O. P. Ernst, D. T. Lodowski, M. Elstner, P. Hegemann, L. S. Brown and H. Kandori, *Chem. Rev.*, 2014, **114**, 126–163.

101 H. Kandori, *Biophys. Rev.*, 2020, **12**, 355–361.

102 K. Kojima, A. Shibukawa and Y. Sudo, *Biochemistry*, 2020, **59**, 218–229.

103 E. Gouaux and R. MacKinnon, *Science*, 2005, **310**, 1461–1465.

104 F. Bezanilla and E. Perozo, *Adv. Protein Chem.*, 2003, **63**, 211–241.

105 M. Piccolino, *Nat. Rev. Mol. Cell Biol.*, 2000, **1**, 149–152.

106 N. Giuseppone and A. Walther, *Out-of-Equilibrium (Supra)molecular Systems and Materials*, Wiley, 2021.

107 M. J. Langton, *Nat. Rev. Chem.*, 2021, **5**, 46–61.

108 Y. R. Choi, B. Lee, J. Park, W. Namkung and K. S. Jeong, *J. Am. Chem. Soc.*, 2016, **138**, 15319–15322.

109 S. Das, O. Biswas, N. Akhtar, A. Patel and D. Manna, *Org. Biomol. Chem.*, 2020, **18**, 9246–9252.

110 G. Park and F. P. Gabbaï, *Chem. Sci.*, 2020, **11**, 10107–10112.

111 J. A. Malla, R. M. Umesh, S. Yousf, S. Mane, S. Sharma, M. Lahiri and P. Talukdar, *Angew. Chem. Int. Ed.*, 2020, **59**, 7944–7952.

112 J. A. Malla, V. K. Sharma, M. Lahiri and P. Talukdar, *Chem. Eur. J.*, 2020, **26**, 11946–11949.

113 J. A. Malla, R. M. Umesh, A. Vijay, A. Mukherjee, M. Lahiri and P. Talukdar, *Chem. Sci.*, 2020, **11**, 2420–2428.

114 J. Zhu, D. Bai, T. Yan, S. Wang, Y. Wang, J. Fu, X. Fang and J. Liu, *Angew. Chem. Int. Ed.*, 2020, **59**, 13602–13607.

115 A. D. Peters, S. Borsley, F. della Sala, D. F. Cairns-Gibson, M. Leonidou, J. Clayden, G. F. S. Whitehead, I. J. Vitórica-Yrezábal, E. Takano, J. Burthem, S. L. Cockroft and S. J. Webb, *Chem. Sci.*, 2020, **11**, 7023–7030.

116 M. Fares, X. Wu, D. Ramesh, W. Lewis, P. Keller, E. Howe, R. Pérez-Tomás and P. Gale, *Angew. Chem. Int. Ed.*, 2020, **59**, 17614–17621.

117 Y. R. Choi, G. C. Kim, H. G. Jeon, J. Park, W. Namkung and K. S. Jeong, *Chem. Commun.*, 2014, **50**, 15305–15308.

118 S. J. Wezenberg, L. J. Chen, J. E. Bos, B. L. Feringa, E. N. W. Howe, X. Wu, M. A. Siegler and P. A. Gale, *J. Am. Chem. Soc.*, 2022, **144**, 331–338.

119 M. Ahmad, D. Mondal, N. J. Roy, T. Vijayakanth and P. Talukdar, *ChemPhotoChem*, 2022, **6**, e202200002.

CHAPTER 2

Chapter 2 Acyclic Halogen and Hydrogen Bonding Anion Transporters

2.1 Introduction

In recent decades, halogen bonding intermolecular interactions have been utilised in receptors for anion recognition, driven by their advantageous properties, including their strict linear geometry and hydrophobicity. There are a diverse range of XB donors employed to host the halogen bond donor which can be neutral (**Figure 2.1**, motifs a and b), or cationic (**Figure 2.1**, motifs c, d and e), depending on the desired application of the receptor.[1] The strength of the halogen bond donor is determined by the size of the sigma hole, which itself is governed by the chosen halogen atom (e.g. Cl, Br or I) and the electron-withdrawing nature of the substituents. However, the ability of these XB donors to bind and sense anions is also affected by their own charge and the surrounding solvent environment. For example, neutral receptors are typically chosen to bind anions in aprotic solvents which are a less competitive media and cationic receptors are employed to bind anions in the more competitive protic solvents.

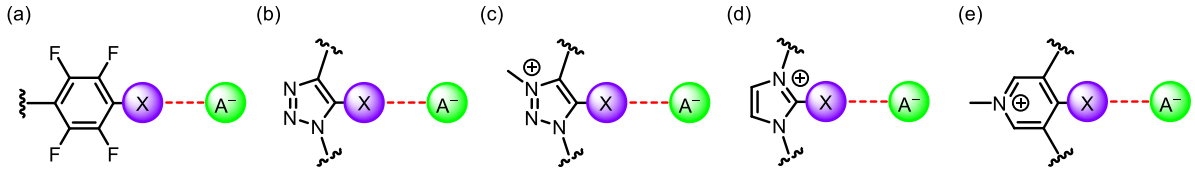


Figure 2.1. Commonly used halogen bonding motifs, X corresponding to the XB donor and A^- the anion. Neutral XB motifs: (a) haloperfluoroarene and (b) halotriazole. Cationic motifs: (c) halotriazolium, (d) haloimidazolium and (e) halopyridinium.

Examples of cationic XB motifs are more common within the literature in comparison to the neutral motifs discussed below because they typically have higher anion binding

affinity and increased solubility in polar solvents.[1,2] This stronger anion affinity results from the increased magnitude of the sigma-hole, and the additional the positive charge on the receptor that supplements anion binding. However, these motifs are not suitable for transmembrane anion transport since charged molecules have low membrane permeability, therefore, receptors for anion transport should be neutral.

Haloperfluoroarene motifs were first investigated by Larsen and Allred in 1965,[3] but it was Metrangolo, Resnati and co-workers who initially presented this motif within an anion receptor framework. Their heteroditopic receptor was capable of binding alkali metal halides using the iodo-perfluorobenzene motifs on their functionalised tripodal receptor (**Figure 2.2a**).[4] The incorporation of these motifs into anion transporters came later, and examples from Matile and Zeng have already been discussed in **Chapter 1 section 1.4.2.2.**[5–7] Notably, Matile demonstrated the reduction in transport activity when substituting the most potent halogen bond donor iodide for less potent halogen bond donors; fluoro- (b), bromo- (c) and iodo- (d) pentafluorobenzene gave EC_{50} values of >2 mM, 1.9 mM and 0.26 mM respectively (**Figure 2.2**).[5] Importantly, this shows the correlation between transport activity and XB donor strength which increases down the group.

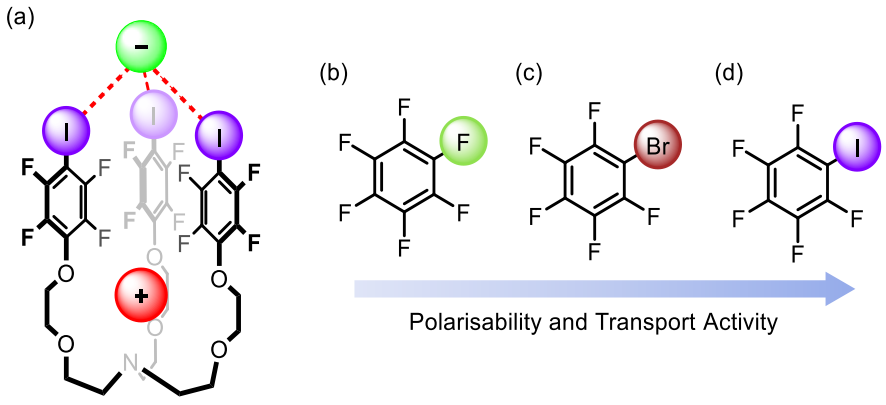


Figure 2.2. (a) Tridentate halogen bonding heteroditopic receptor, and (b) fluoro-, (c) bromo- and (d) iodo-pentafluorobenzene transporters.

Triazole-based heterocycles (**Figure 2.1b, page 54**) are readily accessible and thus became a popular motif within supramolecular chemistry with the emergence of click chemistry. The 2001 Nobel Prize winner Barry Sharpless coined the term click chemistry to describe a group small molecule cycloaddition reactions which are typically high yielding, wide in substrate scope and functional group tolerance, therefore, capable of yielding a diverse range of novel organic molecules.[8] The copper(I)-catalysed azide-alkyne cycloaddition (CuAAC) is a particularly popular method of click chemistry because it is highly versatile, withstands various reaction conditions and can even be performed in water.[9] The CuAAC reaction regioselectively yields 5-membered 1,2,3-triazole products as 1,4-regioisomers from a reaction of an alkyne with an organic azide. The use of halogenated alkyne precursors allows for the incorporation of halogen bond donors into the scaffold.[10] The iodo-triazole motif has been used extensively by Beer and co-workers for binding anions within sophisticated foldamer and rotaxane structures alongside ion-pair sensing in solution.[11–13] The incorporation of iodotriazoles into anion receptors can greatly enhance recognition; as mentioned in **chapter 1 section 1.4.2.2**, Beer and co-workers reported a water-soluble [2]rotaxane which bound iodide with two orders of magnitude higher affinity than its HB analogue in pure water.[14] The following chapter describes the use of iodo-triazoles for anion transport purposes for the first time.

2.1.1 Chapter Aims

The overall goal of this chapter is to synthesise acyclic halogen bonding anion receptors that can perform anion transport across lipid bilayer membranes. The receptors will be designed to have 5-iodo-1,2,3-triazoles for halogen bonding anion recognition and transport. Their prototriazole analogues will be synthesised and tested for comparison. The triazole-based heterocycles will be synthesised from alkyl azides and electron deficient aromatic alkynes. Increasing the alkyl chain lengths will enable tuning of the carrier's lipophilicity and varying the aryl substituents will allow investigations into how the electron-withdrawing nature of the substituents affects XB donor potency.

There are then two specific objectives: firstly, to prepare the HB and XB receptors then investigate their initial anion binding affinity and transporter activity. Then secondly, to examine the halide selectivity of the transport process and in particular, the chloride over hydroxide selectivity. Following this, computational investigations will be used to provide rationale for the results found experimentally. This chapter will go into the details behind the publication entitled 'Transmembrane anion transport mediated by halogen bonding and hydrogen bonding triazole anionophores' published in *Chemical Science*.[15]

2.2 Synthesis

A series of acyclic halogen bonding anion receptors, and their hydrogen bonding analogues were synthesised using high yielding click chemistry to give readily accessible anion transporters with the general design presented in **Figure 2.3**.

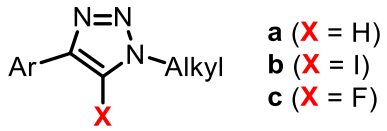


Figure 2.3. General receptor design of acyclic anion transporters with aryl and alkyl substituents.

These transporters are minimalistic in design in order to explore the transport activity and intrinsic selectivity of the hydrophobic C–I XB- and C–H HB-mediated anion transport processes. Since iodide is the most polarisable and therefore potent XB donor,[16] the iodotriazole moiety was specifically chosen to facilitate transport. In addition to this, when used within drug design, the triazole motif shows mild antibiotic effects which may prove advantageous for the medicinal applications of the carriers.[17] Variation of the substituents enabled the investigation into the importance of electron-withdrawing nature and the effects of hydrophobicity. Firstly, three different aryl substituents were chosen each with differing Hammett constants (**Figure 2.4**) since this was anticipated to have a profound effect on XB donor potency and in turn transport activity and efficiency.

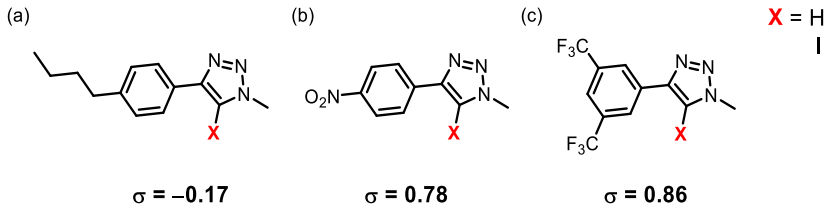
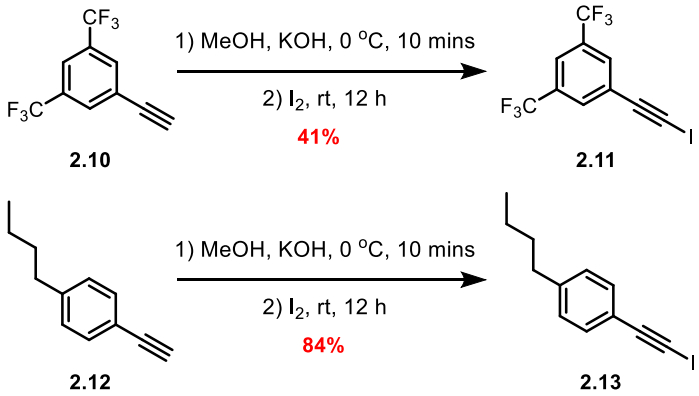


Figure 2.4. Hammett constants for truncated triazole motifs with differing aryl substituents.[18]

Secondly, the carrier must be sufficiently lipophilic to partition into the lipid bilayer, yet not too hydrophobic leading to inactivity. Carriers with a calculated lipophilicity value between 4 and 6 typically leads to activity, with a cLogP value of 5 typically being optimum and generally accepted as the lipophilicity to aim for when designing new anion transporters.[19,20,21] However, the correlation between activity and log *P* is complex, because transport efficiency is also strongly dependent on other factors including anion binding affinity and molecular size, which are not easily decoupled. Here, tuning the lipophilicity is achieved by altering the length of the alkyl chain with the use of three different alkyl azides.

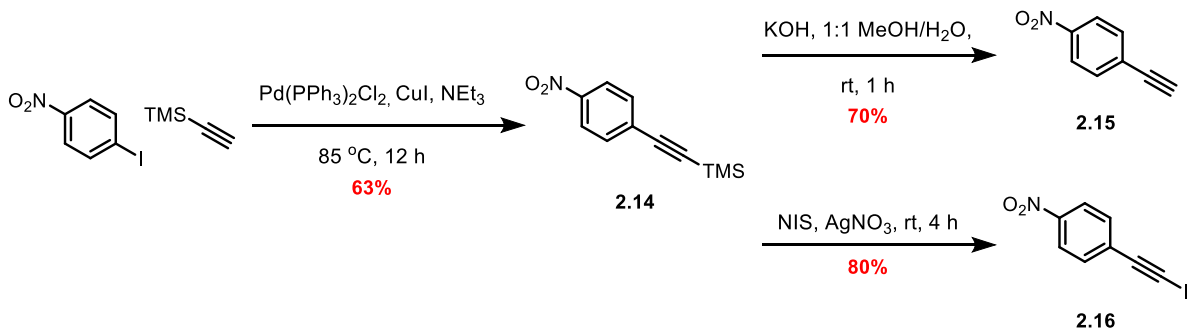
Treatment of proto-alkynes **2.10** and **2.12** with KOH in methanol and subsequent reaction with elemental iodine afforded iodoalkyne **2.11** and **2.13** in yields of 41 and 84% respectively (**Scheme 2.1**).



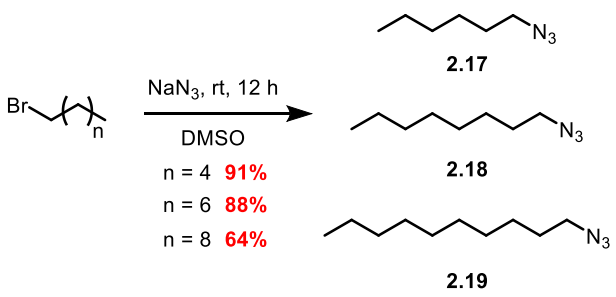
Scheme 2.1. Synthesis of proto- and iodo-aryl-alkynes **2.11** and **2.13**.

The third iodo-alkyne precursor was synthesised from 1-iodo-4-nitrobenzene which was subjected to a Sonogashira cross coupling reaction with TMS acetylene to yield the TMS-protected alkyne **2.14** (63%). This could be either deprotected to yield proto-alkyne

2.15 (70%), or reacted further with $AgNO_3$ and NIS in acetone to yield the iodo-alkyne **2.16** (80%) (**Scheme 2.2**). To synthesise the alkyl azides, the corresponding alkyl bromides were treated with sodium azide and stirred in DMSO overnight to yield hexyl (**2.17**), octyl (**2.18**) and decyl azide (**2.19**) ready for the subsequent click reaction (**Scheme 2.3**).



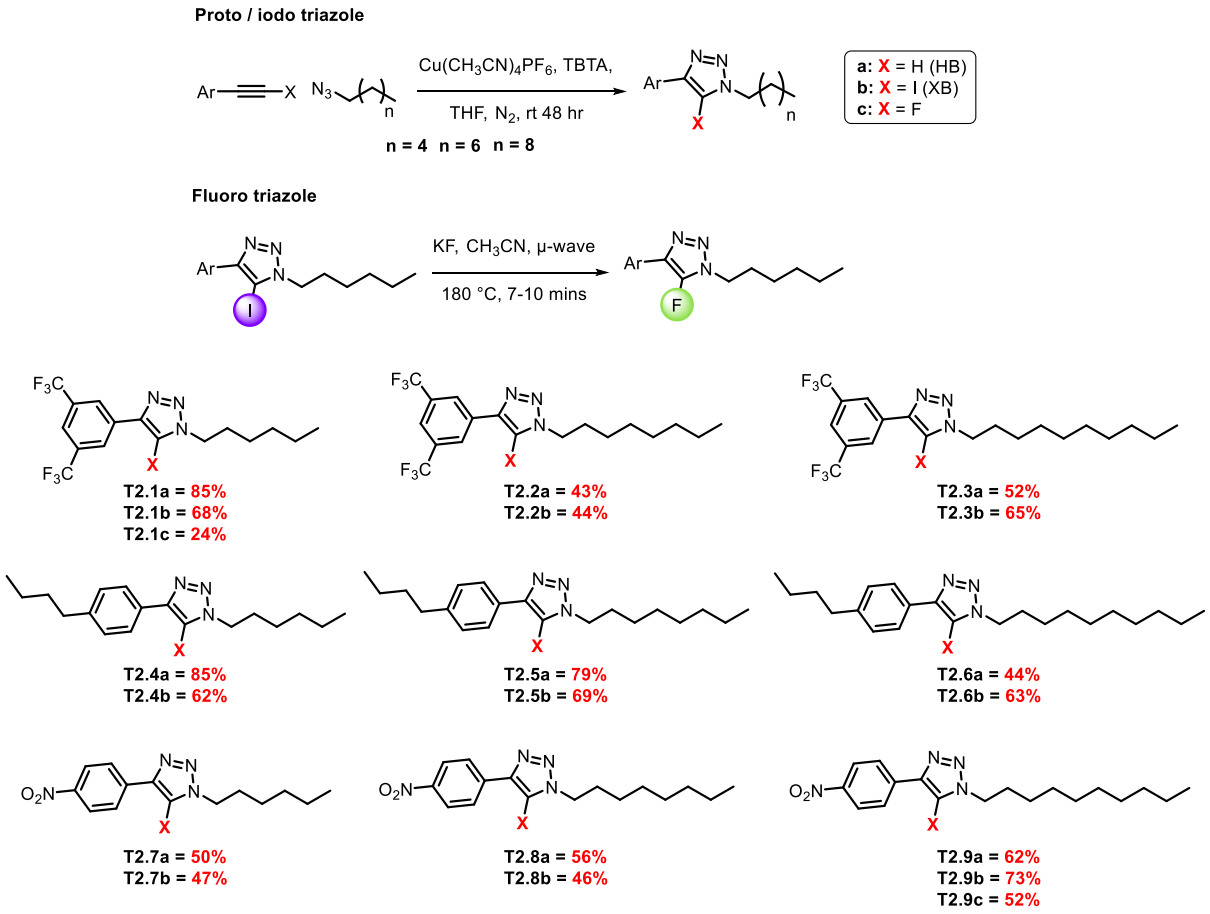
Scheme 2.2. Synthesis of proto- and iodo-aryl- alkynes **2.15** and **2.16**.



Scheme 2.3. Synthesis of hexyl (**2.17**), octyl (**2.18**) and decyl azide (**2.19**).

The family of 1,4-disubstituted-1,2,3-triazoles were prepared by Cu(I)-catalysed azide–alkyne cycloaddition of the respective iodo-/proto- aryl-alkyne (**Scheme 2.2**) and alkyl azide (**Scheme 2.3**), in the presence of tris[(1-benzyl-1*H*-1,2,3-triazol-4-yl)methyl]amine (TBTA) (**Scheme 2.4**) with yields ranging from 44 to 85%. They are numbered transporter **T2.X** with **a**, **b**, or **c** representing HB, XB and the fluorotriazoles respectively. The fluoro-triazole analogues **T2.1c** and **T2.9c** were synthesised as negative control compounds, since

they are unable to form HB or XB interactions. **T2.1c** and **T2.9c** were prepared via an S_NAr reaction from the corresponding iodo-triazole carriers **T2.1b** and **T2.9b** by heating with potassium fluoride in a microwave, giving yields of 24% and 52% respectively (**Scheme 2.4**). All receptors and their precursors were then characterised by ^{1}H NMR, ^{13}C NMR, ^{19}F NMR where applicable and ESI-HRMS.



Scheme 2.4. Synthesis of triazole anion transporters by CuAAC and S_NAr reactions.

2.2.1 Anion Recognition

The anion recognition capabilities of representative proto-triazole **T2.1a** and iodo-triazole **T2.1b** were investigated by ^{1}H NMR host-guest binding titration experiments with $Bu_4N^+X^-$ in acetone-d_6. The binding induced chemical shift perturbations of the proto-triazole H and adjacent aryl protons were monitored over the course of the titration upon addition of the halides, Cl^-, Br^- and I^-, and NO_3^- (**Figure 2.5**).

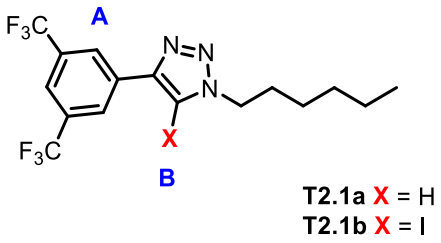


Figure 2.5. The structure of **T2.1** depicting the protons followed throughout the NMR titration experiments.

The chemical shift perturbations upon addition of the anions were indicative of anion binding and the data could be fitted to a 1:1 binding model (all binding isotherms are available in the appendix). The 1:1 stoichiometric association constants (K_a) presented in **Table 2.1** were determined using the Bindfit program.[22] The data revealed an overall anti-Hofmeister binding selectivity trend of $Cl^- > Br^- > I^-$ for both **T2.1a** and **T2.1b**, and approximately one order of magnitude enhancement of halide binding affinity for the XB iodo-triazole receptor **T2.1b** compared to HB proto-triazole **T2.1a**. The C–H hydrogen bonding carrier **T2.1a** showed particularly weak binding while XB **T2.1b** had an increased binding affinity which is anticipated to help to overcome solvation effects of the anion during transport experiments. For both compounds, no measurable binding of nitrate was observed under these conditions.

Table 2.1. Anion binding association constants, for carrier **T2.1a** and **T2.1b** calculated using Bindfit.[22]

K_a / M^{-1}	**T2.1a**	**T2.1b**
Cl^{-}[a]	17 ± 1	197 ± 14
Br^{-} [a]	9 ± 7	110 ± 35
I^{-} [a]	< 3	38 ± 9
NO_3^{-} [a]	-[b]	-[b]

[a]Anions added as the TBA salt in d_6-acetone, data fitted to a 1:1 binding model using Bindfit. [b]Perturbations too small to obtain binding constant. Errors at the 95% confident limit. (298 K, 500 MHz).

2.3 Anion Transport Activity

The ability and efficiency of the novel acyclic XB and HB receptors to transport anions across lipid bilayers membranes was initially determined in lipid bilayer vesicles using the fluorescence-based HPTS assay which was introduced in **chapter 1 section 1.3.1.1**. The mechanism of their action, and selectivity towards particular anions was then determined using additional fluorescence assays in vesicle-based experiments which are outlined below.

2.3.1 The HPTS Assay

The HPTS assay was performed with 1-palmitoyl-2-oleoyl-*sn*-glycero-3-phosphocholine large unilamellar vesicles (POPC LUVs) loaded with 8-hydroxypyrene-1,3,6-trisulfonic acid dye (HPTS) and buffered to pH 7.0 in NaCl solution, NaOH is added as a base pulse to generate a pH gradient across the bilayer.[5,23] In the HPTS assay, transport mediated by small synthetic carriers can occur by the two differing co-transport mechanisms, firstly, via the antiport of OH^{-}/Cl^{-} or Na^{+}/H^{+}, or secondly, via the symport of a Na^{+} or H^{+} cation along with an OH^{-} or Cl^{-} anion (**Figure 2.6**). Once the NaOH base pulse has been added, the carriers work via these transport mechanisms to dissipate the ion concentration gradient either side of the membrane.

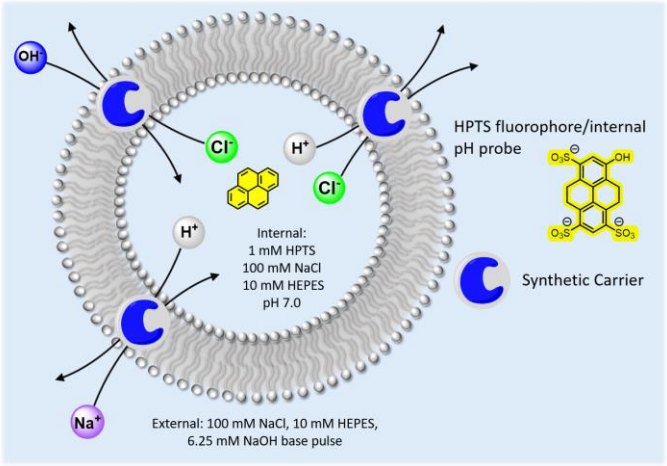


Figure 2.6. Potential symport and antiport mechanisms that can occur within the HPTS assay to dissipate the applied pH gradient.

Once the pH gradient is generated and the carrier has been added, the time-dependent change in fluorescence intensity (λ_{em} = 510 nm) is monitored simultaneously at λ_{ex} = 405 nm (acidic form of HPTS) and λ_{ex} = 460 nm (basic form), before calibration of the assay with Triton-X100 detergent added at the end of the experiment to lyse the vesicles and completely dissipate the gradient. Representative data displaying the change in ratiometric emission over time upon addition of **T2.1b** is shown in **Figure 2.7**.

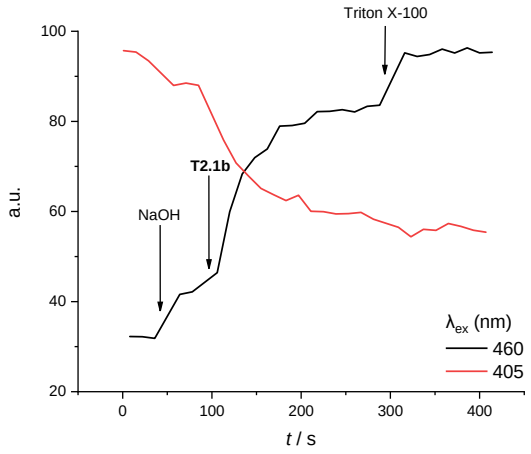


Figure 2.7. The change in ratiometric emission (λ_{em} = 510 nm; λ_{ex1} = 405 nm, λ_{ex2} = 460 nm) upon addition of **T2.1b** (2.5 µM) to POPC vesicles containing 1 mM HPTS, 100 mM internal and external NaCl, buffered with 10 mM HEPES at pH 7.0. A pH gradient is generated by NaOH (0.5 M) and vesicle lysis by Triton X-100 calibrates the assay. Performed at 25 °C.

HPTS has two absorption wavelengths corresponding to the deprotonated and protonated forms of the molecule, which both emit at 510 nm. This dual emission makes it a ratiometric fluorophore thus allowing for ratiometric analysis using equation 2.1,

$$ratio = \frac{\lambda ex\ 460}{\lambda ex\ 405} \quad (2.1)$$

followed by calculation of the fractional fluorescence intensity (I_{rel}) using equation 12,

$$I_{rel} = \frac{R_t - R_0}{R_d - R_0} \quad (2.2)$$

where R_t is the fluorescence ratio at time t, R_0 is the fluorescence ratio at time 0, and R_d is the fluorescence ratio after the addition of detergent. This was performed for each carrier at increasing concentrations and repeated at least twice. Representative data showing the change in fractional fluorescence intensity over time upon addition of **T2.1b** is shown in **Figure 2.8** and the original data for all other compounds is available in the appendix.

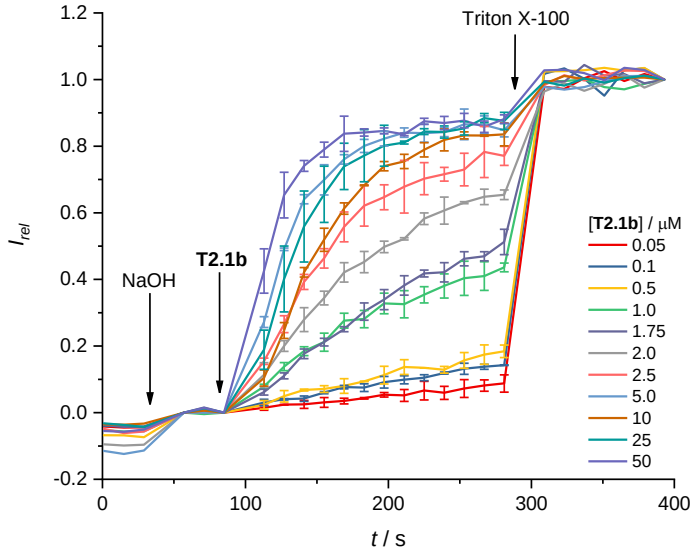


Figure 2.8. The change in fractional fluorescence intensity (I_{rel}) (λ_{em} = 510 nm; λ_{ex1} = 405 nm, λ_{ex2} = 460 nm) upon addition of **T2.1b** in DMSO (0.05–50 µM) to POPC vesicles containing 1 mM HPTS, 100 mM internal and external NaCl, buffered with 10 mM HEPES at pH 7.0. A pH gradient is generated by addition of a NaOH base pulse (0.5 M), followed by **T2.1b** at t = 90 s. Vesicle lysis by Triton X-100 calibrates the assay. Performed at 25 °C.

2.3.1.1 Hill Analysis

Analysis of the concentration dependence of the anion carriers was carried out using Hill analysis, in which fitting of the dose-responsive curves to the Hill equation is used to quantify the transport activity with two key parameters: the effective concentration, EC_{50}, value and the Hill coefficient, *n*. The EC_{50} value is defined as the carrier concentration that gives 50% transport activity in the particular assay, therefore, a low EC_{50} value corresponds to higher transport activity. It is presented either as a substrate concentration (in the cuvette) or as a mole percentage with respect to the lipid concentration. The Hill coefficient value provides insight into the stoichiometry of the supramolecular complex involved in the transport process.[24,25,26]

For analysis of these transporters, the fractional fluorescence intensity (I_{rel}) at 288 s just prior to lysis, defined as the fractional activity *y* (which represents activity), was plotted as a function of the ionophore concentration (**x** / µM) to generate dose-responsive curves. Hill coefficients and EC_{50} values were calculated by fitting to the Hill equation (2.3) using OriginLab.

$$y = y_0 + (y_{max} - y_0) \cdot \frac{x^n}{(EC_{50})^n + x^n} \qquad (2.3)$$

where y_0 is the fractional activity in the absence of transporter, y_{max} is the fractional activity with excess transporter and x represents the transporter concentration in the cuvette for a particular run of the assay. Hill plots were fitted to at-least 8 data points spanning the required concentration range (**Figure 2.9**). Representative data for **T2.1b** is shown in **Figure 2.9** and the Hill plots for all other compounds is available in the appendix.

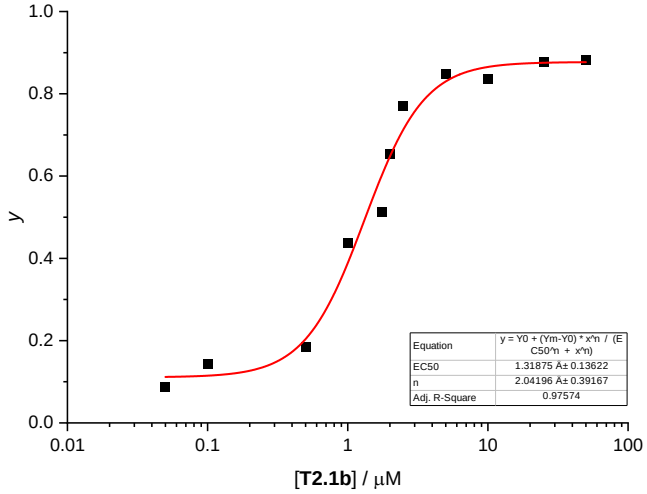


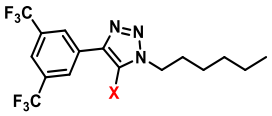
Figure 2.9. Anion transport mediated by XB transporter **T2.1b** in the HPTS assay. The dependence of fractional activities (*y*, the relative intensity at *t* = 288 s just prior to lysis) on concentration of **T2.1b** (black squares), and fit to the Hill equation (red line).

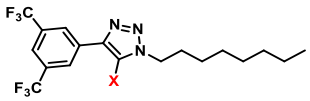
2.3.1.2 Results and Discussion

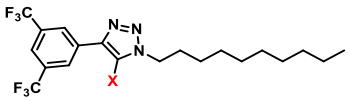
The EC_{50} and *n* values for the proto-, iodo- and fluoro-triazoles are shown in **Table 2.2** alongside the cLogP values which were calculated using the Virtual Computational Chemistry Laboratory.[21] In general, the activity of carriers' **T2.1-T2.9** was dependant on the structure of the carrier; comparison of the Hammett σ values for each aryl substituent demonstrates that the more electron-withdrawing the substituent is the greater the observed transport activity of carriers are (**Figure 2.4**).

Table 2.2. EC_{50}, *n* and cLogP values for carriers **T2.1- T2.9**. Experimental values quantified from the HPTS assay, raw data available in the appendix.

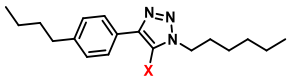
a: X = H (HB)
b: X = I (XB)
c: X = F

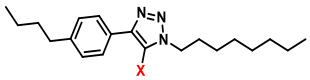


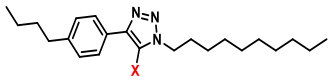




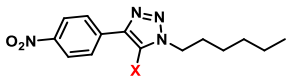
	T2.1a	T2.1b	T2.1c	T2.2a	T2.2b	T2.3a	T2.3b
EC_{50} / µM	2.0	1.3	>1000	0.9	1.1	>100	>100
n	2.4	2.0	-	3.7	2.6	-	-
cLogP	4.4	5.4	4.7	5.1	6.2	5.8	6.8

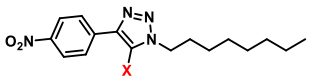


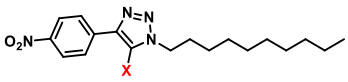




	T2.4a	T2.4b	T2.5a	T2.5b	T2.6a	T2.6b
EC_{50} / µM	6.2	3.3	>200	>200	>500	>500
n	5.6	2.0	-	-	-	-
cLogP	5.7	5.7	6.5	6.3	7.2	6.3







	T2.7a	T2.7b	T2.8a	T2.8b	T2.9a	T2.9b	T2.9c
EC_{50} / µM	14.8	1.8	2.9	3.6	2.7	1.2	>1000
n	5.7	3.1	3.6	2.7	7.0	2.0	-
cLogP	3.9	4.4	4.8	5.2	5.6	6.0	5.3

Transport activities of the proto- and iodo-triazole transporters ranged from being very active (**T2.2b** EC_{50} = 1.06 µM), to poor activity (**T2.7a** EC_{50} = 14.77 µM), to showing complete inactivity (**T2.3**, **T2.5** and **T2.6**). Carriers **T2.1b**, **T2.2** (both HB and XB analogues) and **T2.9b** exhibiting the best transport activity with EC_{50} values as low as 1 µM. In general,

the *n* values for all active carriers were lower when employing the iodotriazole analogue in comparison to their prototriazole counterparts (**Table 2.2**), and the activities of carriers with high *n* values were very sensitive to changes in concentration (see appendix for all data plots).

Carriers **T2.1** and **T2.2** were highly active anion transporters and halogen bonding **T2.1b** (EC_{50} = 1.3 μM) was twice as active as carrier hydrogen bonding **T2.1a** (EC_{50} = 2.0 μM). The addition of the 3,5-bis(trifluoromethyl)benzene substituent to carriers **T2.1** to **T2.3** was chosen not only because of the electron-withdrawing nature but also because the carbon–fluorine bonds enhance hydrophobicity, potentially increasing the ability of these carriers to penetrate the hydrophobic bilayer. The addition of the decyl chain on carrier **T2.3** increased the lipophilicity of the carrier to a cLogP value above 6, causing inactivity.

The electron-donating 4-butylbenzene substituent lead to a decrease in receptor activity, this is consistent with the Hammett constant values and the reduced XB and HB bond donor strength of these substituents in comparison to the electron-withdrawing substituents (**Figure 2.4**, **Page 58**). Carrier **T2.4** was the only carrier to be active with the butyl benzene substituent. Like carrier **T2.3**, carriers **T2.5** and **T2.6** were inactive due to their high lipophilicity. The transport-inactivity likely arises from their reduced mobility and the organization of longer chain derivatives within the lipid bilayer.[27] These results indicate that the addition of an electron-withdrawing substituent was not essential, since carrier **T2.4** was transport-active, but the lipophilicity must be tuned to account for the reduced potency of the bond donor which can lower the transport activity when they are not present. Interestingly, the cLogP values of **T2.4a** and **T2.4b** are both 5.7 but the EC_{50} values of these carriers are 6.16 μM and 3.28 μM, respectively. This shows how simply the introduction halogen bonding into the structure can lead to a large increase in transport

activity. The increase in activity of the XB carriers over the HB analogues was found for most of the anion carriers, and is in agreement with the ^{1}H NMR titration experiments in which the XB receptor had a higher anion binding affinity in comparison to the HB receptor. However, strict comparison between the measured association constants in organic solvent and transport kinetics in membranes should be treated with caution since the observed rate of transport is also dependent on many other factors including desolvation, anionophore-ion complex mobility in the membrane, and competing binding interactions of the transporter with the phosphate head groups.[20]

Carriers **T2.7** to **T2.9** incorporated a *para* electron-withdrawing nitro group because it has been previously shown to enhance transport ability in a thiourea based system due to its high Hammett constant.[20] In a similar fashion to carrier **T2.4,** the EC_{50} values of carrier **T2.7** dropped significantly from 14.77 μM (**T2.7a**) to 1.78 μM (**T2.7b**) when halogen bonding was introduced. Since the cLogP values of carrier **T2.7a** and **T2.7b** were 3.9 and 4.4 respectively, the increased activity is not only attributed to the strength of the halogen bond but also to its increased hydrophobicity. Unlike the other carriers in this family, carrier **T2.9b** was highly active with an EC_{50} of 1.15 μM despite the long alkyl chain. This emphasises the importance of balancing the lipophilicity for each carrier and again how structure-dependent the activity is.

Importantly, the electron-deficient halogen bonding transporters **T2.1b** and **T2.9b** were approximately 3× more active than iodoperfluorohexane (EC_{50} = 3.1 μM),[5] and over two orders of magnitude more active than the XB donor iodoperfluorobenzene (EC_{50} = 260 μM, comparable assay conditions) presented by Matile and co-workers.[5,6] As a result, it was concluded that carriers **T2.1a/b** and **T2.9a/b** were the best carriers to take forward into further membrane transport experiments due to their high activity.

2.3.1.3 Fluorotriazole Transport

Anion transport is expected to be wholly mediated by the C–H hydrogen and C–X halogen bond donors themselves rather than proton transport via triazole protonation causing H^+/Cl^- symport, since the pK_aH of 1-methyl-4-phenyl-1,2,3-triazole is about 0.1.[28] This is supported by the previously reported anion antiport activity of XB iodofluoroalkene/arene transporters, which do not possess any basic atoms.[5] To confirm that the C–I XB and C–H HB interactions mediate the anion transport process fluoro-triazole carriers were synthesised from their iodo-triazole analogues (**Scheme 2.4, page 61**) and tested as a negative control (**Figure 2.10**). Fluorine is very electronegative and thus the least polarizable halogen, therefore, it is known to be a poor sigma-bond donor and unable to form XB interactions through the triazole motif.[29] Inactivity of fluorotriazole carrier **T2.1c** in the HPTS assay confirmed the crucial role of the triazole C–H hydrogen bond and C-I halogen bond in the transport processes (**Figure 2.10**). Analogous results for carrier **T2.9c** can be found in the appendix.

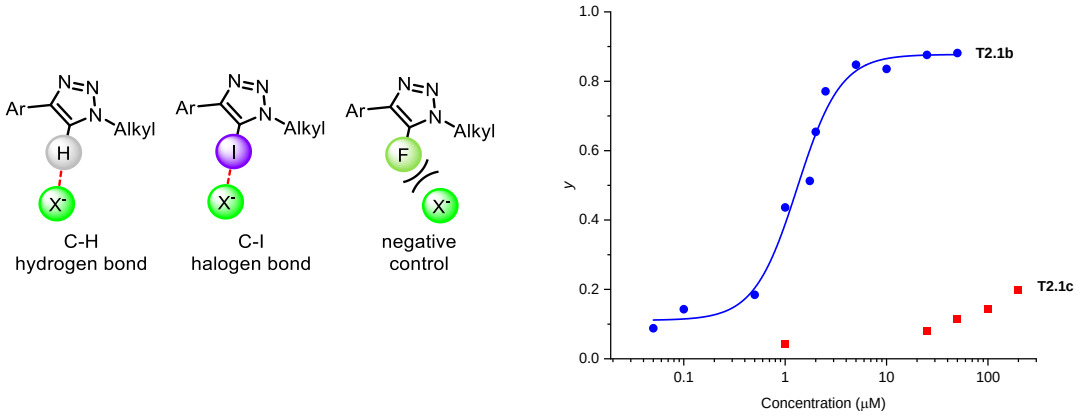


Figure 2.10. Left, C–H hydrogen and C-I halogen bonding and fluorotriazole negative control incapable of forming halogen bonds. Reproduced from reference [15] with permission from the Royal Society of Chemistry. Right, Dependence of the fractional transport activity, *y*, on the concentration for fluorotriazole **T2.1c** (red) and **T2.1b** (blue) in the HPTS assay.

2.4 Anion Transport Mechanistic Studies

In order to elucidate the carriers' mechanism of action, vesicle-based control experiments were performed. This section will outline the control experiments and their role within this investigation.

2.4.1 Mobile Carrier Mechanism

The test ionophore has the potential to damage the integrity of the liposome membrane which can cause non-specific transport of ions, or leakage of encapsulated molecules. This can be investigated using the carboxyfluorescein leakage assay. In this assay the self-quenching dye 5(6)-carboxyfluorescein (CF) is loaded into POPC LUVs which are suspended in NaCl HEPES buffer (**Figure 2.11**). Upon addition of the carrier, the time-dependent change in fluorescence intensity can be monitored (λ_{ex} = 492 nm, λ_{em} = 517 nm). If the transporter causes a breakdown in the structure of the liposome or forms pores in the bilayer, the CF dye will leak from the vesicles into the external buffer which dramatically dilutes the fluorophore leading to an increase in fluorescence.[6]

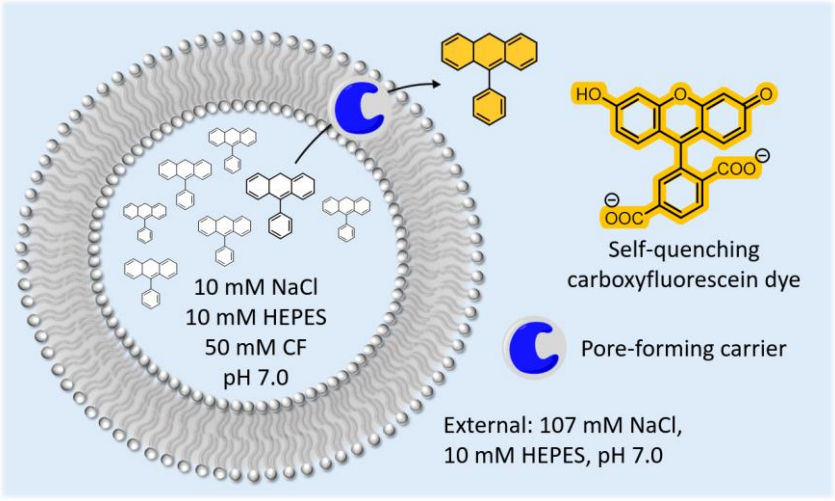


Figure 2.11. The carboxyfluorescein (CF) leakage assay.[6]

The CF assay was completed for all 21 carriers and a change in fluorescence was not observed upon addition of any of the carriers in this series, even at high concentrations (200 μM), which indicates that these systems do not cause vesicle leakage and confirms that the change in fluorescence seen within the HPTS assay, results from carrier-mediated anion transport. Representative data is shown in **Figure 2.12** and the data for all other carriers can be found in the appendix.

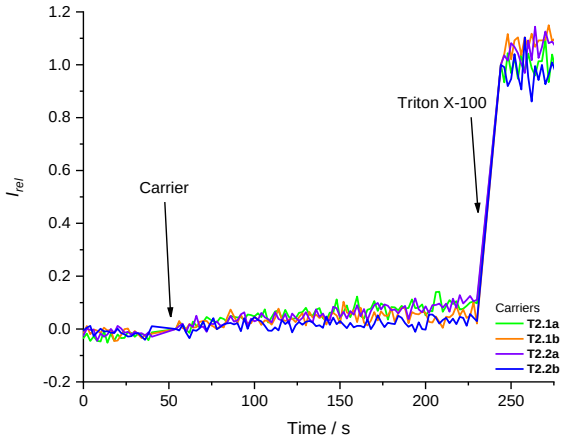


Figure 2.12. The time-dependent change in fluorescence intensity (λ_{ex} = 492 nm, λ_{em} = 517 nm) upon addition of carriers **T2.1** and **T2.2** in the CF assay (POPC LUVs (31.25 μM); inside 10 mM NaCl, 10 mM HEPES and 50 mM CF pH 7.0 and outside: 107 mM NaCl, 10 mM HEPES, pH 7.0). Synthetic carrier added at 50 s (200 μM, 5 μL DMSO). The assay was calibrated at 250 s with Triton X-100 detergent (40 μL, 7:1 (v/v) H_2O-DMSO). Performed at 25 °C.

The HPTS assay was then performed with dipalmitoyl phosphatidylcholine (DPPC) lipid vesicles (**Figure 2.13**) in place of the POPC LUVs, to investigate whether transport was facilitated by a mobile carrier or by a membrane-spanning channel. DPPC LUVs are in gel phase at room temperature and therefore do not allow the movement and rotation of mobile carriers to mediated transmembrane transport. When heated above the DPPC LUVs' phase transition temperature of 41 °C, the bilayer undergoes a gel to fluid phase transition and mobile carrier transport is restored. If transport is inhibited in the gel phase (at 25 °C) a

mobile carrier mechanism is inferred. On the other hand, if transport is mediated by a pore-forming channel it will not be significantly affected by the fluidity of the bilayer.

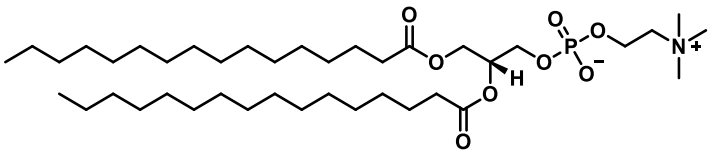


Figure 2.13. Dipalmitoyl phosphatidylcholine (DPPC) lipid.

Carriers **T2.1** and **T2.9** were added at a consistent concentration (2 μM in 5 μL DMSO) throughout and the assay was repeated at temperatures ranging from 15 to 45 °C using a Peltier thermostated cell holder. These XB and HB transporters could only perform transport once the cuvette was heated to 45 °C, indicating that the transporters work via a mobile carrier mechanism and do not assemble into membrane-spanning ion channels. Representative data for carrier **T2.1b** is shown in **Figure 2.14**. Analogous results for carrier **T2.9b** can be found in the appendix.

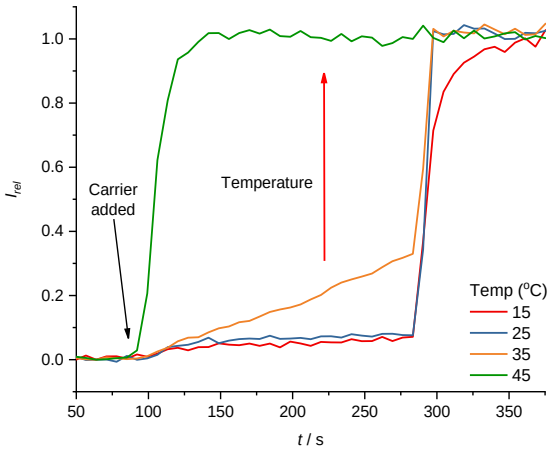


Figure 2.14. The change in the fractional fluorescence intensity (I_{rel}) (λ_{em} = 510 nm; λ_{ex1} = 405 nm, λ_{ex2} = 460 nm) upon addition of **T2.1b** in DMSO (2 μM) to DPPC LUVs containing 1 mM HPTS, 100 mM internal and external NaCl, buffered with 10 mM HEPES at pH 7.0. A pH gradient is generated by addition of a NaOH base pulse (0.5 M), followed by **T2.1b** at t = 90 s. The temperature was increased from 15 to 45 °C. Vesicle lysis by Triton X-100 calibrates the assay. The results are an average of at least 2 repeats and performed at 25 °C.

2.4.2 Mediation of Anion Specific Transport

Transport can occur by the antiport of OH^-/Cl^- or H^+/Na^+, or the symport of H^+/Cl^- (**Figure 2.15**). These mechanisms cannot be distinguished from each other during the transport assays completed so far because are they are functionally equivalent. The assays described below provide clarity on what species are involved in the carrier mediated transmembrane transport.

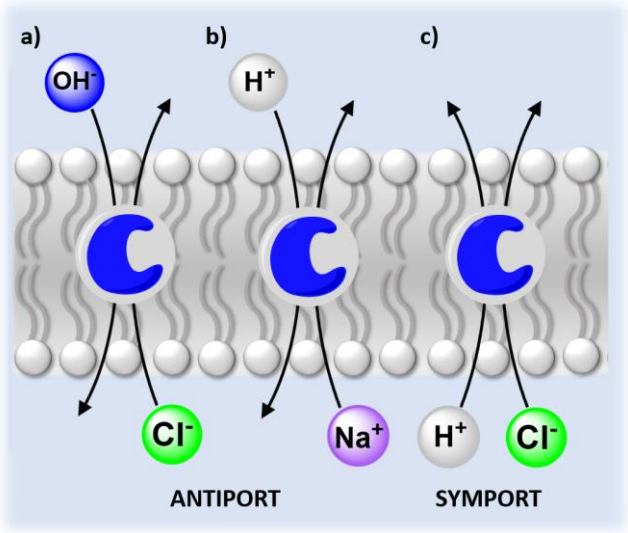


Figure 2.15. Transport mechanisms that can occur within the HPTS assay. (a) OH^-/Cl^-, (b) H^+/Na^+ antiport, or (c) H^+/Cl^- symport.

To decipher the role of cationic species in the transport mechanism, the HPTS assay was performed using egg-yolk phosphatidylglycerol (EYPG) LUVs or 1-palmitoyl-2-oleoyl-*sn*-glycero-3-phospho-(1'-*rac*-glycerol) 16:0-18:1 PG (POPG) LUVs instead of zwitterionic POPC LUVS. EYPG and POPG both have a net negative charge and thus repel anions, inhibiting their transport across the membrane (**Figure 2.16**). Thus, suppression of transport with anionic lipids indicates that anion transport is involved in the rate limiting transport process.

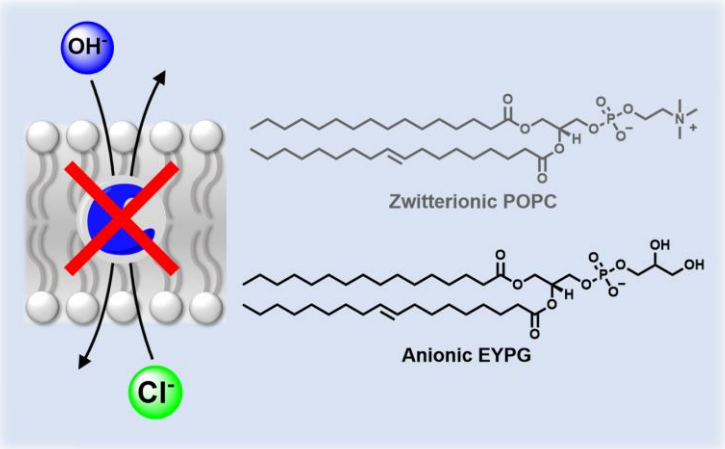


Figure 2.16. Zwitterionic POPC, and anionic EYPG lipids which restrict the anion antiport transport process.

This anionic lipid assay was performed with carriers **T2.1b** and **T2.9b** over a range of concentrations such that an EC_{50} value could be determined (**Table 2.3**). The activity of both carriers dropped over 5-fold, for example, the EC_{50} value of carrier **T2.1b** rose from 1.2 µM to 6.2 µM with the use of EYPG lipids (**Figure 2.17**). This indicates that formation of an anionic complex is required in the rate limiting transport process and that cations do not play a large role in the transport mechanism. We can conclude a Cl^-/OH^- antiport mechanism is likely to dominate over Cl^-/H^+ symport, given these results and the low basicity of the triazole motif.

Table 2.3. EC_{50} values associated with transport mediated by carrier **T2.1b** and **T2.9b** when changing the vesicles from POPC lipids to EYPG lipids in the HPTS assay. Temperature maintained at 25 °C.

Carrier	Vesicles	EC_{50} (µM)
T2.1b	POPC	1.16 (±0.18)
	EYPG	6.17 (±0.07)
T2.9b	POPC	1.15 (±0.07)
	EYPG	5.76 (±0.59)

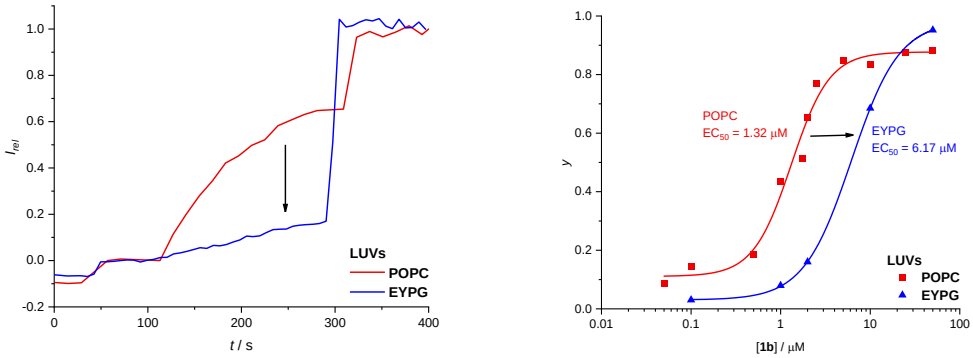


Figure 2.17. Left, The change in I_{rel} (λ_{em} = 510 nm; λ_{ex1} = 405 nm, λ_{ex2} = 460 nm) at 25 °C upon addition of carrier **T2.1b** (2 μM) to POPC LUVs (red) and EYPG LUVs (blue). Right, Hill plots associated with transport mediated by **T2.1b** using POPC LUVs (red) and EYPG LUVs (blue). Values represent the fluorescence intensity (y) at 288 s.

Additional selectivity experiments were then carried out to further support the cation independency of the transport process. The HPTS assay was repeated with the iso-osmolar replacement of the external Na^+ cation with Li^+, K^+, Rb^+ and Cs^+ to determine whether the carriers are selective for a particular cation. Generally, the transport activity of the carrier was not significantly affected by the exchange of cations in the external buffer. The lack of cation selectivity suggests that the rate limiting transport process is likely to be cation independent, supporting the Cl^-/OH^- antiport mechanism determined with the anionic lipid assay (**Figure 2.18**).

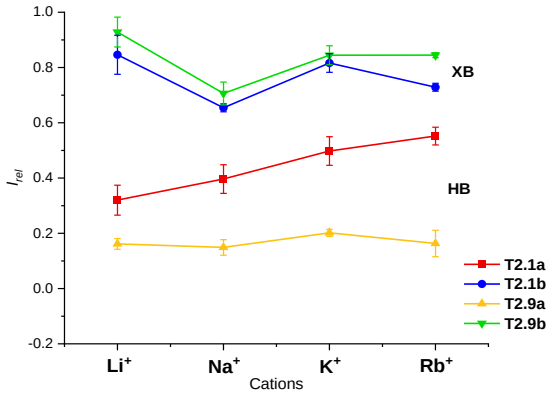


Figure 2.18. The dependence of the I_{rel} at 288 s on the external cation upon addition of **T2.1** and **T2.9** (2 μM) at 25 °C. POPC vesicles: 1 mM HPTS, 100 mM internal and external M^+Cl^- (M^+ = Li^+, Na^+, K^+, Rb^+), buffered with 10 mM HEPES at pH 7.0. M^+OH^- base pulse (0.5 M) generates a pH gradient, followed by the carrier at t = 90 s. Vesicle lysis by Triton X-100 calibrates the assay. The results are an average of at least 2 repeats.

The HPTS assay was then performed with sodium gluconate in place of sodium chloride in the buffer. Gluconate is a large hydrophilic anion that cannot cross the bilayer (**Figure 2.19**) and so OH^-/gluconate antiport or H^+/gluconate symport mechanisms cannot occur because of the insurmountable dehydration penalty of gluconate.[30] Carriers **T2.1** and **T2.9** did not show any transport activity in this assay (**Figure 2.19**), therefore, the absence of detectable transport indicates that H^+/Na^+ cation antiport process (which is independent of gluconate transport) is negligible. These results support a cation independent mechanism.

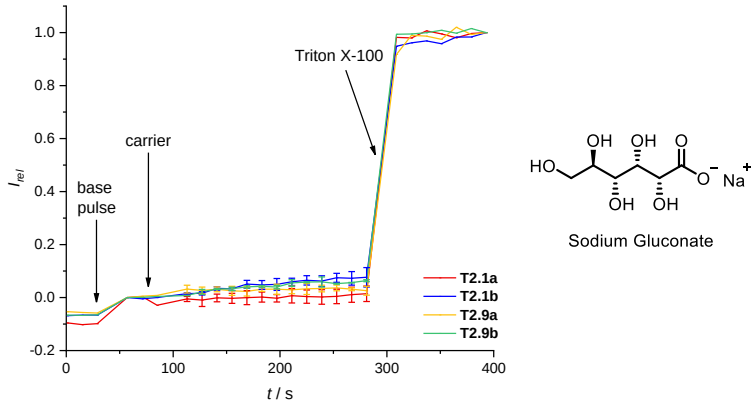


Figure 2.19. The change in fractional fluorescence intensity (I_{rel}) (λ_{em} = 510 nm; λ_{ex1} = 405 nm, λ_{ex2} = 460 nm) at 25 °C upon addition of carriers **T2.1** and **T2.9** (2 μM) to POPC vesicles containing 1 mM HPTS, 100 mM internal and external sodium gluconate, buffered with 10 mM HEPES at pH 7.0. A pH gradient is generated by addition of a NaOH base pulse (0.5 M), followed by the carrier at t = 90 s. Vesicle lysis by Triton X-100 calibrates the assay. The results are an average of at least 2 repeats.

2.5 Anion Selectivity

2.5.1 Chloride Over Hydroxide Selectivity

Synthetic anion carriers ideally must show selectivity towards a particular anion to be suitable for medicinal applications. For the treatment of channelopathies, Cl^- > OH^- selectivity is particularly important so that the carrier can replace the faulty chloride

channels without disrupting cellular pH gradients. Gale, Davis and co-workers have developed variations of the HPTS assay in order to probe the anion transporters' chloride over hydroxide selectivity.[30–32] They initially developed the FCCP assay; here the HPTS assay is performed but with the addition of the weak acid protonophore, carbonyl cyanide-*p*-trifluoromethoxy phenylhydrazone (FCCP) (or carbonyl cyanide *m*-chlorophenylhydrazone, CCCP). FCCP transports protons via transmembrane shuttling of both its protonated and deprotonated forms. At the low concentration used for the assay (0.25 µM) FCCP cannot cause appreciable dissipation of the transmembrane pH gradient alone, but once the synthetic transporter is added, FCCP will facilitate fast electrogenic proton transport, allowing the test ionophore to transport anions only (**Figure 2.20**).[33] The assay is therefore performed with and without FCCP and if the rate of transport increases with the addition of FCCP it implies that the transport of OH^- is rate limiting, and thus the synthetic carrier is selective for Cl^- over OH^-.

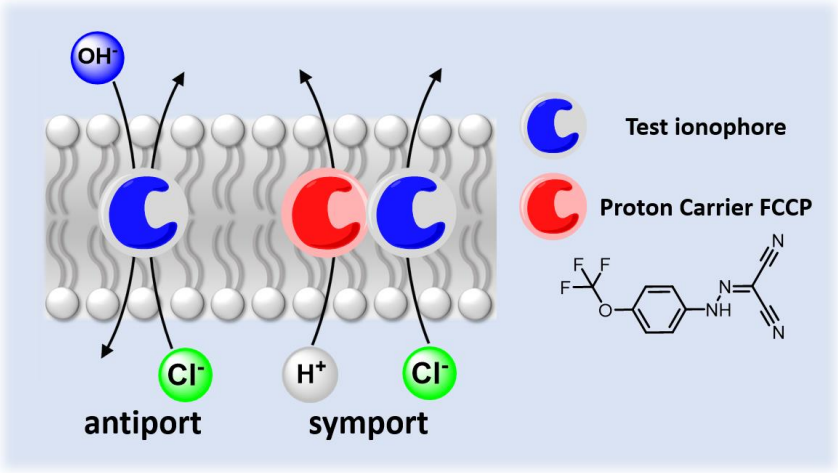


Figure 2.20. Ion transport mechanisms for anionophore-mediated dissipation of a transmembrane pH gradient in the absence (Cl^-/OH^- antiport) and presence of cyanide-*p*-trifluoromethoxyphenylhydrazone (FCCP) (H^+/Cl^- symport).

FCCP (0.25 μM) was added to the HPTS assay along with the NaOH base pulse at 50 s and the EC_{50} values for compounds **T2.1a** and **T2.1b** with and without the addition of FCCP are reported in **Table 2.4**. Representative Hill plots are shown in **Figure 2.21**. The Cl^- over OH^- selectivity value (*S*) under these assay conditions, was quantified by the ratio of EC_{50} values in the absence and presence of FCCP (**Table 2.4**, column 3). With a selectivity value close to 1, FCCP had little effect on the transport activity of carrier **T2.1a** (HB), implying that the transport of the chloride anion itself is the rate limiting step in the transport mechanism and that this carrier is not selective for chloride over hydroxide (**Figure 2.21**, left). On the other hand, there was a four-fold increase in transport activity for XB transporter **T2.1b** in the presence of FCCP, revealing Cl^- over OH^- selectivity for this halogen bonding carrier (**Figure 2.21**, right).

Table 2.4. FCCP dependence of transporters **1a** and **1b**.

	EC_{50} / μM[a]	EC_{50}^{FCCP} / μM[b]	*S* (EC_{50}/ EC_{50}^{FCCP})
T2.1a	2.0 ± 0.1	2.2 ± 0.5	0.9
T2.1b	1.3 ± 0.1	0.3 ± 0.05	4.0

[a]EC_{50} in the absence of FCCP. [b]EC_{50} in the presence of 0.25 μM FCCP.

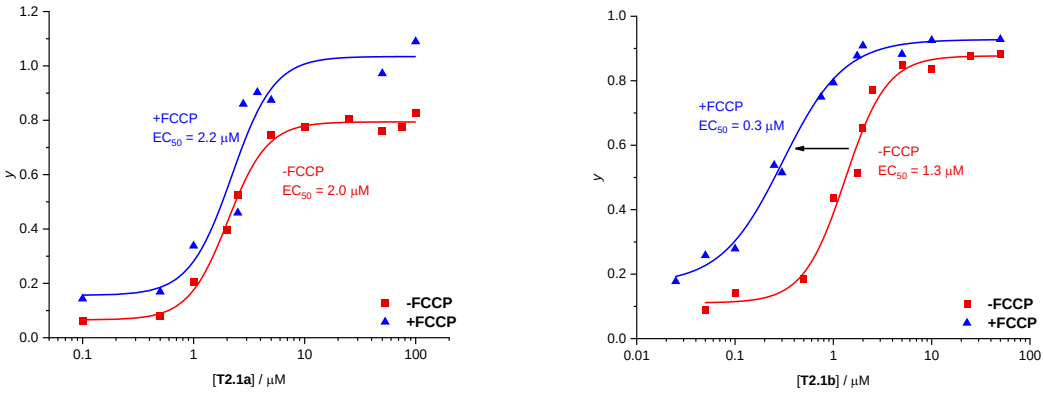


Figure 2.21. Hill plots associated with transport with and without FCCP. (Left) Carrier **T2.1a** and, (right), carrier **T2.1b**. Values represent the fractional fluorescence intensity (y) at 288 s for each measured concentration calculated from the fluorescent traces of the HPTS assay ± FCCP (0.25 μM).

Alongside this, upon addition of FCCP, carrier **T2.1b** achieved nanomolar activity with an EC_{50} value of 300 nM (**Figure 2.21**). Not only does this carrier have intrinsic chloride over hydroxide selectivity but it also has very high transport activity. As previously mentioned, maintaining these two properties simultaneously is extremely hard to achieve with acyclic C–H or N–H hydrogen bonding carriers, therefore, these results highlight the potential of the iodo-triazole motif to mediate active *and* selective transmembrane anion transport.

2.5.2 Halide Selectivity

Having demonstrated Cl^- > OH^- selectivity of the XB carriers, the selectivity of the carriers towards other anions was evaluated. Initially, the HPTS assay was performed with the iso-osmolar replacement of the external chloride anion (Na^+X^- where X^- = Cl^-, Br^-, I^- and NO_3^-).[5] The assay was performed with each carrier at 2 μM with and without the addition of FCCP, and repeated for each anion at least twice, in order to decipher the role of hydroxide in the transport mechanism with the different external anions.

Across all anions, iodotriazole carrier **T2.1b** was 2× more active compared to their prototriazole counterpart (**Figure 2.22**), correlating to the stronger association constants determined through ^{1}H NMR titration experiments of the XB receptors (**Table 2.1**, **page 63**). Comparison of the relative activities revealed an overall selectivity profile of OH^- > Cl^- > Br^- > I^- > NO_3^- for carrier **T2.1a** (**Figure 2.22**, left). Whilst the analogous XB anionophore **T2.1b** exhibits a selectivity profile of NO_3^- > Cl^- > Br^- > OH^- > I^- (**Figure 2.22**, right).

FCCP had little effect on the transport activity of prototriazole **T2.1a** because of its inherent preference to transport OH^-. For carrier **T2.1b**, the rate of transport of Br^- and NO_3^- increased in the presence of FCCP indicating that it is selective for Br^- and NO_3^- over OH^-.

However, the same increase was not observed for iodide and so the EC_{50} values with and without FCCP for iodide transport were determined (**Table 2.5**). The EC_{50} value of carrier **T2.1a** and **T2.1b** did not change significantly upon addition of FCCP, presenting *S* values of 0.9 and 1.0 respectively, indicating that the transport of iodide is the rate limiting process. This is attributed to the weaker interaction between the receptor and the larger halide. These results demonstrate how tuning the host-guest bond strength can be used to alter selectivity and transport activity.

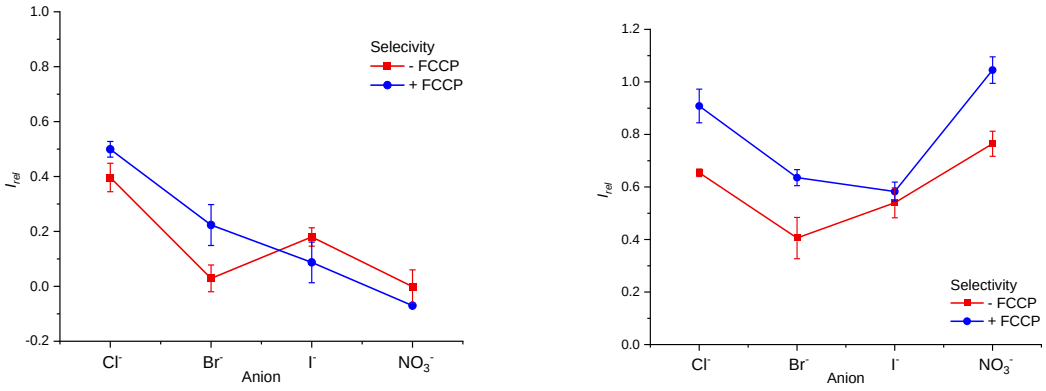


Figure 2.22. The dependence of the fractional fluorescence intensity (I_{rel}) at 288 s on the external anion upon addition of carriers **T2.1a** (left) and **T2.1b** (right) (2 μM). POPC vesicles containing 1 mM HPTS, 100 mM internal and external Na^+X^- (X^- = Cl^-, Br^-, I^-, NO_3^-), buffered with 10 mM HEPES at pH 7.0. A pH gradient is generated by addition of a NaOH base pulse (0.5 M), followed by the carrier at t = 90 s. Vesicle lysis by Triton X-100 calibrates the assay. The assay was repeated with, and without FCCP. Error bars represent standard deviations.

Table 2.5. EC_{50} values associated with transport mediated by carrier **T2.1a** and **T2.1b** with and without FCCP performed using the HPTS assay with either NaCl or NaI HEPES buffer.

Carrier	Anion	EC_{50} / μM[a]	EC_{50}^{FCCP} / μM[b]	EC_{50}/ EC_{50}^{FCCP}
T2.1a	Cl^-	2.03 (±0.11)	2.20 (±0.56)	0.9
	I^-	3.34 (±0.34)	3.95 (±0.38)	0.9
T2.1b	Cl^-	1.16 (±0.18)	0.30 (±0.03)	4.0
	I^-	1.92 (±0.16)	1.58 (±0.06)	1.0

The fractional fluorescence intensity was then plotted against the hydration energy ΔG_{hyd} of extravesicular anions (external: 100 mM NaX, internal: 100 mM NaCl) in the presence of 0.25 µM protonophore FCCP, highlighting the remarkable nature of the carriers' anion selectivity (**Figure 2.23**). Both HB and XB transporters show anti-Hofmeister selectivity trends which is unusual because in general hydrogen bonding anion transporters exhibit Hofmeister selectivity, where more weakly hydrated anions are selectively transported across the membrane due to ease of desolvation.[34–37]

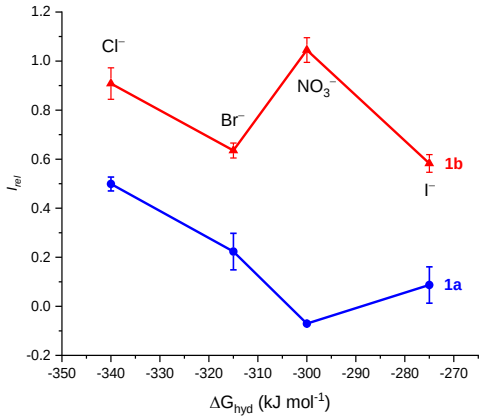


Figure 2.23. Dependence of the activity of **T2.1a** (black circles) and **T2.1b** (blue triangle) on the hydration energy ΔG_{hyd} of extravesicular anions (100 mM NaX, inside 100 mM NaCl) in the presence of 0.25 µM protonophore FCCP, reporting on relative rate of electrogenic X^- transport. Error bars represent standard deviations. Reproduced from reference [15] with permission from the Royal Society of Chemistry.

2.6 Computational Rationale

Computational investigations were undertaken by Dr Alistair Sterling and Prof. Fernanda Duarte to further probe the origins of the transport selectivity and activity. In depth details of the computational analysis and levels of theory used can be found in **chapter 5 section 5.6.1**. To reduce computational cost, all analysis was performed on carriers with truncated alkyl chains. It was confirmed by comparing the electrostatic potential for the full and simplified model (ΔESP_{max} < 0.1 kcal mol^{-1}), that this structural modification did not affect the calculated ESP values and allowed for efficient evaluation of binding with each anion (Cl^-, Br^-, I^- and NO_3^-). The calculated electrostatic surface potentials (ESP) reveal the characteristic iodine-centred sigma-hole associated with halogen bond donors,[38,39] and the accumulation of δ^+ surrounding the triazole protons active in hydrogen bonding (**Figure 2.24**).

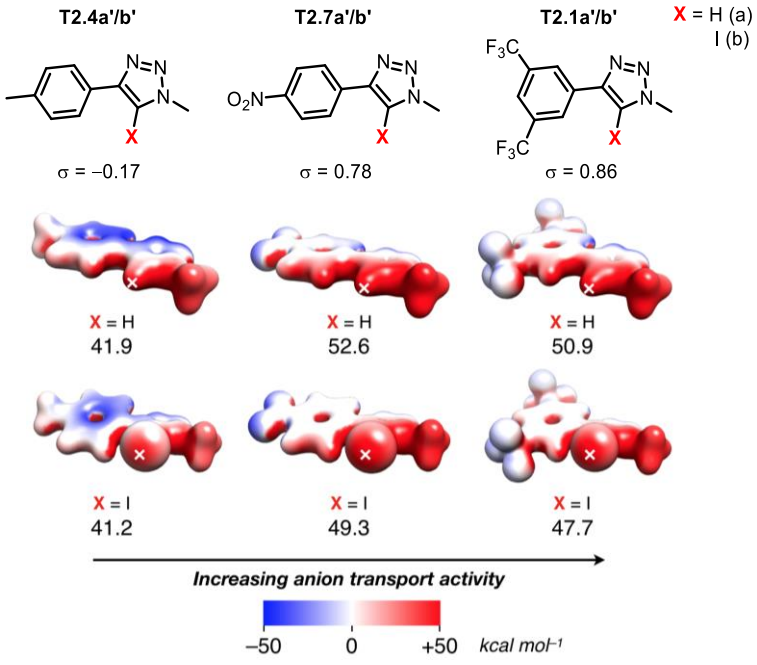


Figure 2.24. Calculated electrostatic potential surfaces (isovalue = 0.04 a.u.) for truncated transporter ligands **T2.4a'/b'**, **T2.7a'/b'** and **T2.1a'/b'** calculated at the SMD($CHCl_3$)-ωB97X-D/def2-TZVP level of theory. Maximum ESP values are located at the position of each cross, and reported beneath each transporter in kcal mol^{-1}. Reproduced from reference [15] with permission from the Royal Society of Chemistry.

To probe the binding energies and structures of the anionophore-anion complexes, the relative binding enthalpies for both 1:1 and 2:1 model carrier-anion complexes were calculated (**section 5.6.1**).[40–45] This was performed in $CHCl_3$ implicit solvent which acts as a membrane-mimetic environment. Bidentate binding was found to be preferred in the model HB system **T2.1a'** in which hydrogen bonds from both the alkyl C(sp^3)–H1 and triazole C(sp^2)–H2 could be involved (**Figure 2.25**). This finding is in line with the result of the ESP calculations in **Figure 2.24**. Interestingly, the results indicate that in the 2:1 complex, four HB C–H···anion interactions per anion exists for **T2.1a'**, while only one XB C–I···anion interaction is present for **T2.1b'** (**Figure 2.25**). Additionally, bond order and second-order perturbation theory analysis, which allows for the quantification of bond energies ($E^{(2)}$), indicates that the addition of the second transporter weakens the total XB interactions when compared with the 1:1 carrier-anion complex ($E^{(2)}_{XB}$ = 40.6 vs 30.7 kcal mol^{-1}) (**Figure 2.25**). However, this is partially compensated by dispersion interactions between the two transporter ligands ($E_{T1\text{-}T2}$ = 16.0 kcal mol^{-1}) and a C–H interaction (10.1 kcal mol^{-1}), which leads to an overall larger stabilisation energy ($E^{(2)}$total = 56.8 kcal mol^{-1}).

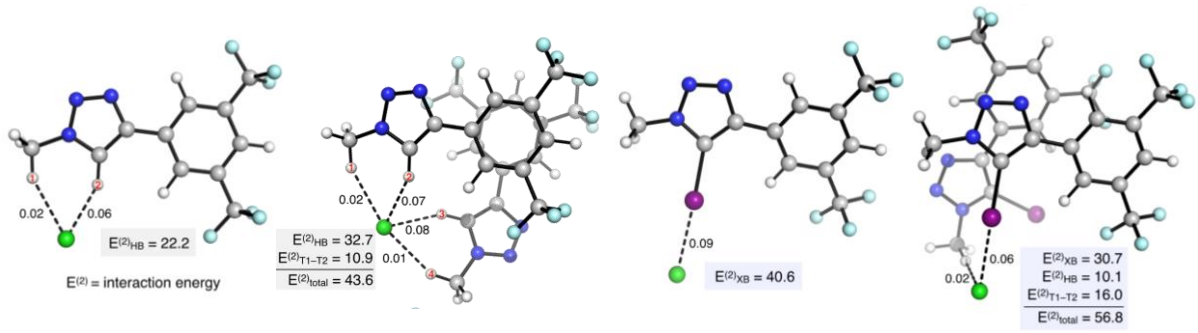


Figure 2.25. Mayer bond orders (dashed lines), their associated HB/XB bond energies ($E^{(2)}_{HB/XB}$), and interaction energy between ligands ($E^{(2)}_{T1–T2}$) in kcal mol^{-1} were calculated at the [NBO/SMD($CHCl_3$)- ωB97X-D3/def2-SVP (ma-def2-TZVP on Cl, I)//ωB97X-D3/def2-SVP (ma-def2-SVP on Cl, I)] level of theory. Free energies were calculated using a quasi-RRHO approximation and corrected for a 1 M standard state at 298.15 K.[45] Reproduced from reference [15] with permission from the Royal Society of Chemistry.

Calculations reveal that for chloride binding, $\Delta H_{bind}(2:1) > 2 \times \Delta H_{bind}(1:1)$ (**Figure 2.26**), because 2:1 binding is enhanced by π-stacking between the arenes. This demonstrates how the strength of the non-covalent interactions are sufficient to overcome the entropic cost of 2:1 complex formation.

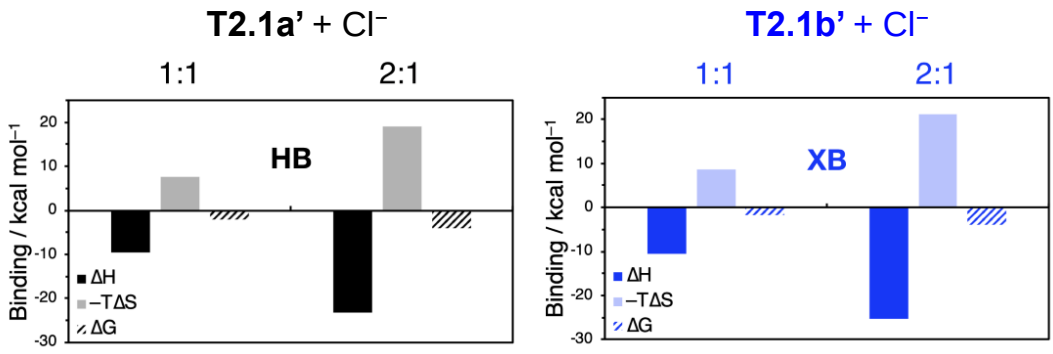


Figure 2.26. Characterisation of 1:1 and 2:1 binding of **T2.1a'** and **T2.1b'** to chloride. Enthalpies, entropies and free energies of binding (kcal mol^{-1}) were calculated at the [SMD($CHCl_3$)-DLPNO-CCD(T)/def2-TZVP (ma-def2-TZVP on Cl, I)//ωB97X-D3/def2-SVP (ma-def2-SVP on Cl, I)] level of theory. Reproduced from reference [15] with permission from the Royal Society of Chemistry.

Analysis of the partial charges on each anion in the 1:1 and 2:1 binding modes suggest a correlation between the transport ability and the ability of the transport to stabilise the anion charge (**Figure 2.27**). For Cl^-, Br^- and I^-, the negative charge is more effectively delocalised over the XB anionophore than the HB analogue (**Figure 2.27**). This is expected to decrease the barrier to transport across the hydrophobic membrane, and thus aligns with the experimentally observed trend of the XB anionophores to have enhanced anion transport rates compared to the analogous HB carrier systems. This is consistent with previous results from donor K-edge X-ray absorption spectroscopy experiments which revealed significant covalency in the XB interaction between related iodo-triazole XB donors and chloride anions (comparable to that in transition metal chloride complexes), in contrast

to proto-triazole analogues with negligible charge transfer contribution to the HB interaction.[46]

However, in the case of nitrate the observed transport activity does not correlate with the increased calculated partial charge. This behaviour may be due to the greater number of thermally-accessible conformations for the binding of the trigonal nitrate anion, with each of them having a different charge distribution. In this case, the most stable conformer in solution is likely not the most active for membrane transport.

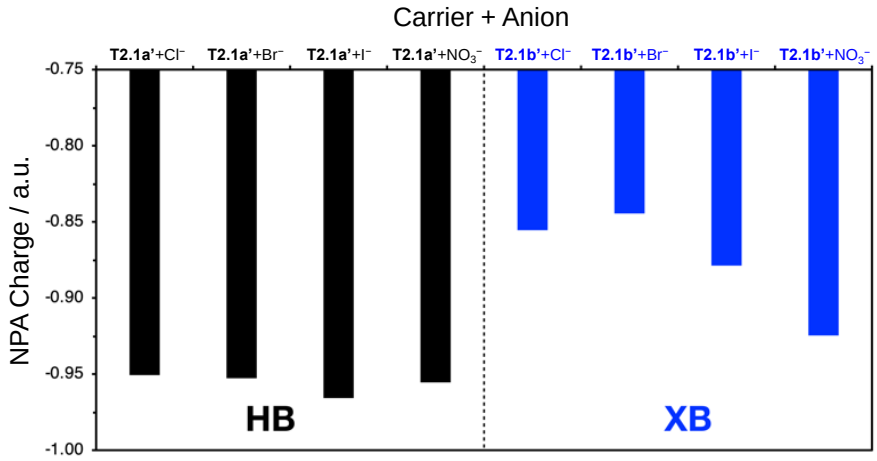


Figure 2.27. Partial charges on each anion for 1:1 anionophore-anion complexes of **T2.1a'** and **T2.1b'**, calculated using natural population analysis (NPA) at the [NBO/SMD($CHCl_3$)-ωB97X-D3/def2-SVP (ma-def2-SVP on anion)] level of theory. Reproduced from reference [15] with permission from the Royal Society of Chemistry.

2.7 Chapter Conclusions

The research presented in this chapter demonstrates that despite the relative simplicity of the design, acyclic halogen bonding iodo-triazoles can efficiently transport anions across lipid bilayer membranes with enhanced activity in comparison to hydrogen bonding proto-triazole analogues.

Initially, the binding affinity of **T2.1a** and **T2.1b** was evaluated using ^{1}H NMR titration experiments which revealed stronger anion binding affinity of the XB receptor and unusual anti-Hofmeister selectivity. This was supported by computational investigations into the calculated ESP surface values and the partial charges on each anion for 1:1 anionophore-anion complexes which showed a larger accumulation of δ^{+} surrounding the XB iodo-triazole bond donors.

Following this, the anion transport activity of all 21 carriers was assessed using the HPTS assay and a series of additional kinetic fluorescence assays were performed to determine the transport mechanism and the $Cl^{-} > OH^{-}$ selectivity of the carriers. The HPTS assay revealed enhanced transport activity of the halogen bonding anionophores vs the hydrogen bonding analogues across all receptors and anions. XB carriers **T2.1b** and **T2.9b** are among the most active halogen bonding transporters reported within the literature with EC_{50} values of 1.16 μM and 1.15 μM respectively. The results indicated that the electron-withdrawing nature of 3,5-bis(trifluoromethyl)benzene and 4-nitrobenzene, quantified by the Hammett constants, led to the excellent transmembrane transport activity.

The mobile carrier and cation-independent mechanism of the receptors was then confirmed and an antiport mechanism of anions was deciphered. The selectivity of the transport process was explored and an anti-Hofmeister bias for halide transport was determined. This correlated with anion binding affinities determined by ^{1}H NMR titration

experiments and demonstrated the dominant role of host-guest binding within anion transport. Importantly, unusual $Cl^- > OH^-$ selectivity for the halogen bonding anionophores was achieved, highlighting the potential of this XB motif to provide the starting point for designing highly active novel ionophores with enhanced selectivity for potential future application in channelopathy therapeutics.

2.8 References

1 J. Pancholi and P. D. Beer, *Coord. Chem. Rev.*, 2020, **416**, 213281.

2 I. Iribarren, G. Sánchez-Sanz and C. Trujillo, *Molecules*, 2020, **25**, 798.

3 D. W. Larsen and A. L. Allred, *J. Phys. Chem.*, 1965, **69**, 2400–2401.

4 A. Mele, P. Metrangolo, H. Neukirch, T. Pilati and G. Resnati, *J. Am. Chem. Soc.*, 2005, **127**, 14972–14973.

5 A. V. Jentzsch, D. Emery, J. Mareda, S. K. Nayak, P. Metrangolo, G. Resnati, N. Sakai and S. Matile, *Nat. Commun.*, 2012, **3**, 905.

6 L. M. Lee, M. Tsemperouli, A. I. Poblador-Bahamonde, S. Benz, N. Sakai, K. Sugihara and S. Matile, *J. Am. Chem. Soc.*, 2019, **141**, 810–814.

7 C. Ren, X. Ding, A. Roy, J. Shen, S. Zhou, F. Chen, S. F. Yau Li, H. Ren, Y. Y. Yang and H. Zeng, *Chem. Sci.*, 2018, **9**, 4044–4051.

8 H. C. Kolb, M. G. Finn and K. B. Sharpless, *Angew. Chem. Int. Ed.*, 2001, **40**, 2004–2021.

9 E. Haldón, M. C. Nicasio and P. J. Pérez, *Org. Biomol. Chem.*, 2015, **13**, 9528–9550.

10 D. N. Barsoum, N. Okashah, X. Zhang and L. Zhu, *J. Org. Chem.*, 2015, **80**, 9542–9551.

11 A. Borissov, J. Y. C. Lim, A. Brown, K. E. Christensen, A. L. Thompson, M. D. Smith and P. D. Beer, *Chem. Commun.*, 2017, **53**, 2483–2486.

12 X. Li, J. Y. C. Lim and P. D. Beer, *Faraday Discuss.*, 2017, **203**, 245–255.

13 J. Y. C. Lim, T. Bunchuay and P. D. Beer, *Chem. Eur. J.*, 2017, **23**, 4700–4707.

14 M. J. Langton, S. W. Robinson, I. Marques, V. Félix and P. D. Beer, *Nat. Chem.*, 2014, **6**, 1039–1043.

15 L. E. Bickerton, A. J. Sterling, P. D. Beer, F. Duarte and M. J. Langton, *Chem. Sci.*, 2020, **11**, 4722–4729.

16 A. Brown and P. D. Beer, *Chem. Commun.*, 2016, **52**, 8645–8658.

17 R. Kharb, P. C. Sharma and M. S. Yar, *J. Enzyme Inhib. Med. Chem.*, 2011, **26**, 1–21.

18 C. Hansch, A. Leo and R. W. Taft, *Chem. Rev.*, 1991, **91**, 165–195.

19 Virtual Computational Chemistry Laboratory, http://www.vcclab.org/, (accessed 13 July 2019).

20 N. Busschaert, S. J. Bradberry, M. Wenzel, C. J. E. Haynes, J. R. Hiscock, I. L. Kirby, L. E. Karagiannidis, S. J. Moore, N. J. Wells, J. Herniman, G. J. Langley, P. N. Horton, M. E.

Light, I. Marques, P. J. Costa, V. Félix, J. G. Frey and P. A. Gale, *Chem. Sci.*, 2013, **4**, 3036–3045.

21 I. V. Tetko, J. Gasteiger, R. Todeschini, A. Mauri, D. Livingstone, P. Ertl, V. A. Palyulin, E. V. Radchenko, N. S. Zefirov, A. S. Makarenko, V. Y. Tanchuk and V. V. Prokopenko, *J. Comput. Aided. Mol. Des.*, 2005, **19**, 453–463.

22 BindFit v0.5 | Supramolecular, http://app.supramolecular.org/bindfit/.

23 N. Busschaert, R. B. P. Elmes, D. D. Czech, X. Wu, I. L. Kirby, E. M. Peck, K. D. Hendzel, S. K. Shaw, B. Chan, B. D. Smith, K. A. Jolliffe and P. A. Gale, *Chem. Sci.*, 2014, **5**, 3617–3626.

24 S. Bhosale and S. Matile, *Chirality*, 2006, **18**, 849–856.

25 N. Matile, S. & Sakai, *Analytical Methods in Supramolecular Chemistry*, Wiley, 2nd edn., 2012.

26 J. S. Lolkema and D.-J. Slotboom, *J. Gen. Physiol.*, 2015, **145**, 565–574.

27 S. J. Edwards, I. Marques, C. M. Dias, R. A. Tromans, N. R. Lees, V. Félix, H. Valkenier and A. P. Davis, *Chem. – A Eur. J.*, 2016, **22**, 2004–2011.

28 J. M. Abboud, C. Foces-Foces, R. Notario, R. E. Trifonov, A. P. Volovodenko, V. A. Ostrovskii, I. Alkorta and J. Elguero, *European J. Org. Chem.*, 2001, **2001**, 3013–3024.

29 T. Clark, M. Hennemann, J. S. Murray and P. Politzer, *J. Mol. Model.*, 2007, **13**, 291–296.

30 X. Wu, L. W. Judd, E. N. W. Howe, A. M. Withecombe, V. Soto-Cerrato, H. Li, N. Busschaert, H. Valkenier, R. Pérez-Tomás, D. N. Sheppard, Y. B. Jiang, A. P. Davis and P. A. Gale, *Chem*, 2016, **1**, 127–146.

31 S. Matile and N. Sakai, *Anal. Methods Supramol. Chem.*, 2012, 711–742.

32 X. Wu, E. N. W. Howe and P. A. Gale, *Acc. Chem. Res.*, 2018, **51**, 1870–1879.

33 R. Benz and S. McLaughlin, *Biophys. J.*, 1983, **41**, 381–398.

34 S. K. Berezin and J. T. Davis, *J. Am. Chem. Soc.*, 2009, **131**, 2458–2459.

35 S. K. Berezin, *Supramol. Chem.*, 2013, **25**, 323–334.

36 Y. Yang, X. Wu, N. Busschaert, H. Furuta and P. A. Gale, *Chem. Commun.*, 2017, **53**, 9230–9233.

37 X. Wu, J. R. Small, A. Cataldo, A. M. Withecombe, P. Turner and P. A. Gale, *Angew. Chem. Int. Ed.*, 2019, **58**, 15142–15147.

38 P. Politzer, J. S. Murray and T. Clark, *Phys. Chem. Chem. Phys.*, 2013, **15**, 11178–

11189.

39 J. Y. C. Lim and P. D. Beer, *Chem*, 2018, **4**, 731–783.

40 F. Neese, *Wiley Interdiscip. Rev. Comput. Mol. Sci.*, 2012, **2**, 73–78.

41 C. Riplinger and F. Neese, *J. Chem. Phys.*, 2013, **138**, 034106.

42 J.-D. Chai and M. Head-Gordon, *Phys. Chem. Chem. Phys.*, 2008, **10**, 6615–6620.

43 F. Weigend and R. Ahlrichs, *Phys. Chem. Chem. Phys.*, 2005, **7**, 3297–3305.

44 A. V. Marenich, C. J. Cramer and D. G. Truhlar, *J. Phys. Chem. B*, 2009, **113**, 6378–6396.

45 S. Grimme, *Chem. Eur. J.*, 2012, **18**, 9955–9964.

46 S. W. Robinson, C. L. Mustoe, N. G. White, A. Brown, A. L. Thompson, P. Kennepohl and P. D. Beer, *J. Am. Chem. Soc.*, 2015, **137**, 499–507.

CHAPTER 3

Chapter 3 Multidentate Chalcogen, Halogen and Hydrogen Bonding Anion Transporters with Non-Protonophoric Activity

3.1 Introduction

Highly selective anion binding is crucial to ensure the correct function of the biological machinery within living organisms. Nature achieves anion discrimination by employing a multipoint recognition strategy based on strong interactions provided by multiple donors inside preorgnized binding cavities which are buried in the core of a protein's structure.[1] The most prominent examples of such strategy are the sulphate binding protein (SBP) and phosphate binding protein (PBP) (**Figure 3.1**, a and b respectively).[2,3] These are highly active *and* selective anion transporters composed of a single polypeptide chain. They both use an array of convergent hydrogen bond donors to control the uptake and transport of sulphate or phosphate within bacteria.

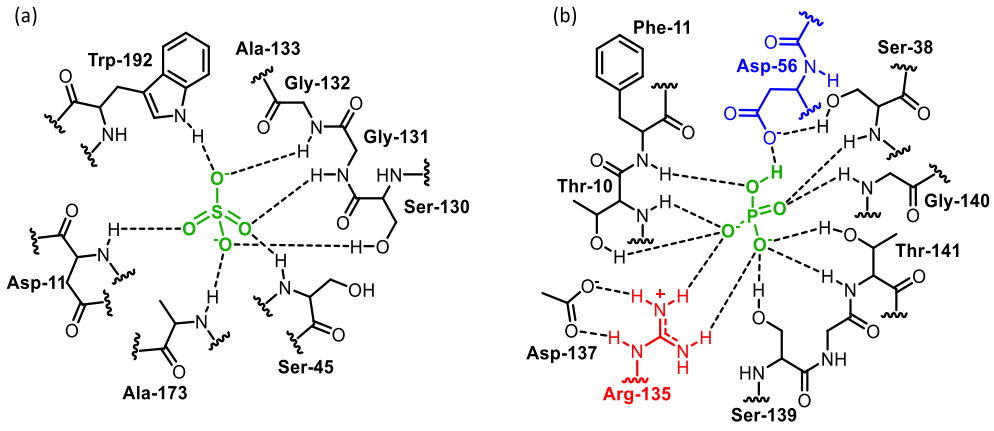


Figure 3.1. Schematic representation of the array of convergent hydrogen bonds which bind the anion in (a) sulfate-[2] and (b) phosphate-binding proteins.[3]

The sulphate binding protein uses seven hydrogen bonding interactions from neutral HB donors to bind a dehydrated sulphate anion. In contrast, the phosphate binding protein uses twelve hydrogen bonding interactions from 10 neutral HB donors and two from the cationic guanidinium motif of the Arg-135 residue. Both proteins bind their oxyanion deep within the hydrophobic core structure of the protein, shielding anions from the surrounding aqueous environment and enhancing the strength of the hydrogen bond interactions. For example, phosphate is bound about 8 Å below the surface of the phosphate binding protein. One key difference between the binding cavities of these two proteins is the presence of the carboxylate side chain found in Asp-56 of the phosphate binding protein. It serves as a hydrogen bond acceptor to accommodate the proton present in phosphate but not in sulphate. As a result, the PBP is capable of discriminating phosphate from sulphate, binding 5 orders of magnitude stronger than sulphate, and from arsenate by 3 orders of magnitude (among other tetrahedral fully ionized divalent oxyanions). Such selectivity remains unparalleled by artificial systems. This example clearly highlights the crucial role of each hydrogen bond for the function of these proteins.

Maximising receptor preorganisation and geometric complementarity towards a guest anion, to match up to the selectivity found within nature, is therefore the task that bears dominance when creating highly active *and* selective anion transporters. As discussed in **chapter 1, section 1.4.1,** Davis and co-workers achieved high Cl^- over OH^- selectivity (~100 fold) with a macrocyclic cholaphane transporter with four urea HB donors, it was able to remain highly transport-active whilst being Cl^- selective, this is unlike many selective HB transporters which often sacrifice some transport-activity.[4]

In light of the results presented by Davis, a series of previously reported tripodal tren-based tris-(thio)urea transporters, with the potential to form 6 hydrogen bonds, were tested for chloride selectivity by Gale and co-workers (**Figure 3.2**).[5–7] Tripodal carriers (a) and (b) gave high Cl^- > OH^- selectivity factors of 33 and 55 respectively, indicating they are very selective for Cl^- over OH^-. This contrasts with analogous monodentate urea-based anion transporters which do not present any selectivity.[8] However, carriers (a) and (b) have EC_{50} values of 9.77 mol% and 0.12 mol% (transporter to lipid) respectively, and are therefore not particularly active. Attempts were made to increase the activity of the carriers by increasing the acidity and therefore potency of the NH HB-donors with the addition of electron-withdrawing groups, however, this had a detrimental effect on the Cl^- selectivity. For example, the highly fluorinated carrier (**Figure 3.2c**) was the most active carrier in this series of tren-based receptors (EC_{50} = 0.00036 mol%) but did not show any chloride selectivity.[5] These results indicate that hydrogen bonding interactions may not be suitable to mediate highly active *and* selective transport.

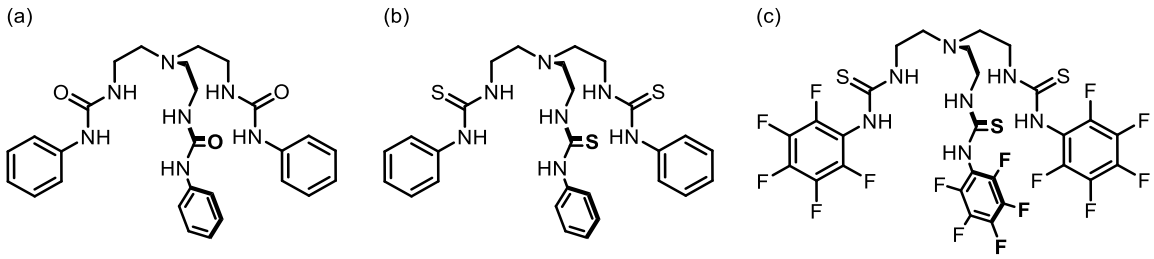


Figure 3.2. (a) Tripodal tren-based tris-urea transporter and tris-(thio)urea transporters (b) and (c).[5]

Chalcogen bonding is the non-covalent interaction between a region of positive electrostatic potential on the chalcogen atom and a Lewis base such as an anion and is thus directly analogous to halogen bonding.[9] The chalcogens include oxygen, sulphur, selenium and tellurium, with tellurium being the most polarisable and therefore the most potent bond donor. Chalcogen bond donors exhibit contrasting anion selectivities and are often more hydrophobic in comparison to XB donors which may prove advantageous in the context of anion transport.[10] Although chalcogen bonding has been described predominantly within crystal engineering in the solid state,[9] it is postulated to play a role in proteins due to the presence of sulphur in the amino acids' methionine and cysteine.[11,12] The use of chalcogen bonding within supramolecular chemistry is currently rare, but there are some notable examples of their incorporation into macrocycles,[13] rotaxanes[14] and mechanosensitive membrane probes.[15] In addition to this, halogen bonding,[16–21] and more recently chalcogen[22] and pnictogen[23–25] bonding transporters represent effective alternatives to hydrogen bonding systems.

Taylor, Seferos and co-workers reported a series of substituted benzotelluradiazoles, which were preliminary examples of chalcogen bonding being used for anion recognition in solution (**Figure 3.3**, receptor a and b).[26] UV-vis anion binding studies with TBA anion salts revealed that these receptors bind anions with a selectivity trend of $Cl^- > Br^- > I^- > NO_3^-$, correlating with the anions' charge density and basicity. Perfluorination of the aromatic ring to yield receptor (b) enhanced the anion binding potency of the receptor in comparison to parent receptor (a), consistent with previous findings with XB systems that increasing the electron withdrawing ability of the substituent increases the magnitude of the sigma-hole.

The Beer group have previously reported chalcogen bonding rotaxanes,[14] and have more recently presented a series of acyclic ChB anion receptors for anion recognition (**Figure 3.3**, c and d).[27] The 3,5-bis-triazole pyridine scaffold of these receptors was functionalised with electron donating and withdrawing aryl substituents which were systematically varied in order to assess the effects of the substituents on anion binding potency. For comparison, analogous C-H hydrogen and C-I halogen bonding receptors were also synthesised and the substituents attached to the chalcogen atom were also varied. They found that the chalcogen bonding receptors showed a general anion selectivity trend of $Cl^- > Br^- > I^-$ correlating with the decreasing basicity of the halides and, importantly, had much higher anion binding affinities in comparison to the HB receptors. Hammett plots revealed that in all cases the receptor-halide binding affinity correlates with the aryl substituent σ-parameters, demonstrating the ability to fine tune the anion binding potency and selectivity through the selection of the bond donor and addition of electron withdrawing substituents.

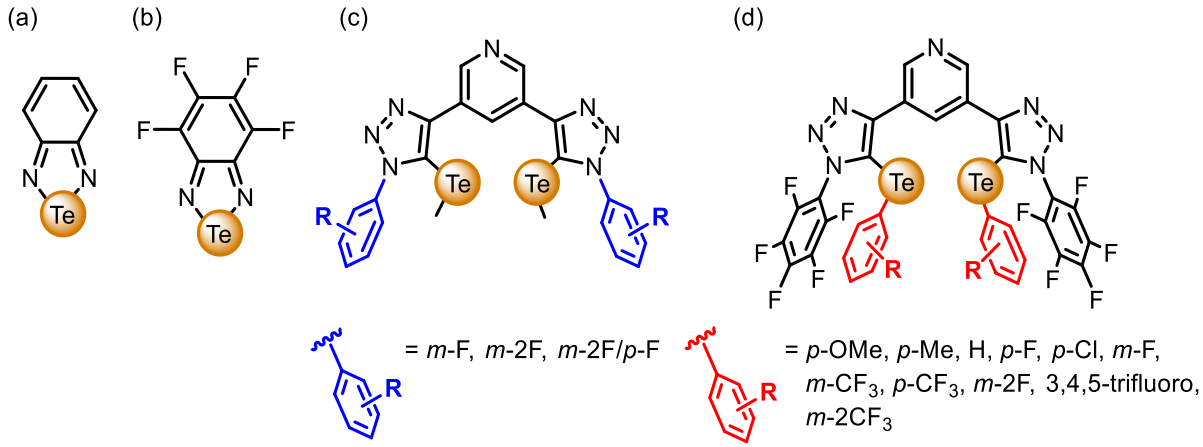


Figure 3.3. Chalcogen bonding motifs for anion recognition.[26,27]

Anion recognition is also a powerful tool within catalysis,[28] and chalcogen bonding has shown potential in this area.[29] For example, Matile and co-workers reported a bidentate ChB motif (**Figure 3.4a**) which was able to strongly bind chloride and successfully enhance the rate of transfer hydrogenation of quinolines by multiple orders of magnitude. They attributed this to the strength and directionality of the chalcogen bonding interactions.[30] The same group subsequently went on to develop chalcogen bonding receptors for anion transport purposes. They reported the ability of electron deficient dithieno[3,2-*b*;2',3'-*d*]thiophenes to perform transmembrane anion transport using the HPTS assay and the most active carrier (**Figure 3.4b**) showed activities as low as 1.9 μM.[22] Another notable example is the tellurium-centred ChB carrier (**Figure 3.4c**) previously discussed in **chapter 1 section 1.4.2.3** which was capable of anion transport with an EC_{50} value of 0.22 μM.[23] Despite these promising results, examples of anion transport mediated by ChB remain rare. The following chapter describes the use of synthetically facile telluromethyl-triazoles for anion transport purposes, for the first time.

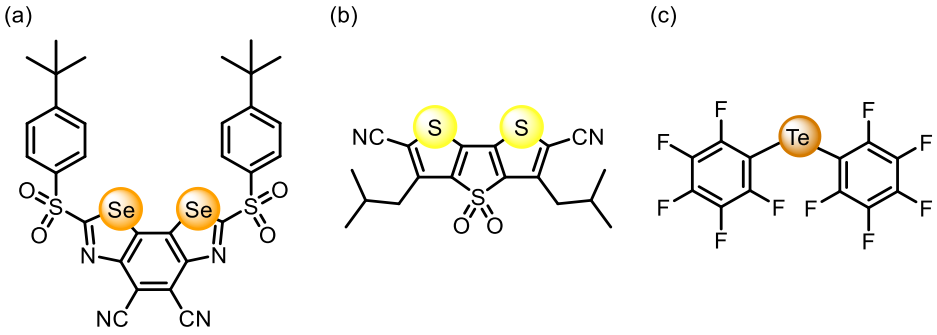


Figure 3.4. Chalcogen bonding motifs for anion recognition and transport.[13,14,24]

3.1.1 Chapter Aims

The overall aims of this chapter are to design and synthesise multidentate XB and ChB anion receptors which not only show strong anion binding in organic solvent but also selectively transport chloride across lipid bilayers. Their anion affinities and transport activities will then be compared with analogous HB systems in order to define the role of the sigma-hole bond donors within the transporters.

Triazole-based mono-, bi- and tri-dentate anion receptors will be synthesised from proto-, iodo- or telluromethyl- alkynes and electron deficient aromatic azides. Increasing the denticity of the carriers will be used to investigate the effects of anion encapsulation on anion binding and anion transport ability. Fluorescence-based transport experiments in LUVs, such as the HPTS assay, will then determine the transport activity of all synthesised carriers. Following this, in depth investigations into the chloride selectivity of nominated carriers will take place.

Computational analysis will be used to provide insight into the anion binding and transport process, including the chloride selectivity of the sigma-hole based transporters. Not only will the calculations assess the host:guest binding stoichiometry first described experimentally by the ^{1}H NMR titration experiments, but also the binding enthalpies upon chloride recognition, and the role of anion dehydration in the transport process.

This chapter delves into the details of the publication entitled 'Highly Active Halogen Bonding and Chalcogen Bonding Chloride Transporters with Non-Protonophoric Activity' published in *Chemistry-A European Journal.*[31]

3.2 Synthesis

A series of readily accessible mono-, bi- and tridentate ChB, XB and HB anion receptors were designed for investigation (**Figure 2.3**). The triazole groups of the bidentate receptor are situated in the 3,5- positions to enable cooperative anion binding assisted by the two bond donors. An electron withdrawing nitro group on the bidentate receptor further polarizes the molecule resulting in a stronger association with anions. The tridentate receptor is based on 1,3,5-substituted benzene, which is a common platform for the synthesis of tripodal anion receptors.[32] Typically the central benzene ring in such structures are separated from the binding motifs by a flexible linker. In this design, triazole rings are attached directly to the aromatic platform, which increases rigidity of the receptor and places the HB, XB and ChB bond donors closer to each other. To the increase binding potency of the donors atoms, the triazoles are again connected to electron-poor aromatic rings.

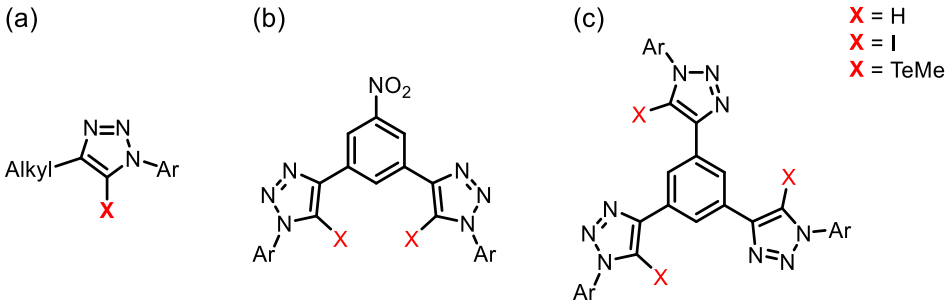
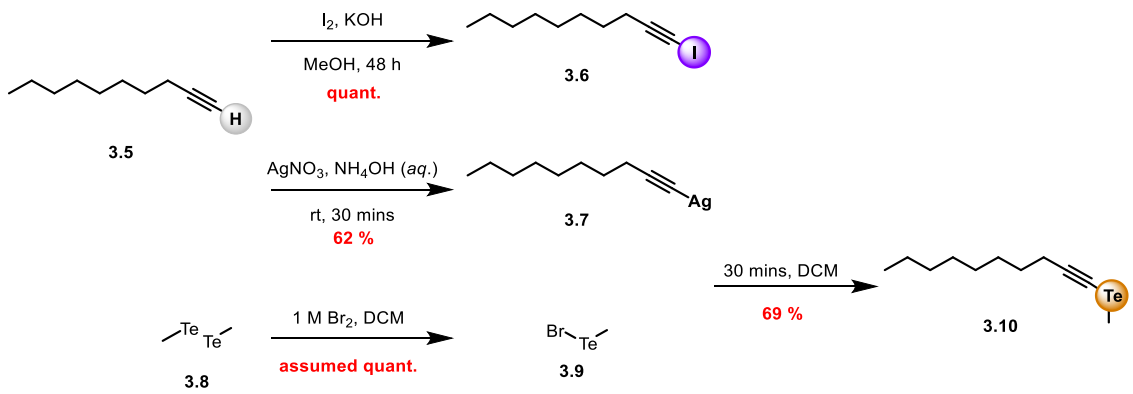


Figure 3.5. General receptor design of monodentate (a), bidentate (b) and tridentate (c) ChB, XB and HB anion receptors.

All target transporters were synthesised via a copper-catalyzed azide−alkyne cycloaddition (CuAAC) reaction between the appropriately functionalised alkyne and azide

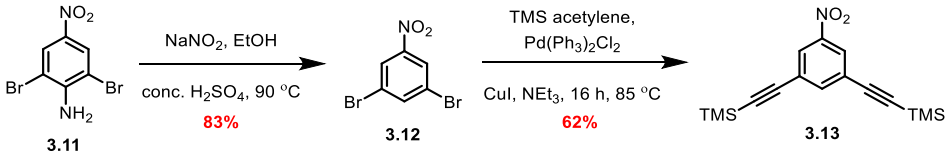
precursors. They are numbered transporter **T3.X** with **a**, **b**, or **c** representing HB, XB and ChB respectively. Dr Andrew Docker synthesised the three bidentate receptors and their precursors (**T3.2a-c**). The prerequisite proto-, iodo-, and telluromethyl-functionalised alkyne precursors for the synthesis of the monodentate carriers were prepared from 1-decyne (**Scheme 3.1**). Treatment of 1-decyne with KOH in methanol and subsequent reaction with elemental iodine afforded iodoalkyne **3.6** quantitatively. The intermediary silver acetylide **3.7** was prepared from 1-decyne stirred with freshly ground $AgNO_3$ in methanol in the presence of $NH_4OH_{(aq)}$. Dimethyl ditelluriude **3.8** was prepared according to literature procedures from methyllithium and tellurium powder,[44] and reacted immediately with bromine to yield MeTeBr **3.9**. Acetylide **3.7** could then be stirred with a freshly prepared solution of **3.9** to give the telluromethyl-functionalised alkyne **3.10** in 69% yield.



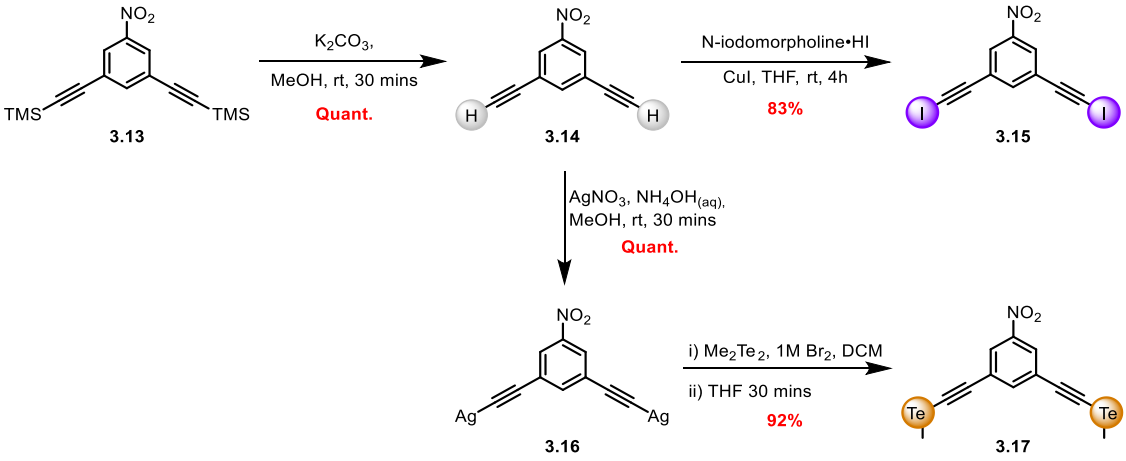
Scheme 3.1. Synthesis of alkyne precursors for monodentate receptors **3.6** and **3.10**.

The proto-, iodo- and telluromethyl-functionalised alkyne precursors for the bidentate receptors were prepared from 1,3-bis((trimethylsilyl)ethynyl)nitrobenzene **3.13** by Dr Andrew Docker. TMS Protected alkyne **3.13** was itself obtained from 2,6-dibromo-4-

nitroaniline **3.11** using previously reported procedures (**Scheme 3.2**).[33] TMS deprotection using K_2CO_3 yielded 1,3-diethynylnitrobenzene **3.14** which could then be treated with *N*-iodomorpholine hydroiodide in the presence of catalytic copper (I) iodide in anhydrous THF solution to afford the target bis-iodoalkyne **3.15** in 83% yield (**Scheme 3.3**). 1,3-diethynylnitrobenzene **3.14** was reacted with freshly ground $AgNO_3$ in methanol in the presence of $NH_4OH_{(aq)}$ to give the required silver acetylide intermediate **3.16**, which was subsequently reacted with a freshly generated solution of methyl tellurium bromide to afford **4.17** in an 89% yield.

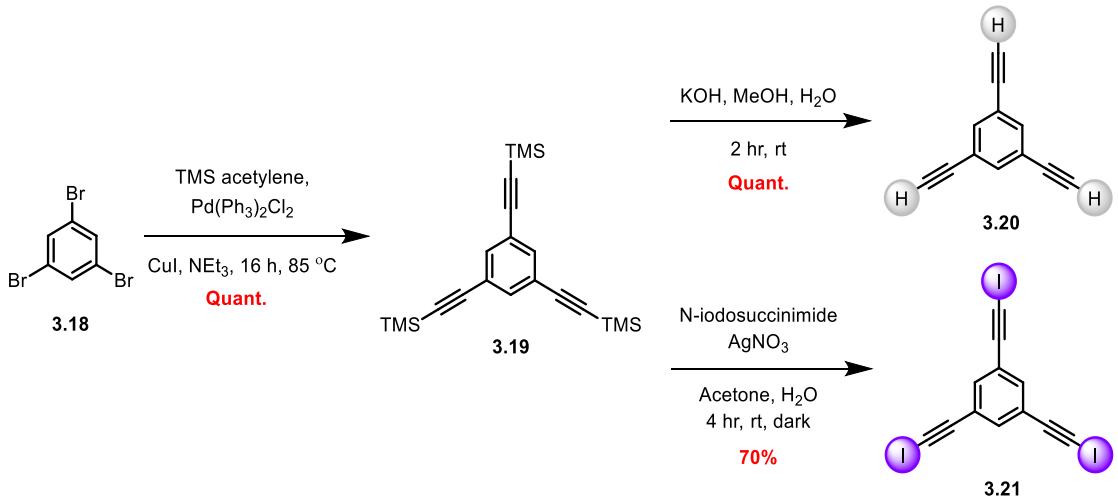


Scheme 3.2. Synthesis of alkyne precursors **3.13** prepared by Dr Andrew Docker.

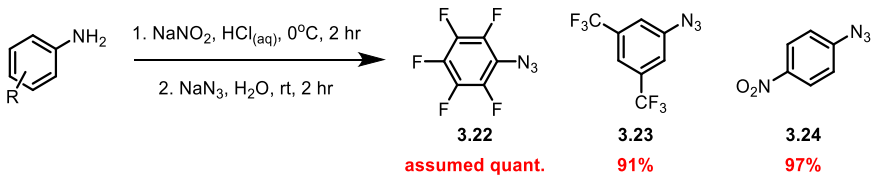


Scheme 3.3. Synthesis of alkyne precursors **3.14**, **3.15** and **3.17** for bidentate receptors prepared by Dr Andrew Docker.

The alkyne precursors for the tridentate receptors were synthesised from 1,3,5-tribromobenzene **3.18** which could be subjected to a Sonogashira cross coupling reaction with TMS acetylene to yield TMS-protected alkyne **3.19** (**Scheme 3.4**). Deprotection with KOH in a 1:1 MeOH and water mixture yielded 1,3,5-triethynylbenzene **3.20** quantitatively. Direct conversion of the TMS protected alkyne to the iodo-alkyne **3.21** could be achieved with NIS and $AgNO_3$ in acetone and water with a 70% yield. The azide precursors were synthesised from their analogous anilines using the Sandmeyer reaction with sodium nitrite in aqueous HCl and subsequent treatment with sodium azide (**Scheme 3.5**). The yield of low molecular weight organic azide **3.22** was assumed quantitative to avoid loss of mass when the solvent was removed in vacuo, and because it is potentially explosive.

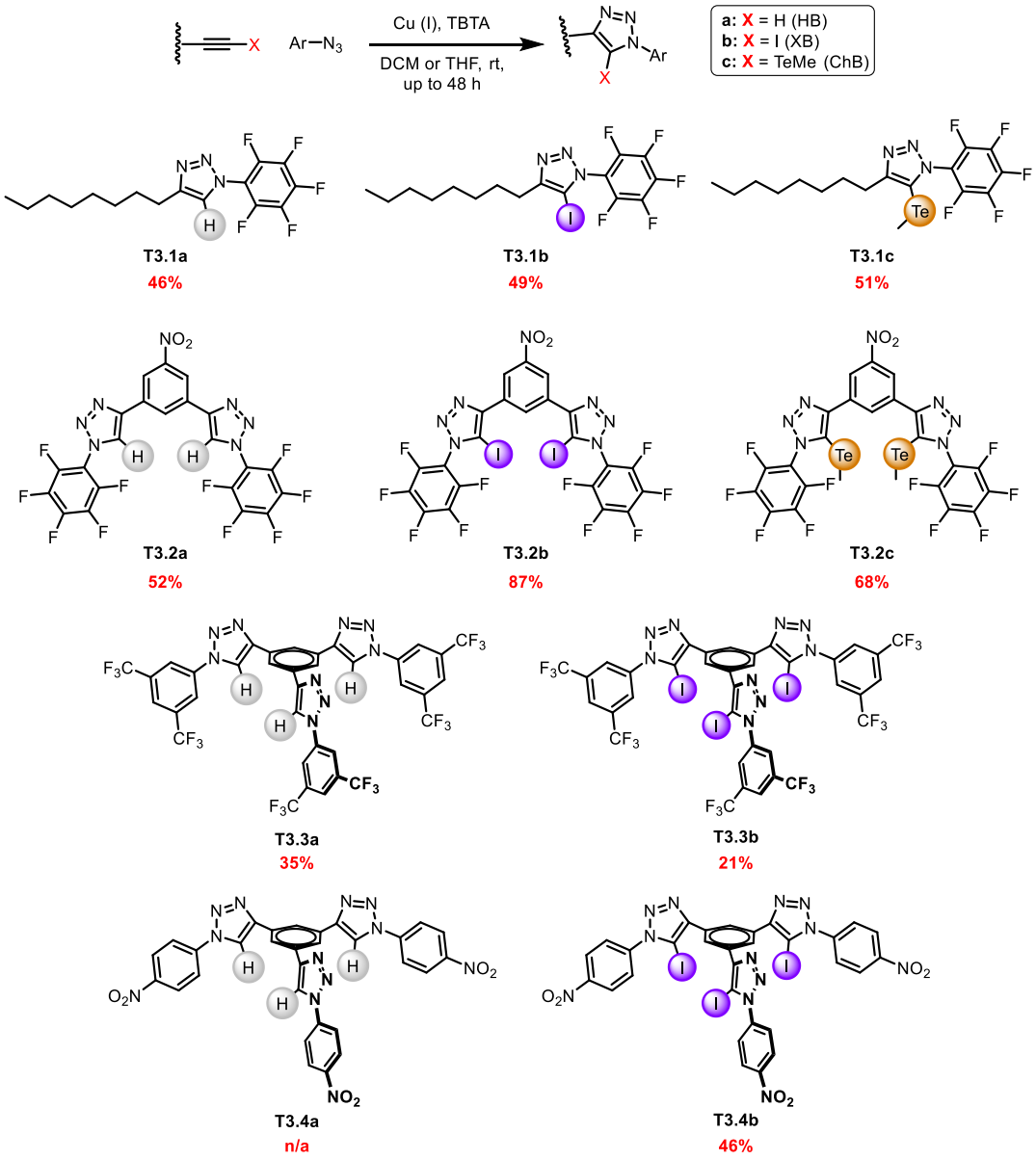


Scheme 3.4. Synthesis of alkyne precursors **3.20** and **3.21** for the tridentate receptors.



Scheme 3.5. Synthesis of azide precursors **3.22**, **3.23** and **3.24**.

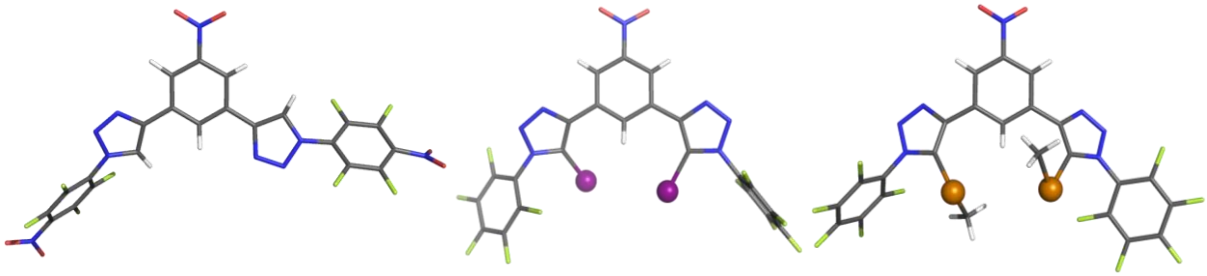
The azide and alkyne precursors were subjected to CuAAC reactions in the presence of $[Cu(MeCN)_4]PF_6$, or CuI in the case of the tripods, and the stabilising ligand tris(benzyltriazolyl) amine (TBTA), affording the monodentate, bidentate and tridentate anionophores in yields ranging from 21–87% (**Scheme 3.6**). The synthesis of tripod **T3.4a** was unsuccessful due to the formation of insoluble by-products.



Scheme 3.6. CuAAC reaction to afford monodentate, bidentate and tridentate receptors.

3.2.1 Solid State Analysis

The bidentate carriers **T3.2a**, **T3.2b** and **T3.2c** were characterised in the solid-state. The single crystals suitable for X-ray diffraction were grown via slow evaporation of chloroform solutions by Dr Andrew Docker, and the crystal structures were subsequently solved by Heike Kuhn (**Figure 3.6**). Analysis of the solid-state structures gave insight into the nature and potency of the sigma-hole donors. Crystallographic data analysis revealed that the sigma-hole donors point inwards, forming a well-defined binding cavity and demonstrating signs of preorganisation in the solid state. In contrast, the HB receptor does not display a preorganised binding cavity, since one of the HB donors points inwards and the other outwards. In addition, the XB and ChB donors can participate in intermolecular interactions with the nitrogen atoms of triazole rings on another receptor, forming arrays of intermolecular N···I XB or N···Te ChB interactions (**Figure 3.7**). Of particular note is the significant 84% and 83% contraction in the van der Waals radii for I1···N1 and Te1···N3, respectively, indicative of strong intramolecular XB and ChB sigma hole interactions in the solid state (**Table 3.1**).



T3.2a **T3.2b** **T3.2c**

Figure 3.6. X-ray crystallographic structures of **T3.2a**, **T3.2b** and **T3.2c.** Grey = carbon, blue = nitrogen, white = hydrogen, red = oxygen, green = fluorine, purple = iodine, orange = tellurium. Solvent molecules omitted for clarity.

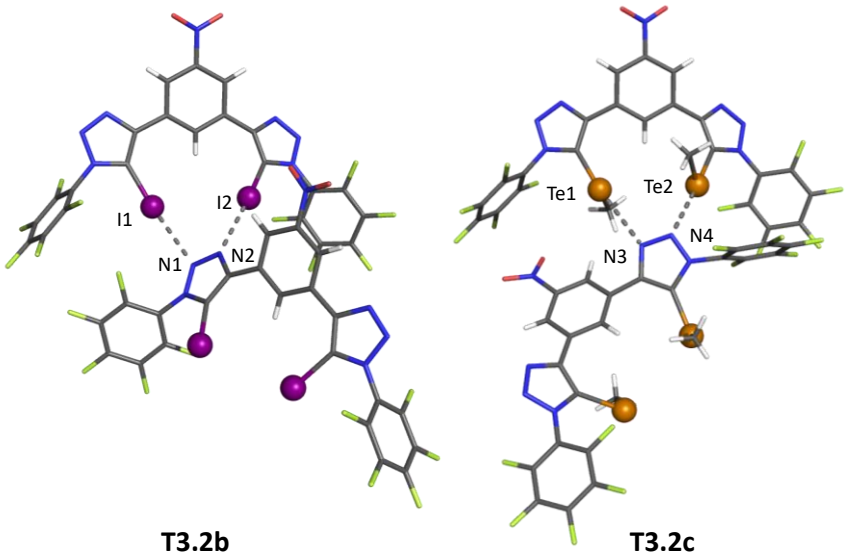


Figure 3.7. X-ray crystallographic structures **T3.2b** and **T3.2c** with XB and ChB interactions shown as dashed lines. Adapted with permission from reference [31] © 2021 Bickerton et al. Chemistry - A European Journal published by Wiley-VCH GmbH

Table 3.1. Selected solid state XB and ChB contacts in **T3.2b** and **T3.2c.**

Contact	Interatomic Distances (Å)[a]	Angle (°)[a],[b]	%VdW
I1···N1	2.954 (5)	172.94 (19)	84
I2···N2	3.161 (5)	158.45 (19)	90
Te1···N3	3.303 (4)	176.27 (18)	83
Te2···N4	2.982 (4)	170.99 (15)	91

[a] standard deviation in parenthesis. [b] Contact angle (degrees) with respect to the C-X bond. X = I or TeMe.

3.2.2 Anion Recognition

The chloride binding ability of the receptors was investigated by ^{1}H NMR titration experiments with tetrabutylammonium chloride in acetone-d_6, and with the addition of 2.5 % D_2O where necessary. In the case of monodentate receptors **T3.1a**, **T3.1b** and **T3.1c**, protons A, B and C respectively were perturbed upon the addition of TBACl, indicative of anion binding, and this was monitored over the course of the titration (**Figure 3.8**). The titration experiments of **T3.2a**, **T3.2b** and **T3.2c** were conducted by Dr Andrew Docker and for comparison the internal proton signal D was monitored for all bidentate receptors. In the case of the tripods **T3.3a** and **T3.3b** all protons labelled E-H were used for fitting simultaneously.

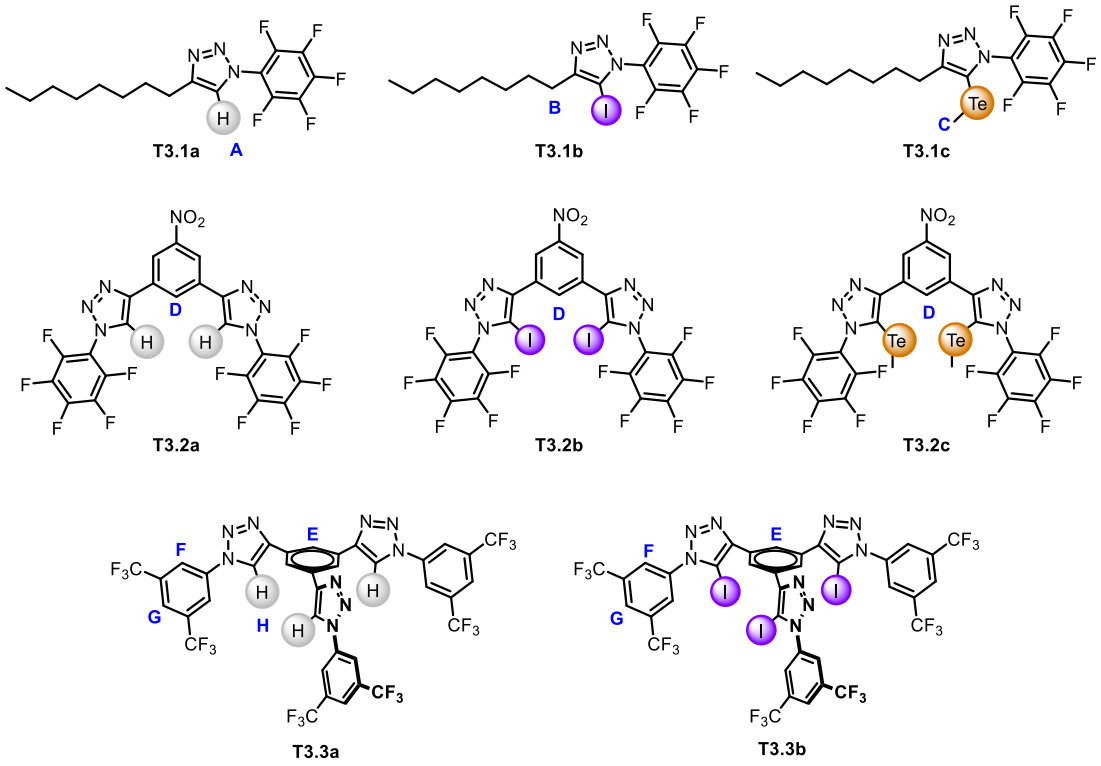


Figure 3.8. Receptors with highlighted protons followed for ^{1}H NMR titration experiments.

Upon addition of TBACl, the ^{1}H NMR signal of proton A in HB carrier **T3.1a** shifted downfield, indicative of hydrogen bond formation with Cl^{-}. Signal B of XB receptor **T3.1b** shifted upfield (**Figure 3.9**, left), likely caused by the increased electron density on the triazole ring due to the formation of halogen bonds with the anion. Interestingly, signal C of ChB receptor **T3.1c** experienced downfield perturbations as a result of contact between Te and Cl^{-} (**Figure 3.9**, right). The data was fitted to a 1:1 host:guest binding model and the stoichiometric 1:1 association constants were determined using the Bindfit program (**Table 3.2**).[34]

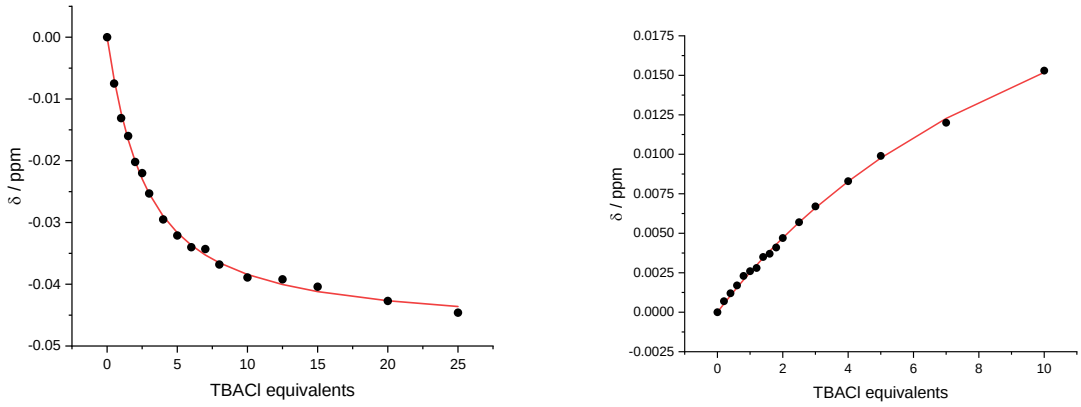


Figure 3.9. Anion binding isotherm for **T3.1b** (left) and **T3.1c** (right). in acetone-d_6. Experimental data is shown by ● and fitted 1:1 binding isotherm is shown by solid line.

Proton D in the three bidentate carriers all showed downfield shifts upon addition of TBACl indicative of anion binding within the cavities. The binding of chloride by bidentate XB receptors **T3.2b** and **T3.2c** was too strong to be determined in acetone-d_6 alone (K_a >10^5 M^{-1}). To obtain more quantitative values for chloride association constants, the ^{1}H NMR titrations were conducted in more competitive mixture of acetone-d_6/D_2O 97.5/2.5 (**Table**

3.2). Cooperative bidentate binding significantly enhanced the chloride affinity relative to the monodentate analogues (**Table 3.2**). The data revealed an overall chloride affinity trend of XB > ChB > HB for the mono- and bidentate carriers, and in addition, the bidentate XB receptor **T3.2b** revealed a forty-fold enhancement in binding affinity compared to ChB receptor **T3.2c**. All original data and the corresponding fitted binding isotherms can be found in the Appendix.

Table 3.2. Chloride Binding affinities for monodentate and bidentate receptors.

K_1^{Cl} (M^{-1})[a]	T3.1a	T3.1b	T3.1c	T3.2a	T3.2b	T3.2c
acetone	18	440	66	1012	$>10^5$	18543
acetone + 2.5% D_2O	-[c]	-[c]	-[c]	-[b]	6073	156

[a] 1 : 1 association constant for chloride binding in acetone-d_6 or acetone-d_6 + 2.5% D_2O. Chloride added as the TBA salt. Errors of fit are less than <7%. [b] Anion induced chemical shift perturbations too small to determine association constant. [c] Not determined. (298 K, 500 MHz)

During the course of the titration with Cl^- the prototriazole signal H of tripod **T3.3a** experienced a large downfield shift (δ 9.62 to 10.78) indicative of strong hydrogen bonding with the anion. The internal proton E also showed a large downfield shift. Interestingly, proton E of the iodotriazole tripod **T3.3b** initially shifted downfield, but after the addition of 3 equivalents of TBACl, it shifted back upfield (**Figure 3.11**), indicating the likely formation of a 1:2 host:anion complex (**Figure 3.10**). Therefore, the titration data for tripods **T3.3a** and **T3.3b** were fitted to a 1:2 host:guest binding model. The observed chemical shifts and fitted binding isotherm for tripod **T3.3b** is shown in **Figure 3.11** and the binding association constants are shown in **Table 3.3**.

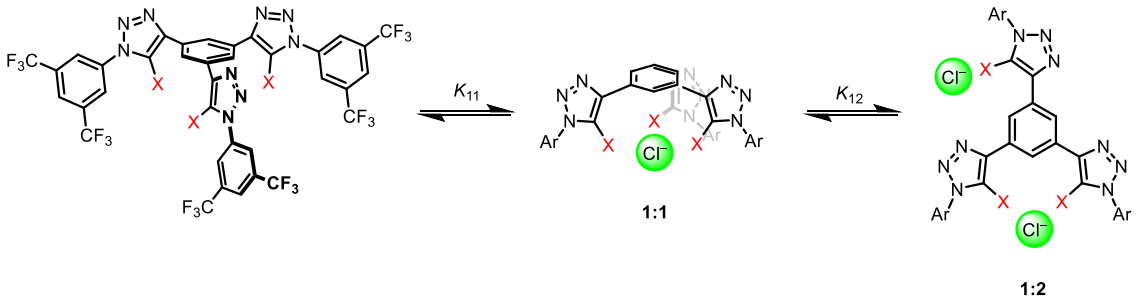


Figure 3.10. Tripod **3.3**:Cl^- 1:1 and 1:2 complexes.

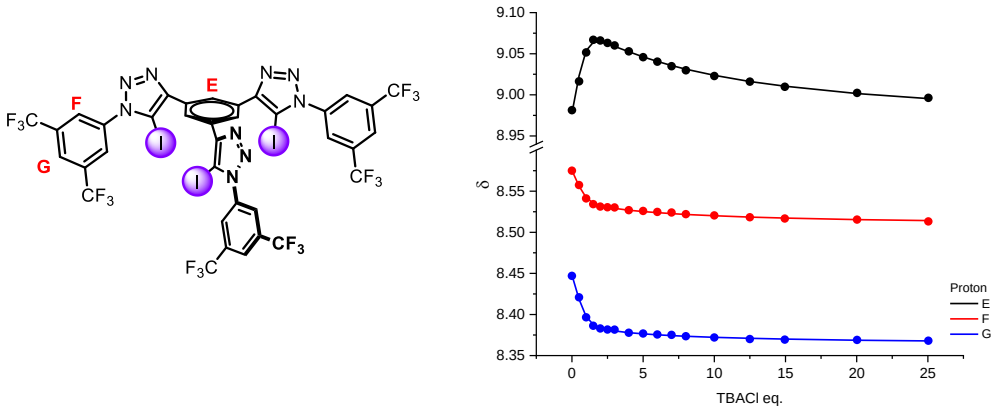


Figure 3.11. Anion binding isotherm for tripod **T3.3b** in acetone-d_6. Experimental data is shown by ● and fitted 1:1 binding isotherm is shown by solid line.

Table 3.3. Chloride Binding affinities for tripodal receptors **T3.3a** and **T3.3b**.

	T3.3a		**T3.3b**	
	***K*$_{11}$**	***K*$_{12}$**	***K*$_{11}$**	***K*$_{12}$**
K^{Cl} acetone (M^{-1})[a]	8464	651	11812	93

[a] 1 : 1 association constant for chloride binding in acetone-d_6. Cl^- added as the TBA salt. Errors of fit less than <7%. (298 K, 500 MHz)

As with the bidentate carriers, the tripods had much higher binding association constants compared to the monodentate receptors. The XB tripod **T3.3b** bound Cl^- one order of magnitude stronger than HB tripod **T3.3a,** with an association constant of K_{11} = 11812 M^{-1} (**Table 3.3**). In excess chloride, a 1:2 complex is formed, presumably in which the first chloride anion bound in a cooperative bidentate fashion and the second chloride anion associates to the third tripodal arm (**Figure 3.10**). Interestingly, K_{11} for **T3.3a** and **T3.3b** is much stronger compared to the corresponding K_{12} values indicating the tripodal state is very stable and breaking this conformation is unfavourable (**Figure 3.10**).

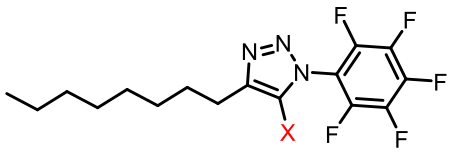
3.3 Anion Transport

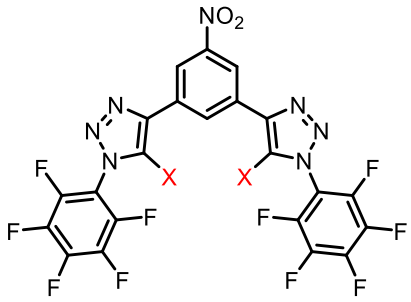
3.3.1 Initial Transport Activity

The transport ability of the multidentate receptors was first determined using the HPTS assay described in **chapter 1** and **2**, original data can be found in the appendix and the EC_{50}, Hill coefficient, *n*, and cLogP values are shown below in **Table 3.4**.

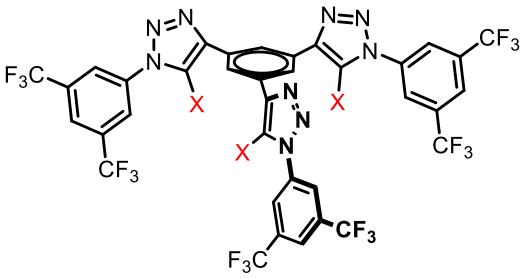
Table 3.4. EC_{50}, *n* and cLogP values for the multidentate carriers. Experimental values quantified from the HPTS assay, raw data available in the appendix.

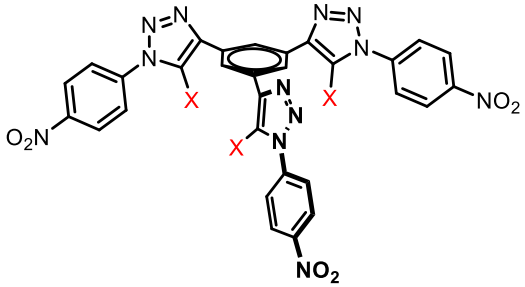
X = H (a)
I (b)
TeMe (c)





	T3.1a	T3.1b	T3.1c	T3.2a	T3.2b	T3.2c
EC_{50} / µM	2.7	0.9	1.2	0.048	0.003	0.032
n	3.4	3.9	2.8	1.9	0.7	1.1
cLogP	5.1	5.4	5.1	4.7	5.2	4.9





	T3.3a	T3.3b	T3.4a	T3.4b
EC_{50} / µM	1.2	2.3	-	23
n	0.9	1.2	-	0.8
cLogP	6.37	6.66	4.68	4.48

HPTS assay: the I_{rel} (λ_{em} = 510 nm; λ_{ex1} = 405 nm, λ_{ex2} = 460 nm) at 25 °C was monitored upon carrier addition (0.001–50 µM) to POPC vesicles containing 1 mM HPTS, 100 mM internal and external NaCl, buffered with 10 mM HEPES at pH 7.0. A pH gradient is generated by addition of a NaOH base pulse (0.5 M), followed by the carrier at t = 90 s. Vesicle lysis by Triton X-100 calibrates the assay. Hill analysis allows for quantification of transport activity.

The data revealed an overall transport ability trend of XB > ChB > HB, in agreement with the binding trend determined with ^{1}H NMR titration experiments. The monodentate control compounds were an order of magnitude less active than their bidentate counterparts, consistent with reduced chloride binding affinity. Increasing the denticity of the receptors from 1 to 2 greatly increased the transport activity resulting in high nM activity for all bidentate carriers (EC_{50} <0.05 mol% with respect to lipid), and indeed carrier **T3.2b** is the most active halogen bonding carrier reported to date. The activity exceeds that of the archetypal XB donor iodoperfluorobenzene by five orders of magnitude (EC_{50} = 260 μM),[23] and exceeds iodo-perfluorohexane (EC_{50} = 3 μM) by 3 orders of magnitude.[17] Alongside this, they exceed the activity of the iodotriazole XB anionophores presented in **chapter 2** by two orders of magnitude under identical assay conditions. The activity of chalcogen bonding anion carrier **T3.2c** was also excellent (EC_{50} = 32 nM), favourably comparing to the previously reported bis(pentafluorophenyl)tellurium anionophore (**Figure 3.4, Page 99,** EC_{50} = 200 nM).[23]

Surprisingly, introduction of a third HB/XB bond donor led to a reduction in transport activity with EC_{50} values of 1.2 μM and 2.3 μM for the hydrogen and halogen bonding tripods **T3.3a** and **T3.3b** respectively. Their cLogP values were 6.4 and 6.7 respectively, therefore, this reduced activity in comparison to the bidentate carriers is most likely due to the detrimental increase in lipophilicity that comes with the addition of a third transporter 'arm' on the central aryl unit. On the other hand, tripod **T3.4b** had a lower clog *P* of 4.5 but was highly inactive, with an EC_{50} value of 23 μM. In this case, replacement of the lipophilic -

CF_3 groups (**T3.3**) for electron-withdrawing -NO_2 groups (**T3.4**) resulted in the tripod not being lipophilic enough to partition effectively into the bilayer for transport.

Interestingly, Hill analysis of the dose response curves for the monodentate anionophores reveal *n* values close to 3, implying that such transport-active trimers represent a minority population in the membrane, with the majority coexisting as inactive monomers. Bi- and tridentate receptors resulted in Hill coefficients of 1 suggesting active monomeric complexes for these carriers. The increased activity of the multidentate receptors in comparison to the monodentate receptors is in agreement with results from the ^{1}H NMR titrations suggesting that enhanced binding affinity plays an important role. Furthermore, by increasing the denticity of the anion receptors, efficient anion transport is achieved resulting from sufficient encapsulation of the anion.

3.3.1.1 Mechanistic Investigations

The control experiments described in **chapter 2 section 2.4.1** which probed the transport mechanism were also performed for these carriers as detailed below. The transport activities of all anionophores were independent of the iso-osmolar replacement of the external Na^+ cation with Li^+, K^+ or Rb^+. In addition, a reduction in transport activity was observed upon replacement of chloride with the hydrophilic gluconate anion, and upon replacement of the zwitterionic POPC lipids with anionic EYPG lipids, in the HPTS assay. These results allow us to conclude that these receptors perform transmembrane transport via a cation independent Cl^-/OH^- antiport mechanism, in the same manner as the previously reported monodentate systems in **chapter 2**.

As evident from the leakage assay with carboxyfluorescein, non-specific leakage and membrane damage by the anion carriers could be ruled out. The suppression of carrier activity in gel phase DPPC LUVs at 25 °C**,** and subsequent restoration of activity in the fluid lipid phase at 45 °C, provided evidence for these carriers working via a mobile carrier mechanism rather than stacking into a membrane-spanning channel. All experimental data can be found in the appendix.

3.3.2 The NMDG Assay

The chloride selectivity of the bidentate carriers was then investigated experimentally and computationally. The monodentate carriers on the other hand were used simply for comparison when investigating the effects of anion encapsulation and thus chloride selectivity experiments were carried out when necessary.

To investigate the chloride over hydroxide selectivity of these carriers, a variation of the HPTS assay was performed. In **chapter 2 section 2.5.1,** the Cl^- > OH^- selectivity was investigated with the FCCP assay, however, FCCP itself is anionic and therefore, there could be interactions between FCCP and the test anionophore, particularly those such as the bidentate systems which have a strong anion affinity. To avoid potentially disruptive interactions, Gale, Davis and co-workers developed an assay with *N*-methyl-D-glucamine chloride (NMDG−Cl) in the internal and external vesicle buffer instead of NaCl, and NMDG as the base pulse (5 mM) in place of NaOH.[35,36] NMDG is a sugar alcohol which cannot cross the bilayer and therefore this assay only allows transport to occur via H^+/Cl^- symport or Cl^-/OH^- antiport. The experiments are conducted with and without the addition of the

proton channel gramicidin D, it is a linear peptide which assembles into a channel to facilitate fast electrogenic H^+ transport, much like FCCP. In the presence of gramicidin an overall coupled H^+/Cl^- symport process dominates (**Figure 3.12**). Using the same principles as the FCCP assay, this assay gives insight into the relative rates of Cl^- and H^+/OH^- transport. In the case where H^+/OH^- transport is rate limiting, addition of gramicidin leads to acceleration of the pH gradient dissipation; where Cl^- is rate limiting, the rate of pH gradient dissipation is unaffected by gramicidin.

The assay was performed in a similar manner to the previously described HPTS assay and once performed for each carrier the ratio of EC_{50} values in the absence and presence of gramicidin was calculated to provide a measure of the $Cl^- > H^+/OH^-$ selectivity, *S*, (where $S = EC_{50}^{NMDG}/EC_{50}^{gramicidin}$). The EC_{50} values for each carrier with and without gramicidin are presented below in **Table 3.5** and the original date can be found in the appendix.

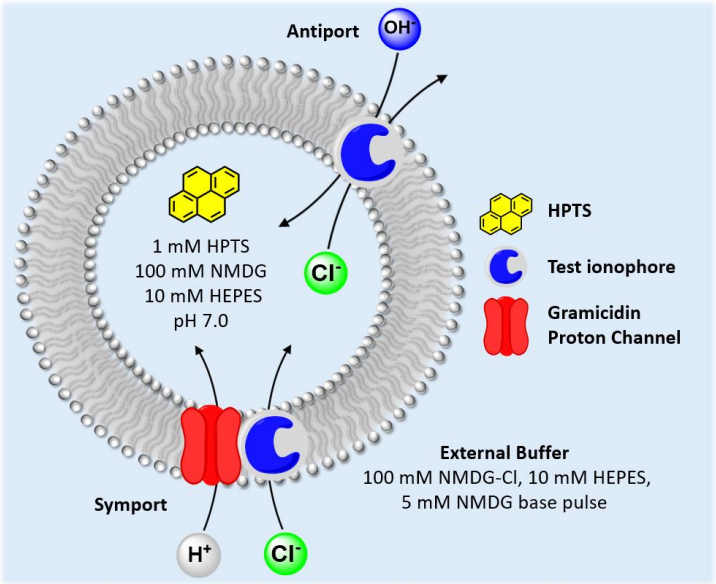
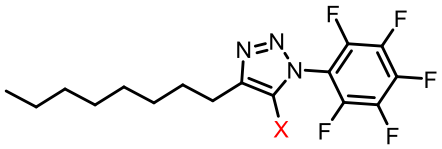
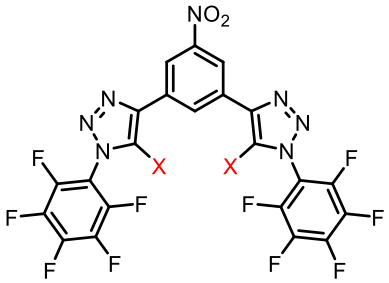


Figure 3.12. The transport mechanisms occurring in the NMDG assay in the absence of gramicidin: Cl^-/OH^- exchange (antiport), or H^+/Cl^- co-transport (symport), alongside the structure of the proton channel gramicidin.

Table 3.5. NMDG assay results for monodentate carriers **T3.1b** and **T3.1c** and monodentate carriers **T3.2a**, **T3.2b and T3.2c**.

X = H (a)
I (b)
TeMe (c)





	T3.1b	T3.1c	T3.2a	T3.2b	T3.2c
EC_{50} / µM [a]	5.4	6.5	0.28	0.048	0.8
n [a]	2.4	2.3	1.7	1.0	0.5
EC_{50} / µM [b]	2.6	4.1	0.178	0.009	0.012
n [b]	2.9	1.7	2.4	1.2	1.0
Selectivity, *S* [c]	**2.1**	**1.6**	**1.6**	**5.3**	**67**

NMDG assay: the I_{rel} (λ_{em} = 510 nm; λ_{ex1} = 405 nm, λ_{ex2} = 460 nm) at 25 °C was monitored upon carrier addition (0.001–50 µM) to POPC vesicles containing 1 mM HPTS, 100 mM internal and external NMDG-Cl, buffered with 10 mM HEPES at pH 7.0. A pH gradient is generated by addition of an NMDG base pulse (0.5 M), followed by the carrier at t = 90 s. Vesicle lysis by Triton X-100 calibrates the assay. Hill analysis allows for quantification of transport activity. [a] NMDG assay without gramicidin. [b] In the presence of 0.1 mol% gramicidin D. [c] Defined as EC_{50}^{NMDG} / $EC_{50}^{Gramicidin}$. Errors at 95% confidence limit.

The data revealed an overall chloride selectivity trend of ChB > XB > HB and for each carrier, cooperative bidentate chloride binding significantly enhanced the binding affinity relative to the monodentate analogues (**Table 3.5**). When increasing the denticity from mono- to bidentate the selectivity of the XB systems increased over two-fold (*S* = 2.1 vs 5.3). In the case of the chalcogen bonding telluromethyl carriers, the additional chalcogen bond donor in **T3.2c**, led to exceptional selectivity (**T3.2c** *S* = 67, **Table 3.5**), despite the relatively simple, planar bidentate structure of the carrier. Its transport activity increased from an EC_{50} value of 80 nM to 12 nM upon addition of 0.1 mol% of gramicidin and representative data is

shown in **Figure 3.13**. For comparison, the comparable bidentate HB carrier **T3.2a** and analogous monodentate carrier **T3.1c** exhibited minimal selectivity (*S* = 1.6, **Figure 3.13**).

To date only a handful of compounds have been reported with *S* > 10, the preorganised macrocyclic cholaphane scaffold presented by Davis and co-workers discussed in **chapter 1 section 1.4.1**, achieved *S* = 100, but it has a much more complex steroidal three-dimensional structure.[35] As previously discussed in the introduction of this chapter, enhancing anion transport by increasing receptor acidity (such as by adding electron withdrawing groups) is typically detrimental to the selectivity of the receptor. However, here Cl^- > OH^- selectivity *and* high transport activity was achieved despite the significant electron withdrawing nature of the substituents conjugated to anionophores **T3.2b** and **T3.2c.**

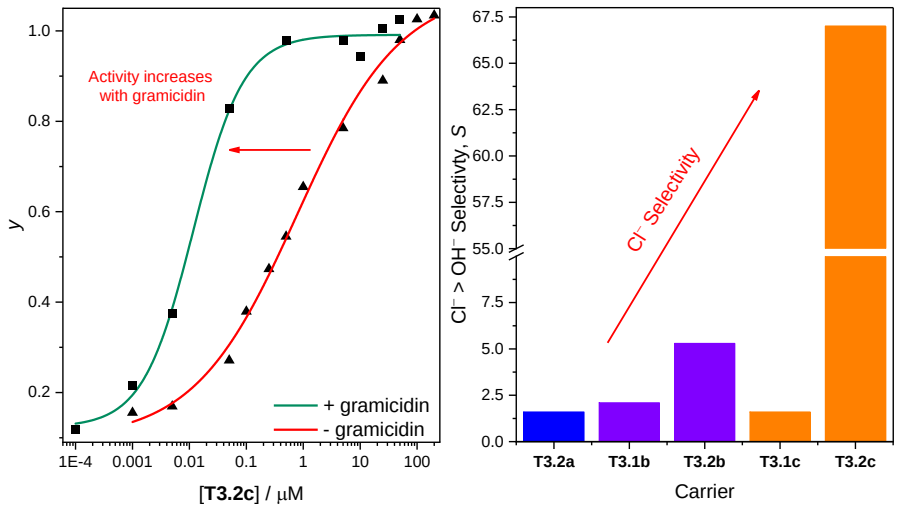


Figure 3.13. Chloride selectivity assay results. Left, dependence of fractional activities (y, the relative intensity at t = 288 s just prior to lysis) on concentration of **T3.2c** in the presence (▪) and absence (▲) of gramicidin, and fit to the Hill equation (red and blue solid lines, respectively). Right, summary of transport selectivity data, where Cl^- > OH^- selectivity = $EC_{50}^{NMDG}/EC_{50}^{Gramicidin}$. Adapted with permission from reference [31] © 2021 Bickerton et al. Chemistry - A European Journal published by Wiley-VCH GmbH

Interestingly, the chloride selectivity trend of ChB > XB > HB does not correlate with the trend found within ^{1}H NMR titration experiments or with the transport activity (XB > ChB > HB). Huber, Kozuch and co-workers found a similar trend with their bidentate anion binding catalysts, in which the XB analogue (**Figure 3.14a**) showed superior anion binding, while the ChB analogue (**Figure 3.14b**) was the better catalyst.[37] Stronger anion binding by XB donors over analogous ChB donors has been reported previously,[27] and thus in principle XB systems would be the better catalyst/anion transporter due their high Lewis acidity. However, this isn't what has been reported. Huber, Kozuch and co-workers attribute this to the unique properties of chalcogen bonding and that solvation effects play a crucial role in this paradox. Therefore, in depth computational analysis of the transport process was carried out in an attempt to explore the reasoning behind the difference in activity and selectivity of the XB and ChB transporters.

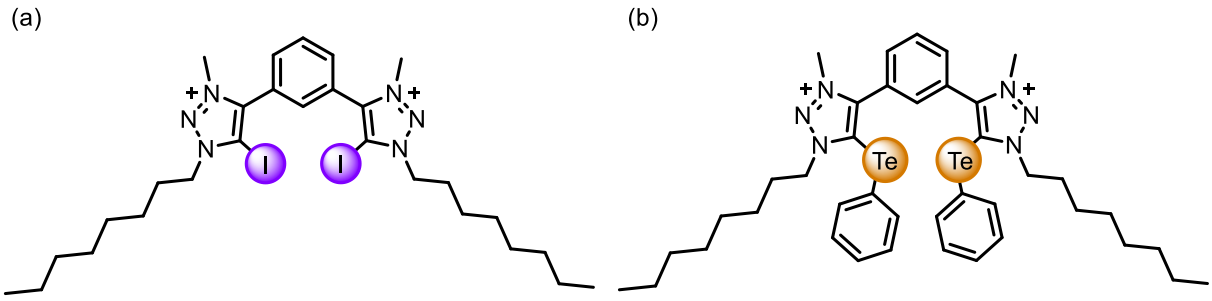


Figure 3.14. Bidentate (a) halogen and (b) chalcogen bonding catalyst.[37]

3.4 Computational Chemistry

Computational studies were undertaken in collaboration with Dr Alistair Sterling and Prof. Fernanda Duarte to provide insight into the anion binding and transport process, and the chloride selectivity of the bidentate sigma-hole based transporters. In depth details of the computational analysis and levels of theory used can be found in **chapter 5 section 5.6.2**.

Initially the electrostatic potential (ESP) surfaces of the halogen and chalcogen bonding bidentate carriers were calculated (**Figure 3.15**). As expected, this revealed one iodine-centred sigma-hole per iodine atom (V_{max} = 62 kcal mol^{-1}),[38,39] and two tellurium-centred sigma-holes per Te atom. In the case of tellurium, the sigma-hole opposite to the triazole C-Te bond was the largest in size and magnitude compared to the second supplementary sigma-hole (V_{max} = 58.0 vs 34.5 kcal mol^{-1}) (**Figure 3.15**).

The 1:1 carrier-chloride complex was then calculated to probe the binding stoichiometry and binding enthalpies upon chloride recognition. Similar to the studies conducted in **chapter 2**, this was done in chloroform as a membrane-mimetic environment (similar dielectric constant). The computationally determined 1:1 bidentate anion coordination found for both sigma-hole based carriers is in agreement with the successful fitting of these compounds to a 1:1 binding model during ^{1}H NMR titration experiments, and the Hill coefficient values of 1 found within the HPTS transport assay. The calculated binding enthalpies suggest a stronger C–I···Cl^{-} interaction in comparison to C–Te···Cl^{-}, in agreement with larger chloride binding constants determined by ^{1}H NMR titrations, and the increased magnitude of the iodine-centred sigma-hole in comparison to the tellurium-centred sigma-hole.

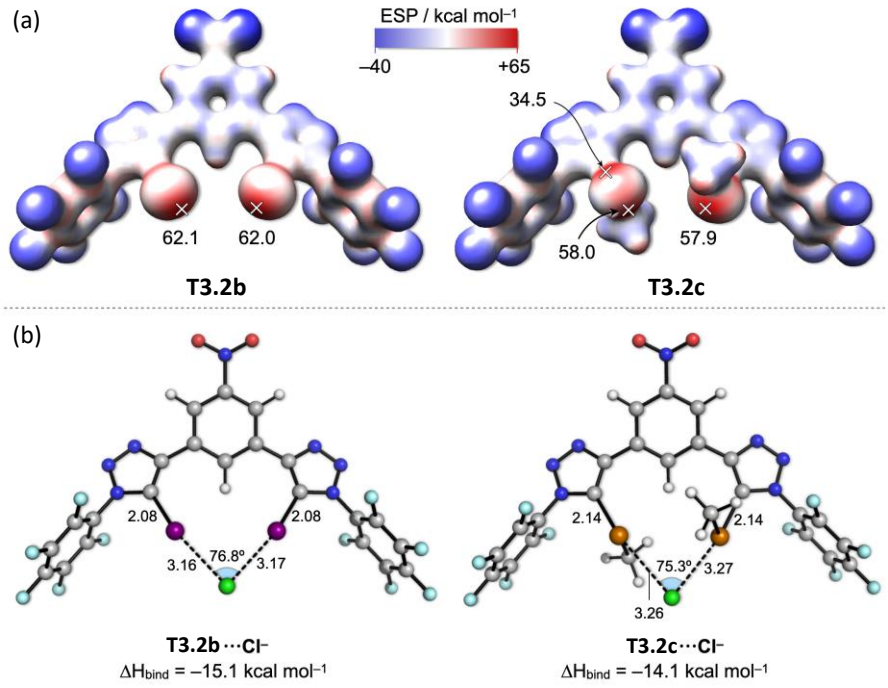


Figure 3.15. (a) Calculated electrostatic potentials (ESPs, kcal mol^{-1}) on the van der Waal's surface of **T3.2b** and **T3.2c**, with maximum values for sigma-holes marked with crosses. (b) Calculated structures of the chloride complexes of **T3.2b** and **T3.2c**, showing key distances (Å) and angles (º). Adapted with permission from reference [31] © 2021 Bickerton et al. Chemistry - A European Journal published by Wiley-VCH GmbH

A computational model was then developed to probe the role of sigma-hole mediated anion recognition within the selective transmembrane anion transport process. This model accounts for both anion binding affinity to the XB and ChB anionophores (**T3.2b** and **T3.2c**) and chloride and hydroxide anion dehydration at the aqueous-membrane interface, in order to enable the dehydration and binding free energies to be calculated. This model assumes that the hydrophobic transporter is confined within the membrane bilayer, and binds the anion at the water/membrane interface (**Figure 3.16A**). This binding event incurs an anion dehydration penalty, where the equilibrium position depends on the balance of anion dehydration with the strength of binding to the transporter. The

dehydration free energies (ΔG_{dehyd}) for Cl^- and OH^- when being transferred from implicit water to membrane-mimetic chloroform, and the respective binding free energies (ΔG_{bind}) of these anions to carriers **T3.2b** and **T3.2c** in the implicit chloroform were calculated (**Figure 3.16B**).[40] The sum of these terms could then be used to describe the anion transport process as a whole: $\Delta G_{total} = \Delta G_{dehyd} + \Delta G_{bind}$.

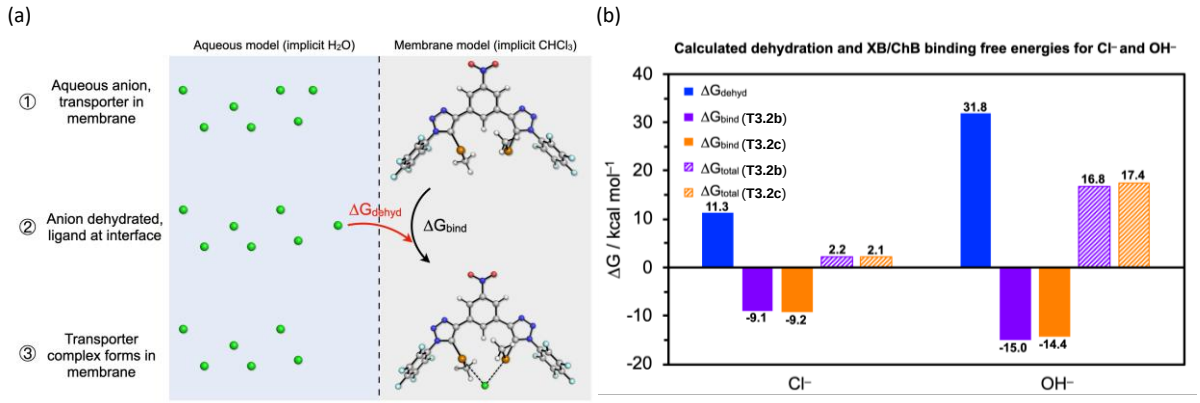


Figure 3.16. (a) Schematic representation of the computational model for anion binding at a membrane/water interface. (b) Calculated dehydration and binding free energies (298 K) for **T3.2b** and **T3.2c**, with Cl^- and OH^-. Adapted with permission from reference [31] © 2021 Bickerton et al. Chemistry - A European Journal published by Wiley-VCH GmbH

Dehydration of OH^- is strongly disfavoured (ΔG_{dehyd} = 31.8 kcal mol^{-1}) in comparison with Cl^- (ΔG_{dehyd} = 11.3 kcal mol^{-1}), highlighting the intrinsic difficulty of transporting OH^- across lipid bilayers. Interestingly, the free energies (ΔG_{bind}) of OH^- binding in chloroform are lower than that of Cl^- binding (**Figure 3.16**, –15 vs –9 kcal mol^{-1}, respectively), which is likely due to a combination of stronger binding and underestimation of short-range solvent-OH^- interactions that can occur within implicit solvent models. However, the stronger OH^- binding, is not sufficient to overcome the dehydration penalty of OH^-. Therefore, this results

in the Cl^- > OH^- selectivity observed in anion transport experiments. Computational analysis also revealed that OH^- binding by **T3.2c** is weaker and Cl^- binding is stronger in comparison with **T3.2b**, which is also in agreement with the increased selectivity observed experimentally for **T3.2c** receptor.

Bidentate binding of the sigma-hole based carriers to OH^- leaves at least one vacant coordination site on OH^- that could be occupied by a water molecule via a hydrogen bond (**Figure 3.17**). In light of this, we also explored the possibility that a water molecule could accompany the OH^- anion into and across the membrane to stabilise the naked anion, a process which aligns with the strongly disfavoured OH^- dehydration process (**Figure 3.16**, ΔG_{dehyd} = 31.8 kcal mol^{-1}). Calculations were therefore conducted to account for an additional water molecule in the transport of hydroxide. The binding of $[OH\cdots H_2O]^-$ and OH^- to carrier **T3.2b** is similar (**Figure 3.18**, ΔG_{bind} = –15.1 vs –15.0 kcal mol^{-1} respectively), whereas the binding of $[OH\cdots H_2O]^-$ to **T3.2c** is weaker than that of OH^- (ΔG_{bind} = –12.2 vs –14.4 kcal mol^{-1} respectively). The resulting difference in ΔG_{total} between **T3.2b** and **T3.2c** increases from 0.6 kcal mol^{-1} to 3.0 kcal mol^{-1} (**Figure 3.18**). These findings suggest that water is likely to be transported across the bilayer at least with halogen bonding carrier **T3.2b**. The reduced ability of the chalcogen bonding carrier to transport $[OH\cdots H_2O]^-$ in comparison to halogen bonding mediated transport is in even better agreement with the observed Cl^- > OH^- selectivity enhancement for **T3.2c** in comparison with **T3.2b**.

Furthermore, it has previously been shown that XB and ChB mediated anion binding interactions are known to be more hydrophobic than acidic hydrogen bond donors and exhibit a significant covalent contribution to the bonding.[10,41–43] In addition, sigma-hole

interactions in many cases possess halide > oxoanion binding selectivity.[38,44–48] It is therefore suggested that a combination of these effects contribute to the observed Cl^- > OH^- selectivity concomitant with high activity, in which binding and transport of the less hydrated and less basic chloride anion is favoured.

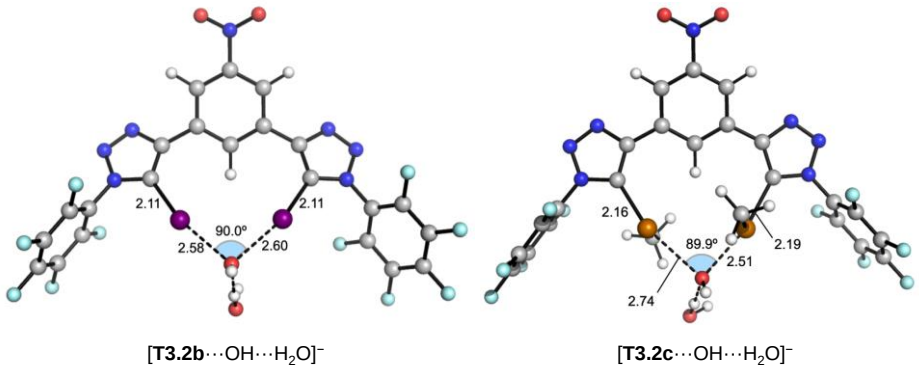


Figure 3.17. Calculated geometry of [**T3.2b**···OH···H_2O]$^-$ and [**T3.2c**···OH···H_2O]$^-$ at the SMD($CHCl_3$)-ωB97X-D3/def2- SVP (ma-def2-SVP on I) level of theory. Key distances are shown in Å, and angles in degrees. Adapted with permission from reference [31] © 2021 Bickerton et al. Chemistry - A European Journal published by Wiley-VCH GmbH

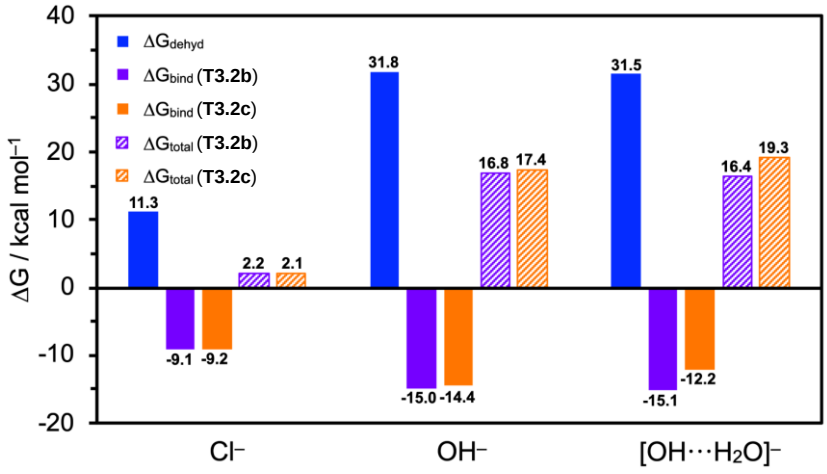


Figure 3.18. Calculated dehydration (ΔG_{dehyd}) and binding (ΔG_{bind}) free energies at 298.15 K for **T3.2b** and **T3.2c** with [OH···H_2O]$^-$ in comparison with Cl^- and OH^-, at the SMD-[ωB97X-D3/def2-TZVPP (ma- def2-TZVPP on anions, I and Te)//ωB97X-D3/def2-SVP (ma-def2-SVP on anions, I and Te)] level of theory. $\Delta G_{total} = \Delta G_{dehyd} + \Delta G_{bind}$, all values in kcal mol^{-1}. Adapted with permission from reference [31] © 2021 Bickerton et al. Chemistry - A European Journal published by Wiley-VCH GmbH.

3.5 Chapter Conclusions

In this chapter the design, synthesis, and anion transport properties of mono- bi-, and tridentate halogen bonding and chalcogen bonding iodo- and telluromethyl-triazole based transporters have been presented.

^{1}H NMR titration experiments with chloride revealed an overall affinity trend of XB > ChB > HB, with monodentate receptors binding weakly and bidentate receptors outperforming them to the extent that their binding was too strong to determine in acetone-d_6 alone. Interestingly, the tripodal carriers bound one anion in a similar manner to the bidentate carriers, followed by a second anion binding to the third remaining bond donor.

Initial transport experiments show that increasing the number of Lewis acidic HB/XB/ChB donors from one to two can not only increase the transport activity by an order of magnitude but also decrease the Hill coefficient to 1, meaning the bidentate transporters are more efficient anion transporters compared to their monodentate analogues, which required multiple carriers to encapsulate the anion and facilitate transport. The addition of a third bond donor in the tripodal systems led to a reduction in transport activity, which was hypothesised to be due to the detrimental increase in lipophilicity and decreased solubility. Overall, optimum denticity was determined to be two bond donors and thus the chloride selectivity of the bidentate carriers was explored.

Using the NMDG assay, outstanding Cl^- > OH^- transport selectivity for the chalcogen bonding anionophore was revealed. Importantly, the unique nature of such sigma-hole

interactions enables both high activity and high selectivity to be achieved in a relatively simple molecular design.

Computational calculations were used to explore the anion binding and transport process, and the chloride selectivity shown by the bidentate sigma-hole based transporters. A new computational model was developed that accounted for both anionophore-anion binding in a membrane-mimetic environment and anion solvation. Analysis revealed that the OH^- dehydration process is strongly disfavoured (ΔG_{dehyd} = 31.8 kcal mol^{-1}) and is likely to be transported with a water molecule making it more unfavourable for transport by ChB carrier **T3.2c**. The stronger binding sigma-hole based carriers are also able to overcome the penalty of dehydration associated with chloride (which they are less able to do for OH^-) making its transport considerably more favourable. Overall, computational studies demonstrate the critical role of anion dehydration in achieving efficient and selective anion transport.

Maintaining $Cl^- > OH^-$ selectivity whilst ensuring the carrier is highly transport-active is intrinsically difficult to achieve with HB anion transporters and therefore, this research demonstrates how the careful selection of non-covalent interactions within abiotic transporters is a powerful approach to engineering selectivity and activity. The extensive computational analysis demonstrates the dependency of anion transport on successful anion dehydration and highlights the significant potential for exploiting halogen and chalcogen bonding interactions in biological contexts.

3.6 References

1 G. G. Jeremy M. Berg, Lubert Stryer, John Tymoczko, *Biochemistry*, W.H. Freeman;, Ninth Edit., 2019.

2 W. Pflugrath and F. A. Quiocho, 1985, 19–22.

3 H. Luecke and F. A. Quiocho, *Nature*, 1990, **347**, 402–406.

4 B. A. McNally, A. V. Koulov, T. N. Lambert, B. D. Smith, J. B. Joos, A. L. Sisson, J. P. Clare, V. Sgarlata, L. W. Judd, G. Magro and A. P. Davis, *Chem. Eur. J.*, 2008, **14**, 9599–9606.

5 L. A. Jowett, E. N. W. Howe, X. Wu, N. Busschaert and P. A. Gale, *Chem. Eur. J.*, 2018, **24**, 10475–10487.

6 N. Busschaert, M. Wenzel, M. E. Light, P. Iglesias-Hernández, R. Pérez-Tomás and P. A. Gale, *J. Am. Chem. Soc.*, 2011, **133**, 14136–14148.

7 I. Marques, A. R. Colaço, P. J. Costa, N. Busschaert, P. A. Gale and V. Félix, *Soft Matter*, 2014, **10**, 3608–3621.

8 N. Busschaert, S. J. Bradberry, M. Wenzel, C. J. E. Haynes, J. R. Hiscock, I. L. Kirby, L. E. Karagiannidis, S. J. Moore, N. J. Wells, J. Herniman, G. J. Langley, P. N. Horton, M. E. Light, I. Marques, P. J. Costa, V. Félix, J. G. Frey and P. A. Gale, *Chem. Sci.*, 2013, **4**, 3036–3045.

9 L. Vogel, P. Wonner and S. M. Huber, *Angew. Chem. Int. Ed.*, 2019, **58**, 1880–1891.

10 D. J. Pascoe, K. B. Ling and S. L. Cockroft, *J. Am. Chem. Soc.*, 2017, **139**, 15160–15167.

11 S. P. Thomas, D. Jayatilaka and T. N. Guru Row, *Phys. Chem. Chem. Phys.*, 2015, **17**, 25411–25420.

12 M. Iwaoka and N. Isozumi, *Molecules*, 2012, **17**, 7266–7283.

13 P. C. Ho, P. Szydlowski, J. Sinclair, P. J. W. Elder, J. Kübel, C. Gendy, L. M. Lee, H. Jenkins, J. F. Britten, D. R. Morim and I. Vargas-Baca, *Nat. Commun.*, 2016, **7**, 11299.

14 J. Y. C. Lim, I. Marques, A. L. Thompson, K. E. Christensen, V. Félix and P. D. Beer, *J. Am. Chem. Soc.*, 2017, **139**, 3122–3133.

15 M. Dal Molin, Q. Verolet, A. Colom, R. Letrun, E. Derivery, M. Gonzalez-Gaitan, E. Vauthey, A. Roux, N. Sakai and S. Matile, *J. Am. Chem. Soc.*, 2015, **137**, 568–571.

16 A. Vargas Jentzsch, D. Emery, J. Mareda, P. Metrangolo, G. Resnati, S. Matile, A. Vargas Jentzsch, D. Emery, J. Mareda, P. Metrangolo, G. Resnati, S. Matile, A. Vargas Jentzsch, D. Emery, J. Mareda, P. Metrangolo, G. Resnati and S. Matile, *Angew. Chem. Int. Ed.*, 2011, **50**, 11675–11678.

17 A. V. Jentzsch, D. Emery, J. Mareda, S. K. Nayak, P. Metrangolo, G. Resnati, N. Sakai and S. Matile, *Nat. Commun.*, 2012, **3**, 905.

18 A. Vargas Jentzsch, S. Matile, A. V. Jentzsch and S. Matile, *J. Am. Chem. Soc.*, 2013, **135**, 5302–5303.

19 C. Ren, X. Ding, A. Roy, J. Shen, S. Zhou, F. Chen, S. F. Yau Li, H. Ren, Y. Y. Yang and H. Zeng, *Chem. Sci.*, 2018, **9**, 4044–4051.

20 L. E. Bickerton, A. J. Sterling, P. D. Beer, F. Duarte and M. J. Langton, *Chem. Sci.*, 2020, **11**, 4722–4729.

21 A. Vargas Jentzsch, *Pure Appl. Chem.*, 2015, **87**, 15–41.

22 S. Benz, M. Macchione, Q. Verolet, J. Mareda, N. Sakai and S. Matile, *J. Am. Chem. Soc.*, 2016, **138**, 9093–9096.

23 L. M. Lee, M. Tsemperouli, A. I. Poblador-Bahamonde, S. Benz, N. Sakai, K. Sugihara and S. Matile, *J. Am. Chem. Soc.*, 2019, **141**, 810–814.

24 G. Park, D. J. Brock, J.-P. Pellois and F. P. Gabbaï, *Chem*, 2019, **5**, 2215–2227.

25 G. Park and F. P. Gabbaï, *Chem. Sci.*, 2020, **11**, 10107–10112.

26 G. E. Garrett, G. L. Gibson, R. N. Straus, D. S. Seferos and M. S. Taylor, *J. Am. Chem. Soc.*, 2015, **137**, 4126–4133.

27 A. Docker, C. H. Guthrie, H. Kuhn and P. D. Beer, *Angew. Chem. Int. Ed.*, 2021, **60**, 21973–21978.

28 F. Dressler and P. R. Schreiner, *Anion-Binding Catal.*, 2022, 1–77.

29 K. T. Mahmudov, M. N. Kopylovich, M. F. C. Guedes Da Silva and A. J. L. Pombeiro, *Dalt. Trans.*, 2017, **46**, 10121–10138.

30 S. Benz, J. Mareda, C. Besnard, N. Sakai and S. Matile, *Chem. Sci.*, 2017, **8**, 8164–8169.

31 L. E. Bickerton, A. Docker, A. J. Sterling, H. Kuhn, F. Duarte, P. D. Beer and M. J. Langton, *Chem. Eur. J.*, 2021, **27**, 11738–11745.

32 F. AL-Shnani, G. Guisado-Barrios, D. Sainz and E. Peris, *Organometallics*, 2019, **38**,

697–701.

33 J. Charoenpattarapreeda, Y. S. Tan, J. Iegre, S. J. Walsh, E. Fowler, R. S. Eapen, Y. Wu, H. F. Sore, C. S. Verma, L. Itzhaki and D. R. Spring, *Chem. Commun.*, 2019, **55**, 7914–7917.

34 BindFit v0.5 | Supramolecular, http://app.supramolecular.org/bindfit/.

35 X. Wu, L. W. Judd, E. N. W. Howe, A. M. Withecombe, V. Soto-Cerrato, H. Li, N. Busschaert, H. Valkenier, R. Pérez-Tomás, D. N. Sheppard, Y. B. Jiang, A. P. Davis and P. A. Gale, *Chem*, 2016, **1**, 127–146.

36 Y. Yang, X. Wu, N. Busschaert, H. Furuta and P. A. Gale, *Chem. Commun.*, 2017, **53**, 9230–9233.

37 N. Tarannam, M. H. H. Voelkel, S. M. Huber and S. Kozuch, *J. Org. Chem.*, 2022, **87**, 1661–1668.

38 J. Y. C. Lim and P. D. Beer, *Chem*, 2018, **4**, 731–783.

39 P. Politzer, J. S. Murray and T. Clark, *Phys. Chem. Chem. Phys.*, 2013, **15**, 11178–11189.

40 A. V. Marenich, C. J. Cramer and D. G. Truhlar, *J. Phys. Chem. B*, 2009, **113**, 6378–6396.

41 S. W. Robinson, C. L. Mustoe, N. G. White, A. Brown, A. L. Thompson, P. Kennepohl and P. D. Beer, *J. Am. Chem. Soc.*, 2015, **137**, 499–507.

42 C. C. Robertson, R. N. Perutz, L. Brammer and C. A. Hunter, *Chem. Sci.*, 2014, **5**, 4179–4183.

43 G. Cavallo, P. Metrangolo, R. Milani, T. Pilati, A. Priimagi, G. Resnati and G. Terraneo, *Chem. Rev.*, 2016, **116**, 2478–2601.

44 A. Borissov, I. Marques, J. Y. C. Lim, V. Félix, M. D. Smith and P. D. Beer, *J. Am. Chem. Soc.*, 2019, **141**, 4119–4129.

45 G. E. Garrett, E. I. Carrera, D. S. Seferos and M. S. Taylor, *Chem. Commun.*, 2016, **52**, 9881–9884.

46 D. Mungalpara, S. Stegmüller and S. Kubik, *Chem. Commun.*, 2017, **53**, 5095–5098.

47 D. A. Kraut, M. J. Churchill, P. E. Dawson and D. Herschlag, *ACS Chem. Biol.*, 2009, **4**, 269–273.

48 D. A. Decato, E. A. John, O. B. Berryman, M. S. Taylor, A. Docker, P. D. Beer, L. Turunen, M. Erdélyi, S. Wilcox, W. Herrebout, M. Erdelyi, A. Vargas Jentzsch, S. Matile, J. J. Koenig, M. Breugst, R. L. Sutar, C. Fave, B. Schöllhorn, P. S. Ho, D. M. Anderson, K. T. Mahmudov, V. A. Aliyeva, M. F. C. Guedes da Silva and A. J. L. Pombeiro, *Halogen Bonding in Solution*, 2021.

CHAPTER 4

Chapter 4 Stimuli Responsive Anion Transporters

4.1 Introduction

Chemical and biological processes, including anion transport, are part of highly dynamic and carefully controlled biochemical reaction networks.[1] In **chapter 1 section 1.4.3**, the case for stimuli-responsive transport was briefly introduced and in this chapter, the ways in which light can be used to control carrier mobility and transport, will be expanded upon.

The anion transporters described in **chapter 2** and **3** are in a constant 'on' state and continually work to dissipate the applied pH, or anion concentration gradient so long as there is one in place. However, controlling mobile carriers is essential for the selective and tuneable transport of anions, which in turn increases their real-world applicability such as targeted channelopathy treatments.[2] Additional spatiotemporal control over membrane transport processes would also enable supramolecular chemists to work towards sophisticated life-mimicking systems such as artificial signal transduction.[3] Therefore, there is a pressing need for spatiotemporal control in the context of biomimetic anion transport.

In this chapter, an *ortho*-nitrobenzyl (*o*-NB) group will act as a photo-labile linker between a membrane anchor and a mobile carrier enabling the control of anion transport activity using light as the external stimulus. The carriers will be tethered to the bilayer by a membrane targeting group as a means to restrict their motion. This type of control has been termed 'photo-modulated permeability' by Feringa and co-workers who have recently discussed the use of light to control of lipid bilayer assembly and channel function.[4] Examples of chemical-modulated membrane permeability with the use of hydrophilic stoppers have been previously discussed in **chapter 1 section 1.4.3.1**.[5,6] However, the

concept of photo-modulated membrane permeability in which the carrier is tethered to the bilayer by a lipid anchor has not yet been applied to transmembrane anion transporters.

Light is an attractive stimulus for controlling anion transport; it is not invasive, it can be precisely added and removed, and the biocompatibility can be tuned when choosing the photo-protecting group.[7] The *o*-NB photo-protecting group in particular is commonly used within organic synthesis (e.g. natural product synthesis),[12] and biology (e.g. caging biomolecules such as drugs), since it can be removed with spatiotemporal precision.[13,10] Examples of chemically-stimulated and photo-switchable transporters have been discussed in **chapter 1 section 1.4.3**, but photo-caged mobile transporters are rare. Talukdar and co-workers used an *o*-NB group to cage one of the HB donors in their indole-2-carboxamide anion carrier, preventing anion recognition and thus transport (**Figure 4.1a**).[11] Photo-irradiation of the transport-inactive pro-carrier with 365 nm UV light cleaved off the *o*-NB photo-labile protecting-group regenerating the HB binding motif for anion recognition and transport. The transport-active carrier (**Figure 4.1b**) achieved 90.5% transport efficiency with just 3 mins of irradiation and an EC_{50} value of 0.22 μM in the HPTS assay. Caging of the anion binding site as a method of controlling anion transport has been presented previously via cation coordination,[12] however this was the first time the photo-responsive *o*-NB group had been used for this method of caging in the context of mobile anion transport.

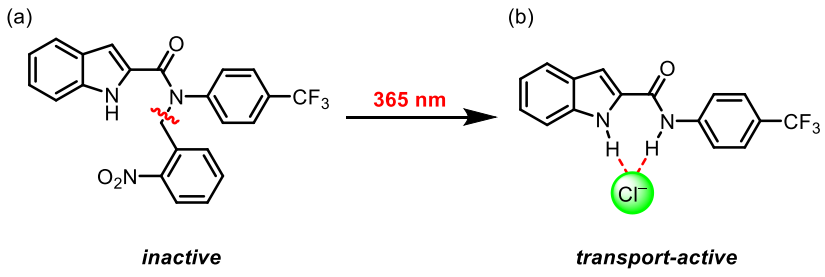


Figure 4.1. Caged and uncaged indole-2-carboxamide anion carrier.[11]

In nature, the function of membrane proteins is highly dependent on their primary structure which ultimately governs their location within the bilayer; stringent insertion and folding pathways then direct the protein to the membrane. Only a couple examples of synthetic mobile carriers have been presented which attempt to ensure that they localise in the bilayer. For example, Smith and co-workers presented a novel approach of restricting mobile carrier motion using a phospholipid anchoring group (**Figure 4.2**).[13] They functionalised a phospholipid with a urea-based mobile carrier which could insert into the bilayer. The mobile carrier was tethered to the bilayer without disrupting the membrane, and was postulated to perform anion transport via a 'relay' mechanism in which carriers pass the anion between transporters in opposite leaflets of the membrane.

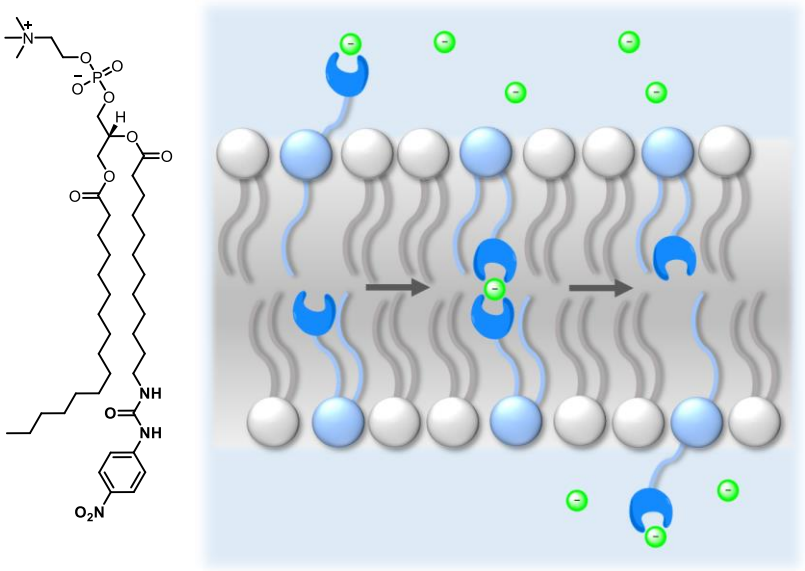


Figure 4.2. Membrane-bound mobile carrier and schematic showing the relay mechanism.[13]

Boa, Qu, Zhu and co-workers presented a [2]rotaxane with an amphiphilic axle that could span across the bilayer. A crown ether macrocycle was used to tether a second crown ether to the axle which could act as a cation transporter (**Figure 4.3**).[14] The transport

mediated by this crown ether was restricted to travelling along the axle which had three cationic binding stations to facilitate motion of the interlocked component. This so-called molecular cable car was capable of transporting K^+ with an EC_{50} value of 3 mol% (with respect to lipid). Although these examples are not stimuli responsive, they present a novel approach to restricting carrier motion within a lipid bilayer.

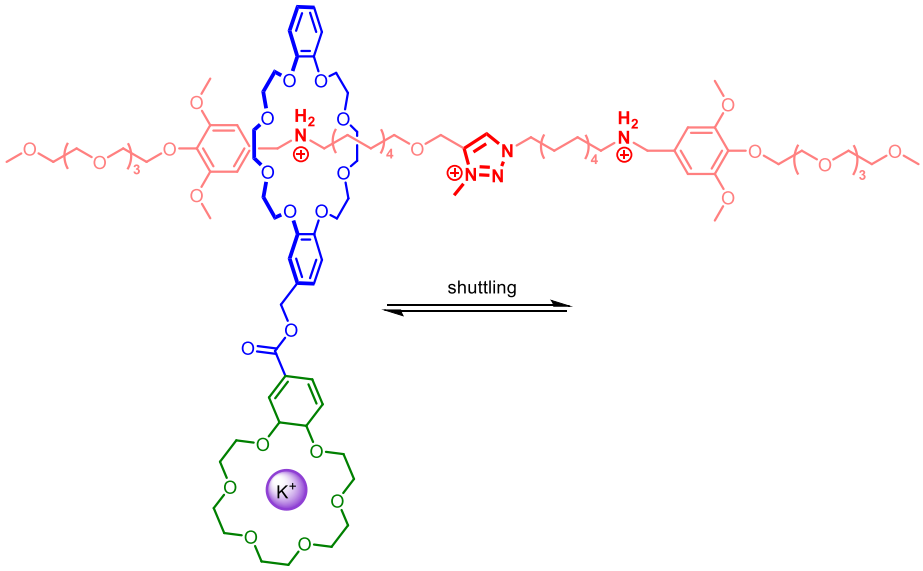


Figure 4.3. Transmembrane rotaxane ion transporter, cationic binding stations shown in bold and cation receptor shown in green.[14]

Within the field of biological sensing, membrane anchoring has been achieved by appending sensor molecules with membrane targeting groups. These additional functional groups can localise within a particular cellular organelle, or can interact with specific cellular sites in order to direct the localisation of a sensor. Rutter, Goldup, Watkinson and co-workers developed a biologically targeting Zn^{2+} sensor using high yielding click chemistry to obtain a modular sensor composed of a Zn^{2+} binding site, a fluorescent 1,8-naphtalimide linker and lipophilic dodedecyl chains.[15] Dipicolylamine was conjugated to the fluorescent

1,8-naphthalimide linker which could then be clicked to the azide functionalised membrane anchor (**Figure 4.4**). Epifluorescence microscopy was used to visualise the sensor targeting the lipid bilayer. Due to the high lipophilicity of the dodecyl chains, the molecule was able to localise on the extracellular surface of the cell membrane, thus acting as a membrane anchor for the sensor. This 'clickable' approach to membrane targeting has the potential to be adapted into abiotic anion transport systems. The long lipophilic chains could act as a membrane anchor, stopping the transporter from translocating across the membrane and the clickable approach allows for synthetic availability and versatility. The photo-activated carriers presented in this chapter will therefore possess this clickable membrane anchor.

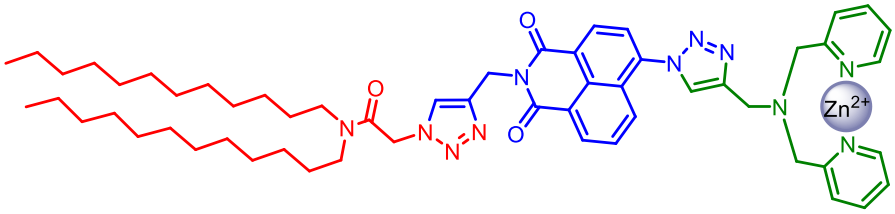


Figure 4.4. Zn^{2+} probe with fluorescent linker and clickable membrane anchor.[15]

4.1.1 Chapter Aims

The overall goal of this chapter is to design, synthesise and test a series of anion transporters that are activated by light. The carrier will be anchored to the vesicle membrane via a lipophilic membrane targeting group which is designed to inhibit the carrier's ability to cross the bilayer freely. For the purposes of photo-caging the carrier, an *o*-nitrobenzyl photo-protecting group will be used as a photo-labile linker connecting the mobile carrier to the membrane anchor to control the carriers' mobility with light. A family of previously reported anion receptors will be used to mediate transport including a thiourea, a squaramide, and a bidentate proto-triazole receptor analogous to those presented in **chapter 3**. Using three different anion transporters allows for effective and thorough investigations into the photo-modulated permeability concept.

Initially, the simple mobile carriers will be synthesised and then their transport ability will be examined using the HPTS assay. Once determined to be successful transmembrane transporters, they will be incorporated into a photo-cleavable carrier scaffold. Following the synthesis of the anchored carriers, the photolability of the *o*-nitrobenzyl group will be monitored by ^{1}H NMR. Transport experiments will then be performed with and without *in-situ* irradiation using LEDs to assess the stimuli-responsive nature of the pro-carriers. Furthermore, to increase the biocompatibility of the light-activated carriers, visible-light activated coumarin derivatives will be explored as an alternative photo-protecting group.

4.2 Design of Anchored Photo-Caged Transporters

The anchor, photo-labile linker and mobile carriers were all synthesised separately such that the components could be interchanged, ensuring maximum versatility and synthetic ease. The membrane anchor was inspired by the previous research of Pancholi et al. in which they had synthesised a membrane targeting supramolecular zinc sensor (**Figure 4.4**, **page 137**).[15] The *o*-NB photo-labile linker requires the functionality to adhere the membrane anchor to it *and* reversibly attach the anion carrier for stimuli-responsive anion transport. The membrane anchor was attached to the *o*-NB group in the para position to the nitro group since it has been shown that substituents in this position have little effect on the quantum yield of this photo-protecting group, and there is a precedent for the synthesis of analogous *o*-NB groups.[8] The anchored photo-caged transporters will therefore have the general design displayed in **Figure 4.5**. Mobile transporters will be numbered **T4.X** and the anchored transporters will be numbered **AT4.X**.

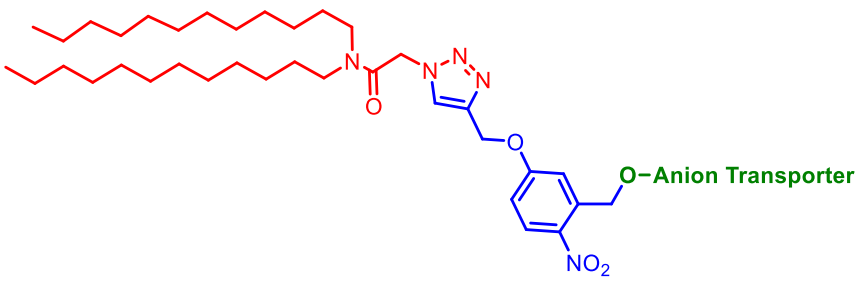


Figure 4.5. Stimuli-responsive transporter scaffold.

The mobile carriers (**T4.1**, **T4.2** and **T4.3**) presented in **Figure 4.6** were chosen for initial transport investigations. To allow facile coupling of the anion transporters to the *o*-NB photo-labile linker, the carriers were appended with a phenol substituent so that the photo-labile linker can be attached by an ether linkage to the carrier. All carriers were appended

with trifluoromethyl substituents or perfluoroaryl substituents to increase the potency of the N–H/C–H HB donors. Carrier **T4.1** in particular was selected as a result of the high transport activity of the bidentate carriers reported in **chapter 3**. Squaramide **T4.3** and thiourea **T4.2** were synthesised since they are well-established in the literature and can serve as good models for comparison.[16,17]

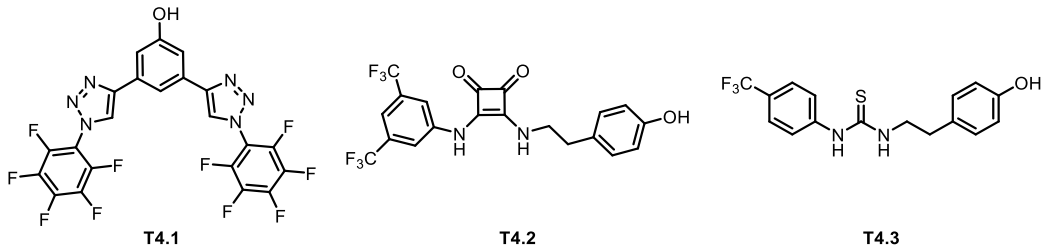
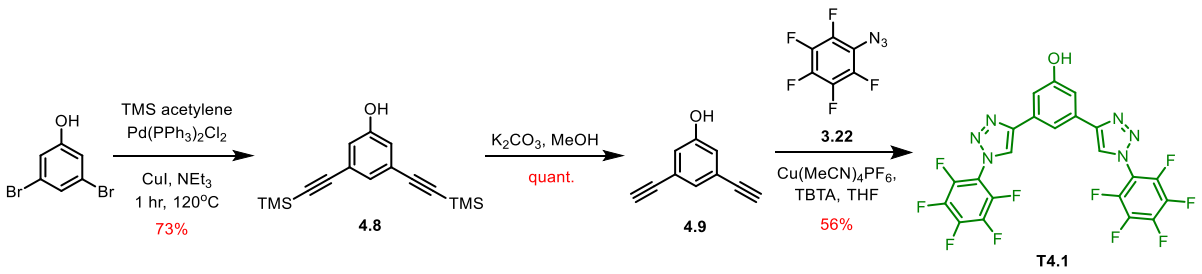


Figure 4.6. Mobile carriers **T4.1, T4.2** and **T4.3.**

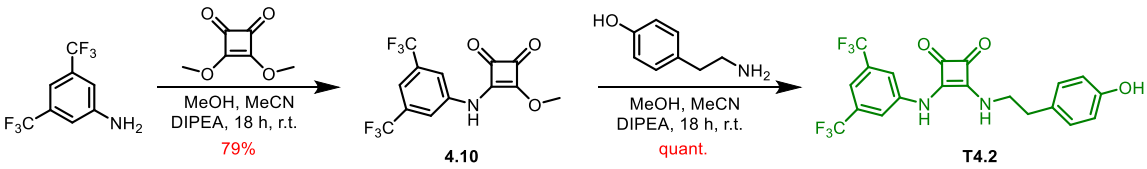
4.3 Synthesis of Mobile Carriers

To synthesise **T4.1**, 3,5-dibromophenol was subjected to a Sonogashira cross coupling reaction with TMS acetylene to yield the TMS-protected alkyne **4.8** (**Scheme 4.1**). Deprotection with KOH in a 1:1 MeOH:water mixture yielded 3,5-diethynylphenol **4.9** in a quantitative yield. Carrier **T4.1** could then be obtained via a copper-catalyzed azide−alkyne cycloaddition (CuAAC) reaction of 1-azido-pentafluorobenzene (**chapter 3, 3.22**) and 3,5-diethynylphenol **4.9** in a 56% yield (**Scheme 4.1**).

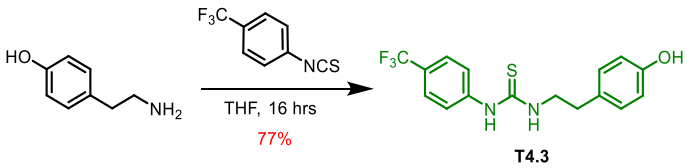


Scheme 4.1. Synthesis of carrier **T4.1** by the click reaction of azide **3.22** and alkyne **4.9** precursors.

Squaramide carrier **T4.2** was formed in 2 steps; first dimethyl squarate was reacted with equimolar 3,5-bis(trifluoromethyl)aniline to generate monosquaramide **4.10** in a 79% yield. This was then reacted with tyramine to form mobile carrier **T4.2** in a quantitative yield (**Scheme 4.2**). The free thiourea mobile carrier **T4.3** was synthesised by stirring 4-(trifluoromethyl)phenyl isothiocyanate with tyramine in THF overnight in a 77% yield (**Scheme 4.3**).



Scheme 4.2. Synthesis of mobile squaramide carrier **T4.2**.



Scheme 4.3. Synthesis of thiourea mobile carrier **T4.3**.

4.3.1 Anion Recognition

The chloride binding ability of the bidentate C–H triazole **T4.1** and squaramide receptor **T4.2** were investigated by ^{1}H NMR titration experiments with tetrabutylammonium chloride in acetone-d_6 and acetone-d_6 +2.5% D_2O. During the course of the titration of **T4.1** in acetone-d_6, the OH signal of bidentate carrier **T4.1**, (**Figure 4.7**, proton A), experienced a large downfield shift (δ 8.9 to 11.4) indicative of strong hydrogen bonding with Cl^-. It is likely that the anion is bound in a cavity formed by protons A, B and D (**Figure 4.8**). The data was fitted to a 1:1 host:guest binding model and the stoichiometric 1:1 association constants were determined using the Bindfit program (**Table 4.1**).[18]

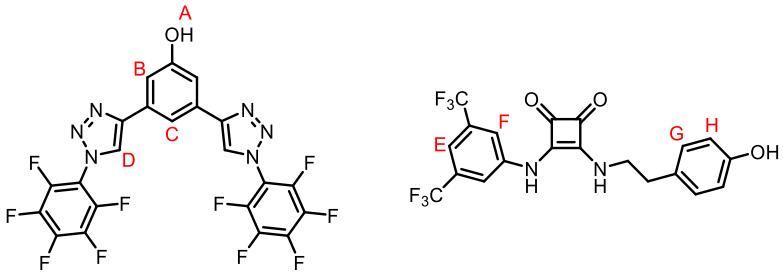


Figure 4.7. Carriers **T4.1** and **T4.2**.

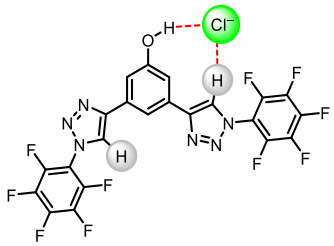


Figure 4.8. Postulated chloride anion binding mode of bidentate carrier **T4.1**.

Table 4.1. Chloride Binding affinities for the triazole and squaramide receptors.

K_1^{Cl} (M^{-1})[a]	T4.1	T4.2
acetone	998	$>10^4$
acetone + 2.5% D_2O	216	$>10^4$

[a] 1 : 1 association constant for chloride binding in acetone-d_6 or acetone-d_6 + 2.5% D_2O. Chloride added as the TBA salt. Errors of fit are less than <7%.

In the case of squaramide **T4.2**, upon addition of TBACl, proton E experienced a large downfield shift from δ 8.15 to 8.45 indicative of strong hydrogen bonding with Cl^- (**Figure 4.9**). The data was fitted to 1:1 model, however the squaramide carrier **T4.2** bound Cl^- very strongly in both acetone-d_6 and acetone-d_6 +2.5% D_2O (**Table 4.1**, K_a^{Cl} = $>10^4$ M^{-1}) and binding constants were too large to be reliably determined by these ^1H NMR titrations. The 1:1 chloride association constant of squaramide **T4.2** is at least 10-fold higher than of bis-triazole **T4.1**. Nevertheless, both receptors **T4.1** and **T4.2** bind chloride and are expected to be active transporters.

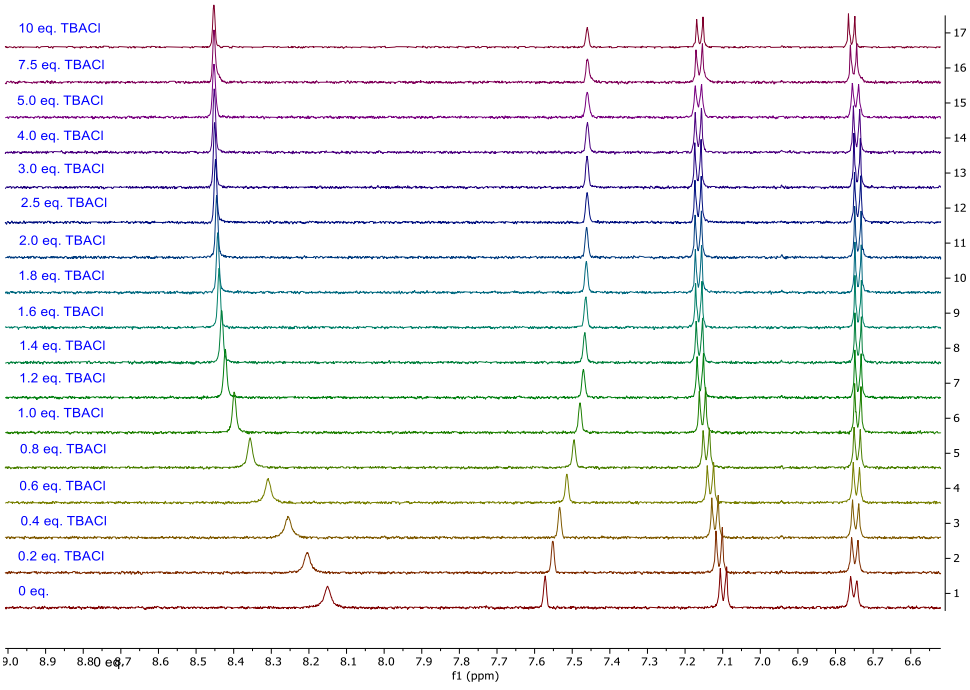


Figure 4.9. ^1H NMR spectra of **T4.2** showing the chemical shift perturbations upon increasing equivalents of TBACl.

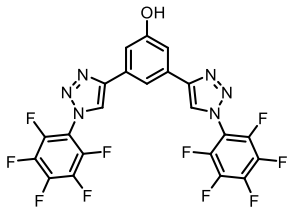
4.4 Transport Activity of Mobile Carriers

4.4.1 The HPTS Assay

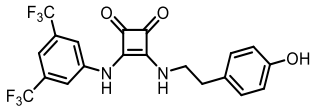
The anion transport ability of mobile carriers **T4.1**, **T4.2** and **T4.3** were tested using the HPTS assay described in **chapter 1** and **2** to determine their viability as transmembrane transporters, prior to incorporation into a light-activated scaffold. The EC_{50}, *n* and cLogP values of free mobile carriers **T4.1**, **T4.2** and **T4.3** are shown in **Table 4.2**. The cLogP values were calculated readily using Chemicalize, the instant cheminformatics program developed by ChemAxon.[19] Bidentate carrier **T4.1** showed similar activity to the monodentate triazole-based carriers presented in **chapter 2** with a modest EC_{50} value of 2.7 μM. This contrasts greatly to the highly active analogous carrier **T3.2** from **Chapter 3** which had an EC_{50} value of 48 nM – three orders of magnitude more active than bidentate carrier **T4.1** presented in this chapter. These carriers have equivalent cLogP values and comparable Cl^- association constants. It is likely that deprotonated forms of carrier **T4.1** exist (phenol pK_a = 9.02)[19] in the assay conditions which lowers its membrane permeability and reduces transport activity.

The squaramide carrier **T4.2** was the most active carrier in this series with an EC_{50} value of 0.5 μM. This is in stark contrast to the thiourea-based carrier **T4.3** which showed very poor activity (EC_{50} = 8.7 μM, **Table 4.2**). These results are unsurprising since the N–H donors in squaramide anion receptors are more acidic which leads to increased binding affinity towards anions and typically improves transport activity when compared to ureas or thiourea anion receptors.[20,21] Due to the lack of activity, thiourea carrier **T4.3** was therefore not incorporated into a light activated scaffold.

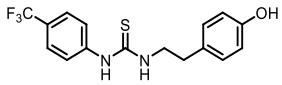
Table 4.2. EC_{50}, Hill coefficient, *n*, and cLogP values for free mobile carriers **T4.1**, **T4.2** and **T4.3**. Experimental values quantified from the HPTS assay, raw data available in the appendix.



T4.1



T4.2



T4.3

	T4.1	T4.2	T4.3
EC_{50} / µM	2.7	0.5	8.7
n	1.1	2.3	1.1
cLogP	6.6	4.5	4.6

HPTS assay: the fractional fluorescence intensity (I_{rel}) (λ_{em} = 510 nm; λ_{ex1} = 405 nm, λ_{ex2} = 460 nm) was monitored upon carrier addition (0.001–50 µM) to POPC vesicles containing 1 mM HPTS, 100 mM internal and external NaCl, buffered with 10 mM HEPES at pH 7.0. A pH gradient is generated by addition of a NaOH base pulse (0.5 M), followed by the carrier at t = 90 s. Vesicle lysis by Triton X-100 calibrates the assay. Subsequent Hill analysis allows for quantification of transport activity.

4.4.2 Control Experiments

The gluconate assay described in **chapter 2** was conducted for the triazole-based carrier **T4.1** and squaramide carrier **T4.2** to test for membrane leakage and to probe the transport mechanism. This assay is performed with sodium gluconate in place of sodium chloride in the buffer; gluconate cannot cross the bilayer and therefore only H^+/Na^+ cation antiport can occur (which is independent of gluconate transport). The absence of detectable transport with sodium gluconate buffer (**Figure 4.10**) supports a cation-independent mechanism, and demonstrates that transport within the initial HPTS assay experiments works via the antiport of Cl^- and OH^- or H^+. The DPPC assay was then performed on carrier **T4.1**. As discussed in **chapter 2 section 2.4.1**, this assay uses lipids in a gel phase at room temperature and only allows for mobile carrier transport in the fluid phase above 45 °C. The

assay confirmed that carrier **T4.1** works via a mobile carrier mechanism rather than stacking into a membrane-spanning channel. The details of these experiments can be found in **chapter 5** and the original data is presented in the appendix.

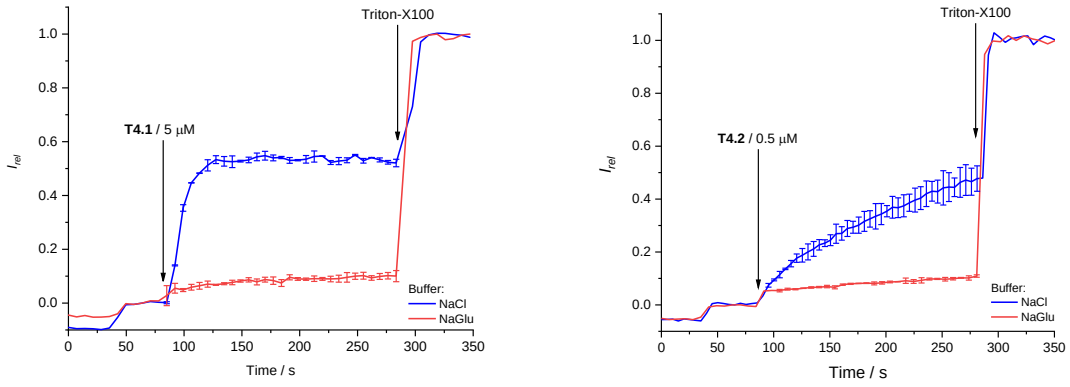


Figure 4.10. The change in fractional fluorescence intensity (I_{rel}) (λ_{em} = 510 nm; λ_{ex1} = 405 nm, λ_{ex2} = 460 nm) upon addition of carriers **T4.1** (left) and **T4.2** (right) (5 µM) to POPC vesicles containing 1 mM HPTS, 100 mM internal and external sodium gluconate, buffered with 10 mM HEPES at pH 7.0. A pH gradient is generated by addition of a NaOH base pulse (0.5 M), followed by the carrier at t = 90 s. Vesicle lysis by Triton X-100 calibrates the assay.

4.5 Synthesis of *ortho*-Nitrobenzyl Photo-Cleavable Carriers

Following the initial studies, the two active carriers **T4.1** and **T4.2** were linked to an *ortho*-nitrobenzyl (*o*-NB) photo-protecting group and subsequently clicked to a membrane anchor, according to the general design displayed in **Figure 4.11**.

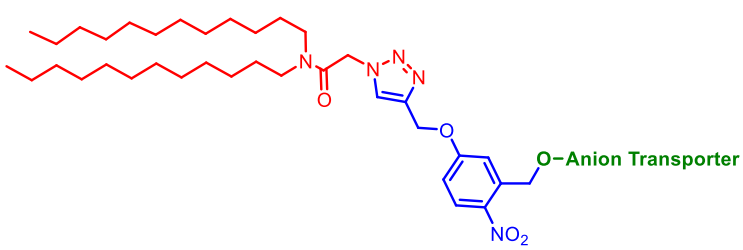
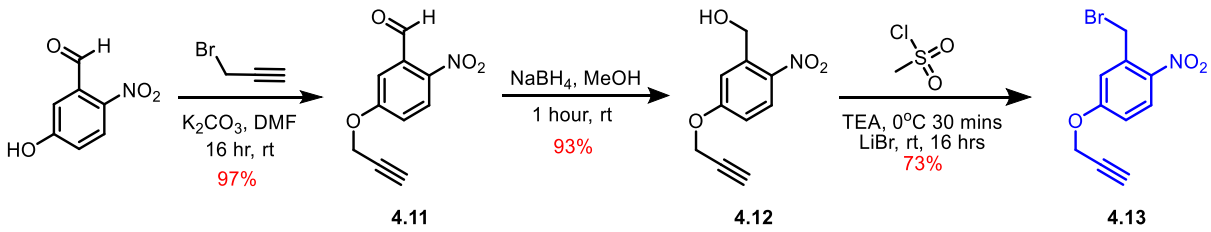


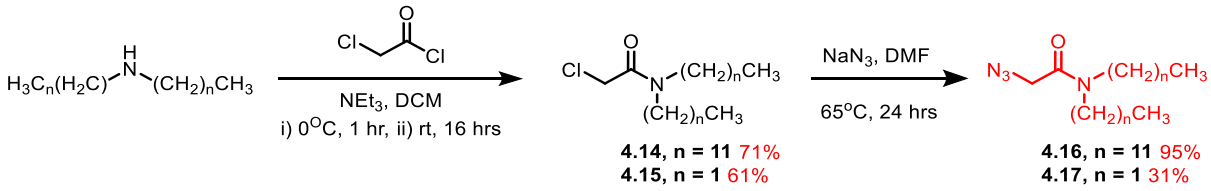
Figure 4.11. Stimuli-responsive transporter scaffold.

The novel *o*-NB photo-labile linker **4.13** was synthesised according to literature procedures from 5-hydroxy-2-nitrobenzaldyhyde in 3 steps (**Scheme 4.4**).[22,23] Initially, 5-hydroxy-2-nitrobenzaldyhyde was treated with propargyl bromide to yield compound **4.11** in a 97% yield, the incorporation of this alkyne functionality facilitates potential click reactions of azido-membrane anchors. Aldehyde **4.11** was then reduced to the alcohol with $NaBH_4$ in MeOH yielding the alcohol **4.12** in a 93% yield. Alcohol **4.12** was subsequently brominated via the corresponding mesylate with mesyl chloride to yield the final photo-labile linker **4.13** in 73% yield (**Scheme 4.4**).



Scheme 4.4. Synthesis of *o*-nitrobenzene photo-labile linker **4.13**.

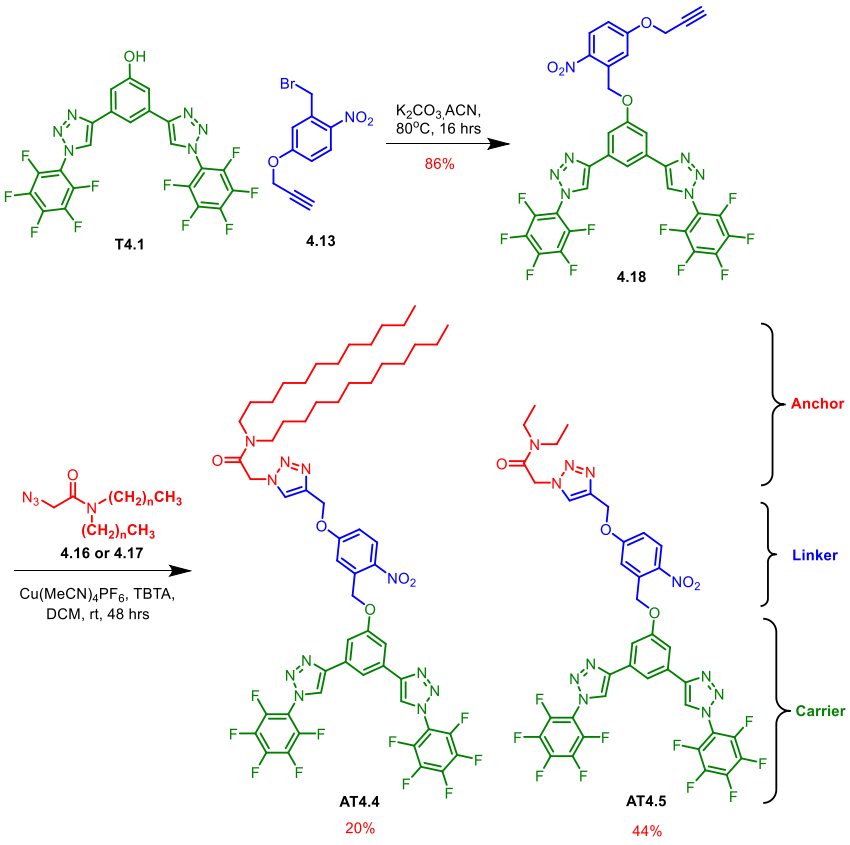
Hydrophobic didodecyl chains have previously been shown to embed within a lipid bilayer and were prepared from previously reported procedurs.[15] Didodecylamine was functionalised with an azide, to allow facile coupling to photo-labile linker **4.13** (**Scheme 4.5**). Didodecylamine was treated with chloroacetyl chloride to form **4.14** in a 71% yield. Alkyl chloride **4.14** could then undergo a reaction with sodium azide yielding membrane anchor **4.16** in a 95% yield. To investigate whether the carrier requires such a long membrane anchor to inhibit transport activity, shorter anchor **4.17** was also synthesised in a 31% yield (**Scheme 4.5**).



Scheme 4.5. Synthesis of membrane anchors **4.16** and **4.17**.[15]

4.5.1 Synthesis of Stimuli-Responsive Anchored Transporter (AT4.4)

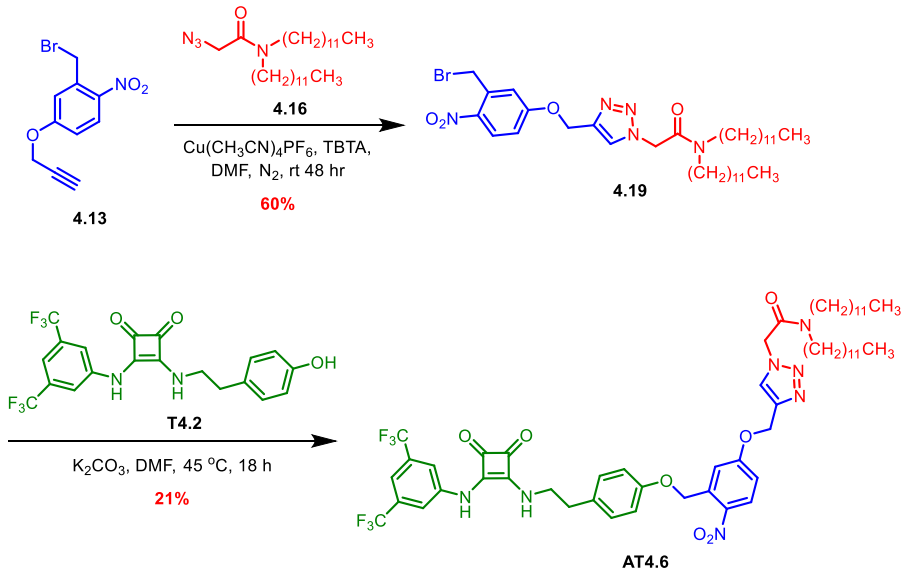
Carrier **T4.1** could then be coupled to the nitrobenzene linker **4.13** through Williamson ether synthesis yielding compound **4.18** in an 86% yield (**Scheme 4.6**). Compound **4.18** was subsequently clicked to the hydrophobic membrane anchors in the presence of TBTA and $Cu(MeCN)_4PF_6$ yielding the two final anchored photo-cleavable transporters **AT4.4** (20%) and **AT4.5** (44%) (**Scheme 4.6**).



Scheme 4.6. The synthesis of membrane anchored carriers **AT4.4** and **AT4.5**.

4.5.2 Synthesis of Stimuli-Responsive Anchored Transporter (AT4.6)

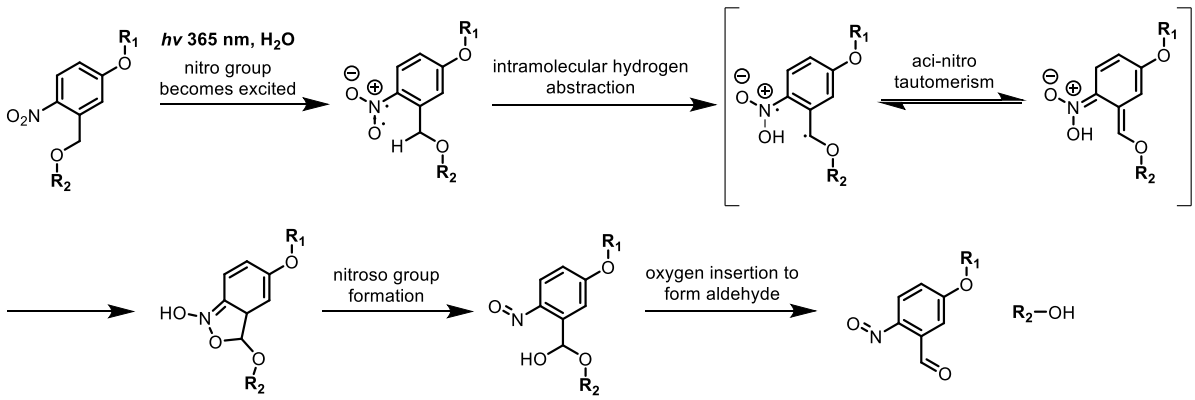
The synthesis of the anchored squaramide carrier began with the Cu(I)-catalysed azide–alkyne cycloaddition of the *o*-NB linker alkyne **4.13** and azide-functionalised membrane anchor **4.16**, in the presence of TBTA, which resulted in compound **4.19** in 60% yield (**Scheme 4.7**). The acidic phenol proton of **T4.2** (pK_a = 10.2)[19] could then be deprotonated with K_2CO_3 ready for subsequent treatment with **4.18** to give **T4.6** in a 21% yield (**Scheme 4.7**).



Scheme 4.7. Synthesis of anchored squaramide carrier **AT4.6**.

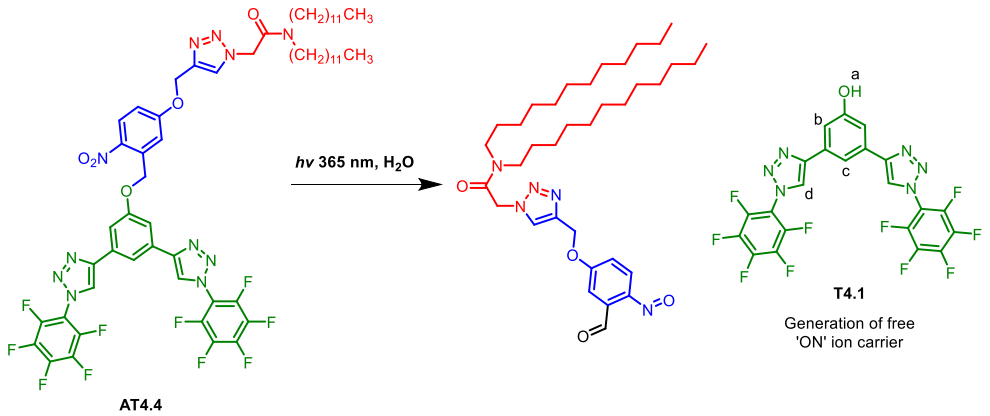
4.6 Photocleavage Experiments

The photo-cleavable properties of *o*-nitrobenzyl groups have been studied extensively due to their successful application as photo-protecting groups.[24] Upon irradiation at 365 nm, the internal oxidation-reduction reaction is known to proceed as shown in **Scheme 4.8**;[25] the nitro group becomes excited inducing intramolecular hydrogen abstraction to form an aci-nitro intermediate followed by formation of a nitroso group. Insertion of oxygen engenders the formation of an aldehyde on the linker and the generation of the mobile unanchored carrier with a hydroxyl group in the *meta* position with respect to the anion binding moieties.



Scheme 4.8. The proposed photo-cleavage mechanism of *o*-NB when irradiated with 365 nm UV light.[25]

The timescale on which this process occurs was monitored via a series of ^{1}H NMR experiments. A 2 mM sample of anchored carrier **AT4.4** in the NMR tube in d_6-DMSO was irradiated with a 365 nm UV LED light (0.88 W), the photocleavage mechanism was monitored using ^{1}H NMR recorded at 30 second intervals from 0 to 3 mins, then further spectra were recorded at 4, 5 and 10 minutes, and then every 10 mins up to 1 hour (**Figure 4.12**). Significant degradation of the linker was observed after 2 minutes and the reaction was complete after 10 minutes.



Scheme 4.9. Generation of **T4.1** when **AT4.4** is irradiated with 365 nm UV light.

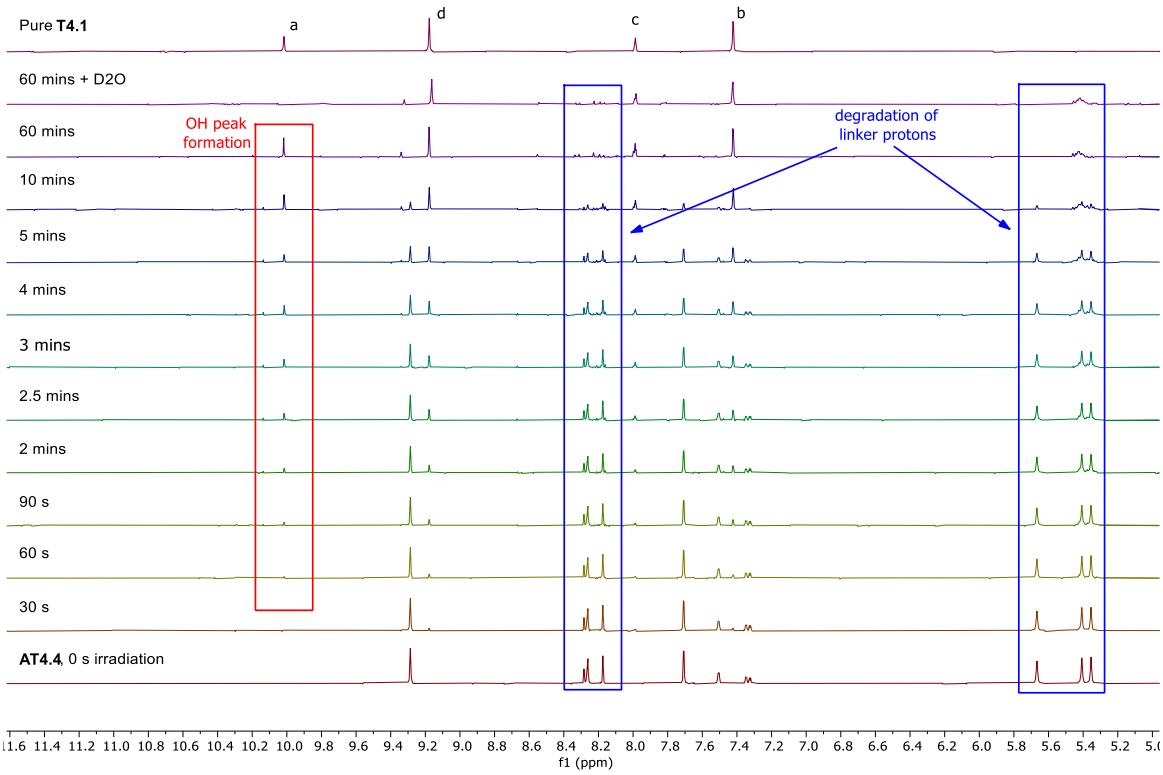


Figure 4.12. Photocleavage of **AT4.4** with 365 nm UV light (2 mM sample in d_6-DMSO) and generation of the free carrier over time from 0 to 60 mins with a pure sample of **T4.1** also shown. Addition of D_2O exchanges the aryl OH peak on the free carrier proving its correct identification. Membrane anchor protons not shown.

Formation of the OH peak on the newly generated mobile carrier could be readily monitored and then to generate the half-life which defines how long it takes to generate 50% of the free carrier (**Figure 4.13**). The half-life of **AT4.4** was calculated by fitting the data

to an exponential decay function (equation 4.1) to generate t_1 (= 2.18), which could then be used to derive a half-life of 91 seconds under these experimental conditions using equation 4.2.

$$y = A_1 e^{\left(\frac{-x}{t_1}\right)} \qquad (4.1)$$

$$t_{\frac{1}{2}} = t_1 ln\,(2) \qquad (4.2)$$

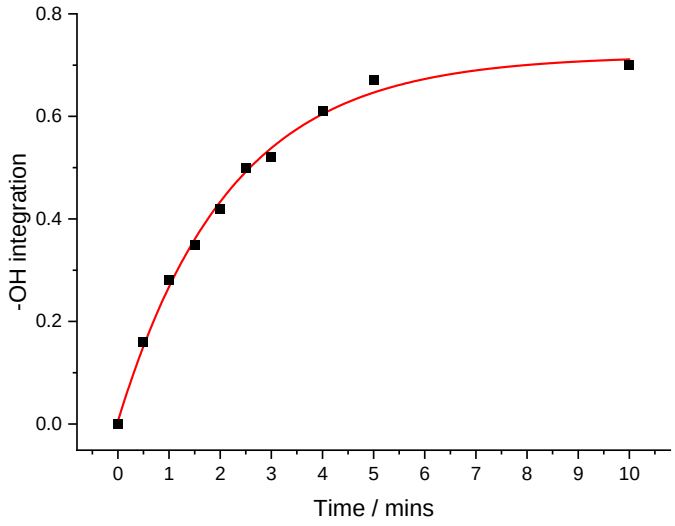
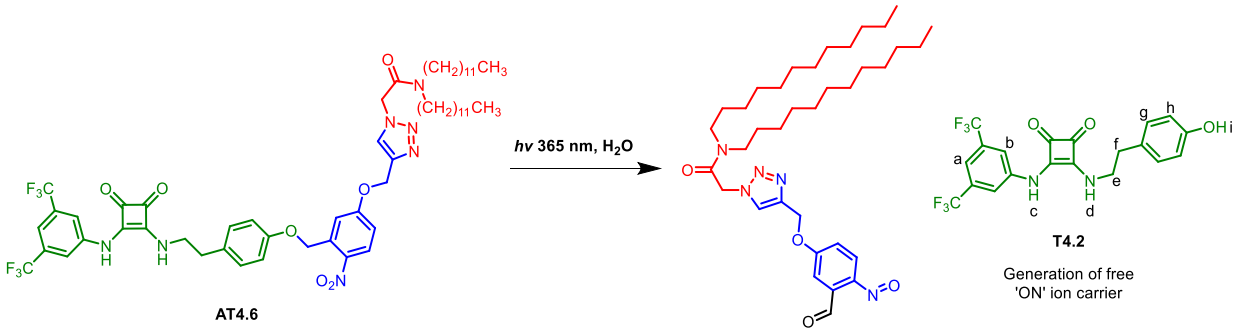


Figure 4.13. The integration of the aryl-OH peak on generated free carrier **T4.1** when a sample of **AT4.4** (2 mM, *d*-DMSO) is irradiated with 365 nm light over time, integrated with respect to the integration of the unchanged anchor protons. The data (■) was fitted to an exponential decay model using equation 4.1 (red line) and the half-life was determined using equation 4.2.

Similar photolytic experiments were also carried out accordingly on the squaramide carrier (**Scheme 4.10**) and the generation of carrier **T4.2** was again followed by ^{1}H NMR over time (**Figure 4.14**). Then the integration of the aryl OH peak was plotted against time relative to the anchor protons (**Figure 4.15**). Fitting this data to an exponential decay function (equation 4.1) generated a t_1 of 1.98 minutes, which could then be used to derive a half-life of 82 seconds under these experimental conditions using equation 4.2.



Scheme 4.10. Generation of **T4.2** when **AT4.6** is irradiated with 365 nm UV light.

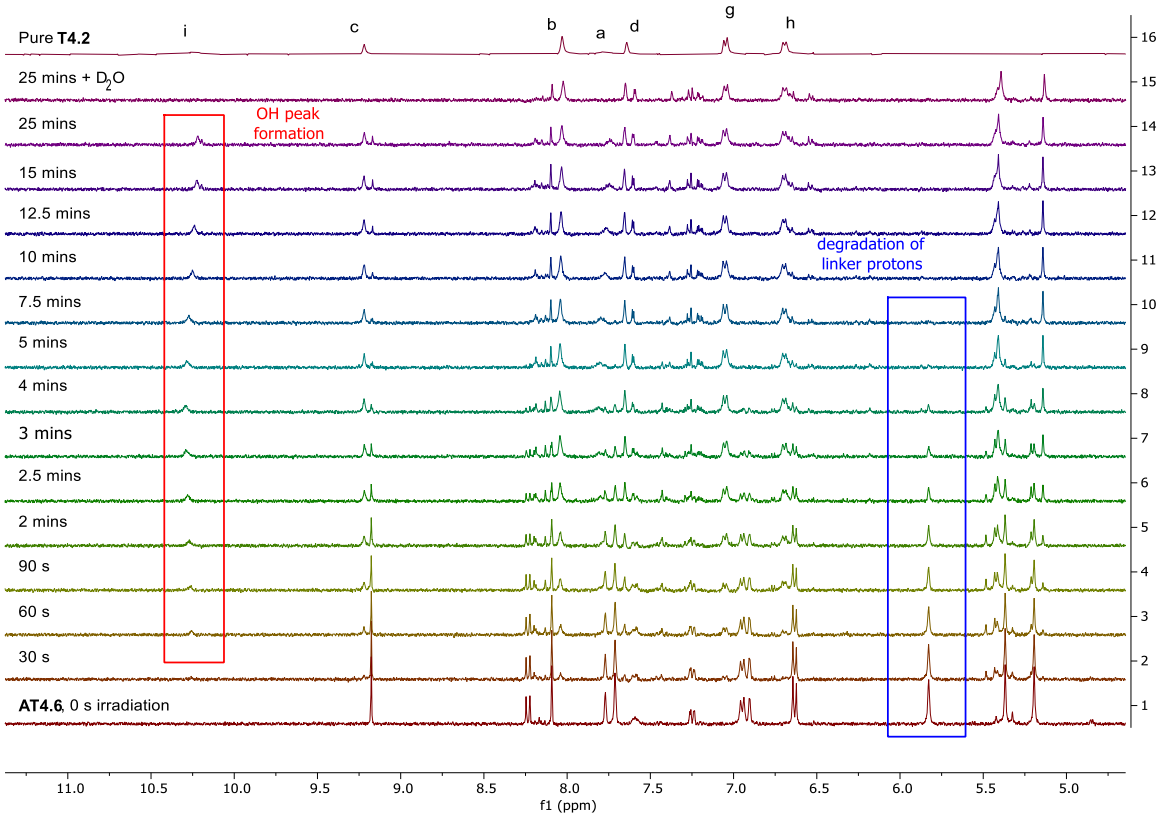


Figure 4.14. Photocleavage of **AT4.6** nitrobenzyl group with 365 nm UV light (2 mM sample in *d*-DMSO) leading to the generation of the free carrier **T4.2** over time from 0 to 25 mins. A pure sample of free carrier **T4.2** is also shown. Membrane anchor protons not shown.

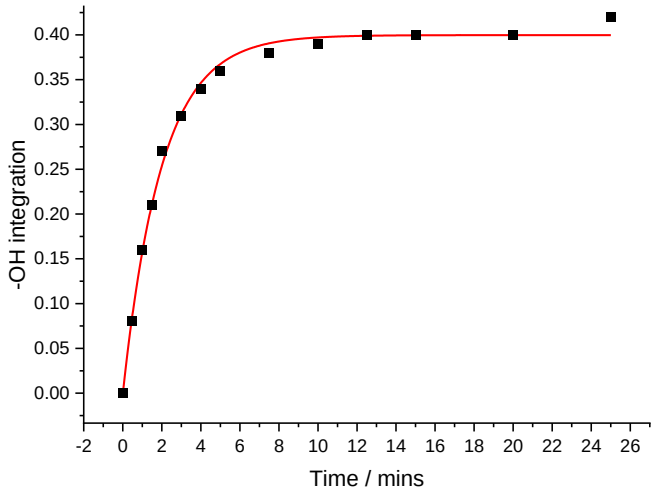


Figure 4.15. The integration of the aryl-OH peak on generated free carrier **T4.2** when a sample of **AT4.6** (2 mM, *d*-DMSO) is irradiated with 365 nm light over time, integrated with respect to the integration of the unchanged anchor protons. The data (■) was fitted to an exponential decay model using equation 4.1 (red line) and the half-life was determined using equation 4.2.

4.7 Photo-controlled Ion Transport Experiments

4.7.1 The HPTS Assay

The HPTS assay was first conducted on the anchored carriers without *in-situ* photo cleavage to investigate the performance of the long dodecyl chains as a lipid membrane anchor. **AT4.4** and **AT4.6** were inactive even at high concentrations, and therefore EC_{50} values were unable to be determined with Hill analysis (**Figure 4.16**). This suggests the extended hydrophobic dodecyl tails of the anchor are effective enough to inhibit transmembrane transport. Since we do not observe any change in fluorescence over time without irradiation we can assume that anion transport via a 'relay' or 'flip-flop' mechanism of the carrier does not occur.

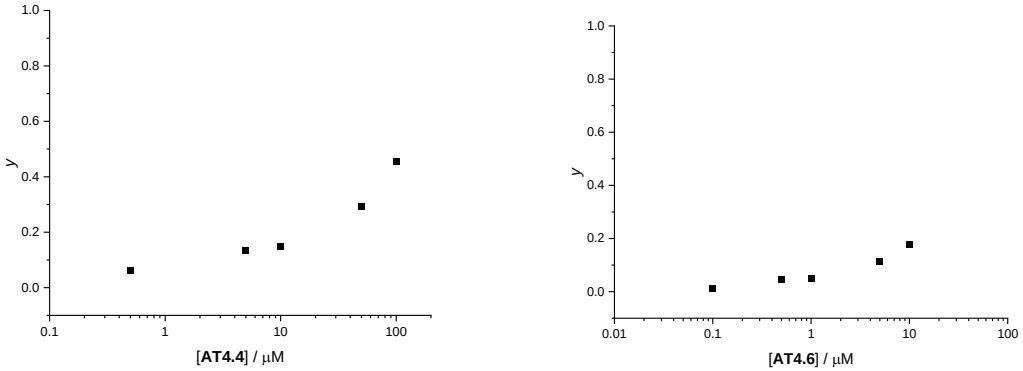


Figure 4.16. Anion transport mediated by **AT4.4** (left) and **AT4.6** (right) in the HPTS assay. The dependence of fractional activities (*y*, the relative intensity at *t* = 288 s just prior to lysis) on concentration (black squares).

The HPTS assay was then modified to allow for *in-situ* irradiation of the anchored carriers, and carried out as follows; anchored carriers **AT4.4** and **AT4.6** were added to the lipid suspension (POPC vesicles containing 1 mM HPTS, 100 mM internal and external NaCl, buffered with 10 mM HEPES at pH 7.0) and stirred for 1 minute to allow for incorporation into the bilayer. The sample was then irradiated with 365 nm UV light using an LED, before transport was initiated with a base pulse of NaOH (0.5 M) at 90 s and the change in ratiometric emission (λ_{em} = 510 nm; λ_{em1} = 405 nm, λ_{em2} = 460 nm) was monitored over time. The assay was calibrated with Triton-X100 at 290 s and then repeated at a range of concentrations. It must be noted that in these *in situ* photo-cleavage transport experiments, the carrier is added prior to the NaOH base pulse contrasting to the typical HPTS assay. Therefore, the jump in fluorescence intensity normally seen upon addition of NaOH now happens simultaneously with the transport of the carrier. To account for this, the initial jump is subtracted during the normalisation of the data outlined in **chapter 5 section 5.5.2.2**. To determine how long irradiation of the sample should be in order to achieve full transport potential, the assay was repeated with increasing irradiation times from 0 to 5

mins (**Figure 4.17**). These transport assay results with **AT4.4** show that photo-cleavage within the membrane reaches completion after 3 minutes of *in situ* irradiation, which aligns with a half-life of 91 seconds for the generation of **T4.1** from **AT4.4** as determined in DMSO solution by NMR experiments

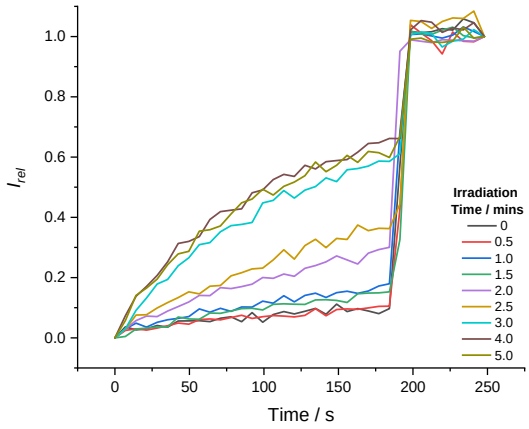
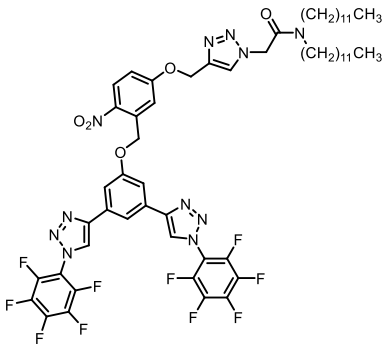


Figure 4.17. Change in ratiometric emission (λ_{em} = 510 nm; λ_{em1} = 405 nm, λ_{em2} = 460 nm) upon addition of carrier **AT4.4** (5 µM) at increasing irradiation times using a 365 nm UV LED**.**

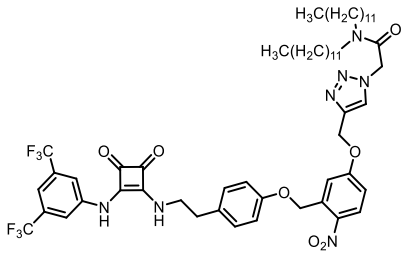
The HPTS assay was then conducted for each anchored carrier at a range of concentrations following 3 mins of *in-situ* irradiation time, in order to obtain an EC_{50} value. The EC_{50}, Hill coefficient, *n*, and cLogP values for anchored carriers **AT4.4** and **AT4.6** are shown in **Table 4.3** and the corresponding Hill plots are shown in **Figure 4.18**. All original data can be found in the appendix. After 3 mins of *in situ* photocleavage, the transport activity of **AT4.4** and **AT4.6** was almost completely restored with the *in-situ* photo-generated free carriers giving EC_{50} values of 4 µM and 2.6 µM respectively. The EC_{50} value of the photocleavage product of compound **AT4.4** (4 µM) was comparable to that of mobile carrier **T4.1** (2.7 µM). In the case of the squaramide, the *in situ* photocleavage seems less effective with the product of **AT4.6** giving an EC_{50} value of 2.6 µM in comparison to the free

squaramide carrier **T4.2** (EC_{50} = 0.5 µM). However, both carriers show very effective 'off' to 'on' activation of transport and this unprecedented anchoring approach to photo-caging anion carrier activity proved successful. This is highlighted in **Figure 4.19** which shows transport activity completely switched off prior to photo-cleavage and then switch on following irradiation for both **AT4.4** and **AT4.6** at 10 µM and 5 µM respectively.

Table 4.3. EC_{50}, Hill coefficient, *n*, and cLogP values for anchored transporters **AT4.4** and **AT4.6** before and after irradiation with 365 nm light. Experimental values quantified from the HPTS assay, raw data available in the Appendix.



AT4.4



AT4.6

	AT4.4		**AT4.6**	
	anchored	**cleaved**	**anchored**	**cleaved**
EC_{50} / µM	-[a]	4	-[a]	2.6
n	-[a]	3.5	-[a]	1.6
cLogP	16.5		14.4	
	T4.1		**T4.2**	
EC_{50} / µM	2.7		0.5	
n	1.1		2.3	
cLogP	6.6		4.5	

HPTS assay: the fractional fluorescence intensity (I_{rel}) (λ_{em} = 510 nm; λ_{ex1} = 405 nm, λ_{ex2} = 460 nm) at 25 °C was monitored upon carrier addition (0.001–50 µM) to POPC vesicles containing 1 mM HPTS, 100 mM internal and external NaCl, buffered with 10 mM HEPES at pH 7.0 with and without 3 mins of *in situ* irradiation with 365 nm light. A pH gradient is generated by addition of a NaOH base pulse (0.5 M) at t = 40 s, followed by the carrier at t = 90 s (reversed for in situ photocleavage experiments). Vesicle lysis by Triton X-100 calibrates the assay. Hill analysis allows for quantification of transport activity. [a] Inactive anchored transporters.

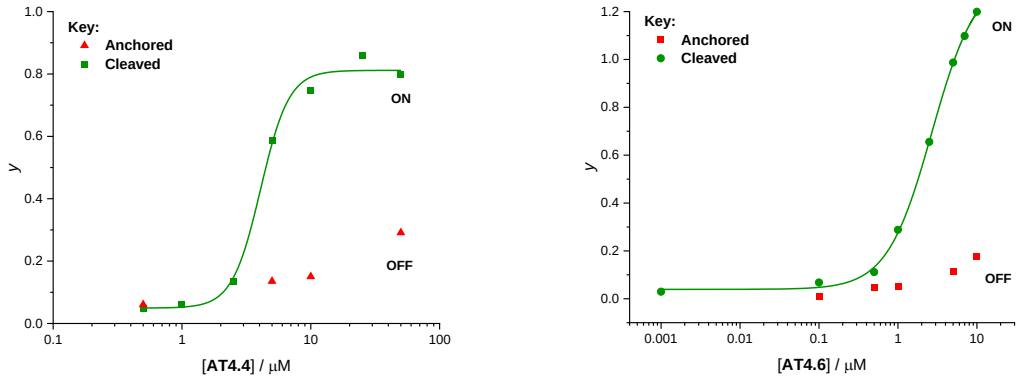


Figure 4.18. The dependence of fractional activities (*y*, the relative intensity at t = 276 s just prior to lysis) on the carrier concentration, and fit to the Hill equation (line), before and after *in-situ* irradiation with 365 nm light in the HPTS assay. Left, triazole **AT4.4** and right, squaramide **AT4.6**.

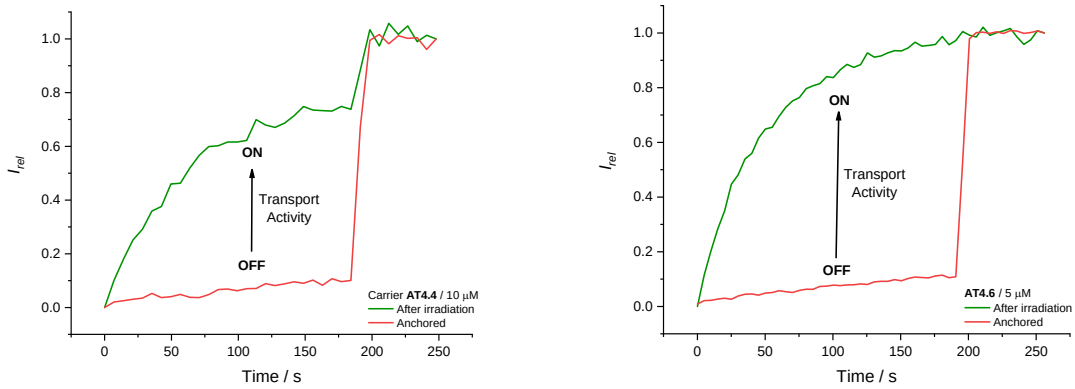


Figure 4.19. The change in ratiometric emission (λ_{em} = 510 nm; λ_{em1} = 405 nm, λ_{em2} = 460 nm) at 25 °C upon addition of **AT4.4** (10 μM, *left*) and **AT4.6** (5 μM, *right*) before and after 3 mins of *in-situ* irradiation with 365 nm light.

4.7.2 Mechanistic Investigations

4.7.2.1 Membrane Tethering Studies

To assess the necessity of the long hydrophobic anchor; **AT4.5** (**Figure 4.20**) was synthesised which has a much shorter anchor motif (**Scheme 4.6**). During the HPTS assay, a modest change in fluorescence intensity was seen over time upon addition of **AT4.5** before photo-cleavage indicating that the short anchor is not as effective as the long anchor at tethering the carrier to the membrane (**Figure 4.21**).

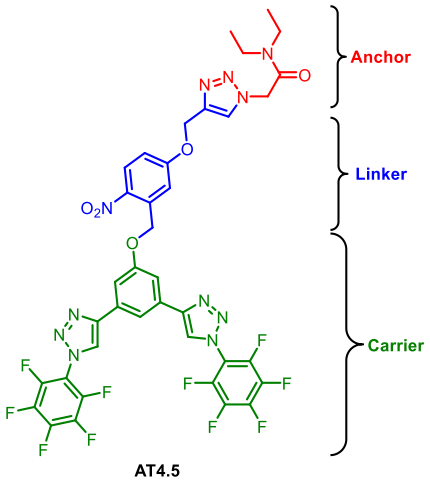


Figure 4.20. The synthesis of membrane anchored carriers **AT4.5**.

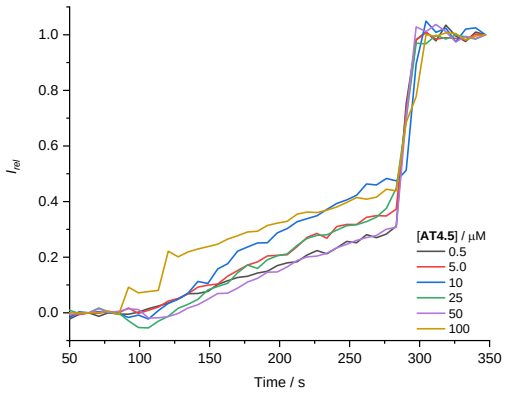


Figure 4.21. *Left*, change in ratiometric emission (λ_{em} = 510 nm; λ_{em1} = 405 nm, λ_{em2} = 460 nm) upon addition of **AT4.5** (0.5-100 μM).

4.7.2.2 Gluconate Assay

The gluconate variation of the HPTS assay described in **chapter 2 section 2.4.2** was performed on compounds **AT4.4** and **AT4.6** before and after *in-situ* irradiation. Since mobile carriers **T4.1** and **T4.2** did not facilitate transport in these conditions (**chapter 4 section 4.4.2**), it was unsurprising that transport was not seen upon addition of **AT4.4** and **AT4.6** (before and after irradiation) when using sodium gluconate buffer (**Figure 4.22**). The lack of transport also indicates that the carriers do not disrupt the integrity of the bilayer and acts as a test for membrane leakage. Regardless, the carboxyfluorescein leakage assay described in **chapter 2** was performed on **T4.1** and **AT4.4** before and after irradiation, which confirmed that neither the carriers, nor irradiation, affects the integrity of the lipid bilayer membranes and all transport see in the HPTS assay is valid (**appendix section A.2.3**).

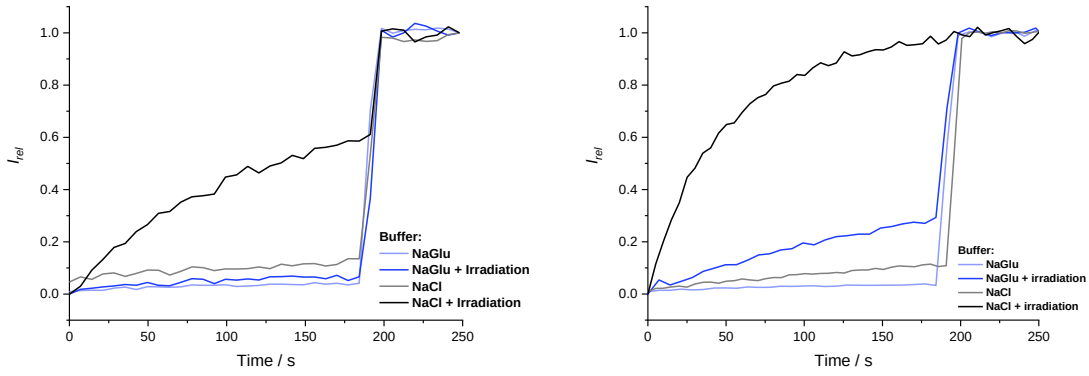
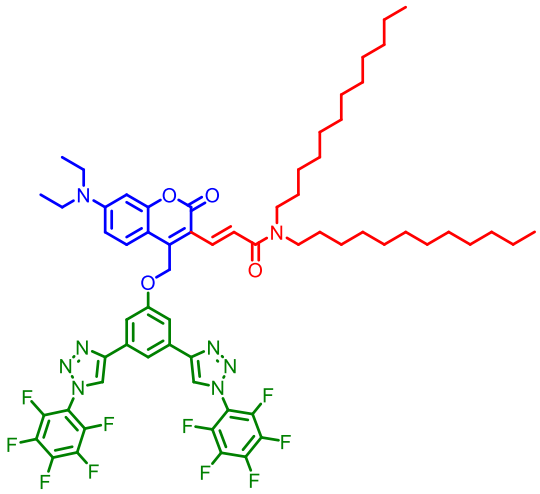


Figure 4.22. Change in ratiometric emission (λ_{em} = 510 nm; λ_{em1} = 405 nm, λ_{em2} = 460 nm) upon addition of **AT4.4** (left) and **AT4.6** (right) (both 5 µM, DMSO) at t = 90 to POPC vesicles containing 1 mM HPTS, 100 mM internal and external sodium gluconate, buffered with 10 mM HEPES at pH 7.0. Results are the average of at least two repeats.

4.8 Coumarin Photolabile Linker

The synthesis of analogous, more biocompatible, photocleavable carrier was attempted with the use of a coumarin-derivative as the photo-labile linker. Coumarin photo-cage derivatives have many applications within molecular biology due to their high biocompatibility. They can be cleaved using green light, which avoids the use of harmful UV light needed for the photolytic reactions of *o*-NB photo-protecting groups. In addition, the absorbance can be red shifted further by conjugating the membrane anchor to the coumarin backbone via a double bond according to the design of **AT4.7** shown in **Figure 4.23**.[9,26] Furthermore, coumarin itself is highly fluorescent which was anticipated to allow for visualisation of the membrane targeting capabilities of the long hydrophobic membrane anchor with fluorescence microscopy in giant unilamellar vesicles (GUVs).

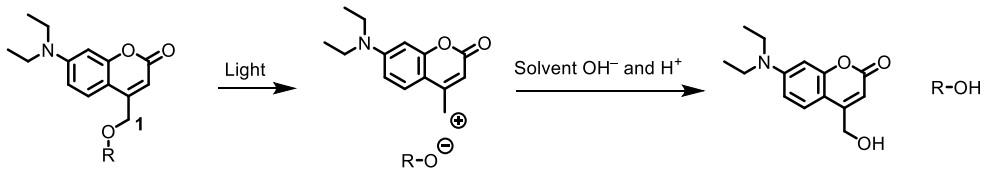


AT4.7

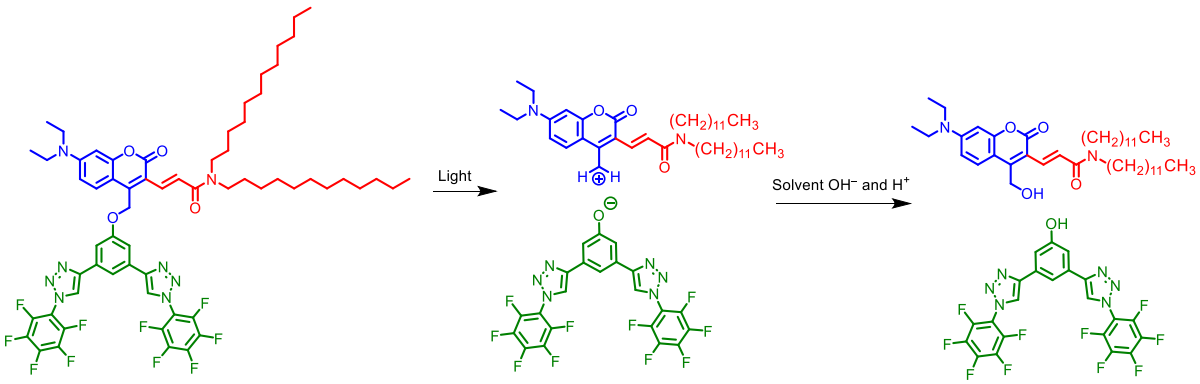
Figure 4.23. Membrane anchored mobile carrier **AT4.7** with coumarin-based photo-labile linker.

The photo-cleavage mechanism of courmarin derived photocages is not as well understood compared to that of *o*-NB groups, however, it has been suggested that it most

likely proceeds via a S_N1 photolytic mechanism involving the formation of an ion-pair transition state (**Scheme 4.11**);[27] upon irradiation with light the coumarin becomes excited inducing photo-heteolytic cleavage of the coumarin C-O bond (position 1, **Scheme 4.11**) resulting in a carbocation on the coumarin and a phenoxide/alkoxide anion. The ion-pair stabilise each other in this transition state and before they each pick up a proton or hydroxide from the solvent. In the case of anchored transporter **AT4.7**, this will therefore form the free carrier and the anchored coumarin-methyl alcohol as the by product (**Scheme 4.12**).



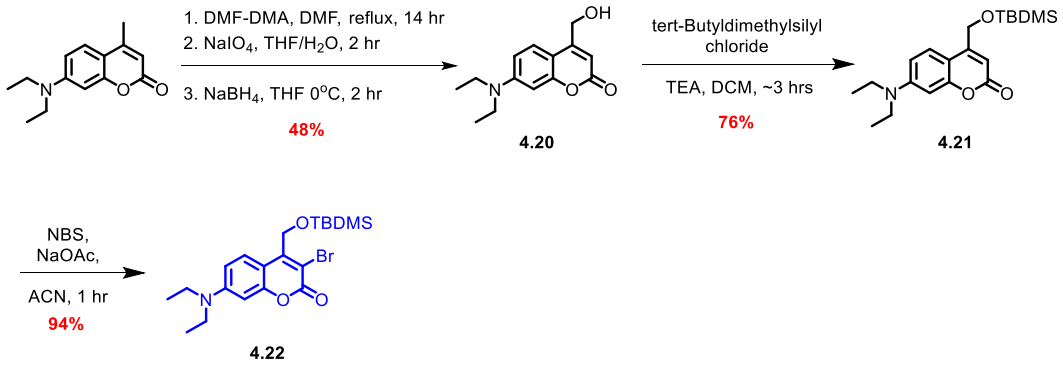
Scheme 4.11. Coumarin S_N1 photolytic cleavage mechanism.[27]



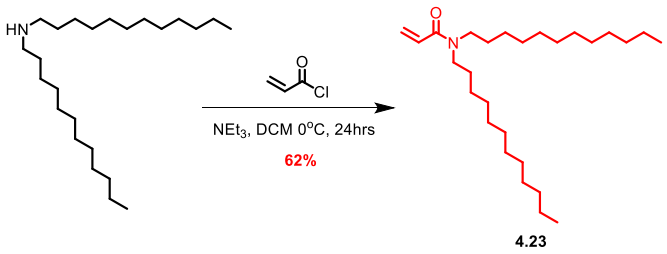
Scheme 4.12. Proposed photolytic cleavage mechanism of **AT4.7** to yield **T4.1**.

4.8.1 Synthesis of Coumarin Linkered Anchored Transporter AT4.7

The coumarin photolabile linker **4.22** was synthesised in three steps according to literature procedures in a 94% yield (**Scheme 4.13**).[26] For this light activated scaffold, didodecyl amine was treated with acryloyl chloride to form alkyne functionalised membrane anchor **4.23** in an 62% yield (**Scheme 4.14**).



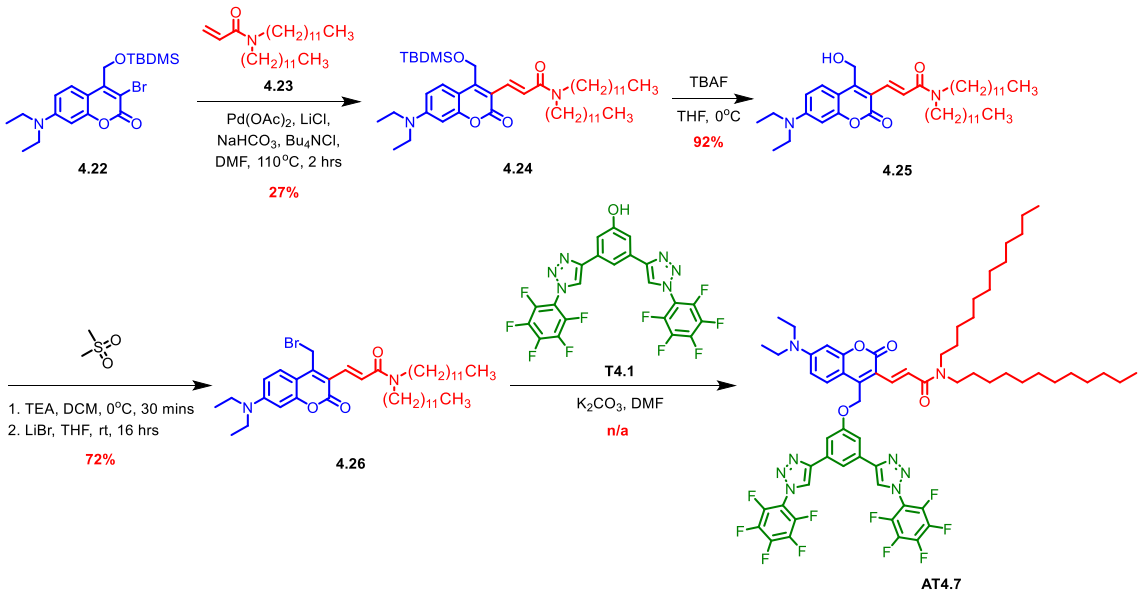
Scheme 4.13. Coumarin photolabile linker **4.22** synthesis.[26]



Scheme 4.14. The synthesis of membrane anchor **4.23**.

Coumarin **4.22** could then be coupled to the anchor **4.23** by a Heck reaction in the presence of $Pd(OAc)_2$ to yield *trans* compound **4.24** stereoselectively in a 27% yield (**Scheme 4.15**). Deprotection with TBAF gave alcohol **4.25** (92%) which could be subsequently brominated to yield compound **4.26**. Mobile carrier **T4.1** could then be coupled to the scaffold through Williamson ether synthesis to yield the final photo-cleavable membrane

anchored carrier **AT4.7**. However, due to high photo-instability of the light-activated carrier **AT4.7** and its precursors the final compound could not be isolated. The crude ^{1}H NMR shown in **Figure 4.24** indicates that the product was formed but it was not stable enough to be isolated by chromatography.



Scheme 4.15. The synthesis of anchored anion carrier **AT4.7** with a photocleavable courmarin moiety.

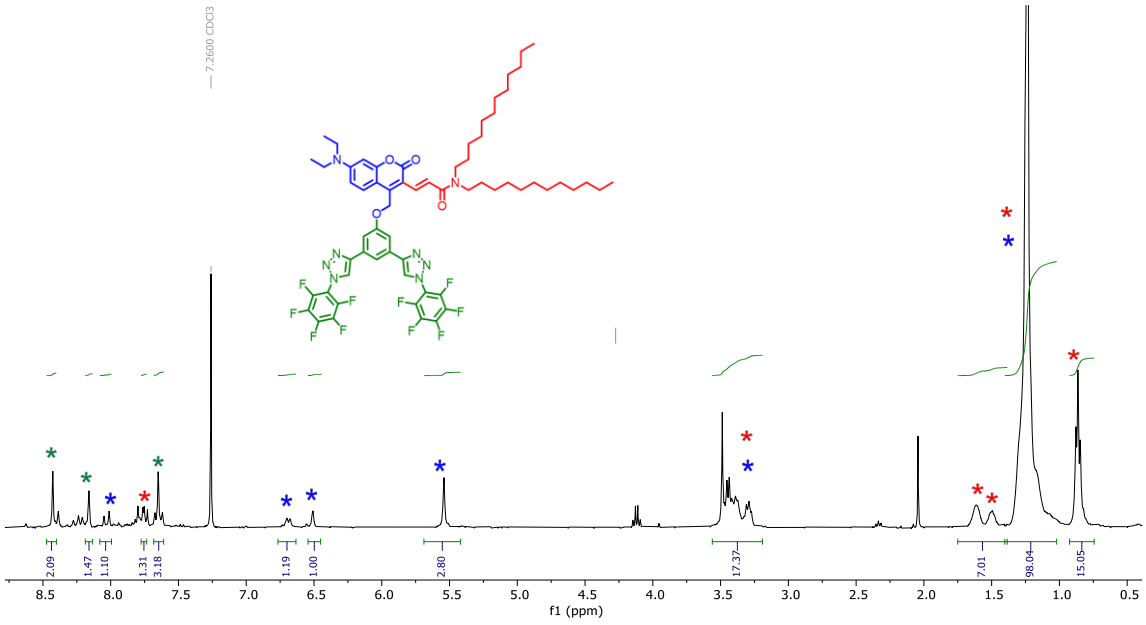
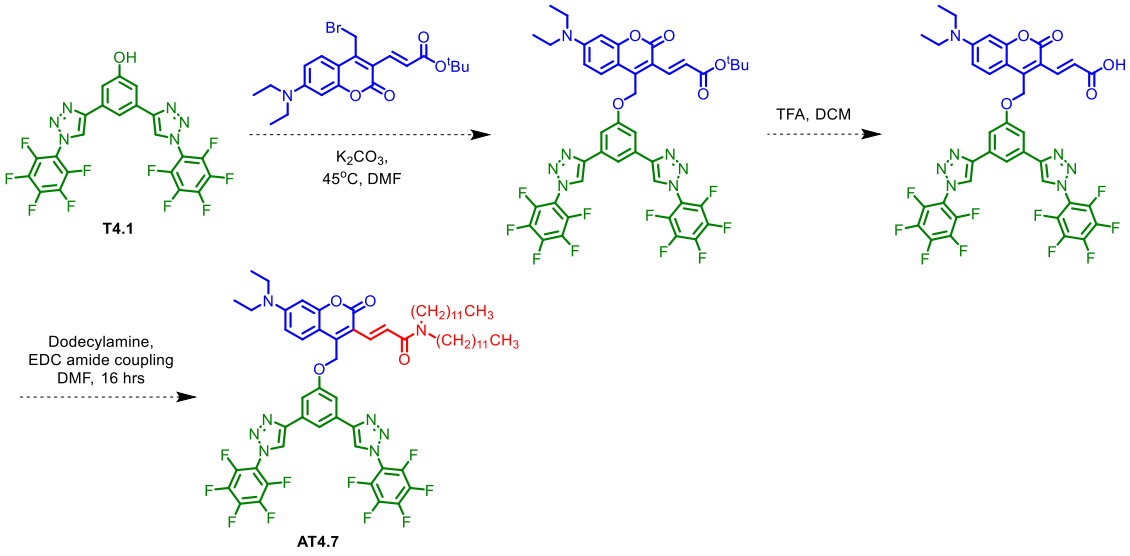


Figure 4.24. Crude ^{1}H NMR Spectrum of **AT4.7** ($CDCl_3$, 298 K, 400 MHz).

In order to yield these compounds in the future, the synthesis would need to be optimised to improve the scalability of the reactions which is inherently difficult due to their instability. One proposed method is show in **Scheme 4.16** which conjugates the carrier to the coumarin linker prior to addition of the anchor, this method also avoids the harsh conditions of the low yielding Heck reaction, however the carrier:linker bond may not be strong enough to be exposed to TFA in the second step.



Scheme 4.16. Alternative synthetic route proposed to yield final compound **AT4.7**.

4.9 Chapter Conclusions

In this chapter, two successful light activated anion transporters have been presented. They were anchored to the membrane by a new method of photo-caging which controls carrier mobility rather than direct modification of anion receptor binding site. Both **AT4.4** and **AT4.6** show exceptional off-on control. This dodecyl chain-based anchor was applicable to different carriers and has the potential to work for systems with different stimuli such as the chemical reduction of a disulphide bond. The unprecedented use of an *o*-NB group acting as a photo-labile linker between the anchor and mobile carrier proved to be an effective method of controlling anion transport activity using light as an external stimulus with anchored carriers being completely inactive until irradiated with 365 nm light for up to 3 mins.

This concept of photo-modulated permeability has the potential to be adapted into biocompatible systems with the use of a coumarin-derived photo-labile linker. The initial synthesis of this compound was described outlining the challenges that arose, and suggesting ways they could be overcome in order to reach the target molecule in sufficient yield.

The research completed in this chapter build a foundation for the development of carriers which facilitate orthogonal anion transport across a network of vesicles. The use of *o*-NB and coumarin photo-labile linkers highlight the potential for wavelength specific activation and intra-vesicular cross-talk. Overall, an effective, and novel method of controlling anion transport has been achieved, with potential for variation of each building block within the scaffold to tune the anion selectivity.

4.10 References

1 G. G. Jeremy M. Berg, Lubert Stryer, John Tymoczko, *Biochemistry*, W.H. Freeman;, Ninth Edit., 2019.

2 N. Akhtar, O. Biswas and D. Manna, *Chem. Commun.*, 2020, **56**, 14137–14153.

3 I. Insua and J. Montenegro, *Chem*, 2020, **6**, 1652–1682.

4 W. SzymaŃski, D. Yilmaz, A. Koçer and B. L. Feringa, *Acc. Chem. Res.*, 2013, **46**, 2910–2923.

5 Y. R. Choi, B. Lee, J. Park, W. Namkung and K. S. Jeong, *J. Am. Chem. Soc.*, 2016, **138**, 15319–15322.

6 S. Das, O. Biswas, N. Akhtar, A. Patel and D. Manna, *Org. Biomol. Chem.*, 2020, **18**, 9246–9252.

7 M. J. Langton, *Nat. Rev. Chem.*, 2021, **5**, 46–61.

8 P. Klán, T. Šolomek, C. G. Bochet, A. Blanc, R. Givens, M. Rubina, V. Popik, A. Kostikov and J. Wirz, *Chem. Rev.*, 2013, **113**, 119–191.

9 M. J. Hansen, W. A. Velema, M. M. Lerch, W. Szymanski and B. L. Feringa, *Chem. Soc. Rev.*, 2015, **44**, 3358–3377.

10 G. C. R. Ellis-Davies, *Nat. Methods*, 2007, **4**, 619–628.

11 S. B. Salunke, J. A. Malla and P. Talukdar, *Angew. Chem. Int. Ed.*, 2019, **58**, 5354–5358.

12 M. Fares, X. Wu, D. Ramesh, W. Lewis, P. Keller, E. Howe, R. Pérez-Tomás and P. Gale, *Angew. Chem. Int. Ed.*, 2020, **59**, 17614–17621.

13 B. A. McNally, E. J. O'Neil, A. Nguyen and B. D. Smith, *J. Am. Chem. Soc.*, 2008, **130**, 17274–17275.

14 S. Chen, Y. Wang, T. Nie, C. Bao, C. Wang, T. Xu, Q. Lin, D.-H. Qu, X. Gong, Y. Yang, L. Zhu and H. Tian, *J. Am. Chem. Soc.*, 2018, **140**, 17992–17998.

15 J. Pancholi, D. J. Hodson, K. Jobe, G. A. Rutter, S. M. Goldup and M. Watkinson, *Chem. Sci.*, 2014, **5**, 3528–3535.

16 N. Busschaert, I. L. Kirby, S. Young, S. J. Coles, P. N. Horton, M. E. Light and P. A. Gale, *Angew. Chem. Int. Ed.*, 2012, **51**, 4426–4430.

17 X. Wu, A. M. Gilchrist and P. A. Gale, *Chem*, 2020, **6**, 1296–1309.

18 BindFit v0.5 | Supramolecular, http://app.supramolecular.org/bindfit/.

19 ChemAxon, Chemicalize, https://chemaxon.com/.

20 J. Alemán, A. Parra, H. Jiang and K. A. Jørgensen, *Chem. Eur. J.*, 2011, **17**, 6890–6899.

21 S. J. Edwards, H. Valkenier, N. Busschaert, P. A. Gale and A. P. Davis, *Angew. Chem. Int. Ed.*, 2015, **54**, 4592–4596.

22 L. Li, X. X. Deng, Z. L. Li, F. S. Du and Z. C. Li, *Macromolecules*, 2014, **47**, 4660–4667.

23 N. Kalva, S. Uthaman, R. Augustine, S. H. Jeon, K. M. Huh, I. K. Park and I. Kim, *Macromol. Biosci.*, 2020, **20**, 1–12.

24 H. Yu, J. Li, D. Wu, Z. Qiu and Y. Zhang, *Chem. Soc. Rev.*, 2010, **39**, 464–473.

25 C. G. Bochet, *J. Chem. Soc. Perkin Trans. 1*, 2002, 125–142.

26 J. P. Olson, H. B. Kwon, K. T. Takasaki, C. Q. Chiu, M. J. Higley, B. L. Sabatini and G. C. R. Ellis-Davies, *J. Am. Chem. Soc.*, 2013, **135**, 5954–5957.

27 I. Cazin, E. Rossegger, G. Guedes, T. Griesser and S. Schlögl, *Polymers (Basel).*, 2020, **13**, 56.

CHAPTER 5

Chapter 5 Experimental

5.1 General Remarks

5.1.1 Experimental Methods

NMR spectra were recorded on a Bruker AVIII 400, Bruker AVII 500 (with He cryoprobe) and Bruker AVIIIHD 500 spectrometers. Chemical shifts are reported as δ values in ppm. Mass spectra were carried out on an Agilent 6120 bench-top single quadrupole, a Waters LCT Premier XE benchtop (oa-TOF) and a Thermo Exactive High-Resolution Orbitrap FTMS spectrometer. Fluorescence spectroscopic data were recorded using a Horiba Duetta fluorescence spectrophotometer, equipped with Peltier temperature controller and stirrer. Experiments were conducted at 25 °C unless otherwise stated. Vesicles were prepared as described below using Avestin "LiposoFast" extruder apparatus, equipped with polycarbonate membranes with 200 nm pores. GPC purification of vesicles was carried out using GE Healthcare PD-10 desalting columns prepacked with Sephadex G-25 medium.

5.1.2 Solvents, Reactants and Reagents

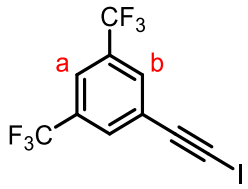
All reagents and solvents were purchased from commercial sources and used without further purification. Lipids were purchased from Avanti polar lipids and used without further purification. Where necessary, solvents were dried by passing through an MBraun MPSP-800 column and degassed with nitrogen. Column chromatography was carried out on Merck® silica gel 60 under a positive pressure of nitrogen. Where mixtures of solvents were used, ratios are reported by volume. TEA was distilled and stored over potassium hydroxide.

5.2 Synthetic Procedures

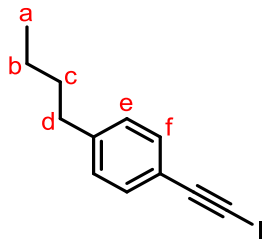
5.2.1 Synthesis of Novel Compounds for Chapter 2

Warning! Low molecular weight organic azides used in this study are potentially explosive and should be used on a small scale. Appropriate protective measures should always be taken when handling these compounds.

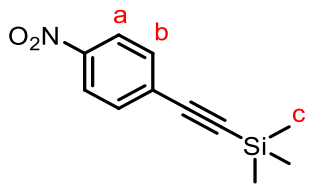
Alkyl-azides were prepared from the corresponding bromo-alkane and sodium azide according to standard literature procedures.[1] Tris[(1-benzyl-1H-1,2,3-triazol-4-yl)methyl]amine (TBTA) was prepared according to literature procedures.[2]



1-iodoethynyl-3,5-bis(trifluoromethyl)benzene 2.11. This known compound was prepared according to an adapted procedure: Under N_2, 3,5-bis(trifluoromethyl)benzene **2.10** (100 mg, 0.786 mmol) and KOH (110 mg, 1.97 mmol) were stirred in MeOH (2 mL) at 0 °C for 10 mins. Iodine (219 mg, 0.862 mmol) was added and the reaction mixture was allowed to warm to rt and stirred overnight. The reaction was diluted with water (20 mL) and the product was extracted with EtOAc (2 x 20 mL) to give a yellow oil of **2.11** (117 mg, 41%). Characterisation data aligns with the literature:[3] ^{1}H NMR (400 MHz, $CDCl_3$) δ 7.87 (s, $2H_b$), 7.81 (s, $1H_a$). HRMS-ESI (m/z) Calculated for $C_{10}H_3F_6I$-K^+: 402.9000; found 403.0000.

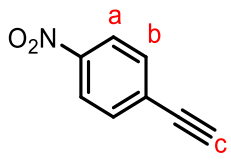


1-iodoethynyl-4-butylbenzene 2.13. Under N_2, 1-butyl-4-ethynyl benzene **2.12** (100 mg, 0.6329 mmol) and KOH (110 mg in 0.5 mL, 1.966 mmol) were stirred in MeOH at 0 °C for 10 mins. Iodine (176 mg, 0.6938 mmol) was added and the reaction mixture was allowed to warm to rt and stirred overnight. The reaction was diluted with water (20 mL) and the product was extracted with EtOAc (2 x 20 mL) to give a dark orange oil (150.1 mg, 84%). ^{1}H NMR (400 MHz, $CDCl_3$) δ 7.35 (d, *J* = 8.2 Hz, $2H_f$), 7.12 (d, *J* = 8.2 Hz, $2H_e$), 2.60 (t, *J* = 7.7 Hz, $2H_d$), 1.58 (quint, *J* = 7.6 Hz, $2H_c$), 1.34 (sext, *J* = 7.4 Hz, $2H_b$), 0.92 (t, *J* = 7.3 Hz, $3H_a$). ^{13}C NMR (126 MHz, $CDCl_3$) δ 144.15, 132.35, 128.48, 120.68, 94.43, 35.73, 33.47, 22.43, 14.06, 4.99. HRMS-ESI (m/z) Calculated for $C_{12}H_{13}I$-H^+: 285.0135; found: 285.0136.

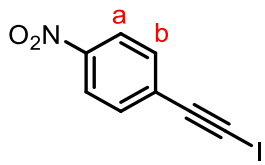


Trimethyl((4-nitrophenyl)ethynyl)silane 2.14. This known compound was prepared according to a modified literature procedure: Under N_2, TMS acetylene (197 mg, 2.01 mmol) was added to a stirred solution of 1-iodo-4-nitrobenzene (200 mg, 0.803 mmol), CuI (8.79 mg, 0.0803 mmol) and $Pd(PPh_3)_2Cl_2$ (28 mg, 0.40 mmol) in NEt_3 (3 mL). The reaction was sealed and stirred overnight at 85 °C. The reaction was diluted with EtOAc (5 mL) and filtered through Celite®. After flushing with copious EtOAc, the solvent was removed *in*

vacuo to afford a thick oil (110 mg, 93%). Characterisation data aligns with the literature:[4] ^{1}H NMR (400 MHz, $CDCl_3$) δ 8.17 (d, *J* = 8.18 Hz, $2H_a$), 7.59 (d, *J* = 7.82 Hz, $2H_b$), 0.27 (s, $9H_c$).



1-ethynyl-4-nitrobenzene 2.15. This known compound was prepared according to a modified literature procedure: To trimethyl((4-nitrophenyl)ethynyl)silane **2.14** (202 mg, 1.09 mmol) in MeOH (5 mL), an aqueous solution of KOH (0.48 M, 5.0 mL) was added and left to stir at rt for 1 hr. The crude product was dissolved in DCM (20 mL), washed with brine (2 x 10 mL), dried with $MgSO_4$ and the solvent was removed *in vacuo* to give the crude product. The residue was purified by silica gel flash chromatography (10% EtOAc in hexane) yielding a white solid (83 mg, 70%). Characterisation data aligns with the literature:[5] ^{1}H NMR (400 MHz, $CDCl_3$) δ 8.19 (dt, *J* = 8.86, 2.07 Hz, $2H_a$), 7.64 (dt, *J* = 8.87, 2.07 Hz, $2H_b$), 3.36 (s, $1H_c$).

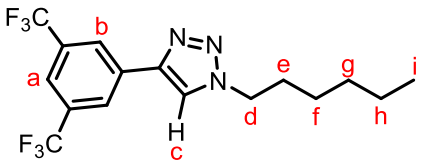


1-(iodoethynyl)-4-nitrobenzene 2.16. This known compound was prepared according to a modified literature procedure: Aqueous $AgNO_3$ (27 mg, 0.1596, 1 mL) was added to a solution of NIS (118 mg, 0.5240 mmol) and trimethyl((4-nitrophenyl)ethynyl)silane **2.14** (100 mg, 0.4560 mmol) in acetone (8 mL). The reaction was stirred in the dark at rt for 4 hrs then diluted with water (10 mL), the product was extracted with DCM (3 x 10 mL). The organic layer was washed with sat. $Na_2S_2O_3$ solution (2 x 10 mL), dried with $MgSO_4$ and the solvent

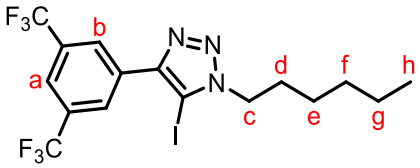
was removed *in vacuo* to yield a yellow solid (100 mg, 80%). Store in the freezer. ^{1}H NMR aligns with the literature:[4] ^{1}H NMR (400 MHz, $CDCl_3$) δ 8.19 (d, *J* = 8.26 Hz, $2H_a$), 7.58 (d, *J* = 7.95 Hz, $2H_b$). ^{13}C NMR and high-resolution mass spectrometry align with the literature.[4]

General click reaction procedure for the synthesis of acyclic triazole anionophores.

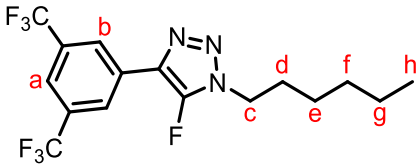
$Cu(CH_3CN)_4PF_6$ (25 mol%) and TBTA (25 mol%) were stirred in dry degassed THF, followed by the addition of iodo/proto-alkyne (concentration 0.025 mmol / mL) and alkyl azide (0.025 mmol / mL). This was stirred under N_2 for 48 hours. The solvent was removed *in vacuo,* and the residue dissolved in chloroform (20 mL). The organic mixture was washed with 10% aqueous EDTA/NH_4OH solution (2 x 10 mL), followed by brine (20 mL) and then dried over $MgSO_4$. The solvent was removed *in vacuo* to give the crude product. The residue was purified by silica gel flash chromatography (EtOAc in hexane).



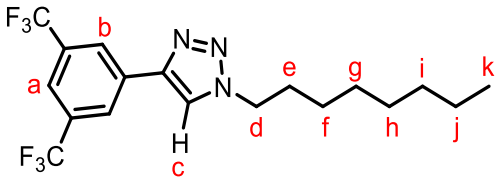
T2.1a. General click reaction procedure was used to react 1-ethynyl-3,5-bis(trifluoromethyl)benzene **2.10** (22.3 µL, 0.126 mmol) and hexyl azide **2.17** (16.0 mg, 0.126 mmol). In this case, an improved yield was obtained by using CuI (11.4 mg, 0.06 mmol) in place of $Cu(CH_3CN)_4PF_6$. Colourless oil, (39 mg, 84%). ^{1}H NMR (400 MHz, $CDCl_3$) δ 8.28 (s, $1H_c$), 7.91 (s, $2H_b$), 7.82 (s, $1H_a$), 4.43 (t, *J* = 7.2 Hz, $2H_d$), 1.97 (quint, *J* = 7.2 Hz, $2H_e$), 1.35 (m, $6H_{f\text{-}h}$), 0.89 (t, *J* = 7.2 Hz, 3 H_i). ^{13}C NMR (126 MHz, $CDCl_3$) δ 145.22, 133.02, 132.52, 132.26, 125.74, 125.71, 124.47, 122.30, 121.66, 121.62, 121.59, 120.56, 50.88, 31.27, 30.42, 26.28, 22.55, 14.08. HRMS-ESI (m/z) Calculated for $C_{16}H_{17}F_6N_3$-H^+: 366.1399; found: 366.1400.



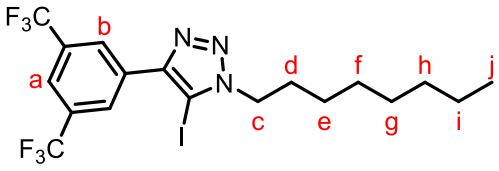
T2.1b. General click reaction procedure was used to react 1-iodoethynyl-3,5-bis(trifluoromethyl)benzene **2.11** (31 mg, 0.085 mmol) with hexyl azide **2.17** (11 mg, 0.085 mmol). Column chromatography (10% EtOAc in hexane) afforded the product as a white solid (29 mg, 68%). ^{1}H NMR (400 MHz, $CDCl_3$) δ 8.48 (s, $2H_b$), 7.90 (s, $1H_a$), 4.48 (t, *J* = 7.4 Hz, $2H_c$), 1.97 (quint, *J* = 7.4 Hz, $2H_d$), 1.36 (m, $6H_{e\text{-}g}$), 0.91 (t, *J* = 7.1 Hz, $3H_h$). ^{13}C NMR (126 MHz, $CDCl_3$) δ 147.06, 132.64, 132.25, 131.99, 127.35, 122.29, 122.15, 51.36, 31.29, 30.01, 26.21, 22.58, 14.11. HRMS-ESI (m/z) Calculated for $C_{16}H_{16}F_6IN_3$-H^+: 492.0366; found: 492.0364.



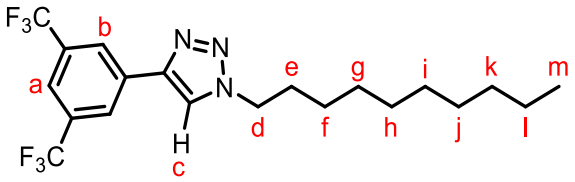
T2.1c. Under N_2, an aqueous solution of KF (25.4 mg, 0.4370 mmol, 4 mL) was added to a solution of carrier **T2.1b** (42.9 mg, 0.0974 mmol) dissolved in MeCN (4 mL). The mixture was allowed to react in a microwave reactor at 180 °C for 10 mins. The reaction mixture was diluted with chloroform (10 mL) and washed with water (2 x 10 mL), followed by brine (20 mL). After drying over $MgSO_4$, the solvent was removed *in vacuo* to give the crude product. Purification by preparative TLC (15% EtOAc in hexane) afforded the product as a white solid (9 mg, 24%). ^{1}H NMR (400 MHz, $CDCl_3$) δ 8.30 (s, 2H, H_b), 7.84 (s, $1H_a$), 4.33 (t, *J* = 7.2 Hz, 2H, H_c), 1.97 (quint, *J* = 7.2 Hz, $2H_d$), 1.36 (m, $6H_{e\text{-}g}$), 0.90 (t, *J* = 7.1 Hz, $3H_h$). ^{13}C NMR (126 MHz, $CDCl_3$) δ 132.49, 131.04, 125.13, 123.29, 121.60, 77.40, 77.35, 77.14, 76.89, 47.76, 31.16, 29.25, 26.19, 22.51, 14.05, 1.15. ^{19}F NMR (471 MHz, $CDCl_3$) δ -63.05 (6F), -150.35 (1F). HRMS-ESI (m/z) Calculated for $C_{16}H_{16}F_7N_3$-H^+: 384.1305; found: 384.2533.



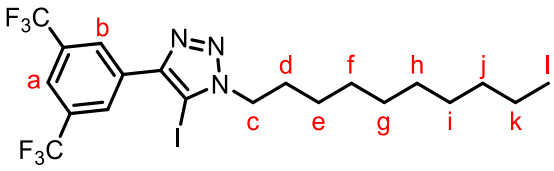
T2.2a. General click reaction procedure was used to react 1-ethynyl-3,5-bis(trifluoromethyl)benzene **2.10** (30 mg, 0.236 mmol) with octyl azide **2.18** (36 mg, 0.236 mmol). Product obtained as a pale yellow oil (40 mg, 43%). ^{1}H NMR (400 MHz, $CDCl_3$) δ 8.29 (s, 1H_c), 7.91 (s, 2H_b), 7.82 (s, 1H_a), 4.44 (t, *J* = 7.2 Hz, 2H_d), 1.97 (quint, *J* = 7.2 Hz, 2H_e), 1.36 – 1.26 (m, 10$H_{f\text{-}j}$), 0.87 (t, *J* = 6.9 Hz, 3H_k). ^{13}C NMR (126 MHz, $CDCl_3$) δ 145.20, 133.04, 132.78, 132.52, 132.25, 131.99, 125.75, 125.72, 125.69, 125.66, 124.46, 122.29, 121.63, 121.60, 121.57, 120.57, 50.87, 31.82, 30.44, 29.15, 29.07, 26.60, 22.71, 14.16. HRMS-ESI (m/z) Calculated for $C_{18}H_{21}F_6N_3$-H^+: 394.1712; found: 394.1711.



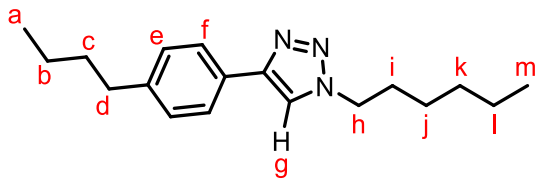
T2.2b. General click reaction procedure was used to react 1-iodoethynyl-3,5-bis(trifluoromethyl)benzene **2.11** (30 mg, 0.083 mmol) with octyl azide **2.18** (13 mg, 0.083 mmol). Column chromatography (15% EtOAc in hexane) afforded the product as a white solid (19 mg, 44%). ^{1}H NMR (400 MHz, $CDCl_3$) δ 8.48(s, 2Hb), 7.90 (s, 1H_a), 4.47 (t, J = 7.4 Hz, 2H_c), 1.97 (quint, *J* = 7.4 Hz, 2H_d), 1.39 – 1.28 (m, 10$H_{e\text{-}i}$), 0.88 (t, *J* = 7.0 Hz, 3H_j). ^{13}C NMR (126 MHz, $CDCl_3$) δ 147.06, 132.65, 132.53, 132.26, 131.99, 131.73, 127.38, 127.35, 126.63, 124.46, 122.29, 122.18, 122.14, 122.11, 122.08, 120.12, 51.36, 31.85, 31.73, 31.08, 30.03, 29.85, 29.18, 29.09, 26.53, 22.80, 22.75, 14.26, 14.21, 1.16. HRMS-ESI (m/z) Calculated for $C_{18}H_{20}F_6IN_3$-H^+: 512.0679; found: 520.0682.



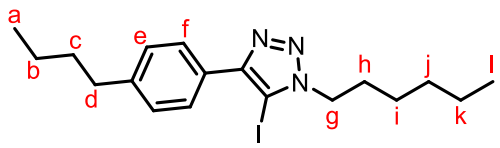
T2.3a. General click reaction procedure was used to react 1-ethynyl-3,5-bis(trifluoromethyl)benzene **2.10** (25.0 mg, 0.196 mmol) with decyl azide **2.19** (35.8 mg, 0.196 mmol). Column chromatography (10% EtOAc in hexane) afforded the product as a colourless oil (43 mg, 52%). ^{1}H NMR (400 MHz, $CDCl_3$) δ 8.29 (s, $1H_c$), 7.90 (s, $1H_a$), 7.82 (s, $2H_b$), 4.44 (t, *J* = 7.2 Hz, $2H_d$), 1.97 (quint, *J* = 7.2 Hz, $2H_e$), 1.36 – 1.26 (m, $14H_{f\text{-}l}$), 0.87 (t, *J* = 7.1 Hz, $3H_m$). ^{13}C NMR (126 MHz, $CDCl_3$) δ 145.21, 133.02, 132.79, 132.52, 132.26, 131.99, 126.63, 125.73, 125.70, 124.46, 122.30, 121.65, 121.62, 121.59, 120.56, 120.13, 50.89, 31.98, 30.45, 29.59, 29.50, 29.38, 29.11, 26.60, 22.79, 14.23. HRMS-ESI (m/z) Calculated for $C_{20}H_{25}F_6N_3$-H^+: 422.2025; found: 422.2022.



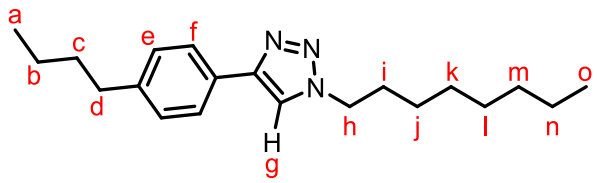
T2.3b. General click reaction procedure was used to react 1-iodoethynyl-3,5-bis(trifluoromethyl)benzene **2.11** (32 mg, 0.088 mmol) with decyl azide **2.19** (16 mg, 0.088 mmol). Column chromatography (20% EtOAc in hexane) afforded the product as a white solid (48 mg, 65%). ^{1}H NMR (400 MHz, $CDCl_3$) δ 8.48 (s, $2H_b$), 7.90 (s, $1H_a$), 4.47 (t, *J* = 7.4 Hz, $2H_c$), 1.97 (quint, *J* = 7.3 Hz, $2H_d$), 1.37 – 1.27 (m, $14H_{e\text{-}k}$), 0.88 (t, *J* = 6.7 Hz, $3H_l$). ^{13}C NMR (126 MHz, $CDCl_3$) δ 147.05, 132.65, 132.52, 132.26, 131.99, 131.72, 127.37, 124.46, 122.29, 122.15, 77.42, 77.37, 77.16, 76.91, 51.36, 32.00, 30.04, 29.61, 29.53, 29.41, 29.14, 26.53, 22.81, 14.25. HRMS-ESI (m/z) Calculated for $C_{20}H_{24}F_6IN_3$-H^+: 548.0989; found: 548.0989.



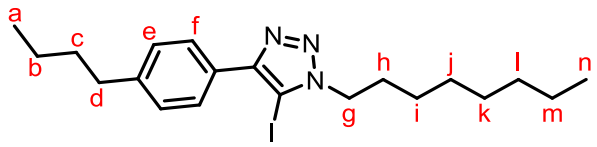
T2.4a. General click reaction procedure was used to react 1-butyl-4-ethynyl benzene **2.12** (40 mg, 0.25 mmol) with hexyl azide **2.17** (32 mg, 0.25 mmol). In this case, an improved yield was obtained by using CuI (24 mg, 0.13 mmol) in place of $Cu(CH_3CN)_4PF_6$. Column chromatography (20% EtOAc in hexane) afforded the product as a white solid (61 mg, 85%). ^{1}H NMR (500 MHz, $CDCl_3$) δ 7.73 (dt, *J* = 8.2 Hz, *J* = 1.7 Hz, $2H_f$), 7.70 (s, $1H_g$), 7.23 (dt, *J* = 8.2 Hz, *J* = 1.9 Hz, $2H_e$), 4.38, (t, *J* = 7.2 Hz, $2H_h$), 2.63, (t, *J* = 7.8 Hz, $2H_d$), 1.94, (quint, *J* = 7.4 Hz, $2H_i$), 1.62, (m, $4H_{c,d}$), 1.33, (m, $6H_{j-l}$), 0.93, (t, *J* = 7.4 Hz, $3H_m$), 0.88. (t, *J* = 7.1 Hz, $3H_a$). ^{13}C NMR (126 MHz, $CDCl_3$) δ 147.98, 143.11, 129.02, 128.27, 125.75, 119.16, 50.54, 35.58, 33.71, 31.32, 30.48, 26.32, 22.58, 22.48, 14.10. HRMS-ESI (m/z) Calculated for $C_{18}H_{27}N_3$-H^+: 286.2278; found: 286.2277.



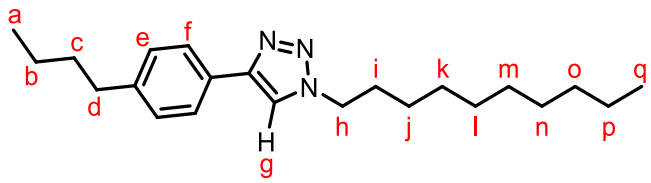
T2.4b. General click reaction procedure was used to react 1-butyl-4-(iodoethynyl)benzene **2.13** (30.0 mg, 0.106 mmol) with hexyl azide **2.17** (13.4 mg, 0.106 mmol). Column chromatography (10% EtOAc in hexane) afforded the product as an off-white solid (27 mg, 62%). ^{1}H NMR (400 MHz, $CDCl_3$) δ 7.84 (d, *J* = 7.5 Hz, $2H_f$), 7.27 (d, $2H_e$), 4.43 (t, *J* = 7.4 Hz, $2H_g$), 2.66 (t, *J* = 7.9 Hz, $2H_d$), 1.95 (quint, *J* = 7.1 Hz, $2H_h$), 1.63 (quint, *J* = 7.5 Hz, $2H_c$), 1.35 (m, $8H_{d,i-k}$), 0.94 (t, *J* = 7.2 Hz, $3H_a$), 0.90 (t, *J* = 6.6 Hz, $3H_l$). ^{13}C NMR (126 MHz, $CDCl_3$) δ 149.90, 143.55, 128.72, 127.83, 127.48, 51.09, 35.63, 33.64, 31.33, 30.07, 26.25, 22.60, 22.51, 14.11. HRMS-ESI (m/z) Calculated for $C_{18}H_{26}IN_3$-H^+: 412.1244; found: 412.1240.



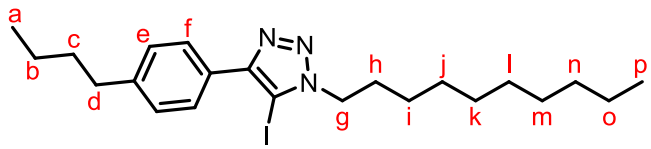
T2.5a. General click reaction procedure was used to react 1-butyl-4-ethynyl benzene **2.12** (40 mg, 0.25 mmol) with octyl azide **2.18** (40 mg, 0.25 mmol). Column chromatography (15% EtOAc in hexane) afforded the product as a white solid (63 mg, 79%). ^{1}H NMR (400 MHz, $CDCl_3$) δ 7.73 (d, *J* = 7.6 Hz, $2H_f$), 7.70 (s, $1H_g$), 7.23 (d, *J* = 7.6 Hz, $2H_e$), 4.38 (t, *J* = 7.1 Hz, $2H_h$), 2.63 (t, *J* = 7.7 Hz, $2H_d$), 1.94 (quint, *J* = 6.9 Hz, $2H_i$), 1.60 (m, $2H_c$), 1.34 – 1.26 (m, $12H_{b,j\text{-}n}$), 0.93 (t, *J* = 7.3 Hz, $3H_a$), 0.87 (t, *J* = 6.1 Hz, $3H_o$). ^{13}C NMR (126 MHz, $CDCl_3$) δ 147.97, 143.10, 129.02, 128.27, 125.74, 119.19, 50.55, 35.58, 33.72, 31.86, 30.52, 29.21, 29.13, 26.65, 22.75, 22.48, 14.21, 14.11. HRMS-ESI (m/z) Calculated for $C_{20}H_{31}N_3$-H^+: 314.2591; found: 314.2591.



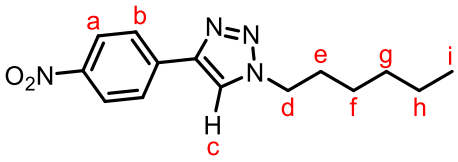
T2.5b. General click reaction procedure was used to react 1-butyl-4-(iodoethynyl)benzene **2.13** (30.0 mg, 0.106 mmol) with octyl azide **2.18** (16.0 mg, 0.106 mmol). Purification by preparative TLC (20% EtOAc in hexane) afforded the product as an off-white solid (32 mg, 69%). ^{1}H NMR (400 MHz, $CDCl_3$) δ 7.84 (dd, ^{3}J = 8.3 Hz, ^{4}J = 4.6 Hz, $2H_f$), 7.28 (dd, $2H_e$), 4.43 (t, *J* = 7.4 Hz, $2H_g$), 2.66 (t, *J* = 7.7 Hz, $2H_d$), 1.95 (quint, *J* = 7.4 Hz, $2H_h$), 1.64 (quint, *J* = 7.6 Hz, $2H_c$), 1.37 – 1.28 (m, $12H_{b,i\text{-}m}$), 0.94 (t, *J* = 7.35 Hz, $3H_a$), 0.88 (t, *J* = 6.9 Hz, $3H_n$). ^{13}C NMR (126 MHz, $CDCl_3$) δ 147.97, 143.10, 129.02, 128.27, 125.74, 119.19, 50.55, 35.58, 33.72, 31.86, 30.52, 29.21, 29.13, 26.65, 22.75, 22.48, 14.21, 14.11. HRMS-ESI (m/z) Calculated for $C_{20}H_{30}IN_3$-H^+: 440.1557; found: 440.1556.



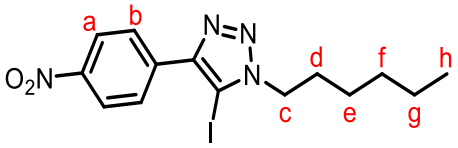
T2.6a. General click reaction procedure was used to react 1-butyl-4-ethynyl benzene **2.12** (30 mg, 0.19 mmol) with decyl azide **2.19** (34.8 mg, 0.190 mmol). Column chromatography (20% EtOAc in hexane) afforded the product as a white solid (29 mg, 44%). ^{1}H NMR (400 MHz, $CDCl_3$) δ 7.73 (dt, *J* = 8.2 Hz, *J* = 1.9 Hz, $2H_f$), 7.70 (s, $1H_g$), 7.23 (d, *J* = 8.2 Hz, $2H_e$), 4.38 (t, *J* = 7.2 Hz, $2H_h$), 2.63 (t, *J* = 7.7 Hz, $2H_d$), 1.94 (quint, *J* = 7.2 Hz, $2H_i$), 1.62 (quint, *J* = 7.6 Hz, $2H_c$), 1.34 – 1.25 (m, $16H_{b,j-p}$), 0.93 (t, *J* = 7.4 Hz, $3H_a$), 0.87 (t, *J* = 6.9 Hz, $3H_q$). ^{13}C NMR (126 MHz, $CDCl_3$) δ 147.95, 143.07, 128.98, 128.26, 125.72, 119.15, 50.52, 35.55, 33.68, 31.97, 30.48, 29.59, 29.51, 29.37, 29.14, 26.62, 22.78, 22.45, 14.22, 14.07. HRMS-ESI (m/z) Calculated for $C_{22}H_{35}N_3$-H^+: 342.2904; found: 342.2901



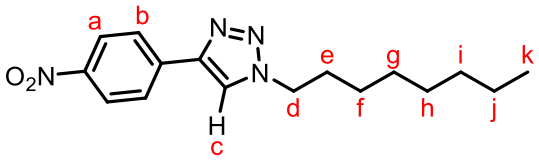
T2.6b. General click reaction procedure was used to react 1-butyl-4-(iodoethynyl)benzene **2.13** (30.0 mg, 0.106 mmol) with decyl azide **2.19** (19.3 mg, 0.106 mmol). Column chromatography (20% EtOAc in hexane) afforded the product as a white solid (32 mg, 63%). ^{1}H NMR (400 MHz, $CDCl_3$) δ 7.84 (d, *J* = 7.7 Hz, $2H_f$), 7.27 (d, *J* = 8.0 Hz, $2H_e$), 4.43 (t, *J* = 7.3 Hz, $2H_g$), 2.66 (t, *J* = 7.6 Hz, $2H_d$), 1.95 (quint, *J* = 7.1 Hz, $2H_h$), 1.63 (m, $2H_c$), 1.37 – 1.26 (m, $16H_{b,i-o}$), 0.94 (t, *J* = 7.3 Hz, $3H_a$), 0.88 (t, *J* = 6.0 Hz, $3H_p$). ^{13}C NMR (126 MHz, $CDCl_3$) δ 149.87, 143.52, 128.69, 127.80, 127.46, 75.82, 51.06, 35.60, 33.61, 31.99, 30.07, 29.60, 29.52, 29.40, 29.15, 26.54, 22.79, 22.48, 14.23, 14.08. HRMS-ESI (m/z) Calculated for $C_{22}H_{34}IN_3$-H^+: 468.1870; found: 468.1868.



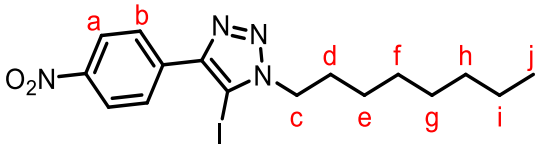
T2.7a. General click reaction procedure was used to react 1-ethynyl-4-nitrobenzene **2.15** (30 mg, 0.19 mmol) with hexyl azide **2.17** (24 mg, 0.19 mmol). Preparative TLC (20% EtOAc in hexane) afforded the product as a pale yellow solid (26 mg, 50%). ^{1}H NMR (400 MHz, $CDCl_3$) δ 8.29 (dt, *J* = 8.9, *J* = 2.1 Hz, $2H_a$), 8.00 (dt, *J* = 9.0, *J* = 2.2 Hz, $2H_b$), 7.89 (s, $1H_c$), 4.44 (t, *J* = 7.3 Hz, $2H_d$), 1.97 (m, *J* = 7.3 Hz, $2H_e$), 1.35 (m, $6H_{f\text{-}h}$), 0.89. (t, *J* = 7.1 Hz, $3H_i$). ^{13}C NMR (126 MHz, $CDCl_3$) δ 147.37, 145.67, 137.14, 126.21, 124.44, 121.04, 50.81, 31.25, 30.40, 26.27, 22.53, 14.06. HRMS-ESI (m/z) Calculated for $C_{14}H_{18}N_4O_2$-H^+: 275.1503; found: 275.1502.



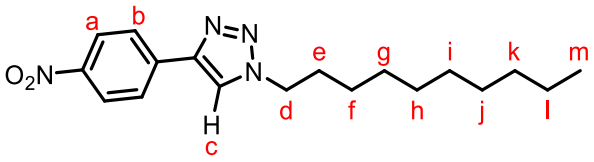
T2.7b. General click reaction procedure was used to react 1-(iodoethynyl)-4-nitrobenzene **2.16** (40.0 mg, 0.147 mmol) with hexyl azide **2.17** (18.7 mg, 0.147 mmol). Column chromatography (10% EtOAc in hexane) afforded the product as a yellow solid (27 mg, 47%). ^{1}H NMR (400 MHz, $CDCl_3$) δ 8.33 (d, *J* = 8.2 Hz, $2H_a$), 8.20 (d, *J* = 8.2 Hz, $2H_b$), 4.47 (t, *J* = 7.3 Hz, $2H_c$), 1.97 (quint, *J* = 7.1 Hz, $2H_d$), 1.35 (m, $6H_{e\text{-}g}$), 0.90 (m, $3H_h$). ^{13}C NMR (126 MHz, $CDCl_3$) δ 147.37, 145.67, 137.14, 126.21, 124.44, 121.04, 50.81, 31.25, 30.40, 26.27, 22.53, 14.06. HRMS-ESI (m/z) Calculated for $C_{14}H_{17}IN_4O_2$-H^+: 401.0469; found: 401.0467.



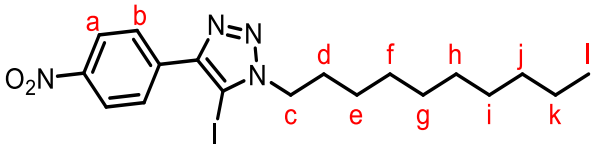
T2.8a. General click reaction procedure was used to react 1-ethynyl-4-nitrobenzene **2.15** (30 mg, 0.19 mmol) with octyl azide **2.18** (29.4 mg, 0.190 mmol). Column chromatography (10% EtOAc in hexane) afforded the product as a yellow solid (32 mg, 56%). ^{1}H NMR (400 MHz, $CDCl_3$) δ 8.29 (dt, *J* = 8.9, *J* = 2.2 Hz, $2H_a$), 8.01 (dt, *J* = 8.9, *J* = 2.2 Hz, $2H_b$), 7.89 (s, $1H_c$), 4.43 (t, *J* = 7.26 Hz, $2H_d$), 1.97 (quint, *J* = 7.3 Hz, $2H_e$), 1.36 – 1.27 (m, $10H_{f\text{-}j}$), 0.87 (t, *J* = 6.9 Hz, $3H_k$). ^{13}C NMR (126 MHz, $CDCl_3$) δ 147.38, 145.67, 137.15, 126.22, 124.45, 121.05, 50.83, 31.82, 30.44, 29.16, 29.07, 26.61, 22.72, 14.19. HRMS-ESI (m/z) Calculated for $C_{16}H_{22}N_4O_2$-H^+: 303.1816; found: 303.1814.



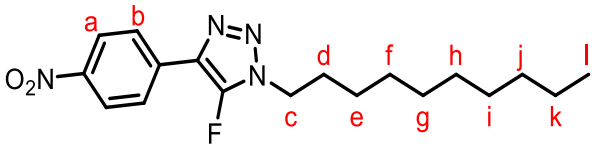
T2.8b. General click reaction procedure was used to react 1-(iodoethynyl)-4-nitrobenzene **2.16** (40.0 mg, 0.147 mmol) with octyl azide **2.18** (22.8 mg, 0.147 mmol). The product was purified by column chromatography (15% EtOAc in hexane) to give a dark yellow solid (29 mg, 46%). ^{1}H NMR (400 MHz, $CDCl_3$) δ 8.33 (d, *J* = 8.3 Hz, $2H_a$), 8.20 (d, *J* = 8.3 Hz, $2H_b$), 4.47 (t, *J* = 7.4 Hz, $2H_c$), 1.97 (m, $2H_d$), 1.39 – 1.28 (m, $10H_{e\text{-}i}$), 0.88 (m, $3H_j$). ^{13}C NMR (126 MHz, $CDCl_3$) δ 147.39, 145.67, 137.16, 126.22, 124.44, 121.04, 50.83, 31.82, 30.44, 29.15, 29.07, 26.61, 22.71, 14.18. HRMS-ESI (m/z) Calculated for $C_{16}H_{21}IN_4O_2$-H^+: 429.0782; found: 429.0780.



T2.9a. General click reaction procedure was used to react 1-ethynyl-4-nitrobenzene **2.15** (25 mg, 0.17 mmol) with decyl azide **2.19** (31 mg, 0.17 mmol). The product was purified by column chromatography (3% EtOAc in hexane) to give a pale yellow solid (34.5 mg, 62%). ^{1}H NMR (400 MHz, $CDCl_3$) δ 8.29 (dt, *J* = 8.9 Hz, *J* = 2.1 Hz, $2H_a$), 8.00 (dt, *J* = 8.9 Hz, *J* = 2.1 Hz, $2H_b$), 7.89 (s, $1H_c$), 4.43 (t, *J* = 7.3 Hz, $2H_d$), 1.97 (quint, *J* = 7.3 Hz, $2H_e$), 1.36 – 1.26 (m, $14H_{f-l}$), 0.87 (t, *J* = 6.8 Hz, $3H_m$). ^{13}C NMR (126 MHz, $CDCl_3$) δ 147.38, 145.67, 137.16, 126.22, 124.45, 121.07, 50.84, 31.97, 30.45, 29.59, 29.50, 29.37, 29.11, 26.61, 22.79, 14.24. HRMS-ESI (m/z) Calculated for $C_{18}H_{26}N_4O_2$-H^+: 331.2129; found: 331.2129.



T2.9b. General click reaction procedure was used to react 1-(iodoethynyl)-4-nitrobenzene **2.16** (25 mg, 0.09 mmol) with decyl azide **2.19** (17 mg, 0.09 mmol). The product was purified by column chromatography (10% EtOAc in hexane) to give the pure yellow solid (60.9 mg, 73%). ^{1}H NMR (400 MHz, $CDCl_3$) δ 8.33 (d, *J* = 8.8 Hz, $2H_a$), 8.20 (d, *J* = 9.0 Hz, $2H_b$), 4.47 (t, *J* = 7.4 Hz, $2H_c$), 1.97 (quint, *J* = 7.2 Hz, $2H_d$), 1.38 – 1.27 (m, $14H_{e-k}$), 0.88 (t, *J* = 6.7 Hz, $3H_l$). ^{13}C NMR (126 MHz, $CDCl_3$) δ 147.68, 147.56, 136.84, 127.97, 124.04, 51.34, 32.00, 30.03, 29.61, 29.52, 29.40, 29.13, 26.54, 22.80, 14.25. HRMS-ESI (m/z) Calculated for $C_{18}H_{25}IN_4O_2$-H^+: 457.1095; found: 457.1095.



T2.9c. Under N_2, an aqueous solution of KF (40 mg, 0.69 mmol, 4 mL) was added to a solution of **T2.9b** (63 mg, 0.14 mmol) dissolved in MeCN (4 mL). The mixture was allowed to react in a microwave reactor at 180 °C for 6 mins. The reaction mixture was diluted with chloroform (10 mL) and washed with water (2 x 10 mL), followed by brine (20 mL). After drying over $MgSO_4$, the solvent was removed *in vacuo* to give the crude product. Preparative TLC (1:1 EtOAc in hexane) afforded the product as a white solid (25.2 mg, 52%). ^{1}H NMR (400 MHz, $CDCl_3$) δ 8.31 (d, *J* = 8.9 Hz, $2H_a$), 8.02 (d, *J* = 8.9 Hz, $2H_b$), 4.31 (t, *J* = 7.2 Hz, $2H_c$), 1.96 (quint, *J* = 7.2 Hz, $2H_d$), 1.36 – 1.25 (m, $14H_{e-k}$), 0.87 (t, *J* = 6.9 Hz, $3H_l$). ^{13}C NMR (126 MHz, $CDCl_3$) δ 150.63, 147.23, 135.15, 125.69, 125.07, 124.46, 47.71, 31.97, 29.57, 29.47, 29.36, 29.30, 29.01, 26.53, 22.78, 14.23. ^{19}F NMR (471 MHz, $CDCl_3$) δ -149.72 (CF-triazole). HRMS-ESI (m/z) Calculated for $C_{18}H_{25}FN_4O_2$-H^+: 349.2034; found: 349.2033.

5.2.2 Synthesis of Novel Compounds for Chapter 3

Tris[(1-benzyl-1H-1,2,3-triazol-4-yl)methyl]amine (TBTA),[2] 1,3-diethynylnitrobenzene **3.14**,[6] 1,3,5-tris(trimethylsilylethynyl)benzene **3.19**,[7] 1,3,5-triethynylbenzene **3.20**,[7] 1,3,5-tris(iodoethynyl)benzene **3.21**,[8] azido-pentafluorobenzene **3.22**,[9] 1-azido-3,5-bis(trifluoromethyl)benzene **3.23**[10] and 1-azido-4-nitrobenzene **3.24**[11,10] were prepared according to literature procedures. Preparation of silver acetylide intermediates **3.7** and **3.16** (general procedure 2) were conducted via a reported procedure.[12]

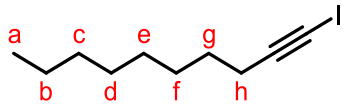
General Procedure 1

$Cu(CH_3CN)_4PF_6$ (0.1 equivalents per alkyne) and TBTA (0.1 equivalents per alkyne) were stirred in anhydrous degassed DCM (ca. 5 mL per 0.30 mmol of alkyne) for 10 minutes under a nitrogen atmosphere, followed by the addition of iodo/proto-alkyne and aryl azide (1.5 equivalents per alkyne) and left to stir overnight. The reaction mixture was diluted with DCM (ca. 50 mL) and the organic phase washed with 10% aqueous EDTA/NH_4OH solution (2 x 10 mL), followed by brine (20 mL) and subsequently dried over $MgSO_4$. The solvent was removed *in vacuo* to give the crude product. The residue was purified by silica gel flash chromatography using either DCM/MeOH or DCM/EtOAc mixtures as the eluent.

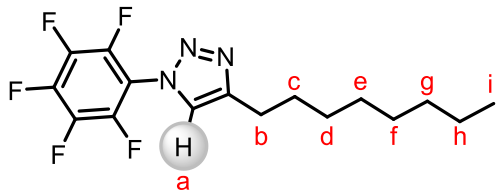
General Procedure 2

The appropriate alkyne (0.30 mmol) was dissolved in the minimum amount of MeOH (ca. 10 mL per 0.30 mmol of alkyne) to which was added $AgNO_3$ (1 equivalent per alkyne) followed by concentrated NH_4OH (0.1 mL) immediately inducing precipitation of the desired silver acetylide. The reaction mixture was left to stir for 30 mins at rt, after which the solvent was removed *in vacuo*. The silver acetylide was subsequently suspended in

anhydrous THF (20 mL) under an atmosphere of nitrogen. In a separate flask Me_2Te_2 (**3.8**) (0.50 equivalents per alkyne) was dissolved in THF (5 mL) and cooled to 0 °C, to the solution of the ditelluride 1 M of Br_2 in DCM (0.50 equivalents per alkyne) was added dropwise, after which time the ditelluride solution darkened indicating the formation of MeTeBr (**3.9**) which was added immediately to the suspension of the silver acetylide dropwise. The reaction mixture was left to stir for 30 mins at rt in the absence of light, after which time it was filtered through Celite® and the reaction mixture was concentrated to dryness *in vacuo*. The crude telluromethyl alkyne was then used immediately for the following CuAAC reaction.

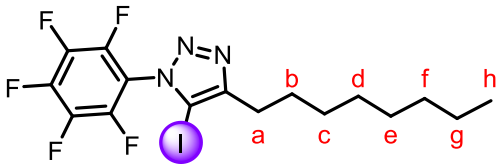


Iododecyne 3.5. Under N_2, decyne (3.623 mmol) and KOH (9.058 mmol) were stirred in MeOH for 10 mins, followed by the addition of I_2 (3.986 mmol). This was stirred at rt for 48 hrs. The reaction was diluted with water and extracted with EtOAc (20 mL). The organic mixture was washed with saturated $Na_2S_2O_3$ solution (2 x 10 mL), followed by brine (20 mL) and then dried over $MgSO_4$. The solvent was removed *in vacuo* to give the pure product (quant.). ^{1}H NMR (400 MHz, $CDCl_3$) δ 2.35 (t, *J* = 7.1 Hz, $2H_h$), 1.51 (m, $2H_g$), 1.36-1.28 (m, $8H_{c\text{-}f}$), 0.88 (t, *J* = 6.9 Hz, $3H_a$). Full characterisation data aligns with the literature.[13]

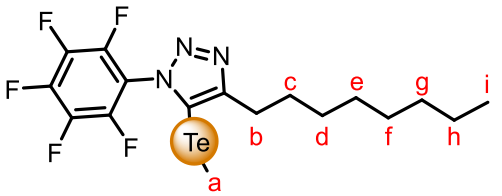


T3.1a. Synthesised according to General Procedure 1 with 1-decyne **3.5** (50 mg, 0.362 mmol) and pentafluorobenzene azide **3.22**. The product was purified by column chromatography (30% EtOAc in hexane) to give a white solid (73.2 mg, 0.211 mmol, 46%).

^{1}H NMR (400 MHz, $CDCl_3$) δ 7.55 (s, 1H_a), 2.82 (t, *J* = 7.7 Hz, 2H_b), 1.75 (quint, *J* = 7.5 Hz, 2H_c), 1.40-1.28 (m, 10H_{d-h}), 0.88 (t, *J* = 6.8 Hz, 3H_i). ^{19}F NMR (471 MHz, $CDCl_3$) δ -145.70 (m), -150.67 (m), -159.73 (m). ^{13}C NMR (126 MHz, $CDCl_3$) δ 149.12, 142.51, 142.19, 138.18, 123.09, 113.41, 31.96, 29.42- 29.25, 25.61, 22.78, 14.21. HRMS-ESI (m/z) Calculated for $C_{16}H_{19}N_3F_5$-H^+:348.1491; found: 348.1494.

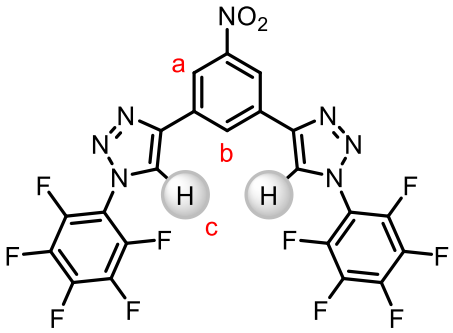


T3.1b. Synthesised according to General Procedure 1 with iododecyne **3.6** (120 mg, 0.454 mmol) and pentafluorobenzene azide **3.22**. The product was purified by column chromatography (30% EtOAc in hexane) to give a white solid (43.7 mg, 0.0923 mmol, 49%). ^{1}H NMR (400 MHz, $CDCl_3$) δ 2.75 (t, *J* = 7.7 Hz, 2H_a), 1.78 (quint, *J* = 7.5 Hz, 2H_b), 1.37-1.28 (m, 10H_{c-g}), 0.89 (t, *J* = 6.9 Hz, 3H_h). ^{19}F NMR (376 MHz, $CDCl_3$) δ -142.32 – -143.12 (m), -147.98 (tt, *J* = 21.4, 3.3 Hz), -159.19 – -159.85 (m). ^{13}C NMR (126 MHz, $CDCl_3$) δ 143.68, 143.33, 138.05, 31.98, 29.39, 29.32, 29.29, 28.87, 26.27, 22.80, 14.25. HRMS-ESI (m/z) Calculated for $C_{16}H_{18}N_3F_5I$-H^+:474.0457; found: 474.0460.

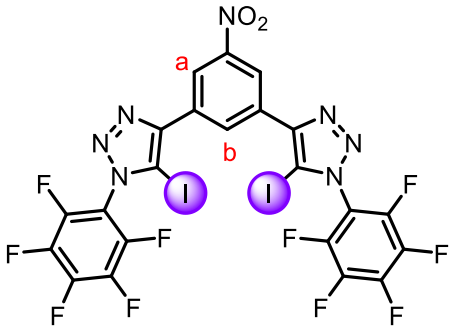


T3.1c. Synthesised according to General Procedure 2 from 1-decyne **3.5** (200 mg, 1.45 mmol) to afford the telluromethyl appended alkyne **3.10**, which was subsequently used immediately in a CuAAC reaction with pentafluorobenzene azide **3.22** according to General

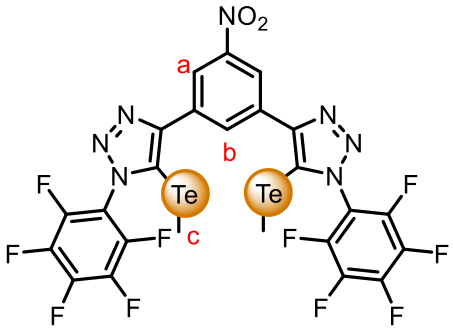
Procedure 1 to afford **T3.1c** (362 mg 0.740 mmol, 51%) as a yellow solid. ^{1}H NMR (500 MHz, $CDCl_3$) δ 2.93 – 2.86 (m, $2H_b$), 1.93 (s, $3H_a$), 1.80 (p, *J* = 7.6 Hz, $2H_c$), 1.47 – 1.21 (m, $10H_{d\text{-}h}$), 0.95 – 0.83 (m, $3H_i$). ^{19}F NMR (470 MHz, $CDCl_3$) δ -143.32 – -143.95 (m), -148.81 – -149.25 (m), -159.66 – -160.40 (m). ^{13}C NMR (126 MHz, $CDCl_3$) δ 157.62, 143.99 (dm, *J* = 217 Hz), 137.54 (dm, *J* = 268 Hz), 114.22, 104.57, 32.01, 30.01, 29.50, 29.48, 29.35, 27.33, 22.82, 14.25, -13.19, -14.01. HRMS-ESI (m/z) Calculated for $C_{17}H_{21}N_3F_5Te\text{-}H^+$: 492.0710; found: 492.0713.



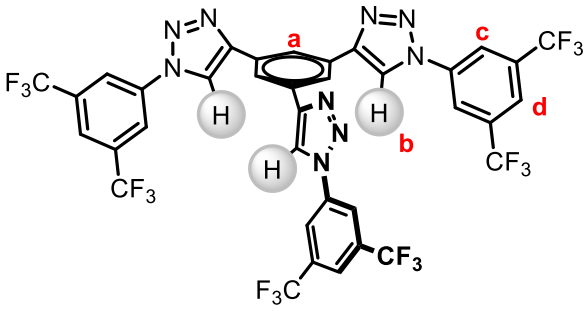
T3.2a. Synthesised according to General Procedure 1 from 1,3-diethynyl-5-nitrobenzene (71 mg, 0.411 mmol) and pentafluorobenzene azide **3.22** to yield carrier **T3.2a** as a white solid (126 mg, 0.214 mmol, 52%). ^{1}H NMR (500 MHz, DMSO) δ 9.51 (s, $2H_c$), 8.99 (t, *J* = 1.5 Hz, $1H_b$), 8.78 (d, *J* = 1.5 Hz, $2H_a$). ^{19}F NMR (470 MHz, DMSO) δ -146.74 – -147.52 (m), -150.65 – -151.27 (m), -160.45 – -161.21 (m). ^{13}C NMR (126 MHz, DMSO) δ 149.19, 144.89, 141.95 (dm, *J* = 255 Hz), 137.74 (dm, *J* = 253 Hz), 131.93, 127.96, 126.07, 119.83, 112.36 (m). HRMS-ESI (m/z) Calculated for $C_{22}H_6O_2N_7F_{10}\text{-}H^+$: 590.0415; found: 590.0418.



T3.2b. 1,3-diethynyl-5-nitrobenzene **3.14** (100 mg, 0.584 mmol) was dissolved in anhydrous THF to which was added CuI (11 mg, 0.0583 mmol) and *N*-iodomorpholine hydroiodide (656 mg, 1.93 mmol) and left to stir for 4 hrs in the absence of light. After which time the reaction mixture was diluted with DCM (300 mL) and filtered through a DCM saturated pad of alumina, the filtrate was concentrated *in vacuo* and adsorbed onto silica. The dry loaded compound was eluted with 10% EtOAC/hexane mixtures (500 mL) and the filtrate concentrated to dryness *in vacuo*. The iodoalkyne **3.15** was isolated as a yellow solid in 83% yield and then immediately used in a CuAAC reaction with pentafluorobenzene azide **3.22** according to general procedure 1, to yield carrier **T3.2b** (428 mg, 0.509 mmol, 87%) as an off white solid. ^{1}H NMR (500 MHz, $CDCl_3$) δ 9.20 (t, *J* = 1.6 Hz, $1H_b$), 9.07 (d, *J* = 1.6 Hz, $2H_a$). ^{19}F NMR (470 MHz, $CDCl_3$) δ -142.18 (m), -146.09 – -146.76 (m), -158.38 – -158.93 (m). ^{13}C NMR (126 MHz, $CDCl_3$) δ 149.00, 148.15, 143.83 (dm, *J* = 262 Hz), 138.21 (dm, *J* = 263 Hz), 131.79, 131.30, 122.31, 112.74 – 111.51 (m), 81.64, 29.84. HRMS-ESI (m/z) Calculated for $C_{22}H_4O_2N_7F_{10}I_2$-H^+: 841.8337; found: 841.8351.

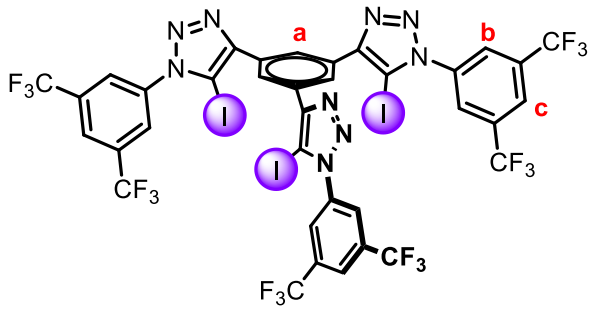


T3.2c. Synthesised according to General Procedure 2 from 1,3-diethynyl-5-nitrobenzene **3.14** (200 mg, 1.17 mmol) to afford the tellluromethyl appended alkyne **3.17**, which was subsequently used immediately in a CuAAC reaction with pentafluorobenzene azide **3.22** according to General Procedure 1 to afford **T3.2c** (695 mg 0.796 mmol, 68%) as a yellow solid. ^{1}H NMR (500 MHz, $CDCl_3$) δ 9.36 (t, *J* = 1.6 Hz, 1H_b), 9.16 (d, *J* = 1.6 Hz, 2H_a), 2.10 (s, 6H_c). ^{19}F NMR (470 MHz, $CDCl_3$) δ -142.72 – -143.58 (m), -147.32 – -14.14 (m), -158.92 – -159.65 (m). ^{13}C NMR (126 MHz, $CDCl_3$) δ 151.52, 148.94, 143.89 (dm, *J* = 253 Hz), 138.14 (dm, *J* = 267 Hz), 132.80, 132.74, 12262, 113.44 (m), 103.77, -12.55. HRMS-ESI (m/z) Calculated for $C_{24}H_{10}O_2N_7F_{10}Te_2$-$H^+$:875.8832; found: 875.8838.

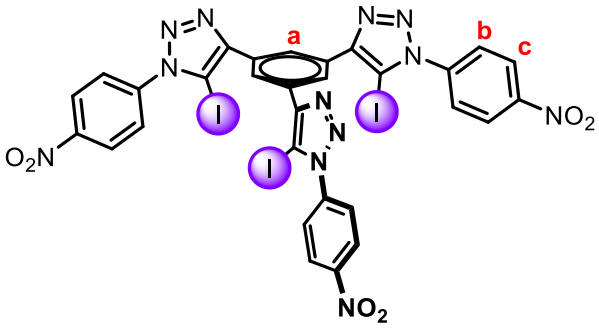


T3.3a. Synthesised according to General Procedure 1 with 1,3,5-triethynylbenzene **3.20** (30 mg, 0.20 mmol, 1 eq.) and 1-azido-3,5-bis(trifluoromethyl)benzene **3.23** (306 mg, 1.20 mmol, 6 eq.), however, THF was the reaction solvent and CuI used as the source of copper. The product was purified by column chromatography (30% EtOAc in hexane) to give a white solid (64 mg, 35%). ^{1}H NMR (500 MHz, Acetone-d_6) δ 9.64 (s, 3H_b), 8.77 (s, 6H_c), 8.67 (s, 3H_a),

8.27 (s, 3H_d). ^{13}C NMR (126 MHz, Acetone-d_6) δ 148.62, 139.43, 132.88, 123.46, 122.90, 121.58, 121.00. ^{19}F NMR (471 MHz, Acetone-d_6) δ -63.43 (18F, 6 x CF_3). HRMS-ESI (m/z) Calculated for $C_{36}H_{15}N_9F_{18}$-H^+: 916.1236; found: 916.1243.



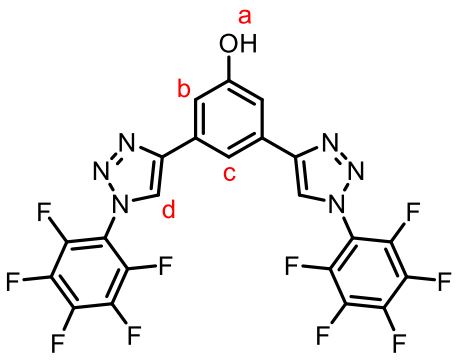
T3.3b. Synthesised according to General Procedure 1 with 1,3,5-tris(iodoethynyl)benzene **3.21** (69 mg, 0.13 mmol, 1 eq.) and 1-azido-3,5-bis(trifluoromethyl)benzene **3.23** (100 mg, 0.392 mmol, 3 eq.), however, THF was the reaction solvent and CuI used as the source of copper. The product was purified by column chromatography (30% EtOAc in hexane) to give a white solid (38 mg, 23%). ^{1}H NMR (600 MHz, $CDCl_3$) δ 8.80 (s, 3H_a), 8.19 (s, 6H_b), 8.12 (s, 3H_c). ^{13}C NMR (151 MHz, $CDCl_3$) δ 150.54, 138.03, 133.47, 130.90, 127.40, 126.92, 124.17, 123.50, 121.69. ^{19}F NMR (376 MHz, $CDCl_3$) δ -62.92 (18F, 6 x CF_3). HRMS-ESI (m/z) Calculated for $C_{36}H_{12}N_9F_{18}I_3$-H^+: 1293.8135; found: 1293.8123.



T3.4b. Synthesised according to General Procedure 1 with 1,3,5-tris(iodoethynyl)benzene **3.21** (40 mg, 0.075 mmol, 1eq.) and 1-azido-4-nitrobenzene **3.24** (74 mg, 0.45 mmol, 6 eq.), however, THF was the reaction solvent and CuI used as the source of copper. The product was purified by column chromatography (30% EtOAc in hexane) to give a white solid (77 mg, 46%). ^{1}H NMR (500 MHz, DMSO) δ 8.91 (s, $3H_a$), 8.54 (d, *J* = 8.9 Hz, $6H_b$), 8.09 (d, *J* = 9.0 Hz, $6H_c$). ^{13}C NMR (126 MHz, DMSO) δ 148.68, 148.26, 141.43, 131.21, 128.14, 125.40, 124.97, 83.96. HRMS-ESI (m/z) Calculated for $C_{30}H_{15}O_6N_{12}I_3$-H^+: 1020.8444; found: 1020.8444.

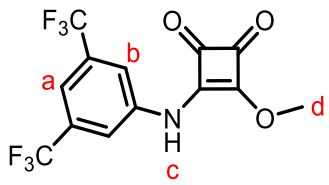
5.2.3 Synthesis of Novel Compounds for Chapter 4

Tris[(1-benzyl-1*H*-1,2,3-triazol-4-yl)methyl]amine (TBTA),[2] azido-pentafluorobenzene **3.22**,[9] 1,3-diethynylphenol **4.9**,[14] 2-nitro-5-(prop-2-yn-1-yloxy)benzaldehyde **4.11**,[15] (2-nitro-5-(prop-2-yn-1-yloxy)phenyl)methanol **4.12**,[16] 2-azido-*N*,*N*-didodecylacetamide **6.16**,[17] 2-azido-*N*,*N*-diethylacetamide **4.17**,[18] and 3-bromo-4-(((*tert*-butyldimethylsilyl)oxy)methyl)-7-(diethylamino)-2*H*-chromen-2-one **4.22**,[19] were all prepared according to literature procedures.

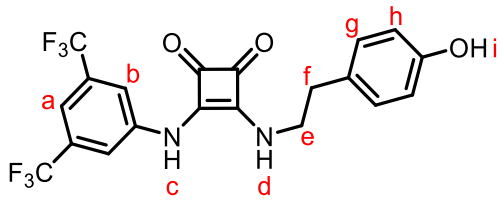


T4.1. $Cu(CH_3CN)_4PF_6$ (105 mg, 0.282 mmol, 0.5 eq.) and TBTA (75.0 mg, 0.141 mmol, 0.25 eq.) were stirred in dry degassed THF (5 mL), followed by the addition of 3,5-diethynylphenol 3 (80.0 mg, 0.563 mmol, 1 eq.) with azido-pentafluorobenzene 4 (706 mg, 3.38 mmol, 6 eq.). The reaction was stirred under N2 for 48 hours. The solvent was removed in vacuo, and the residue dissolved in chloroform (20 mL). The organic mixture was washed with 10% aqueous EDTA/NH4OH solution (2 x 10 mL), followed by brine (20 mL) and then dried over MgSO4. The solvent was removed in vacuo to give the crude product. The product was purified by column chromatography (30% EtOAc in hexane) to give a white solid (197 mg, 62%). ^{1}H NMR (600 MHz, DMSO) δ 10.02 (s, $1H_a$), 9.26 (s, $2H_d$), 7.99 (q, J = 1.8 Hz, $1H_c$), 7.42 (d, J = 1.5 Hz, $2H_b$). ^{13}C NMR (126 MHz, DMSO) δ 158.64, 146.69, 141.84, 141.70, 137.60, 131.23, 124.65, 113.66, 112.41.^{19}F NMR (565 MHz, DMSO) δ -147.24 (s, 4F),

-151.22 (t, *J* = 23.0 Hz, 2F), -160.82 (quintet, *J* = 21.2 Hz, 4F). HRMS-ESI (m/z) Calculated for $C_{22}H_7ON_6F_{10}$-H^+: 561.0516; found: 561.0514.

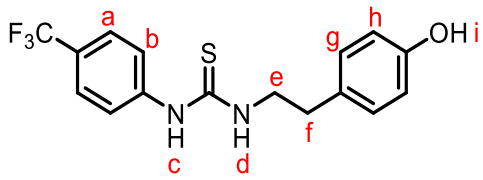


4.10. Synthesised according to literature procedures as follows;[20] 3,4-dimethoxy-3-cyclo-butene-1,2-dione (700 mg, 4.9296 mmol 1 eq.) and 3,5-bis(trifluoromethyl)aniline (1.015 g, 4.4366 mmol, 0.9 eq.) were stirred together in MeOH (20 mL) at rt overnight. The solid residue was washed with cold MeOH (20 mL) then dissolved in MeCN (minimum) and adsorbed onto silica. The dry loaded compound was eluted with DCM to afford the product as a pure white solid. (1.23 g, 82%). ^{1}H NMR (600 MHz, DMSO) δ 11.17 (s, 1H$_c$), 8.03 (s, 2H$_b$), 7.75 (s, 1H$_a$), 4.41 (s, 3H$_d$). ^{19}F NMR (565 MHz, DMSO) δ -61.82 (s, 6F). ^{13}C NMR (126 MHz, DMSO) δ 187.40, 184.49, 179.92, 169.14, 140.22, 131.18, 123.08, 119.31, 116.27, 60.95. HRMS-ESI (m/z) Calculated for $C_{13}H_6O_3NF_6$-H^+: 338.0246; found 338.0251.

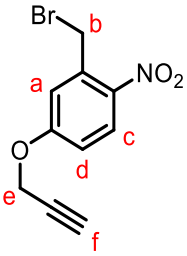


T4.2. Tyramine (100 mg, 0.2950 mmol, 1 eq.) was dissolved in MeOH (minimum) and treated with dropwise additions of DIPEA (114.2 mg, 0.8850 mmol, 3 eq.). A solution of **4.10** (40 mg, 0.2950 mmol, 1 eq.) in MeCN (minimum) was added and the reaction was stirred at rt overnight. The solid residue was washed with cold MeOH (5 mL) and MeCN (5 mL) to

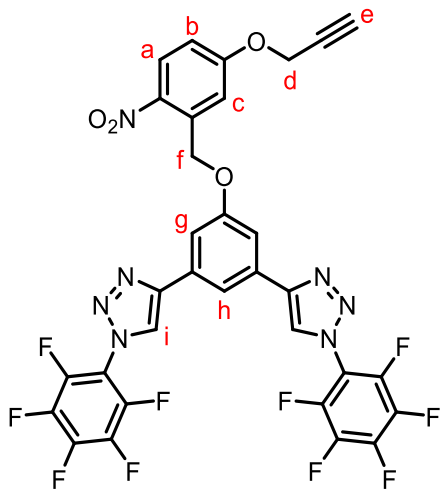
afford the pure product (109 mg, 83%). ^{1}H NMR (600 MHz, DMSO) δ 10.14 (s, 1H$_c$), 9.21 (s, 1H$_i$), 8.01 (s, 2H$_b$), 7.68 (s, 1H$_d$), 7.62 (s, 1H$_a$), 7.05 (d, *J* = 7.9 Hz, 2H$_g$), 6.70 (d, *J* = 7.9 Hz, 2H$_h$), 3.81 (d, *J* = 7.0 Hz, 2H$_e$), 2.78 (t, *J* = 7.1 Hz, 2H$_f$). ^{19}F NMR (565 MHz, DMSO) δ -61.81 (s, 6F). ^{13}C NMR (126 MHz, DMSO) δ 184.72, 180.35, 169.75, 162.28, 155.96, 141.12, 131.36, 129.73, 128.16, 123.18, 117.95, 115.28, 114.64, 45.44, 35.99. HRMS-ESI (m/z) Calculated for $C_{20}H_{15}O_3N_2F_6$-H$^+$: 445.0981; found 445.0982.



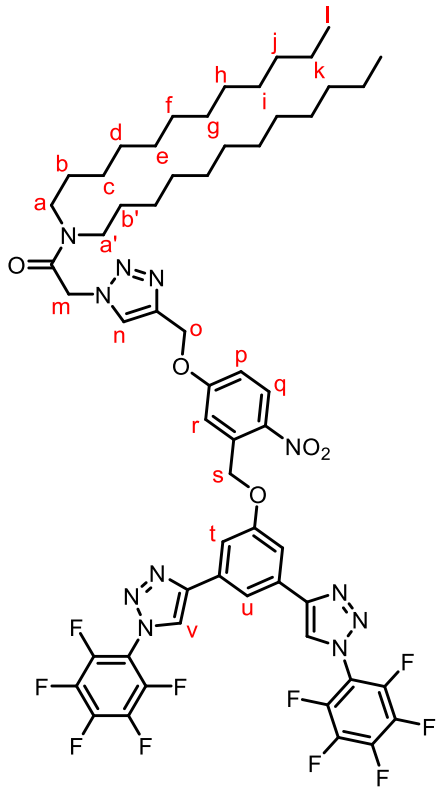
T4.3. Stir tyramine (68 mg, 0.4926 mmol, 1eq) and 4-(trifluoromethyl)phenyl isothiocyanate (100 mg, 0.4926 mmol, 1eq) in THF (5 mL) at room temp for 16 hrs. The pure product precipitated upon addition of hexane (10 mL), after filtration the solid residue was dried to give 1-(4-hydroxyphenethyl)-3-(4-(trifluoromethyl)phenyl)thiourea (135 mg, 81%). ^{1}H NMR (600 MHz, DMSO-d$_6$) δ 9.86 (s, 1H$_c$), 9.20 (s, 1H$_i$), 8.00 (s, 1H$_d$), 7.66 (d, *J* = 8.6 Hz, 2H$_a$), 7.62 (d, *J* = 8.8 Hz, 2H$_b$), 7.10 (m, 2H$_g$), 6.70 (m, 2H$_h$), 3.66 (m, 2H$_e$), 2.77 (t, *J* = 7.4 Hz, 2H$_f$). ^{19}F NMR (565 MHz, DMSO) δ -60.31 (s, 3F). ^{13}C NMR (126 MHz, DMSO) δ 180.19, 155.78, 143.32, 129.56, 129.14, 125.67, 124.42, 123.26, 121.69, 115.21, 45.62, 33.36. HRMS-ESI (m/z) Calculated for $C_{16}H_{16}ON_2F_3S$-H$^+$: 341.0930; found 341.0929.



4.13. (2-nitro-5-(prop-2-yn-1-yloxy)phenyl)methanol **4.12** (3.350 g, 0.01618 mol, 1 eq.) was dissolved in DCM (50 mL), cooled to 0 °C, and treated with TEA (4.5 mL, 0.032 mol, 2 eq.) and methanesulfonyl chloride (2.78 g, 0.0243 mol, 1.5 eq.). The reaction mixture was stirred for 30 mins then washed with sat. Na_2CO_3 solution (2 x 20 mL) and brine (2 x 20 mL) then dried with $MgSO_4$ and the solvent was removed *in vacuo*. The resulting solid was stirred in THF (50 mL) with LiBr (5.62 g, 0.0647 mol, 4 eq.) overnight at rt. The reaction mixture was concentrated *in vacuo* then diluted with DCM and washed with water (2 x 20 mL) and brine (2 x 20 mL) followed by drying over $MgSO_4$. The crude product was purified by silica gel flash chromatography using DCM as the eluent to afford the product as a yellow solid (3.23 g, 74%). ^{1}H NMR (600 MHz, $CDCl_3$) δ 8.14 (d, *J* = 9.1 Hz, 1H$_c$), 7.12 (d, *J* = 2.8 Hz, 1H$_a$), 7.02 (dd, *J* = 9.1, 2.8 Hz, 1H$_d$), 4.85 (s, 2H$_b$), 4.80 (d, *J* = 2.4 Hz, 2H$_e$), 2.60 (t, *J* = 2.4 Hz, 1H$_f$). ^{13}C NMR (151 MHz, $CDCl_3$) δ 161.26, 141.48, 135.74, 128.37, 118.77, 114.98, 56.50, 29.75. The mass spectrum of this compound coupld not be obtained (by either ESI accurate mass or alternative ionisation). NMR characterisation was consistent with the synthesis of the desired product, which was used successfully for the next step.



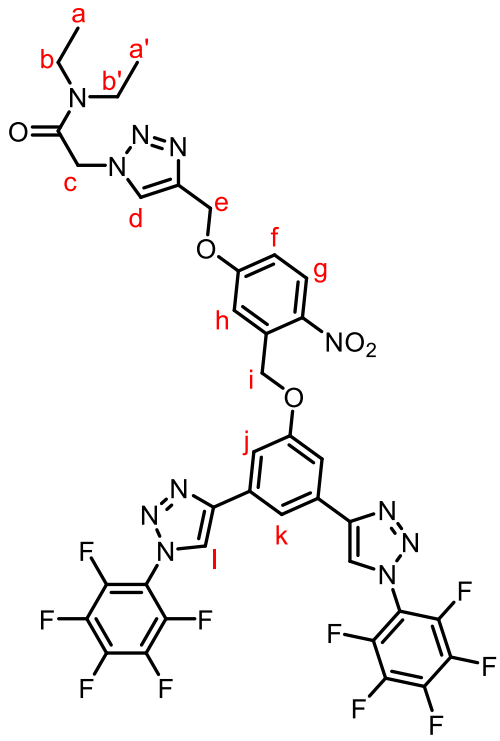
4.18. **T4.1** (56 mg, 0.10 mmol, 1 eq.) and K_2CO_3 (30 mg, 0.22 mmol, 2.2 eq.) were stirred in MeCN (7.5 mL) at 0 °C. The reaction mixture was warmed to rt, **4.13** (54 mg, 0.20 mmol, 2 eq.) was added then the reaction was stirred overnight at 45 °C. The reaction mixture was concentrated in vacuo then diluted with DCM (15 mL) and washed with water (1 x 10 mL) and brine (1 x 10 mL) followed by drying over $MgSO_4$. The crude product was purified by silica gel flash chromatography using DCM as the eluent to afford the solid product (38 mg, 51%). ^{1}H NMR (500 MHz, $CDCl_3$) δ 8.28 (d, *J* = 9.1 Hz, 1H$_a$), 8.18 (s, 2H$_i$), 8.08 (t, *J* = 1.4 Hz, 1H$_h$), 7.62 (d, *J* = 1.5 Hz, 2H$_g$), 7.55 (d, *J* = 2.8 Hz, 1H$_c$), 7.04 (dd, *J* = 9.1, 2.9 Hz, 1H$_b$), 5.68 (s, 2H$_f$), 4.82 (d, *J* = 2.4 Hz, 2H$_d$), 2.56 (t, *J* = 2.4 Hz, 1H$_e$). ^{19}F NMR (471 MHz, $CDCl_3$) δ -144.81 – -146.35 (m, 4F), -149.49 (t, *J* = 21.7 Hz, 2F), -158.53 – -159.63 (m, 4F). ^{13}C NMR (126 MHz, $CDCl_3$) δ 162.16, 159.38, 147.61, 142.58, 140.52, 138.30, 136.79, 131.82, 128.09, 122.63, 117.06, 114.43, 114.13, 113.06, 113.02, 67.48, 56.53, 29.85. HRMS-ESI (m/z) Calculated for $C_{32}H_{14}O_4N_7F_{10}$-H^+: 750.0942; found 750.0934.



AT4.4. Cu(CH3CN)4PF6 (24.5 mg, 0.0658 mmol, 0.5 eq.) and TBTA (17.5 mg, 0.0329 mmol, 0.25 eq.) were stirred in dry degassed DCM (10 mL), followed by the addition of compound 8 (98.6 mg, 0.132 mmol, 1 eq.) and 2-azido-N,N-didodecylacetamide 9 (57.5 mg, 0.132 mmol, 1 eq.). The reaction was stirred under N2 for 48 hours. The solvent was removed in vacuo, and the residue dissolved in chloroform (20 mL). The organic mixture was washed with 10% aqueous EDTA/NH4OH solution (2 x 10 mL), followed by brine (20 mL) and then dried over MgSO4. The solvent was removed in vacuo to give the crude product. The product was purified by preparative TLC (DCM) to give a white solid (76.4 mg, 49%).

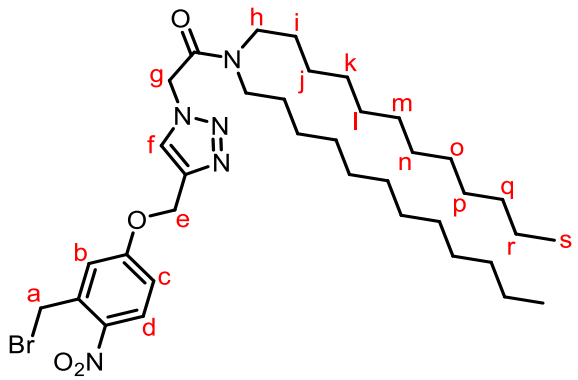
^{1}H NMR (500 MHz, DMSO) δ 9.29 (s, 2H$_{v}$), 8.28 (s, 1H$_{n}$) 8.26 (s, 1H$_{u}$), 8.17 (s, 1H$_{q}$), 7.70 (d, *J* = 1.4 Hz, 2H$_{t}$), 7.50 (d, *J* = 2.8 Hz, 1H$_{r}$), 7.33 (dd, *J* = 9.2, 2.8 Hz, 1H$_{p}$), 5.66 (s, 2H$_{s}$), 5.41 (s, 2H$_{o}$), 5.35 (s, 2H$_{m}$), 3.29 (m, 3H$_{a}$), 3.20 (t, *J* = 7.3 Hz, 2H$_{a'}$), 1.56 (t, *J* = 7.6 Hz, 2H$_{b}$), 1.42 (p, *J* = 7.5 Hz, 3H$_{b'}$), 1.28 – 1.20 (m, 36H$_{c-k}$), 0.84 – 0.81 (m, 7H$_{l}$). ^{19}F NMR (471 MHz, DMSO) δ -146.98 – -147.32 (m, 4F), -151.22 (t, *J* = 23.0 Hz, 2F) -159.44 – -161.86 (m, 4F). ^{13}C NMR (126 MHz,

DMSO) δ 164.79, 162.41, 158.99, 146.49, 141.98, 141.83, 141.25, 140.11, 137.68, 135.81, 131.62, 128.04, 126.82, 125.06, 115.64, 115.23, 113.59, 112.53, 112.08, 66.74, 61.94, 50.59, 46.56, 45.61, 40.12, 40.02, 39.95, 39.86, 39.78, 39.69, 39.61, 39.52, 39.44, 39.35, 39.19, 39.02, 31.29, 29.04-28.92 (m), 28.71, 28.29, 27.09, 26.28, 26.14, 22.09, 13.91. HRMS-ESI (m/z) Calculated for $C_{58}H_{65}O_5N_{11}F_{10}$-$Na^+$: 1208.4903; found 1208.4892.



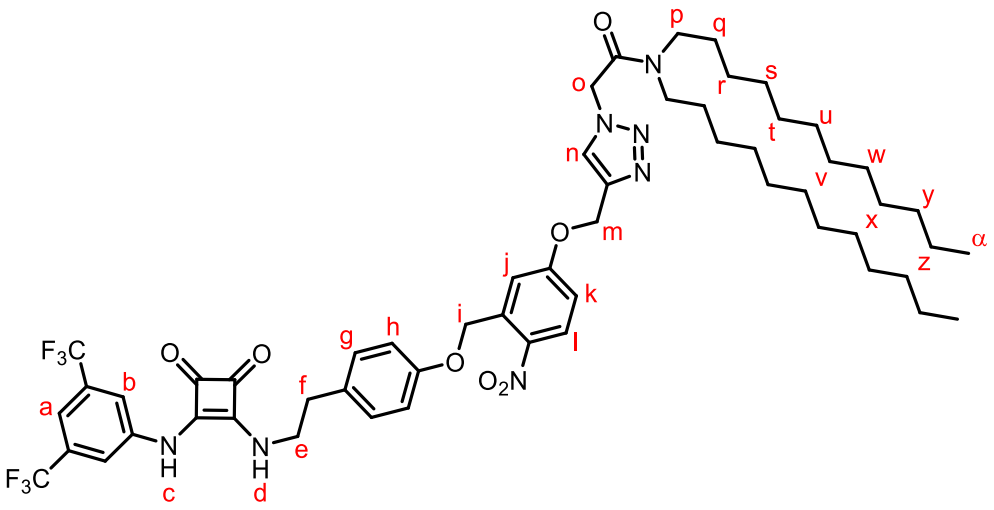
AT4.5. Cu(CH3CN)4PF6 (5.86 mg, 0.0215 mmol, 0.5 eq.) and TBTA (5.69 mg, 0.0107 mmol, 0.25 eq.) were stirred in dry degassed DCM (5 mL), followed by the addition of compound 8 (32 mg, 0.0430 mmol, 1 eq.) with 2-azido-N,N-diethylacetamide 10 (14 mg, 0.0859 mmol, 2 eq.). The reaction was stirred under N2 for 48 hours. The solvent was removed in vacuo, and the residue dissolved in chloroform (20 mL). The organic mixture was washed with 10% aqueous EDTA/NH4OH solution (2 x 10 mL), followed by brine (20 mL) and then dried over MgSO4. The solvent was removed in vacuo to give the crude product. The product was purified by preparative TLC (10% MeOH in DCM) to give a white solid (17 mg, 44%). ^{1}H NMR

(500 MHz, DMSO) δ 9.29 (s, 2H$_l$), 8.28 (s, 1H$_d$), 8.26 (s, 1H$_k$), 8.19 (s, 1H$_g$), 7.71 (s, 2H$_j$), 7.51 (d, *J* = 2.8 Hz, 1H$_h$), 7.34 (dd, *J* = 9.2, 2.8 Hz, 1H$_f$), 5.67 (s, 2H$_i$), 5.43 (s, 2H$_e$), 5.36 (s, 2H$_c$), 3.39 (q, *J* = 7.1 Hz, 2H$_a$), 3.27 (m, 2H$_{a'}$), 1.18 (t, *J* = 7.1 Hz, 3H$_b$), 1.02 (t, *J* = 7.1 Hz, 3H$_{b'}$). ^{19}F NMR (471 MHz, DMSO-d$_6$) δ -147.11 (d, *J* = 20.4 Hz, 4F), -151.15 (t, *J* = 22.8 Hz, 2F), -160.80 (t, *J* = 21.5 Hz, 4F). ^{13}C NMR (126 MHz, DMSO-d$_6$) δ 164.45, 162.39, 159.03, 146.49, 141.98, 141.85, 141.26, 140.18, 137.69, 135.76, 131.62, 126.86, 125.09, 115.66, 115.33, 113.65, 112.51, 112.12, 66.79, 61.93, 50.55, 13.95, 12.83. HRMS-ESI (m/z) Calculated for $C_{38}H_{26}O_5N_{11}F_{10}$-H$^+$: 906.1953; found 906.1946.



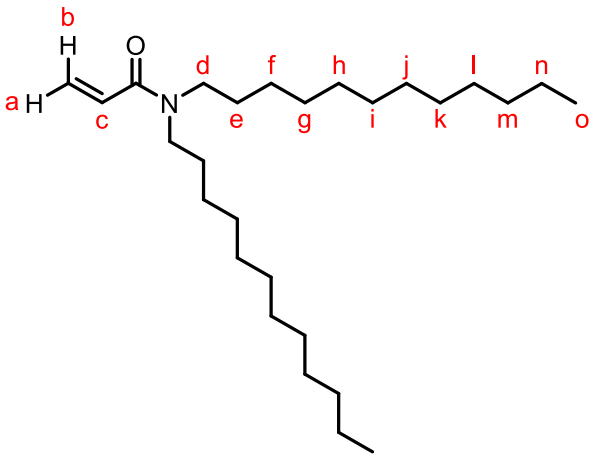
4.19. Cu(CH3CN)4PF6 (252.4 mg, 0.9255 mmol, 0.5 eq.) and TBTA (245.5 mg, 0.4628 mmol, 0.25 eq.) were stirred in dry degassed DCM (15 mL), followed by the addition of compound 7 (500 mg, 1.851 mmol, 1 eq.) and 2-azido-N,N-didodecylacetamide 9 (808 mg, 1.851 mmol, 1 eq.)The reaction was stirred under N2 for 48 hours. The solvent was removed in vacuo, and the residue dissolved in chloroform (20 mL). The organic mixture was washed with 10% aqueous EDTA/NH4OH solution (2 x 10 mL), followed by brine (20 mL) and then dried over MgSO4. The solvent was removed in vacuo to give the crude product. The product was purified by column chromatography (10% EtOAc in DCM) to give a white solid (783 mg, 60%). ^{1}H NMR (600 MHz, DMSO) δ 8.19 (s, 1H$_f$), 8.15 (d, *J* = 9.1 Hz, 1H$_d$), 7.43 (d, *J* = 2.8 Hz,

1H$_b$), 7.28 (dd, *J* = 9.2, 2.8 Hz, 1H$_c$), 5.42 (s, 2H$_a$), 5.33 (s, 2H$_e$), 4.95 (s, 2H$_g$), 3.30 (m, 2H$_h$), 3.23 (t, *J* = 7.6 Hz, 2H$_{h'}$), 1.57 (q, *J* = 7.5 Hz, 2H$_i$), 1.44 (q, *J* = 7.5 Hz, 2H$_{i'}$), 1.30 – 1.23 (m, 32H$_{j-r}$), 0.85 (m, 6H$_s$). ^{13}C NMR (151 MHz, DMSO) δ 164.77, 161.83, 141.14, 140.57, 135.50, 128.24, 126.82, 118.61, 115.17, 61.93, 50.57, 46.57, 45.63, 31.28, 30.37, 29.02, 29.00, 28.97, 28.94, 28.91, 28.70, 28.30, 27.11, 26.29, 26.14, 22.08, 13.90. HRMS-ESI (m/z) Calculated for $C_{36}H_{61}O_4N_5Br$-H$^+$: 706.3901; found 706.3899.



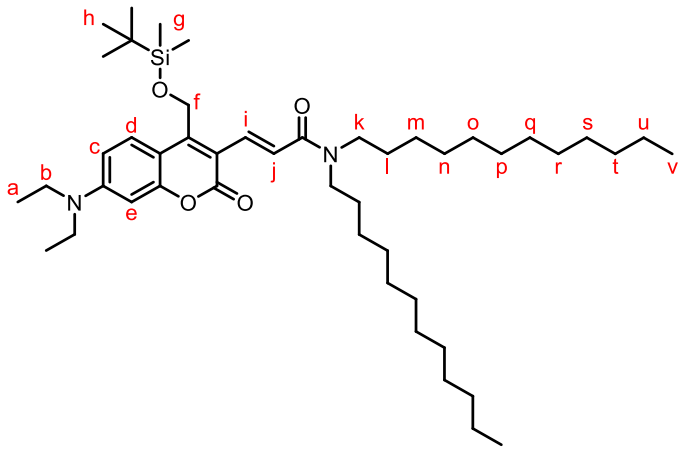
AT4.6. T4.2 (30.0 mg, 0.0674 mmol, 1 eq.) was stirred with K_2CO_3 (23.0 mg, 0.169, 2.5 eq.) in DMF (2.5 mL) at 0 °C for 10 mins. **4.19** (48.0 mg, 0.0674 mmol, 1 eq.) was added, the reaction was warmed to 45 °C and then left to stir for 16 hrs. The solvent was removed in vacuo and the crude was suspended in EtOAc (10 mL), washed with water (2 x 10 mL) then dried over $MgSO_4$. The product was purified by preparative TLC (EtOAc and hexane 1:1) to give a pale yellow solid (15 mg, 21%). ^{1}H NMR (500 MHz, Acetone) δ 8.27 (d, *J* = 9.1 Hz, 1H$_l$), 8.25 (s, 1H$_n$), 8.02 (s, 1H$_a$), 7.72 (s, 1H$_c$), 7.69 (s, 2H$_b$), 7.22 (dd, *J* = 9.2, 2.8 Hz, 1H$_k$), 7.14 (d, *J* = 2.7 Hz, 1H$_j$), 7.07 (t, *J* = 6.2 Hz, 1H$_d$), 7.03 – 6.97 (m, 2H$_g$), 6.71 – 6.64 (m, 2H$_h$), 5.98 (s, 2H$_i$), 5.39 (s, 2H$_m$), 5.27 (s, 2H$_o$), 3.91 (q, *J* = 7.2 Hz, 2H$_e$), 3.44 (t, *J* = 7.8 Hz, 2H$_p$), 3.34 (t, *J* =

7.6 Hz, 2H$_{p'}$), 2.85 – 2.80 (m, 2H$_f$),1.71 (s, 2H$_q$), 1.54 (s, 2H$_{q'}$), 1.40 – 1.27 (m, 36H$_{r-z}$), 0.92 – 0.82 (m, 6H$_\alpha$). ^{19}F NMR (471 MHz, Acetone) δ -63.24 (6F, 2 x CF_3). ^{13}C NMR (126 MHz, Acetone) δ 188.61, 184.94, 171.26, 165.53, 164.17, 163.60, 156.97, 143.48, 142.70, 141.58, 137.14, 133.11, 130.65, 129.76, 129.42, 127.29, 124.27, 121.27, 117.82, 116.19, 115.25, 113.99, 63.12, 53.15, 51.66, 48.04, 47.38, 47.04, 37.66, 32.67, 28.34, 27.66, 27.54, 23.36, 14.39. HRMS-ESI (m/z) Calculated for $C_{56}H_{73}O_7N_7F_6$-H$^+$: 1070.5548; found 1070.5535.



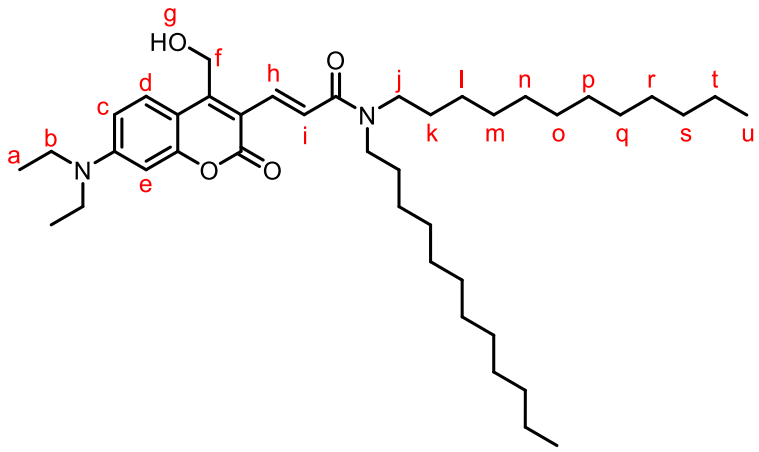
4.23. Acryloyl chloride (130 mg, 1.445 mmol, 1.2 eq.) was dissolved in DCM (10 mL) at 0 °C and a solution of didodecylamine (425 mg, 1.2040 mmol, 1 eq.) and TEA (305 mg, 3.0100 mmol, 2.5 eq.) in DCM (20 mL) was added dropwise. The reaction mixture was then allowed to warm to room temp and then stirred overnight. The reaction was poured into ice water (20 mL) and extracted into DCM (2 x 10 mL). The organic layer was washed with 5% HCl (2 x 10 mL) and dried over $MgSO_4$. The product was purified by column chromatography (DCM) to give the pure product (303 mg, 62%). ^{1}H NMR (600 MHz, $CDCl_3$) δ 6.53 (dd, *J* = 16.7, 10.4 Hz, 1H$_c$), 6.33 (dd, *J* = 16.7, 2.1 Hz, 1H$_b$), 5.64 (dd, *J* = 10.4, 2.1 Hz, 1H$_a$), 3.35 (t, *J* = 7.7 Hz, 2H$_d$), 3.28 (t, *J* = 7.7 Hz, 2H$_{d'}$), 1.55 (m, 4H$_e$), 1.29 – 1.25 (m, 32H$_{f-n}$), 0.88 (t, *J* = 7.0 Hz, 6H$_o$). ^{13}C NMR (151 MHz, $CDCl_3$) δ 166.03, 128.08, 127.60, 48.31, 46.86, 32.06, 29.77, 29.69,

29.59, 29.48, 28.00, 27.25, 26.99, 22.83, 14.25. HRMS-ESI (m/z) Calculated for $C_{27}H_{54}ON\text{-}H^+$: 408.4200; found 408.4192.

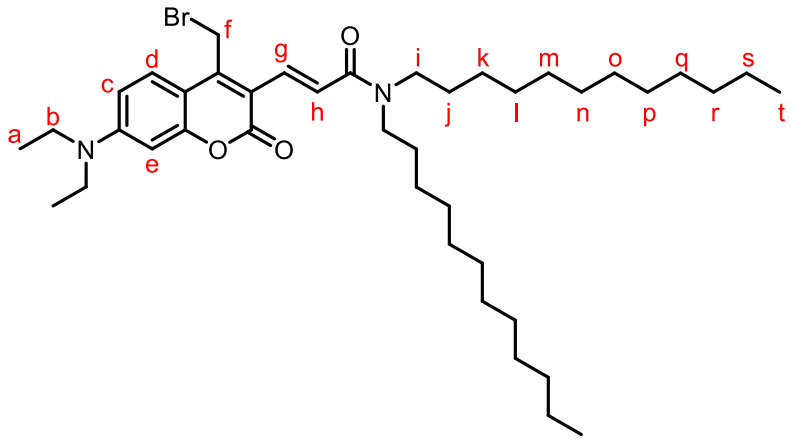


4.24. 4.22 (115 mg, 0.261 mmol, 1 eq.) $NaHCO_3$ (66 mg, 0.78 mmol, 3 eq.), TBACl (80 mg, 0.29 mmol, 1.1 eq.) and LiCl (19 mg, 0.45 mmol, 1.7 eq.) were dissolved in dry degassed DMF (4 mL) in a microwave vial, **4.23** (213 mg, 0.522 mmol, 2 eq.) was added as a solution in dry DMF (1 mL) and the reaction mixture was degassed for 5 mins. $Pd(OAc)_2$ (5.9 mg, 0.026 mmol, 0.1 eq.) was added and the reaction vessel was sealed, heated to 110 °C and left to stir for 1 hour. The reaction mixture was cooled to room temp, diluted with EtOAc (10 mL) and filtered through Celite®. The solvent was concentrated then washed with water (2 x 10 mL) and brine (20 mL) followed by drying over $MgSO_4$. The crude product was purified by column chromatography (10% EtOAc in hexane) and the solvent was removed *in vacuo* to afford the product as a bright yellow solid (55 mg, 27%). ^{1}H NMR (600 MHz, $CDCl_3$) δ 7.83 (d, *J* = 15.0 Hz, $1H_d$), 7.75 – 7.71 (m, $2H_{i,j}$), 6.68 (d, *J* = 8.8 Hz, $1H_c$), 6.52 (s, $1H_e$), 4.98 (s, $2H_f$), 3.42 (m, $8H_{b,k}$), 1.62 (m, $2H_l$), 1.57 (m, $2H_{l'}$), 1.30 – 1.23 (s, $42H_{a,m\text{-}u}$), 0.88 (m, $9H_h$), 0.86 (m, $6H_v$), 0.15 (s, $6H_g$). ^{13}C NMR (151 MHz, $CDCl_3$) δ 167.01, 166.74, 160.83, 155.65, 151.04, 150.92, 148.36, 132.64, 132.03, 128.04, 127.04, 124.15, 123.19, 115.05, 110.60, 107.47, 94.89, 57.88, 48.42, 47.04, 32.09, 32.07, 30.03, 29.85, 29.82, 29.78, 29.74, 29.72, 29.69,

29.65, 29.54, 29.51, 28.19, 27.33, 27.30, 27.06, 27.03, 25.96, 25.92, 25.90, 25.86, 22.84, 18.35, 14.26, 12.53, 1.16. HRMS-ESI (m/z) Calculated for $C_{47}H_{83}O_4N_2Si$-H^+: 767.6117; found 767.6108.

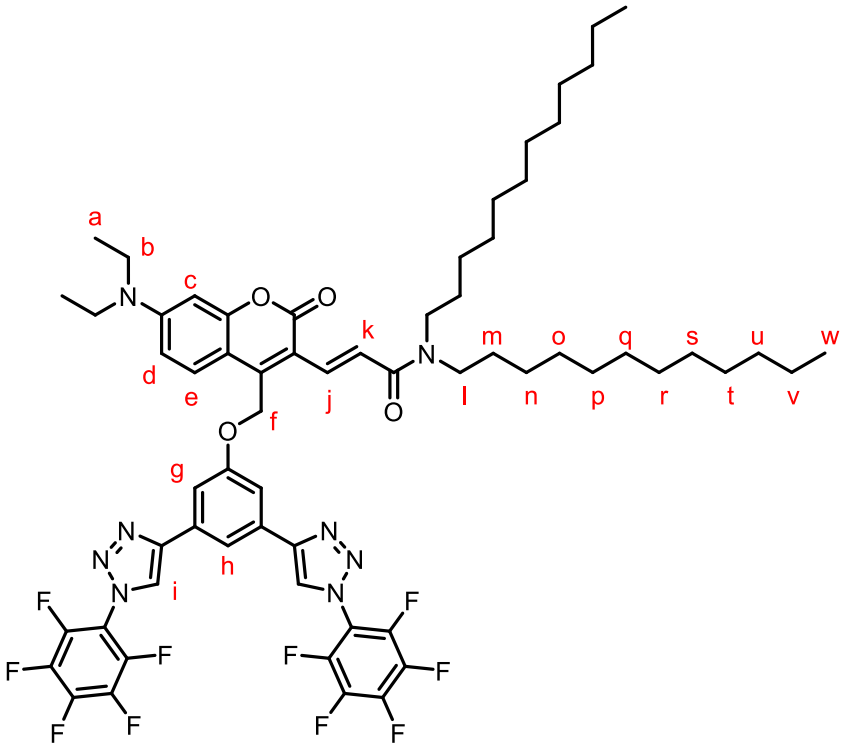


4.25. 4.24 (28 mg, 0.0365 mmol, 1 eq.) was stirred in THF at 0 °C and treated with a solution of TBAF (10.5 mg, 0.0401 mmol, 1.1 eq.) in THF (1 M) and stirred for 45 mins, whilst warming to room temp. The reaction was diluted with EtOAc (10 mL), quenched with water (10 mL), washed with brine (10 mL) and dried over $MgSO_4$. The organic layer was concentrated *in vacuo* and adsorbed to silica then the dry loaded compound was partially purified by column chromatography (EtOAc) to afford the product as a bright yellow solid. (22 mg, 92%). Crude ^{1}H NMR (400 MHz, $CDCl_3$) δ 7.83 (d, *J* = 14.9 Hz, 1H$_d$), 7.74 (s, 1H$_h$), 7.71 (d, *J* = 4.4 Hz, 1H$_i$), 6.65 (d, *J* = 9.4 Hz, 1H$_c$), 6.49 (d, *J* = 2.6 Hz, 1H$_e$), 4.97 (s, 2H$_f$), 3.76 – 2.91 (m, 8H$_{b,j}$), 1.66 – 1.51 (m, 4H$_k$), 1.44 – 1.14 (m, 42H$_{a,l\text{-}t}$), 0.88 (s, 6H$_u$). Crude ^{13}C NMR (151 MHz, $CDCl_3$) δ 166.87, 160.68, 155.51, 150.89, 148.21, 132.50, 131.88, 127.89, 126.90, 124.01, 123.05, 114.91, 110.46, 107.32, 57.74, 48.28, 46.89, 31.93, 29.64, 29.40, 29.37, 28.05, 27.16, 26.89, 25.82, 22.69, 18.21, 14.12, 12.39. HRMS-ESI (m/z) Calculated for $C_{41}H_{69}O_4N_2$-H^+: 653.5252; found 653.5247.



4.26. 4.25 (95 mg, 0.1455 mmol, 1eq.) was dissolved in DCM (2.5 mL), cooled to 0 °C, and treated with TEA (29 mg, 0.2910 mmol, 2 eq.) and methanesulfonyl chloride (25 mg, 0.2183 mmol, 1.5 eq.). The reaction mixture was stirred for 30 mins then washed with $NaHCO_3$ (2 x 2 mL) then dried with $MgSO_4$ and the solvent was removed *in vacuo*. The resulting solid stirred in THF (2.5 mL) with LiBr (50.6 mg, 0.5820 mmol, 4 eq.) overnight at rt. The reaction mixture was concentrated *in vacuo* then the residue was suspended in EtOAc (5 mL) and washed with water (2 x 10 mL). The aqueous was separated and extracted with more EtOAc (2 x 5 mL), the organic layers were combined and washed with brine (10 mL) followed by drying over $MgSO_4$. The crude product was partially purified by preparative TLC using 15% EtOAc in DCM as the eluent to afford the product as a red solid (79 mg, 76%). Crude ^{1}H NMR (400 MHz, $CDCl_3$) δ 7.91 (d, *J* = 15.0 Hz, $1H_d$), 7.75 (d, *J* = 5.8 Hz, $2H_h$), 7.72 (s, $1H_g$), 6.64 (dd, *J* = 9.2, 2.6 Hz, $1H_c$), 6.48 (d, *J* = 2.5 Hz, $1H_e$), 4.99 (s, $2H_f$), 3.56 – 3.22 (m, $8H_{b,i}$), 1.62 (m, $2H_j$), 1.54 (m, $2H_{j'}$), 1.43 – 1.06 (m, $42H_{a,k\text{-}s}$), 0.87 (m, *J* = 6.8, 2.9 Hz, $6H_t$). Crude ^{13}C NMR (151 MHz, $CDCl_3$) δ 160.45, 155.73, 151.22, 147.73, 132.29, 127.78, 126.37, 126.24, 123.69, 114.20, 110.13, 109.59, 107.05, 97.55, 48.53, 47.28, 45.06, 32.07, 29.78, 29.50, 28.17,

27.34, 27.04, 22.84, 14.26, 12.64. HRMS-ESI (m/z) Calculated for $C_{41}H_{68}O_3N_2Br\text{-}H^+$: 715.4408; found: 715.4403.



AT4.7. T4.1 (29 mg, 0.05308 mmol, 1 eq.) and K_2CO_3 (18 mg, 0.1327 mmol, 2.5 eq) were stirred in dry MeCN at 0°C. **4.26** (38 mg, 0.05308 mmol, 1 eq.) was added and the reaction was heated to 45°C and left to stir for 16 hrs. The solvent was removed in vacuo and the residue was suspended in EtOAc (5 mL), washed with water (2 x 5 mL). The aqueous was separated and extracted with more EtOAc (2 x 5 mL), the organic layers were combined and washed with brine (10 mL) followed by drying over $MgSO_4$. The crude product was partially purified by preparative TLC using 15% EtOAc in DCM as the eluent to afford the product as a red solid (79 mg, 76%). Crude ^{1}H NMR (400 MHz, $CDCl_3$) δ 8.43 (s, 2H$_i$), 8.16 (s, 2H$_g$), 8.03 (d, *J* = 14.9 Hz, 1H$_e$), 7.76 (d, *J* = 4.1 Hz, 1H$_j$), 7.65 (s, 1H$_k$), 6.69 (d, *J* = 9.9 Hz, 1H$_d$), 6.51 (s, 1H$_c$), 5.54 (s, 2H$_f$), 3.56 – 3.19 (m, 8H$_{b,l}$), 1.61 (s, 2H$_m$), 1.50 (s, 2H$_{m'}$), 1.24 (m, 42H$_{a,n\text{-}v}$), 0.93 – 0.74 (m, 6H$_w$).

5.3 Single Crystal X-Ray Diffraction Experiments

Single crystals suitable for X-ray diffraction were grown via slow evaporation of chloroform solutions by Dr Andrew Docker, and the crystal structures were subsequently solved by Heike Kuhn. CCDC 2075766 (**T3.2b**) and 2075767 (**T3.2c**) contain the supplementary crystallographic data which can be obtained free of charge from The Cambridge Crystallographic Data Centre via www.ccdc.cam.ac.uk/structures.

The single-crystal X-ray diffraction intensities for **T3.2b** and **T3.2c** were collected at 150 K on Oxford Diffraction/Agilent SuperNovae diffractometers with Cu-Kα (λ = 1.54184 Å) radiation equipped with a nitrogen gas Oxford Cryosystems Cryostream unit.[21] A suitable crystal was chosen and mounted on a 200 µm MiTeGen loop using perfluoropolyether oil. The CrysAlisProsoftware was used for data collection and integration.[22] All structures were solved using SuperFlip and refined using full-matrix least-squares refinement within the CRYSTALS suite.[23,24] All non-hydrogen atoms were refined anisotropically. The hydrogen atoms were positioned at geometrically sensible positions and refined using a riding model.

Table 5.1. Selected solid state XB and ChB contacts **T3.2b** and **T3.2c.**

Contact	**Interatomic Distances (Å)**[a]	**Angle (°)**[a],[b]	**%VdW**
I1···N1	2.954(5)	172.94(19)	84
I2···N2	3.161(5)	158.45(19)	90
Te1···N3	3.303(4)	176.27(18)	83
Te2···N4	2.982(4)	170.99(15)	91
[a] Errors indicated in parenthesis. [b] Contact angle (in degrees) with respect to the C-X bond. X = I or TeMe.			

Table 5.2. Selected Crystallographic and Refinement Data: X-ray Crystal Structures of **T3.2b** and **T3.2c**

	T3.2b	**T3.2c**
Formula	C23 H4 Cl3 F10 I2 N7 O2	C25 H11 Cl2 F10 N7 O2 Te2
Formula Weight	960.48	957.49
a (Å)	14.0124(4)	9.4324(1)
b (Å)	16.5955(3)	14.9145(2)
c (Å)	14.3324(4)	21.8284(3)
α (°)	90	90
β (°)	119.046(3)	99.7769(12)
γ (°)	90	90
Unit cell volume (Å^3)	2913.72(15)	3026.21(7)
Crystal system	monoclinic	Monoclinic
Space group	P 21/c	P 21/c
Z	4	4
Temperature (K)	150 K	150 K
Radiation Type	Copper	Copper
λ (Å)	1.54180	1.54180
Reflections (all)	56438	19516
Reflections (unique)	6127	6333
R_{int}	0.068	0.047
R[I > 2σ(I)]	0.0925	0.0593
wR(F^2) (all data)	0.2223	0.1592
S	1.053	1.005

5.4 ^{1}H NMR Titration Experiments

All anion binding constants were determined by ^{1}H NMR titrations; the spectra were recorded on a Bruker AVIII 500 spectrometer at 298 K. The initial sample volumes were 0.5 mL, at a concentration of 1 mM of host which was dissolved in acetone-d_6 or 2.5% D_2O-acetone-d_6 (v/v). Known volumes of the anion guest, as the tetrabutylammonium (TBA) salt, in acetone-d_6, or 2.5% D_2O-acetone-d_6 (v/v) mixtures, were added to the host and the spectra were recorded after each addition. The chemical shift perturbations of the host spectra were monitored as a function of guest concentration for 17 data points. The spectra were referenced to the residual solvent peak. The data was analysed using a global fit procedure using the Bindfit program,[25,26] using non-linear least squares analysis to obtain the best fit between observed and calculated chemical shifts for the 1:1 binding stoichiometry. Errors in chapter two were calculated as two times the standard deviation from the average value of at-least two independent repeats (95% confidence limit). In chapters 3 and 4, the estimated errors presented due to scarcity of material. In the majority of experiments, the association of guest and host was fast on the NMR timescale. In analogous titrations in the less polar, membrane mimetic $CDCl_3$, significant $TBA^{+}X^{-}$ ion pairing prevented analysis of the weak anionophore-anion interactions. The protons monitored for each transporter and the associated binding constants can be found within the corresponding chapter and the associated fitted binding isotherms can be found in the appendix.

5.5 Anion Transport Experiments

5.5.1 Vesicle Preparation

A thin film of lipid (1-palmitoyl-2-oleoyl-sn-3-phosphatidylcholine (POPC), egg-yolk phosphatidylglycerol (EYPG) or dipalmitoyl phosphatidylcholine (DPPC)) was formed by evaporating a chloroform solution of the lipid under reduced pressure on a rotary evaporator (40 °C) and then under high vacuum for 6 hours. Then the lipid film was hydrated by vortexing with 1 mL of the prepared internal buffer solution. The lipid suspension was then subjected to 5 freeze-thaw cycles using liquid nitrogen and a water bath (40°C) followed by extrusion 19 times through a polycarbonate membrane (pore size 200 nm). Extravesicular components were removed by size exclusion chromatography on a Sephadex G-25 column as follows, the column was flushed with the prepared external buffer solution, the 1 mL vesicles solution was added to the column with 1.5 mL of external buffer. A further 3.5 mL of external buffer was added, and 3.5 mL of prepared vesicles were collected. The concentration of the collected lipid stock is dependent on the initial lipid film concentration.

5.5.2 The HPTS Assay[27,28]

This kinetic ion transport fluorescence assay employs 8-hydroxypyrene-1,3,6-trisulfonic acid trisodium salt (HPTS) as an internal pH probe to monitor the dissipation of the pH gradient induced across the lipid bilayer. The time-dependent change in fluorescence intensity (λ_{em} = 510 nm) can be monitored simultaneously at the λ_{ex} = 405 nm (acidic form of HPTS) and λ_{ex} = 460 nm (basic form) which allows for ratiometric analysis of the internal pH of the vesicles. A portion of POPC in chloroform (266 µL, 25 mg/mL) was taken to prepare POPC LUVs (3.5 mL, 2.5 mM) with an internal solution of 100 mM NaCl, 10 mM HEPES and 1 mM

HPTS, buffered to pH 7.0 and an external solution of 100 mM NaCl and 10 mM HEPES again buffered to pH 7.0, using the procedure described above. In a typical transport experiment, 25 µL of this lipid stock was suspended in 1950 µL of the external buffer to give a final lipid concentration of 31.25 µM in the cuvette. The lipid suspension was gently stirred and a base pulse of NaOH (20 µL, 0.5 M) was added at 40 s to initiate the experiment. At 100 s the test transporter (various concentrations, typically in 5 µL DMSO) was added. The experiment was allowed to run for a further 300 s before the addition of Triton X-100 detergent (25 µL, 7:1 (v/v) H_2O-DMSO) to lyse the vesicles to calibrate the assay. This was repeated at least twice for each concentration of carrier.

5.5.2.1 Ratiometric and Hill Analysis

This allows the quantification of the change in fluorescence caused by the dissipation of the NaOH-induced pH gradient *via* transporter-facilitated Cl^-/OH^- antiport (or Cl^-/H^+ symport) from the HPTS assay. Following ratiometric analysis with equation 5.1, the fractional fluorescence intensity (I_{rel}) was calculated using equation 5.2, where R_t is the fluorescence ratio at time *t*, R_0 is the fluorescence ratio at time 0 (set as 65 seconds in this assay), and R_d is the fluorescence ratio after the addition of detergent.

$$ratio = \frac{\lambda ex\ 460}{\lambda ex\ 405} \qquad (5.1) \qquad I_{rel} = \frac{R_t - R_0}{R_d - R_0} \qquad (5.2)$$

The fractional fluorescence intensity (I_{rel}) at 288 s just prior to lysis, defined as the fractional activity *y*, was plotted as a function of the ionophore concentration (x / µM). Hill coefficients (n) and EC_{50} values were calculated by fitting to the Hill equation (5.3),

$$y = y_0 + (y_{max} - y_0) \cdot \frac{x^n}{EC50^n + x^n} \qquad (5.3)$$

where y_0 is the fractional activity in the absence of transporter, y_{max} is the fractional activity in with excess transporter, x is the transporter concentration in the cuvette. Hill plots were fitted to at-least 8 data points spanning the required concentration range.

5.5.2.2 The HPTS Assay with Photo-irradiation

The HPTS assay was modified to allow for *in-situ* irradiation of the anchored carriers presented in **chapter 4**, and carried out as follows; the desired concentration of the anchored carriers are added to the lipid suspension (POPC vesicles containing 1 mM HPTS, 100 mM internal and external NaCl, buffered with 10 mM HEPES at pH 7.0) and stirred for 1 minute to allow for incorporation into the bilayer. The sample is then irradiated with 365 nm UV light using an LED supplied with a 1A current, and transport was initiated with a base pulse of NaOH (0.5 M) at 90 s and the change in ratiometric emission (λ_{em} = 510 nm; λ_{em1} = 405 nm, λ_{em2} = 460 nm) was monitored over time. The assay was calibrated assay with Triton-X100 at 290 s and then repeated at a range of concentrations.

The initial jump in fluorescence intensity normally seen upon addition of NaOH (due to external HPTS absorbed to the vesicle surface) now happens simultaneously with the transport of the carrier, and therefore the normalisation of the data is carried out as follows, in order to subtract this initial jump (that is not related to transport). The fractional fluorescence intensity (I_{rel}) was calculated using equation 2.2, where R_t is the fluorescence ratio at time t, R_0 is the fluorescence ratio at time 0, usually set as 65 s in the HPTS assay, however, now it is set to 95 s which is immediately after the carrier has been added. This normalisation prevents the initial jump in the fluorescence intensity from being considered transport activity (**Figure 5.1**). (R_d is the fluorescence ratio after the addition of detergent). Hill analysis is performed as usual.

$$I_{rel} = \frac{R_t - R_0}{R_d - R_0} \quad (5.2)$$

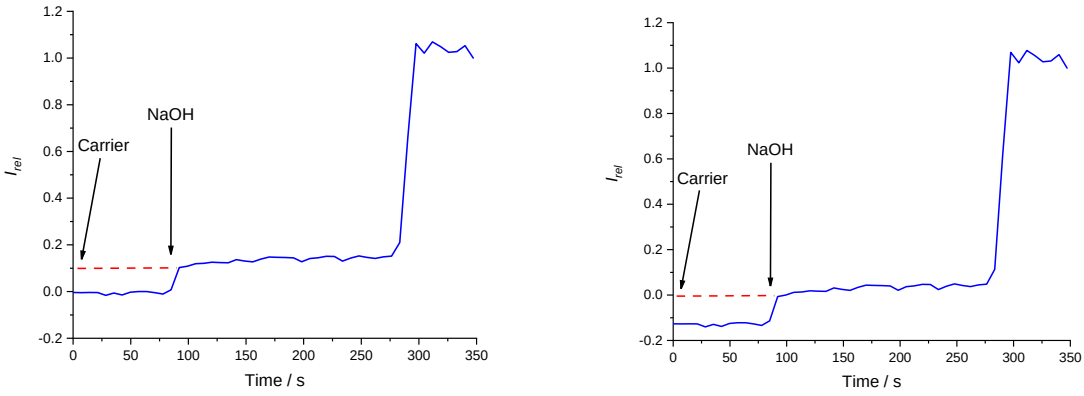


Figure 5.1. Normalisation procedure for *in-situ* photo-irradiation experiments. Data shows the change in fractional fluorescence intensity (I_{rel}) (λ_{em} = 510 nm; λ_{ex1} = 405 nm, λ_{ex2} = 460 nm) upon addition of **AT4.4** (0.05 µM) in DMSO to POPC vesicles containing 1 mM HPTS, 100 mM internal and external NaCl, buffered with 10 mM HEPES at pH 7.0. **AT4.4** was added to the cuvette and stirred for 1 min, before the cuvette was irradiated with 365 nm light for 3 minutes. A NaOH base pulse (0.5 M) was added at t = 90 s. Left, normalisation where R_0 = I_{rel} at 65 s (for the conventional HPTS assay). Right, normalisation where R_0 = I_{rel} at 95 s (for the in-istu irradiation experiments).

5.5.3 Transport Mechanism Studies

5.5.3.1 The Carboxyfluorescein Leakage Assay[29]

The self-quenching dye 5(6)-Carboxyfluorescein (CF) was loaded into POPC LUVs to investigate the effect of the transporter upon vesicle integrity. POPC LUVs were prepared with an internal solution of 10 mM NaCl, 10 mM HEPES and 50 mM CF buffered to pH 7.0 and external buffer of 107 mM NaCl, 10 mM HEPES, pH 7.0. Each transport experiment was carried out as follows: the CF-containing POPC vesicles (25 µL, 2.5 mM) were suspended in the external buffer (1995 µL) at 25 °C and gently stirred. At 50 s, the test transporter (chosen concentration in 5 µL DMSO) was added. The assay was calibrated at 250 s with Triton X-100 detergent (40 µL, 7:1 (v/v) H_2O-DMSO). The time-dependent change in

fluorescence intensity (λ_{ex} = 492 nm, λ_{em} = 517 nm) was monitored, and normalised according to equation 5.4.

$$I_{rel} = \frac{I_t - I_0}{I_{max} - I_0} \qquad (5.4)$$

where $I_0 = I_t$ before transporter addition, $I_{max} = I_t$ after lysis.

5.5.3.2 Mobile Carrier Mechanism HPTS Assay

This assay was used to demonstrate the mobile carrier mechanism of the transporters. The HPTS assay was carried out using the same procedure as described above, however, the POPC LUVs were replaced with dipalmitoyl phosphatidylcholine (DPPC) LUVs. A portion of the DPPC lipid stock (257 µL, 34.06 mM) was taken to prepare the LUVs (3.5 mL, 2.5 mM) with an internal solution of 100 mM NaCl, 10 mM HEPES and 1 mM HPTS, buffered to pH 7.0 and an external solution of 100 mM NaCl and 10 mM HEPES again buffered to pH 7.0. These lipids are extruded at 45 °C. In a typical transport experiment, 25 µL of this lipid stock is suspended in 1950 µL of the external buffer to give a final lipid concentration of 31.25 µM in the cuvette. These lipids do not allow mobile carrier-mediated transport when in a gel phase at room temperature. Transport is restored above the phase transition temperature (41 °C) at 45 °C. For elevated temperature studies, the buffer was equilibrated at 45 °C using the Peltier temperature controller for 2 minutes prior to initiating the experiment. This assay was performed at one chosen concentration for each carrier and repeated at least twice. If no dissipation of the induced pH gradient occurs at 25 °C, a mobile carrier mechanism is inferred.

5.5.3.3 Anion Repulsion HPTS Assay

This assay was used to demonstrate the role of anions in the transport process by replacing the POPC LUVs with either egg-yolk phosphatidylglycerol (EYPG) LUVs or 16:0-18:1 PG (POPG) LUVs, which both have a net negative charge and thus inhibit anion transport. A portion of the lipid stock (POPG: 675 µL, 12.97 mM or EYPG: 685 µL, 12.78 mM) was taken to prepare the LUVs (3.5 mL, 2.5 mM) with an internal solution of 100 mM NaCl, 10 mM HEPES and 1 mM HPTS, buffered to pH 7.0 and an external solution of 100 mM NaCl and 10 mM HEPES again buffered to pH 7.0. In a typical transport experiment, 25 µL of this lipid stock is suspended in 1950 µL of the external buffer to give a final lipid concentration of 31.25 µM in the cuvette. This assay was performed at one chosen concentration for each carrier and repeated at least twice. If no dissipation of the induced pH gradient occurs, a Cl^-/OH^- antiport mechanism is inferred.

5.5.4 Transport Selectivity Studies

5.5.4.1 Sodium Gluconate HPTS Assay

This assay was used to demonstrate the role of anions in the transport process by replacing the chloride in the buffer with gluconate, which cannot cross the membrane. Therefore, POPC LUVs were prepared with an internal solution of 100 mM sodium gluconate, 10 mM HEPES, 1 mM HPTS buffered to pH 7.0 and an external buffer of 100 mM sodium gluconate, 10 mM HEPES, pH 7.0. This assay was performed at one chosen concentration for each carrier and repeated at least twice. If no dissipation of the induced pH gradient occurs, a Cl^-/OH^- antiport mechanism is inferred.

5.5.4.2 Cation Selectivity HPTS Assay

Cation selectivity experiments were also conducted by external ion exchange. The POPC vesicle solution (prepared as above) was added to different external buffers (100 mM M^+Cl^-, 10 mM HEPES, pH 7.0), where M = Li, Na, K or Rb. For each experiment the typical NaOH base pulse was replaced with the relevant M^+OH^- base pulse (20 µL, 0.5 M).

5.5.4.3 Anion Selectivity HPTS Assay

Ion selectivity experiments were conducted by external ion exchange. Thus, the HPTS assay was repeated by adding the POPC vesicle solution (prepared as above) to various external buffers (100 mM Na^+X^-, 10 mM HEPES, pH 7.0), where X = Cl, Br, I or NO_3. In the case of NaI buffer, 5 mM $Na_2S_2O_3$ was added to reduce any iodine that is generated in solution.

5.5.4.4 The FCCP Cl^- vs OH^- Selectivity HPTS Assay

This assay is used to investigate the relative rate of Cl^- vs. OH^- transport. The HPTS assay was carried out using the above procedure, with the addition of the protonophore trifluoromethoxy carbonyl cyanide phenylhydrazone (FCCP) (5 µL of 0.1 mM stock in DMSO) at 50 s, immediately after the base pulse. At this concentration (final concentration of 0.25 µM in the cuvette), FCCP does not cause appreciable dissipation of the transmembrane pH gradient alone.

5.5.4.5 The NMDG Cl^- vs OH^- Selectivity HPTS Assay

This assay is used to investigate the relative rate of Cl^- vs. OH^- transport. This assay uses Gramicidin D (Gra) as a selective proton channel for the purposes of comparison with previous studies, and to avoid competing interactions between the anionophores and mobile protonophores such as FCCP and CCCP.[30] A portion of POPC phospholipids in chloroform (266 µL, 25 mg/mL) were taken to prepare POPC LUVs (3.5 mL, 2.5 mM) with an internal solution of 100 mM NMDG-Cl, 10 mM HEPES and 1 mM HPTS, buffered to pH 7.0 and an external solution of 100 mM NMDG-Cl and 10 mM HEPES again buffered to pH 7.0. In a typical transport experiment the lipid stock (80 µL, 2.5 mM) was suspended in external buffer (1950 µL or 1945 µL upon addition of Gra) to give a final lipid concentration of 0.1 mM. While stirring gently a base pulse of NMDG (20 µL of 0.5 M stock) was added at 40 s to initiate the experiment. At 100 s the test transporter (various concentrations, typically in 5 µL DMSO) was added. The experiment was allowed to run for a further 200 s before the addition of Triton X-100 detergent (40 µL, 7:1 (v/v) H_2O-DMSO) to calibrate the assay. This was repeated at least twice for each concentration of carrier. This assay was carried out with and without the addition of the proton channel Gramicidin D (0.1 mol%, added in 4 µL DMSO), which when added was done so 30 s after the base pulse.

5.6 Computational Chemistry

Computational investigations were carried out by Alisatir Sterling and Prof. Fernanda Duarte. The levels of theory used for each computational experiment completed in **chapter 2** and **chapter 3** are outlined below, more detailed information alongside the original data can be found in the ESI of the published article associated with this research.[31,32]

5.6.1 Chapter 2

For computational analysis, a simplified structure of the anionophores **T2.1a/b, T2.4a/b** and **T2.7a/b** was used with the alkyl chain substituent truncated to a methyl group and numbered **T2.1a'/b', T2.4a'/b'** and **T2.7a'/b'**.

Conformers of 2:1 complexes were generated using the simulated annealing conformational search implemented in the GFN2-xTB. Three runs and 3 subsequent filtering stages were completed and the remaining structures were optimised at the ωB97X-D3/def2-SVP (ma-def2-SVP on anion, I) level of theory ('loose' optimisation criteria), followed by single point energies at the SMD($CHCl_3$)-ωB97X-D3/def2-SVP (ma-def2-SVP on anion, I). The numbers of surviving conformers after each filter was applied can be found in the ESI of '*Transmembrane anion transport mediated by halogen bonding and hydrogen bonding triazole anionophores'* article published in *Chemical Science*.[31]

All optimization and energy evaluation calculations were carried out using the ORCA suite of programs (version 4.1.1).[33] Optimisations were carried out at the ωB97X-D3/def2-SVP (ma-def2-SVP on anions and I) level of theory, which includes Grimme's D3 dispersion correction.[34–38]

The lowest energy conformer for each anion-ligand complex (obtained from the optimization and energy evaluation calculations), was then used to calculate binding

energies at the [SMD(CHCl3)-DLPNO-CCSD(T)/def2-TZVP (ma-def2- TZVP on all anions)] level of theory.[39,40]

Electrostatic potential surfaces were calculated using the Gaussian 16 (rev A.03) suite of programs at the SMD(CHCl3)-ωB97X-D/def2-TZVP level of theory.[41] Non-covalent interaction (NCI) isosurfaces were calculated using MultiWfn v3.6.25 Isosurfaces were visualised using PyMol and Chimera.[42] Second order perturbation theory analysis was carried out using NBO 7.0.

For each 1:1 (**T2.1a'/b'** + anion) system, geometry optimisations were initiated with both the anion proximal to the methyl/triazole C–H bonds, and the triazole/aryl C–H bonds. Mayer bond orders, their associated HB/XB bond energies ($E^{(2)}_{HB/XB}$), and interaction energy between ligands ($E^{(2)}_{T1–T2}$) in kcal mol^{-1} were calculated at the [NBO/SMD($CHCl_3$)- ωB97X-D3/def2-SVP (ma-def2-TZVP on Cl, I)//ωB97X-D3/def2-SVP (ma-def2-SVP on Cl, I)] level of theory.

5.6.2 Chapter 3

Calculations were carried out using the ORCA suite of programs (version 4.2.1).[43] Optimisation and numerical frequency calculations were carried out at the SMD-ωB97X-D3/def2-SVP (ma-def2-SVP on anions, I and Te) level of theory (M1).[34–36,44,45]

Single point energies were calculated at the SMD-ωB97X-D3/def2-TZVPP (ma-def2-TZVPP on anions, I and Te) level of theory (M2). Electrostatic potential surfaces were calculated using the Gaussian 16 (rev A.03)[41] suite of programs at the SMD(CHCl3)-ωB97XD/def2-TZVP level of theory, and visualised with UCSF Chimera.[42] More details can be found in the ESI of '*Highly Active Halogen Bonding and Chalcogen Bonding Chloride Transporters with Non-Protonophoric Activity*' published in *Chemistry – A European Journal*.[32]

5.7 References

1 K. Asano and S. Matsubara, *Org. Lett.*, 2010, **12**, 4988–4991.

2 C. J. Brassard, X. Zhang, C. R. Brewer, P. Liu, R. J. Clark and L. Zhu, *J. Org. Chem.*, 2016, **81**, 12091–12105.

3 M. Kaasik, S. Kaabel, K. Kriis, I. Järving, R. Aav, K. Rissanen and T. Kanger, *Chem. – A Eur. J.*, 2017, **23**, 7337–7344.

4 O. Dumele, D. Wu, N. Trapp, N. Goroff and F. Diederich, *Org. Lett.*, 2014, **16**, 4722–4725.

5 M. O. Akram, P. S. Shinde, C. C. Chintawar and N. T. Patil, *Org. Biomol. Chem.*, 2018, **16**, 2865–2869.

6 J. Charoenpattarapreeda, Y. S. Tan, J. Iegre, S. J. Walsh, E. Fowler, R. S. Eapen, Y. Wu, H. F. Sore, C. S. Verma, L. Itzhaki and D. R. Spring, *Chem. Commun.*, 2019, **55**, 7914–7917.

7 N. Kobayashi and M. Kijima, *J. Mater. Chem.*, 2008, **18**, 1037–1045.

8 J. V. Alegre-Requena, A. Valero-Tena, I. G. Sonsona, S. Uriel and R. P. Herrera, *Org. Biomol. Chem.*, 2020, **18**, 1594–1601.

9 L. M. Jin, X. Xu, H. Lu, X. Cui, L. Wojtas and X. P. Zhang, *Angew. Chem. Int. Ed.*, 2013, **52**, 5309–5313.

10 D. Destro, S. Sanchez, M. Cortigiani and M. F. A. Adamo, *Org. Biomol. Chem.*, 2017, **15**, 5227–5235.

11 L. Ren and N. Jiao, *Chem. Commun.*, 2014, **50**, 3706–3709.

12 A. Docker, T. Bunchuay, M. Ahrens, A. J. Martinez-Martinez and P. D. Beer, *Chem. Eur. J.*, 2021, **27**, 7837–7841.

13 M. Yao, J. Zhang, S. Yang, H. Xiong, L. Li, E. Liu and H. Shi, *RSC Adv.*, 2020, **10**, 3946–3950.

14 Y. Pan, M. Lu, Z. Peng and J. S. Melinger, *J. Org. Chem.*, 2003, **68**, 6952–6958.

15 L. Li, X. X. Deng, Z. L. Li, F. S. Du and Z. C. Li, *Macromolecules*, 2014, **47**, 4660–4667.

16 N. Kalva, S. Uthaman, R. Augustine, S. H. Jeon, K. M. Huh, I. K. Park and I. Kim, *Macromol. Biosci.*, 2020, **20**, 1–12.

17 J. Pancholi, D. J. Hodson, K. Jobe, G. A. Rutter, S. M. Goldup and M. Watkinson, *Chem. Sci.*, 2014, **5**, 3528–3535.

18 M. C. Joshi, K. J. Wicht, D. Taylor, R. Hunter, P. J. Smith and T. J. Egan, *Eur. J. Med. Chem.*, 2013, **69**, 338–347.

19 J. P. Olson, H. B. Kwon, K. T. Takasaki, C. Q. Chiu, M. J. Higley, B. L. Sabatini and G. C. R. Ellis-Davies, *J. Am. Chem. Soc.*, 2013, **135**, 5954–5957.

20 H. Konishi, T. Y. Lam, J. P. Malerich and V. H. Rawal, *Org. Lett.*, 2010, **12**, 2028–2031.

21 B. J. Cosier and A. M. Glazer, *J. Appl. Crystallogr.*, 1986, **19**, 105–107.

22 Rigaku, CrysAlisPRO, https://www.rigaku.com/products/crystallography/crysalis.

23 L. Palatinus and G. Chapuis, *J. Appl. Crystallogr.*, 2007, **40**, 786–790.

24 P. W. Betteridge, J. R. Carruthers, R. I. Cooper, K. Prout and D. J. Watkin, *J. Appl. Crystallogr.*, 2003, **36**, 1487.

25 BindFit v0.5 | Supramolecular, http://app.supramolecular.org/bindfit/.

26 D. Brynn Hibbert and P. Thordarson, *Chem. Commun.*, 2016, **52**, 12792–12805.

27 A. V. Jentzsch, D. Emery, J. Mareda, S. K. Nayak, P. Metrangolo, G. Resnati, N. Sakai and S. Matile, *Nat. Commun.*, 2012, **3**, 905.

28 N. Busschaert, R. B. P. Elmes, D. D. Czech, X. Wu, I. L. Kirby, E. M. Peck, K. D. Hendzel, S. K. Shaw, B. Chan, B. D. Smith, K. A. Jolliffe and P. A. Gale, *Chem. Sci.*, 2014, **5**, 3617–3626.

29 R. E. Dawson, A. Hennig, D. P. Weimann, D. Emery, V. Ravikumar, J. Montenegro, T. Takeuchi, S. Gabutti, M. Mayor, J. Mareda, C. A. Schalley and S. Matile, *Nat. Chem.*, 2010, **2**, 533–538.

30 X. Wu, L. W. Judd, E. N. W. Howe, A. M. Withecombe, V. Soto-Cerrato, H. Li, N. Busschaert, H. Valkenier, R. Pérez-Tomás, D. N. Sheppard, Y. B. Jiang, A. P. Davis and P. A. Gale, *Chem*, 2016, **1**, 127–146.

31 L. E. Bickerton, A. J. Sterling, P. D. Beer, F. Duarte and M. J. Langton, *Chem. Sci.*, 2020, **11**, 4722–4729.

32 L. E. Bickerton, A. Docker, A. J. Sterling, H. Kuhn, F. Duarte, P. D. Beer and M. J. Langton, *Chem. Eur. J.*, 2021, **27**, 11738–11745.

33 F. Neese, *WIREs Comput. Mol. Sci.*, 2018, **8**, e1327.

34 L. N. Anderson, F. W. Aquino, A. E. Raeber, X. Chen and B. M. Wong, *J. Chem. Theory Comput.*, 2018, **14**, 180–190.

35 S. Kozuch and J. M. L. Martin, *J. Chem. Theory Comput.*, 2013, **9**, 1918–1931.

36 Y.-S. Lin, G.-D. Li, S.-P. Mao and J.-D. Chai, *J. Chem. Theory Comput.*, 2013, **9**, 263–272.

37 S. Grimme, S. Ehrlich and L. Goerigk, *J. Comput. Chem.*, 2011, **32**, 1456–1465.

38 S. Grimme, J. Antony, S. Ehrlich and H. Krieg, *J. Chem. Phys.*, 2010, **132**, 154104.

39 C. Riplinger and F. Neese, *J. Chem. Phys.*, 2013, **138**, 034106.

40 D. G. Liakos and F. Neese, *J. Chem. Theory Comput.*, 2015, **11**, 4054–4063.

41 M. J. Frisch, G. W. Trucks, H. B. Schlegel, G. E. Scuseria, M. A. Robb, J. R. Cheeseman, G. Scalmani, V. Barone, G. a. Petersson, H. Nakatsuji, X. Li, M. Caricato, a. V. Marenich, J. Bloino, B. G. Janesko, R. Gomperts, B. Mennucci, H. P. Hratchian, J. V. Ortiz, a. F. Izmaylov, J. L. Sonnenberg, Williams, F. Ding, F. Lipparini, F. Egidi, J. Goings, B. Peng, A. Petrone, T. Henderson, D. Ranasinghe, V. G. Zakrzewski, J. Gao, N. Rega, G. Zheng, W. Liang, M. Hada, M. Ehara, K. Toyota, R. Fukuda, J. Hasegawa, M. Ishida, T. Nakajima, Y. Honda, O. Kitao, H. Nakai, T. Vreven, K. Throssell, J. a. Montgomery Jr., J. E. Peralta, F. Ogliaro, M. J. Bearpark, J. J. Heyd, E. N. Brothers, K. N. Kudin, V. N. Staroverov, T. a. Keith, R. Kobayashi, J. Normand, K. Raghavachari, a. P. Rendell, J. C. Burant, S. S. Iyengar, J. Tomasi, M. Cossi, J. M. Millam, M. Klene, C. Adamo, R. Cammi, J. W. Ochterski, R. L. Martin, K. Morokuma, O. Farkas, J. B. Foresman and D. J. Fox, *Wallingford CT*, 2016, Gaussian 16, Revision A.03.

42 E. F. Pettersen, T. D. Goddard, C. C. Huang, G. S. Couch, D. M. Greenblatt, E. C. Meng and T. E. Ferrin, *J. Comput. Chem.*, 2004, **25**, 1605–1612.

43 F. Neese, *Wiley Interdiscip. Rev. Comput. Mol. Sci.*, 2012, **2**, 73–78.

44 A. V. Marenich, C. J. Cramer and D. G. Truhlar, *J. Phys. Chem. B*, 2009, **113**, 6378–6396.

45 F. Weigend and R. Ahlrichs, *Phys. Chem. Chem. Phys.*, 2005, **7**, 3297–3305.

CHAPTER 6

Chapter 6 Thesis Conclusions

The research described in this thesis presents the first use of halogen bonding iodotriazoles for transmembrane anion transport. The ability of these interactions to perform anion transport with superiority to hydrogen bonding analogues has been established. The unique properties of chalcogen bonding telluromethyl triazoles has also been proven not only to mediate highly active transport, but also to facilitate non-protonophoric selective Cl^- transport. Finally, a novel method of photo-caging transport was presented, mobile carriers were linked to a membrane anchor via a photocleavable ortho-nitrobenzyl group, as a means to inhibit their mobility and develop light-activated transport activity.

Chapter 2 demonstrated the superior activity of simple acyclic halogen bonding transporters in comparison to hydrogen bonding transporters, whilst highlighting the strong dependence of this activity on the structure of the carrier. A balance between lipophilicity and the presence of electron withdrawing substituents was key for function. In addition, a cation independent Cl^-/OH^- antiport mechanism was determined.

In chapter 3 multidentate selective transporters were presented, building upon the research throughout *chapter 2*. This chapter focussed in particular on the host:guest complementarity of the transporter complex, and the use of exotic non-covalent intramolecular interactions for the mediation of selective anion transport. Computational chemistry was used to probe the anion binding and transport process. Exceptional chloride selectivity was observed for the bidentate tellurium transporter. The research in this chapter highlights the overarching role of non-covalent intermolecular interactions and anion dehydration in achieving efficient and selective anion transport.

In *chapter 4* a novel method of photo-caging the anion transport process was reported and spatio-temporal control over a squaramide and a bidentate C–H triazole carrier was established. These mobile carriers were conjugated to a lipophilic membrane anchor by an *o*-NB photo-labile linker which could be cleaved to generate free mobile carriers and switch on the transport activity. This remarkable off to on switching by photo-cleavage of *o*-NB was not only very effective for regulating ion transport but also worked within a matter of minutes for both of the anion receptors under investigation.

In summary, the results described herein demonstrate the power of halogen and chalcogen bonding for mediating anion transport within simple, synthetically accessible acyclic structures. Furthermore, engineering selective and orthogonal transporters with the use of sigma hole interactions and the unprecedented development of photo-modulated mobile carriers, has the potential to impact the field of membrane transport and bio-mimetic supramolecular chemistry as a whole.

APPENDICES

Appendices

A.1 ^{1}H NMR Binding Isotherms 228

A.1.1 Chapter 2 228

A.1.2 Chapter 3 230

A.1.3 Chapter 4 232

A.2 HPTS Transport Assay Data 233

A.2.1 Chapter 2 233

A.2.2 Chapter 3 240

A.2.3 Chapter 4 243

A.3 Transport Mechanism Studies 246

A.3.1 CF Assay 246

A.3.2 DPPC Assay Data 247

A.3.3 Anionic Lipid Assay 251

A.4 Transport Selectivity Experiments 253

A.4.1 Gluconate Assay Data 253

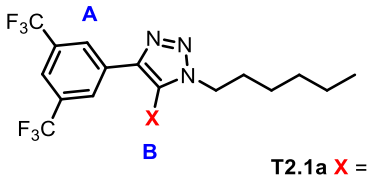
A.4.2 Cation Selectivity HPTS Assay 256

A.4.3 Anion Selectivity and the FCCP Cl^- vs OH^- Selectivity HPTS Assay 257

A.4.4 The NMDG Cl^- vs OH^- Selectivity HPTS Assay 259

A.1 ^{1}H NMR Binding Isotherms

A.1.1 Chapter 2



T2.1a X = H
T2.1b X = I

Figure A.1. The structure of **T2.1** depicting the protons followed throughout the NMR titration experiments.

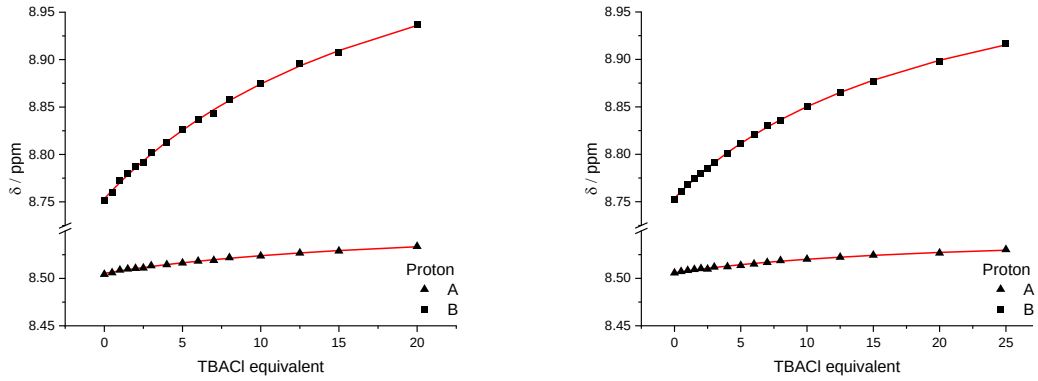


Figure A.2. Chloride binding isotherms for **T2.1a** in acetone-d_6 repeated twice. Experimental data is shown by a symbol and fitted 1:1 binding isotherm is shown by solid line.

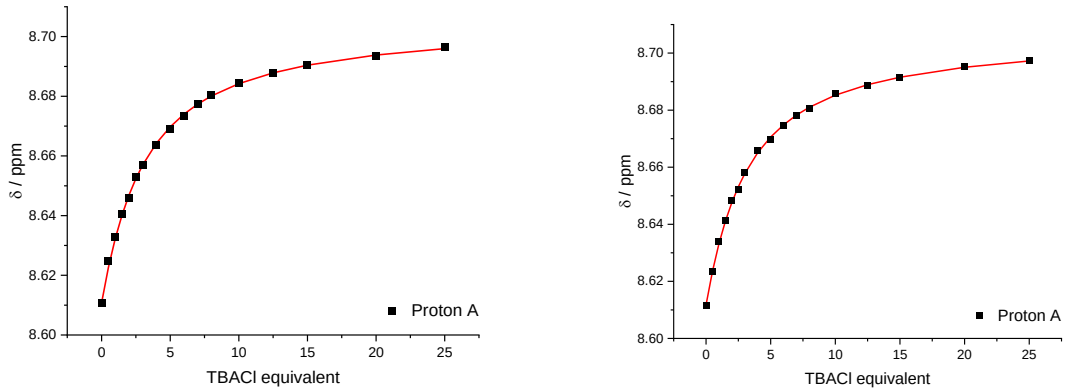


Figure A.3. Chloride binding isotherms for **T2.1b** in acetone-d_6 repeated twice. Experimental data is shown by a symbol and fitted 1:1 binding isotherm is shown by solid line.

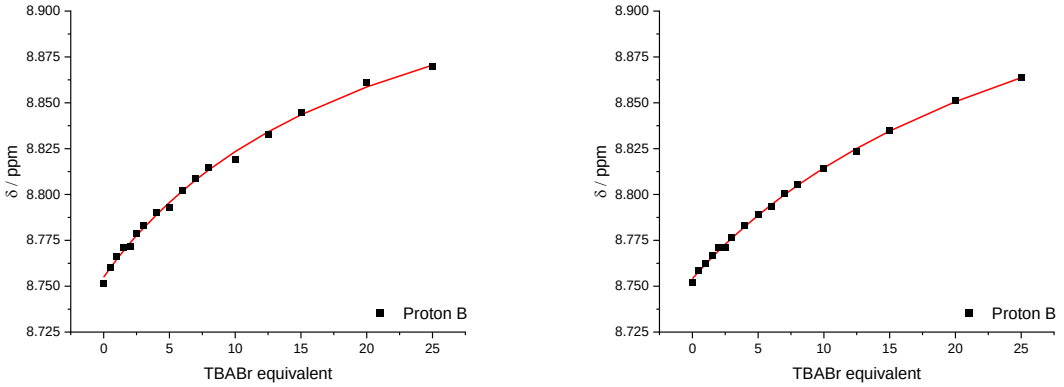


Figure A.4. Bromide binding isotherms for **T2.1a** in acetone-d_6 repeated twice. Experimental data is shown by a symbol and fitted 1:1 binding isotherm is shown by solid line.

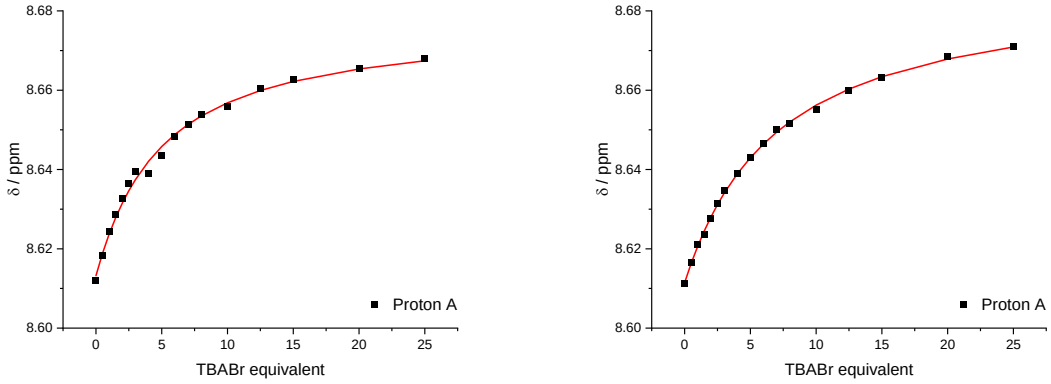


Figure A.5. Bromide binding isotherms for **T2.1b** in acetone-d_6 repeated twice. Experimental data is shown by a symbol and fitted 1:1 binding isotherm is shown by solid line.

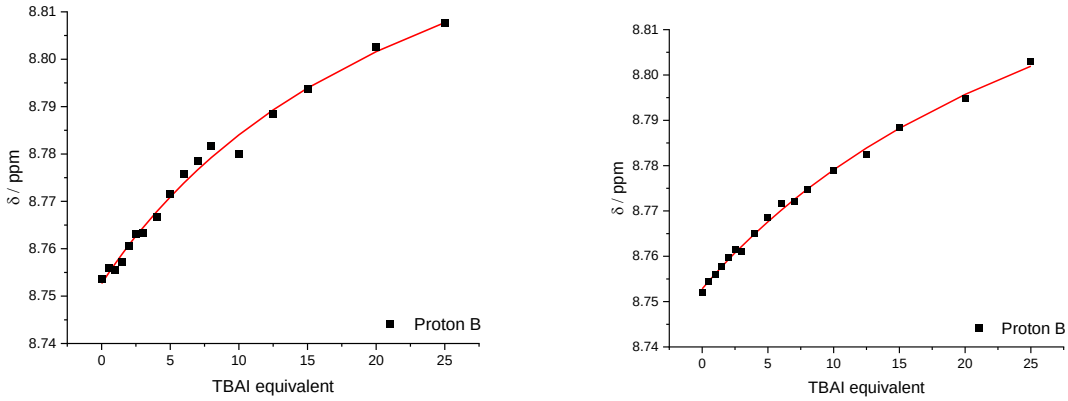


Figure A.6. Iodide binding isotherms for **T2.1a** in acetone-d_6 repeated twice. Experimental data is shown by a symbol and fitted 1:1 binding isotherm is shown by solid line.

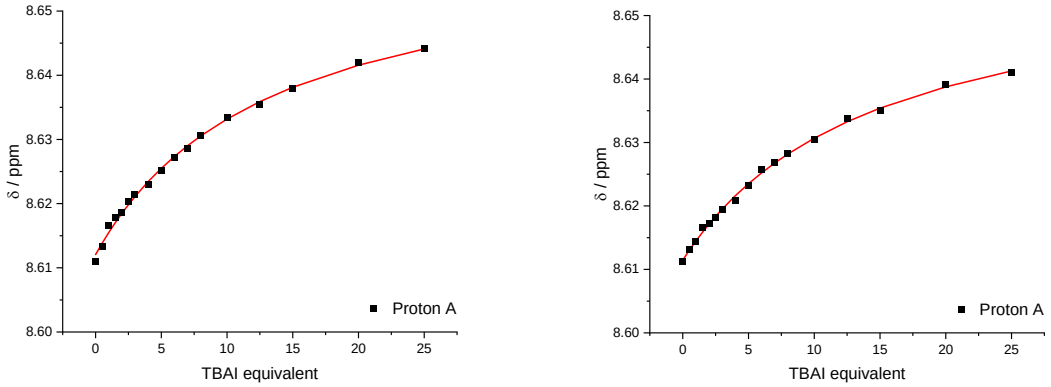


Figure A.7. Iodide binding isotherms for **T2.1b** in acetone-d_6 repeated twice. Experimental data is shown by a symbol and fitted 1:1 binding isotherm is shown by solid line.

A.1.2 Chapter 3

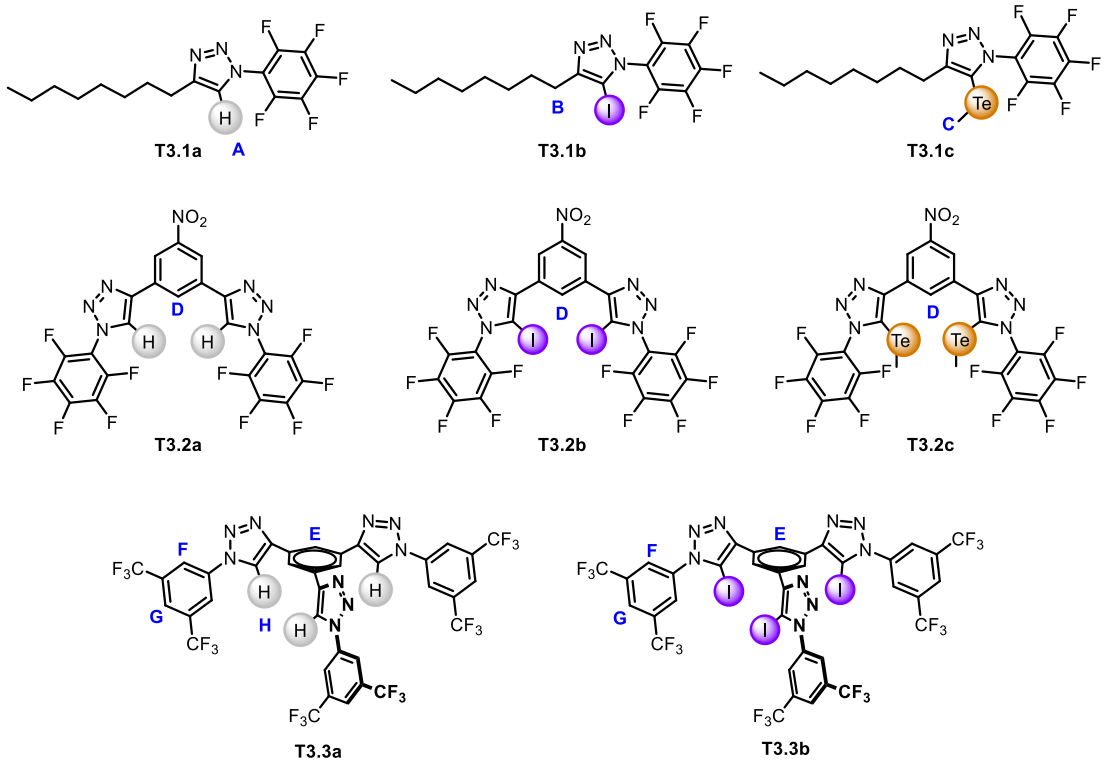


Figure A.8. Receptors with highlighted protons followed for ^{1}H NMR titration experiments.

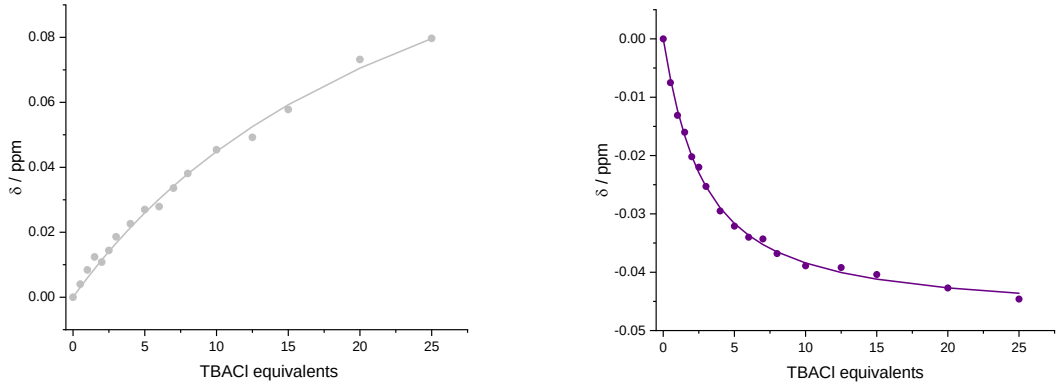


Figure A.9. Chloride binding isotherms for **T3.1a** (left) and **T3.1b** (right) in acetone-d_6. Experimental data shown by ●, fitted 1:1 binding isotherm shown by solid line

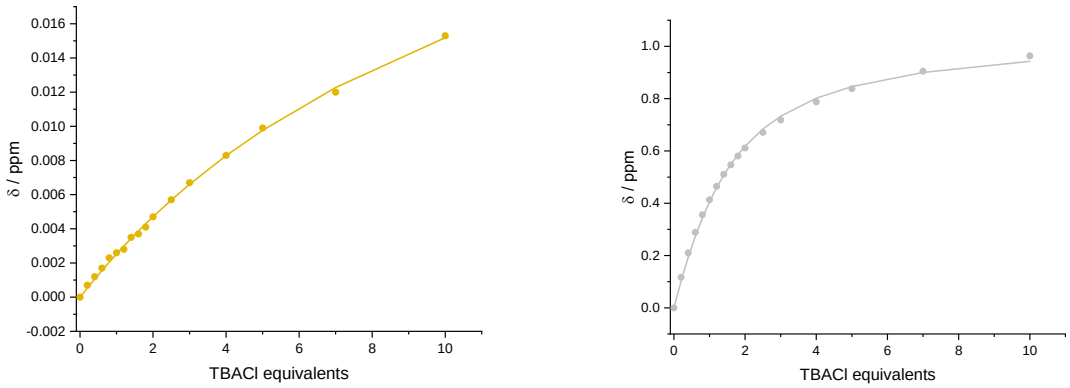


Figure A.10. Chloride binding isotherms for **T3.1c** (left) and **T3.2a** (right) in acetone- d_6. Experimental data shown by ●, fitted 1:1 binding isotherm shown by solid line

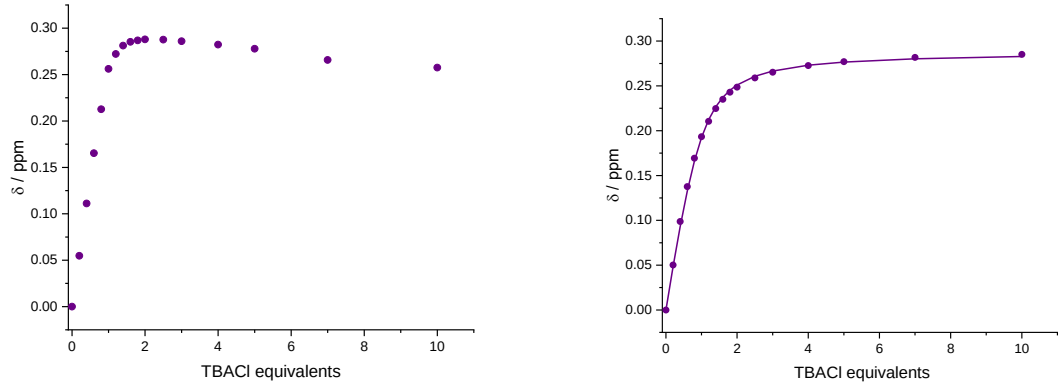


Figure A.11. Chloride binding isotherms for **T3.2b** in acetone-d_6 (left) and in 2.5% D_2O-acetone-d_6 (right). Experimental data shown by ●, fitted 1:1 binding isotherm shown by solid line.

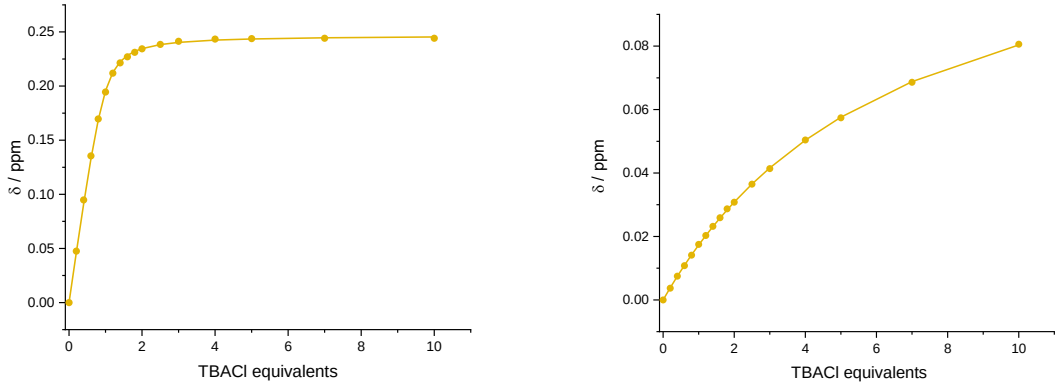


Figure A.12. Chloride binding isotherms for **T3.2c** in acetone-d_6 (left) and in 2.5% D_2O-acetone-d_6 (right). Experimental data shown by ●, fitted 1:1 binding isotherm shown by solid line.

A.1.3 Chapter 4

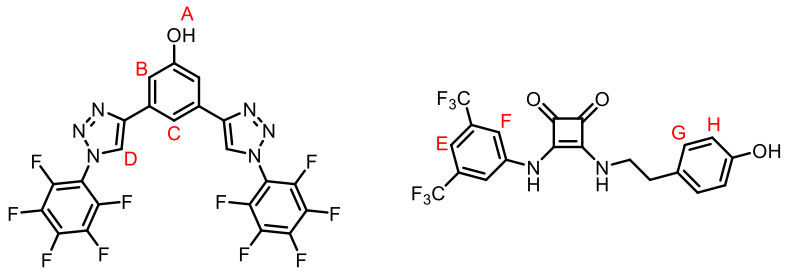


Figure A.13. Carriers **T4.1** and **T4.2**.

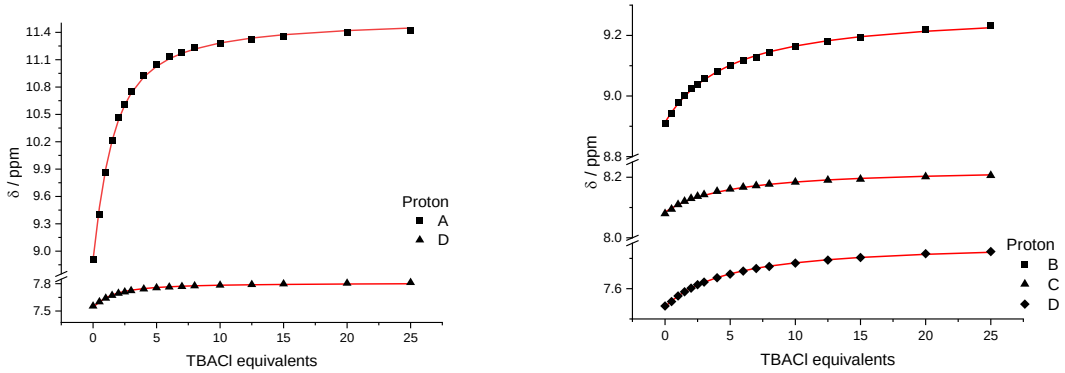


Figure A.14. Chloride binding isotherms for **T4.1** in acetone-d_6 (left) and in 2.5% D_2O-acetone-d_6 (right). Experimental data shown by symbols, fitted 1:1 binding isotherm shown by solid red lines.

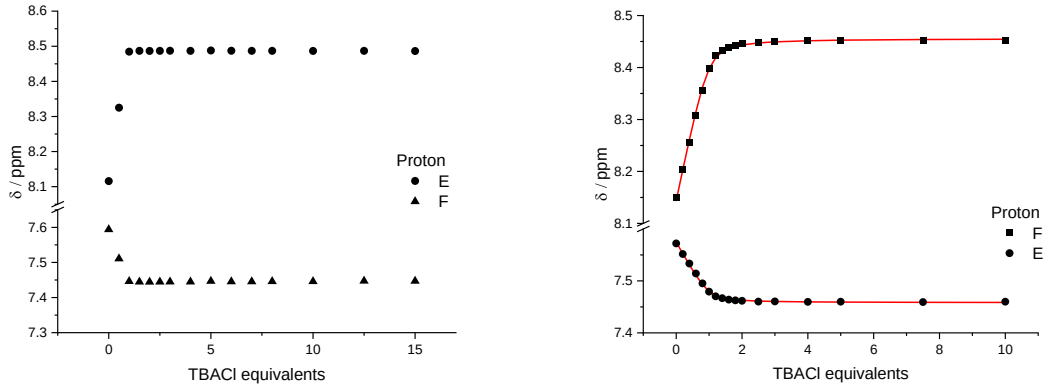


Figure A.15. Chloride binding isotherms for **T4.2** in acetone-d_6 (left) and in 2.5% D_2O-acetone-d_6 (right). Experimental data shown by symbols, fitted 1:1 binding isotherm shown by solid red lines.

A.2 HPTS Transport Assay Data

In the following figures: Left: change in relative fluorescence intensity (I_{rel}) over time in the HPTS assay (LUVs (31.25 µM vesicles); inside 100 mM NaCl, 10 mM HEPES, 1 mM HPTS, pH 7.0; outside: 100 mM NaCl, 10 mM HEPES, pH 7.0). Right: dependence of the fractional transport activity y in the HPTS assay on the concentration of transporter (black squares), and where possible fitted to the Hill equation (red line). The data reported is an average of at least two repeats.

A.2.1 Chapter 2

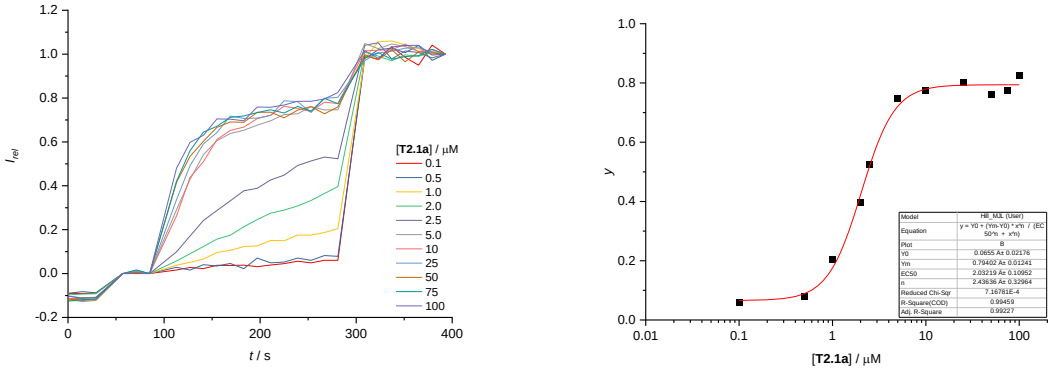


Figure A.16. HPTS assay data for **T2.1a**.

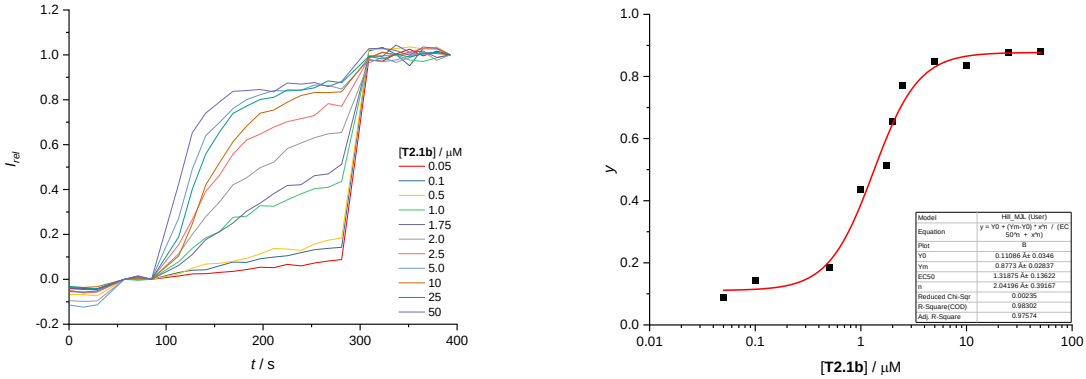


Figure A.17. HPTS assay data for **T2.1b**.

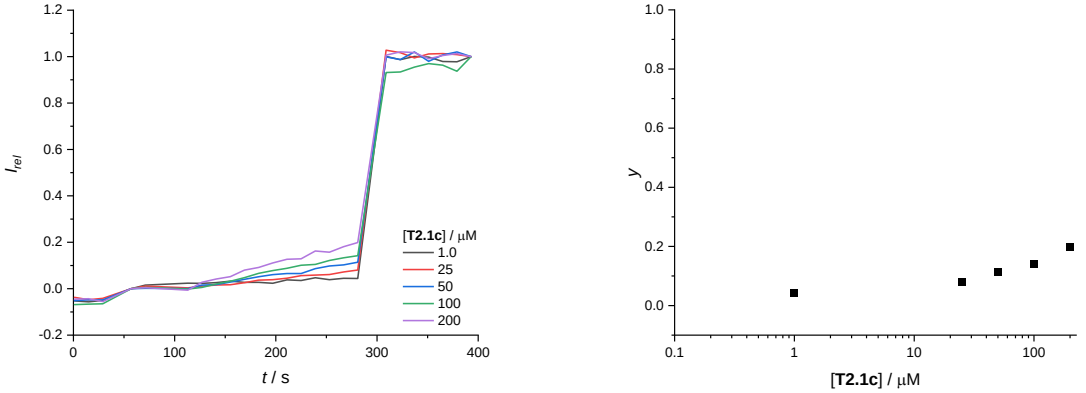


Figure A.18. HPTS assay data for **T2.1c**.

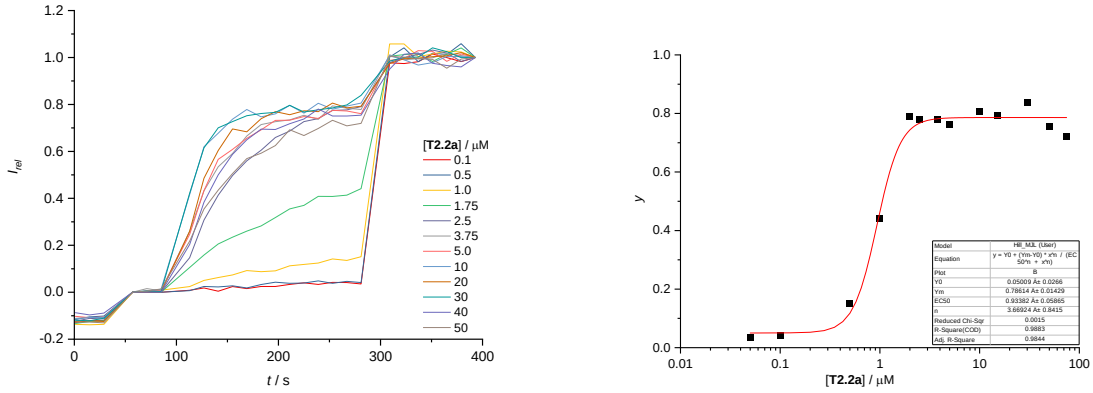


Figure A.19. HPTS assay data for **T2.2a**.

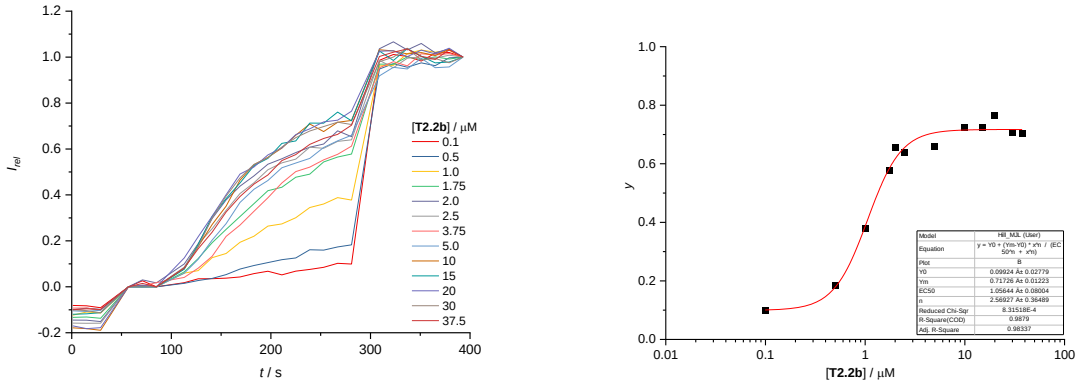


Figure A.20. HPTS assay data for **T2.2b**.

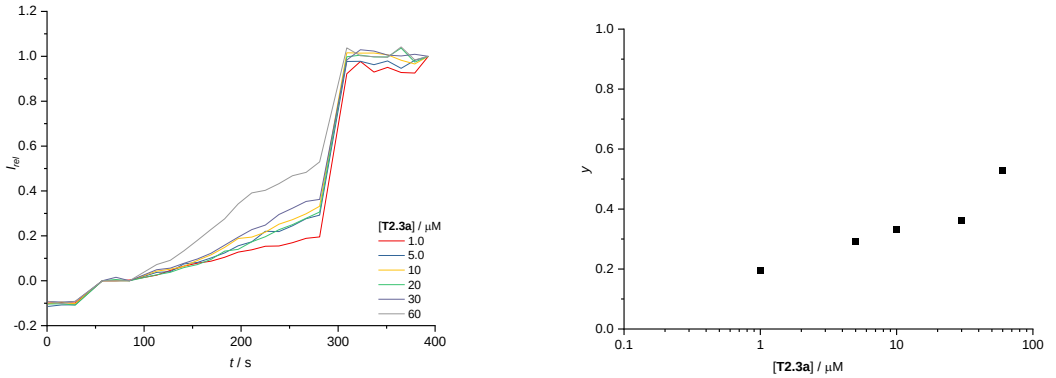


Figure A.21. HPTS assay data for **T2.3a**.

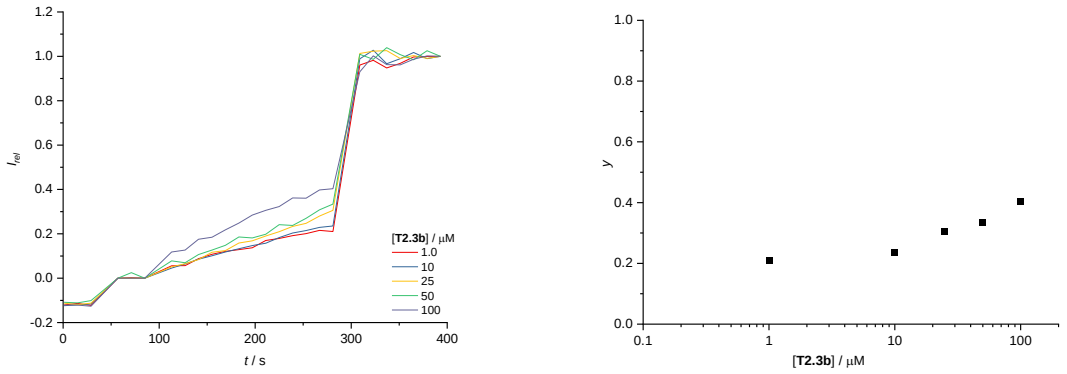


Figure A.22. HPTS assay data for **T2.3b**.

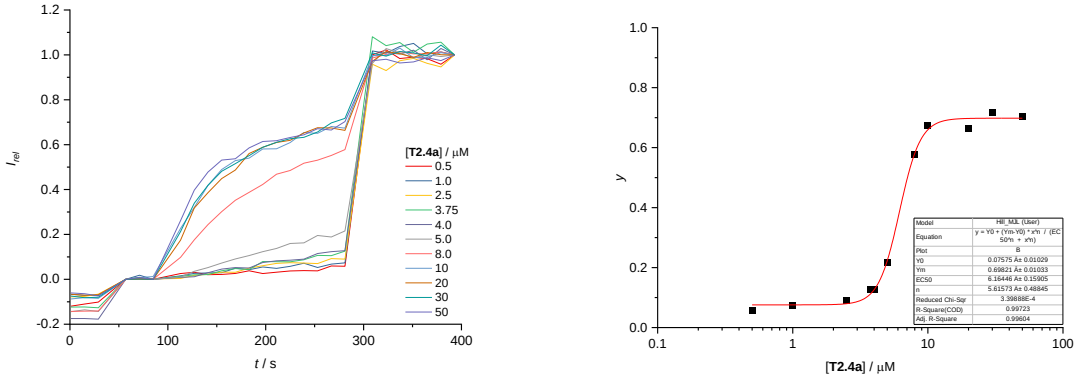


Figure A.23. HPTS assay data for **T2.4a**.

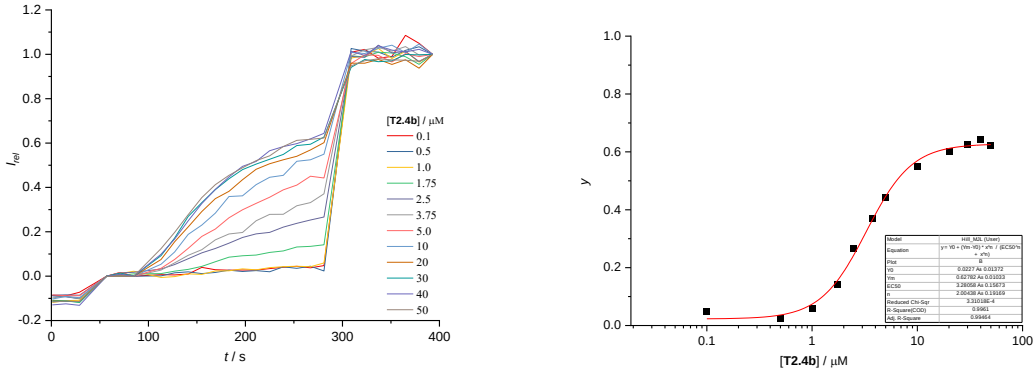


Figure A.24. HPTS assay data for **T2.4b**.

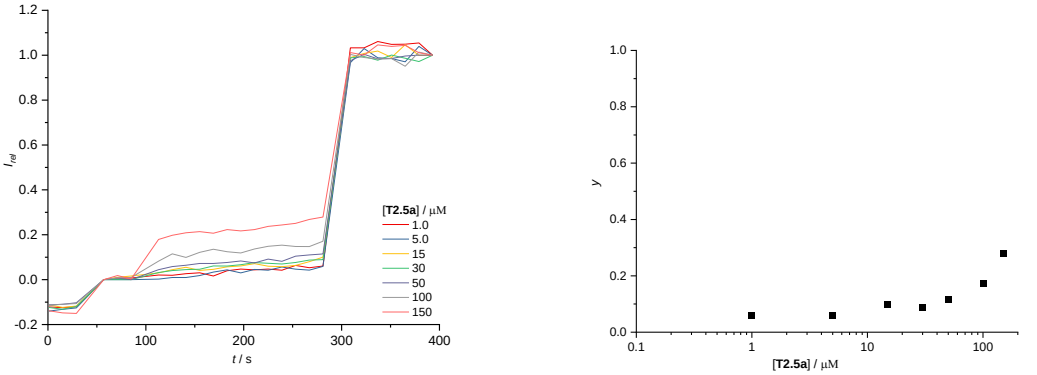


Figure A.25. HPTS assay data for **T2.5a**.

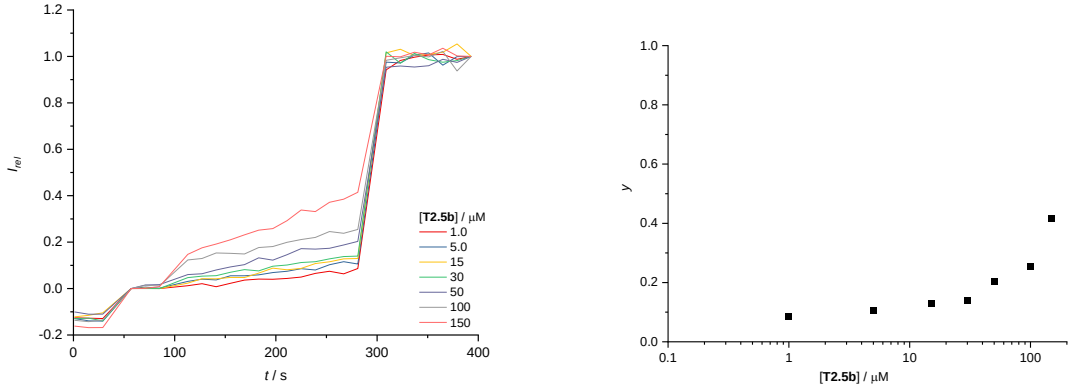


Figure A.26. HPTS assay data for **T2.5b**.

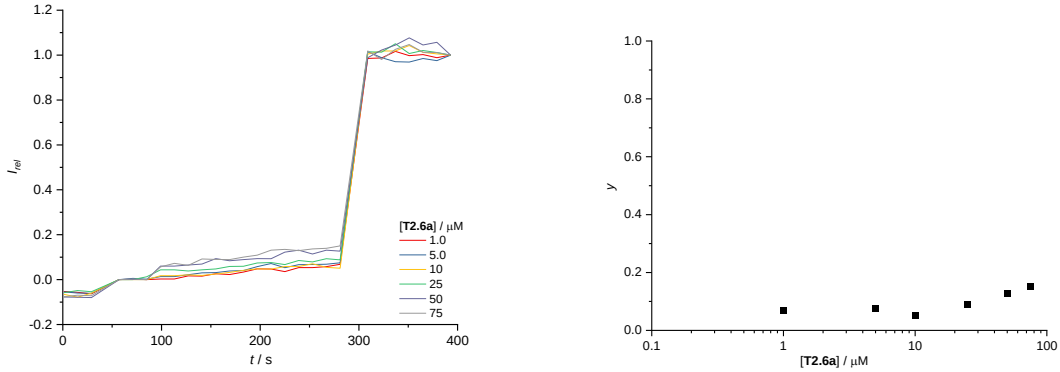


Figure A.27. HPTS assay data for **T2.6a**.

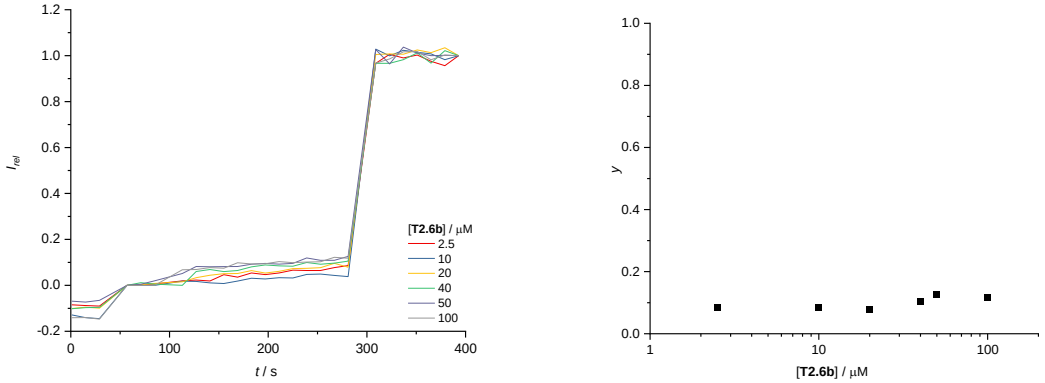


Figure A.28 HPTS assay data for **T2.6b**.

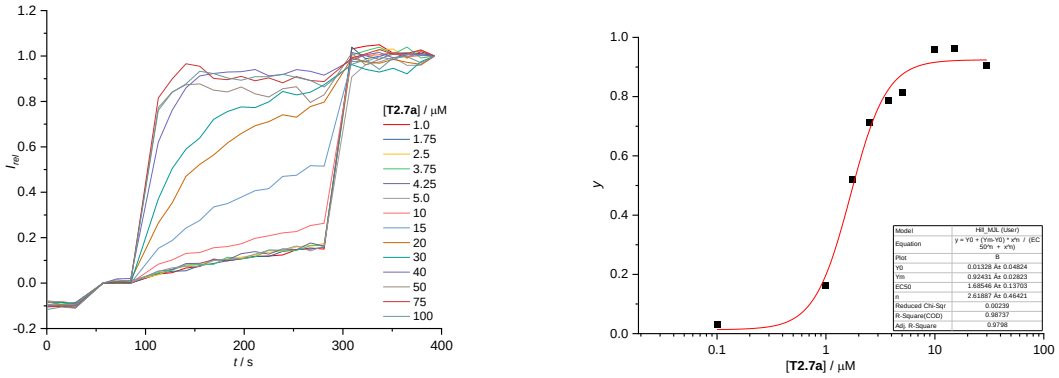


Figure A.29. HPTS assay data for **T2.7a**.

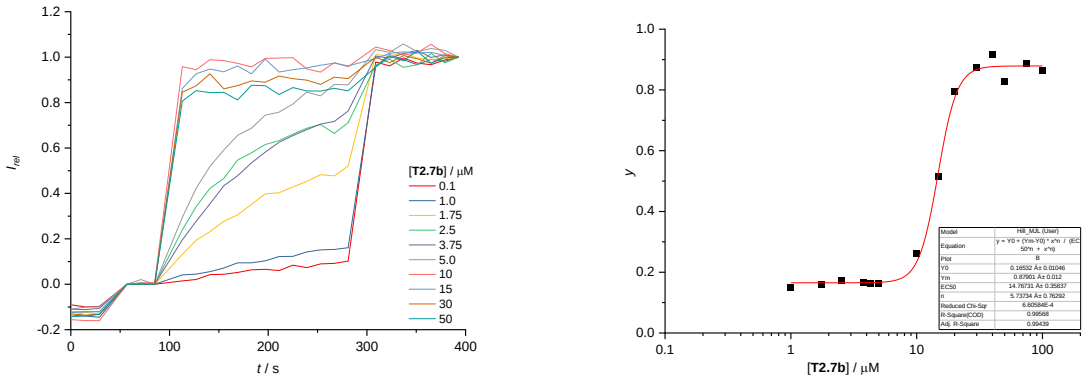


Figure A.30. HPTS assay data for **T2.7b**.

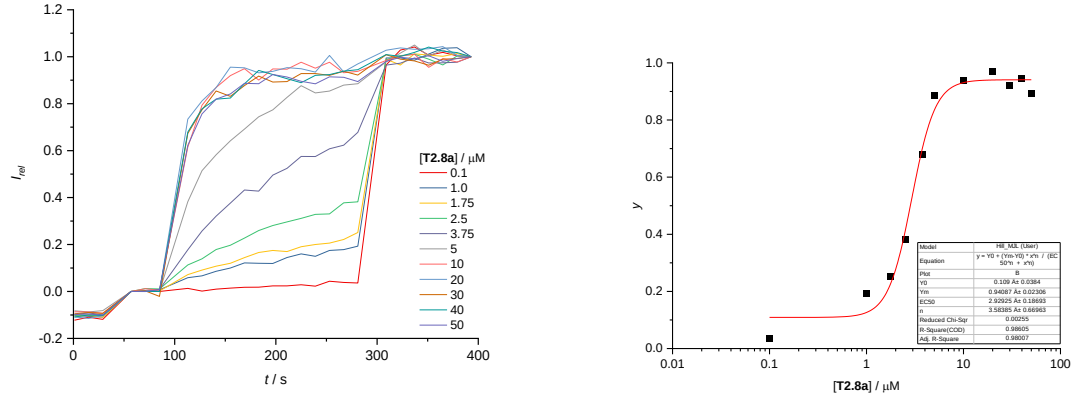


Figure A.31. HPTS assay data for **T2.8a**.

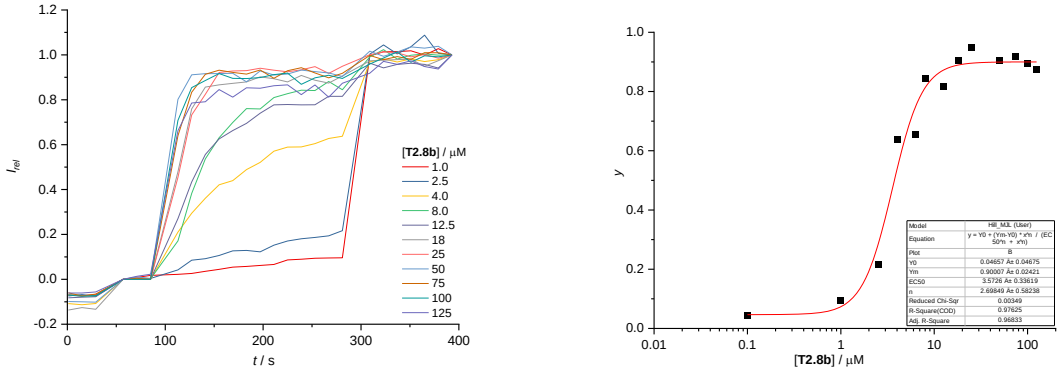


Figure A.32. HPTS assay data for **T2.8b**.

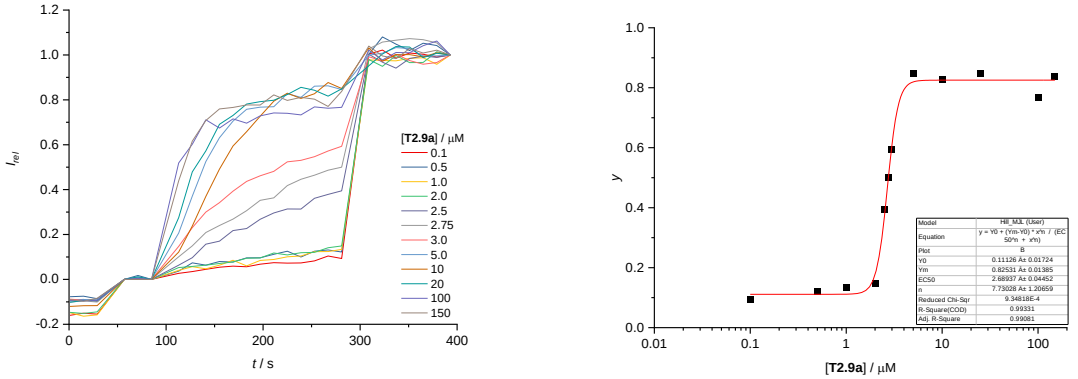


Figure A.33. HPTS assay data for **T2.9a**.

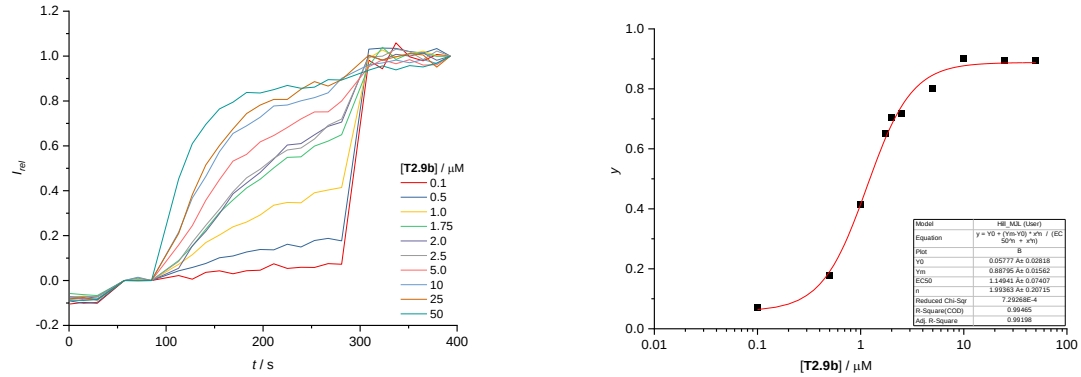


Figure A.34. HPTS assay data for **T2.9b**.

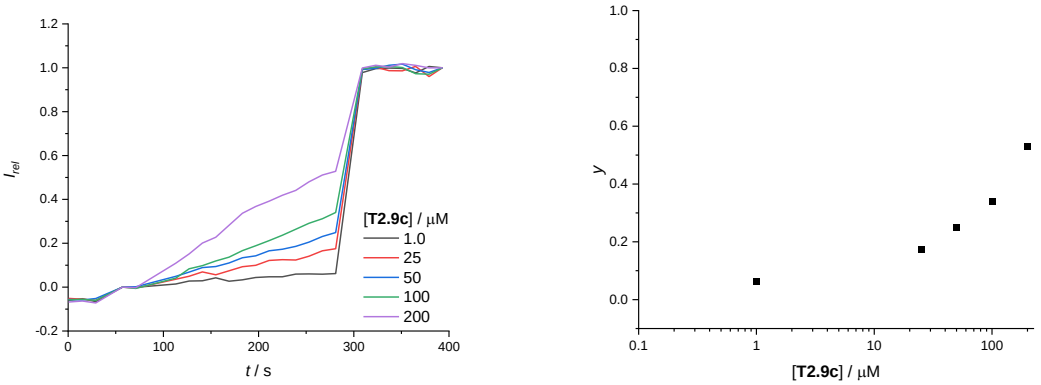


Figure A.35. HPTS assay data for **T2.9c**.

A.2.2 Chapter 3

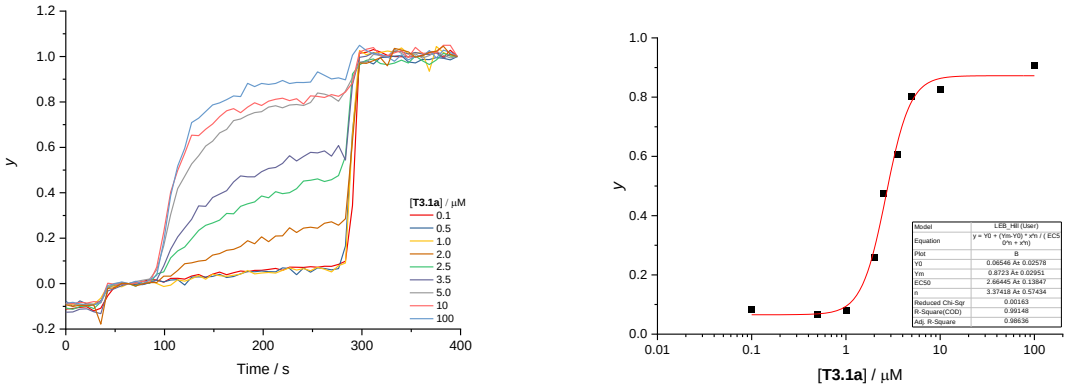


Figure A.36. HPTS assay data for **T3.1a**.

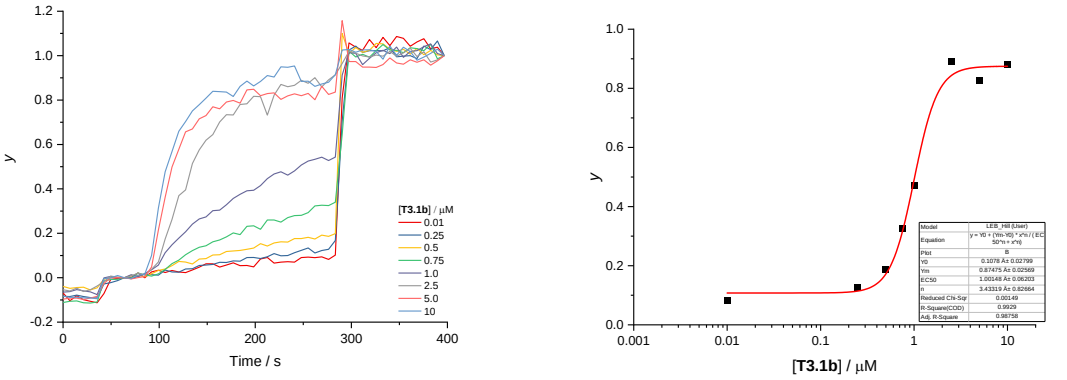


Figure A.37. HPTS assay data for **T3.1b**.

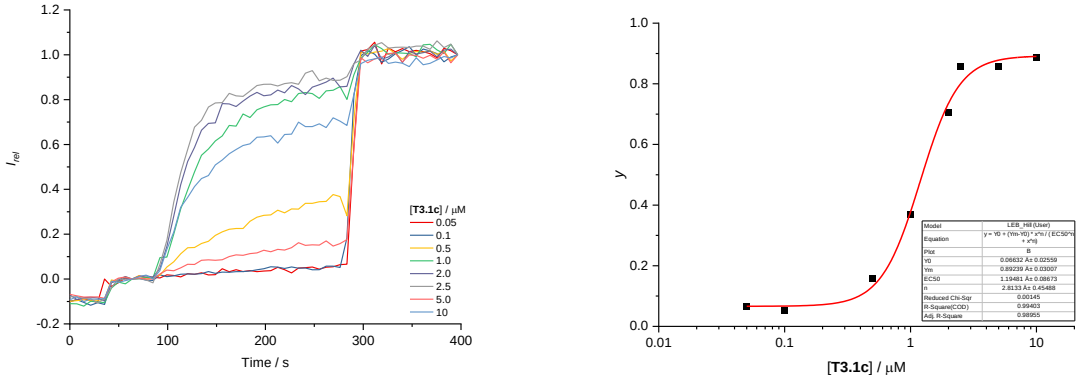


Figure A.38. HPTS assay data for **T3.1c**.

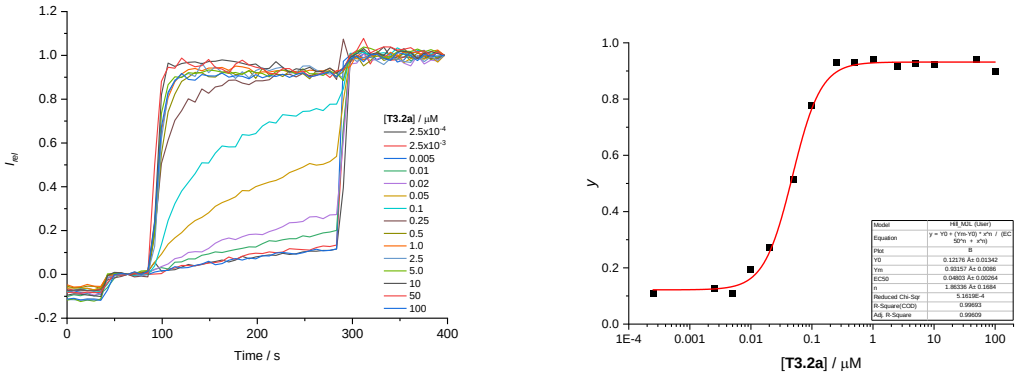


Figure A.39. HPTS assay data for **T3.2a**.

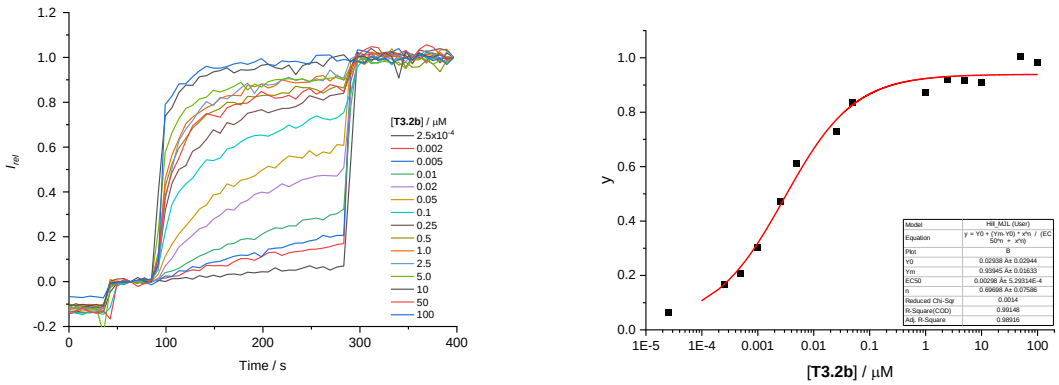


Figure A.40. HPTS assay data for **T3.2b**.

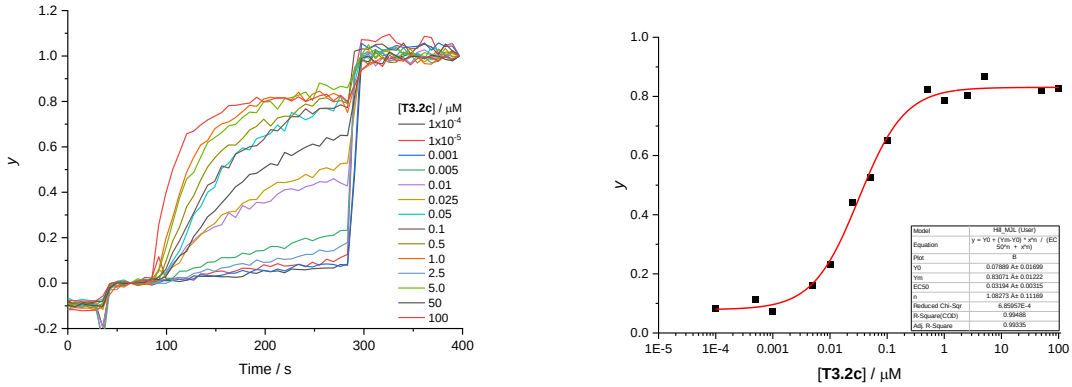


Figure A.41. HPTS assay data for **T3.2c**.

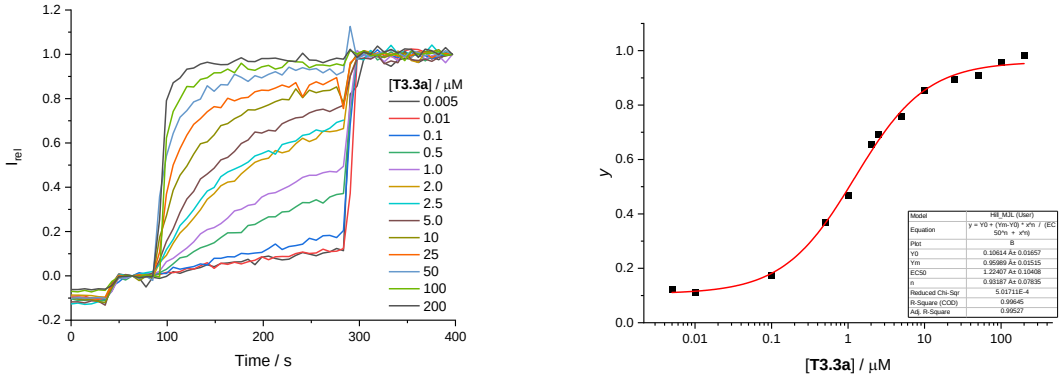


Figure A.42. HPTS assay data for **T3.3a**.

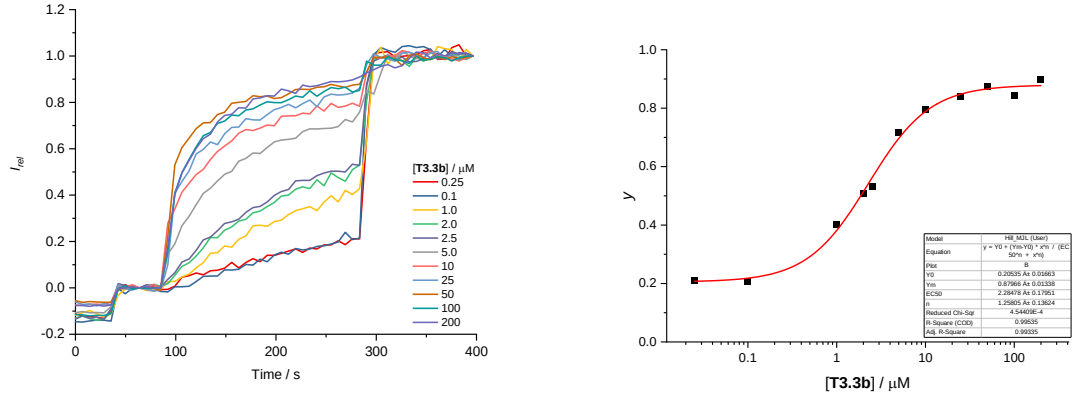


Figure A.43. HPTS assay data for **T3.3b**.

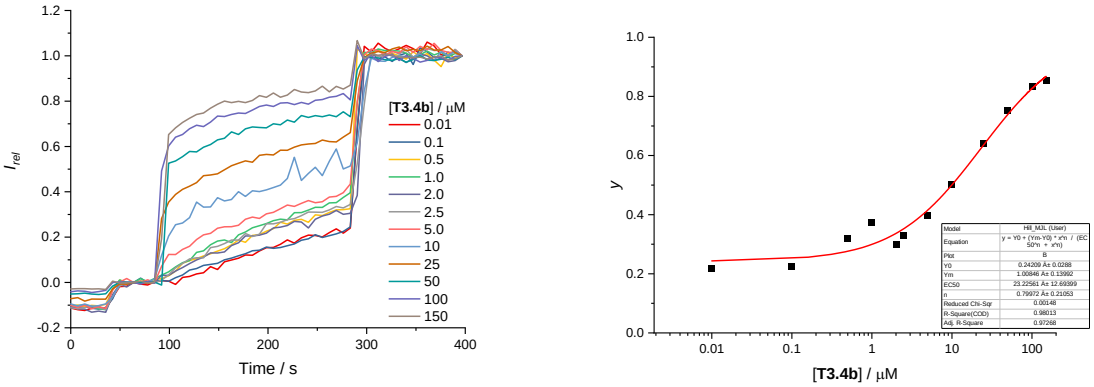


Figure A.44. HPTS assay data for **T3.4b**.

A.2.3 Chapter 4

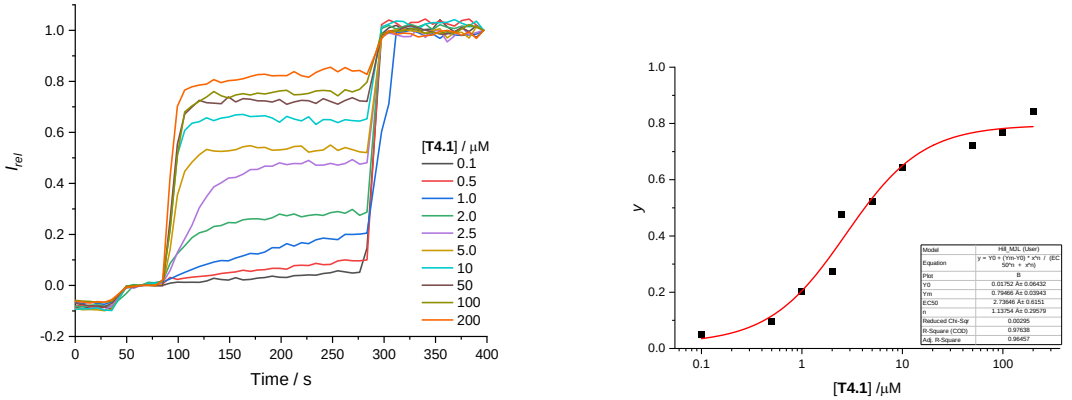


Figure A.45. HPTS assay data for **T4.1**.

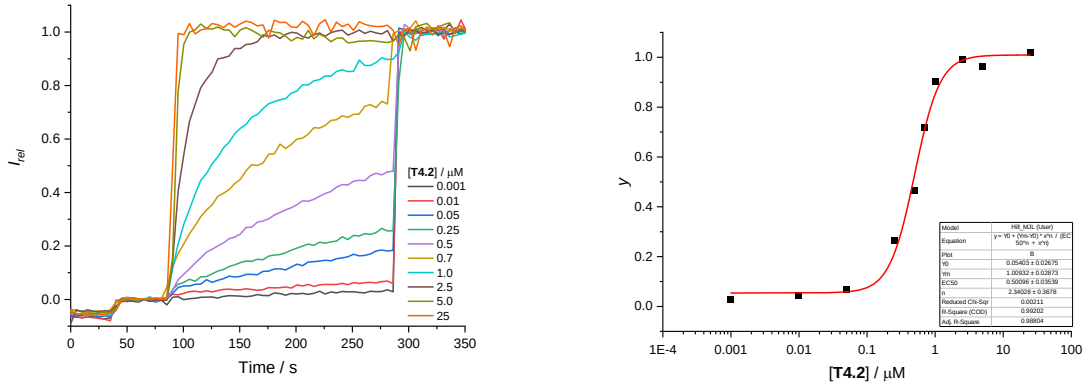


Figure A.46. HPTS assay data for **T4.2**.

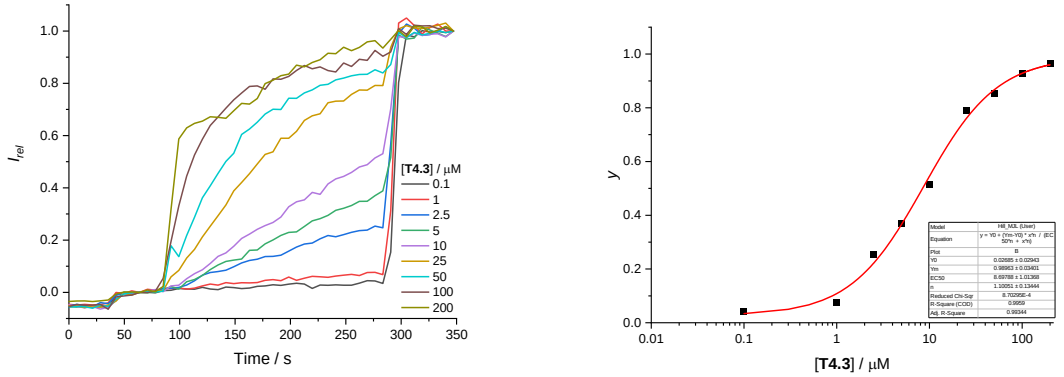


Figure A.47. HPTS assay data for **T4.3**.

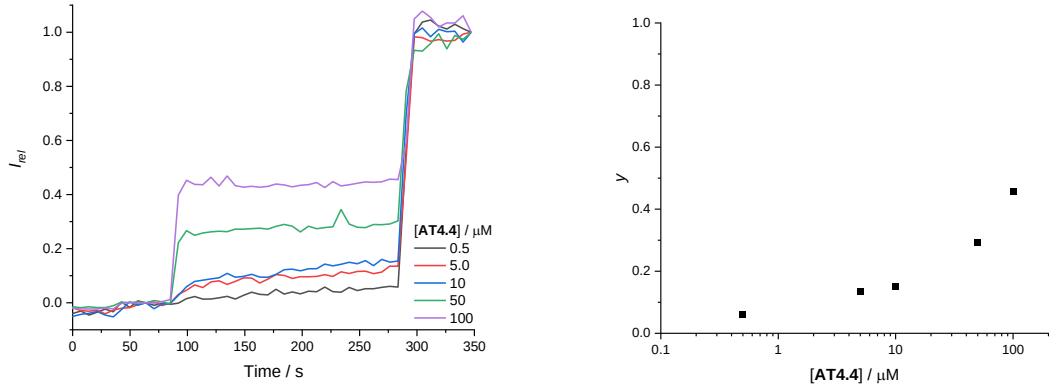


Figure A.48. HPTS assay data for **AT4.4** before in situ photo-cleavage.

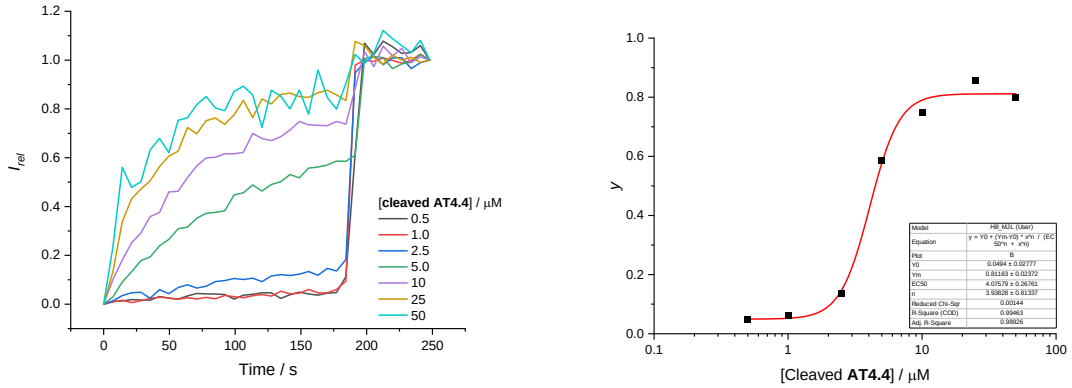


Figure A.49. HPTS assay data for **AT4.4** after 3 mins of in situ photo-cleavage.

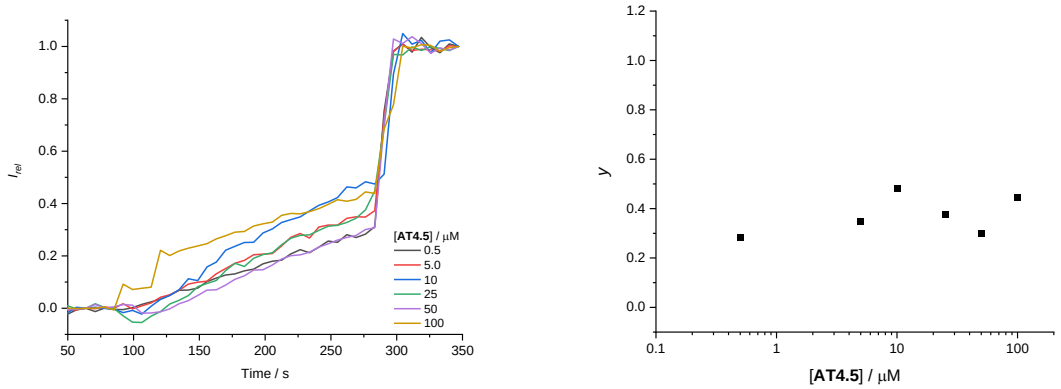


Figure A.50. HPTS assay data for **AT4.5** before in situ photo-cleavage.

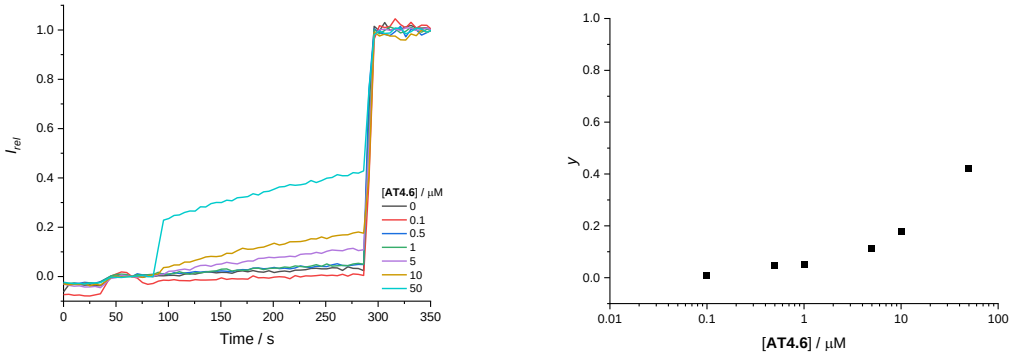


Figure A.51. HPTS assay data for **AT4.6** before in situ photo-cleavage.

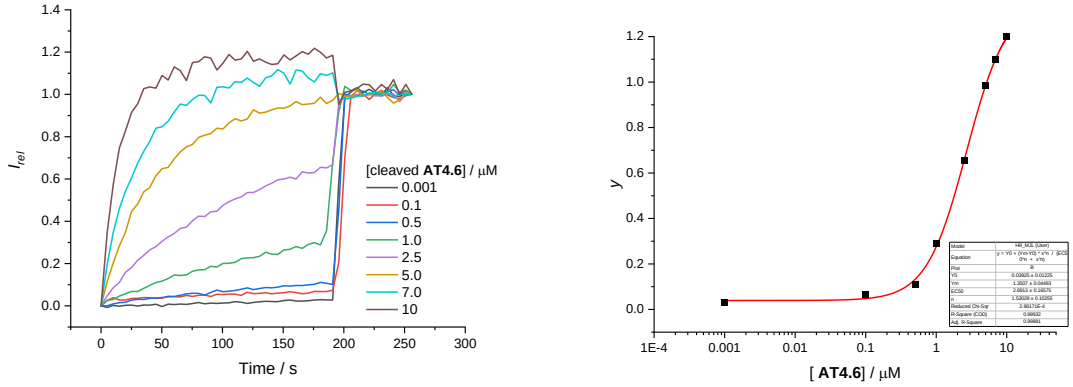


Figure A.52. HPTS assay data for **AT4.6** after 3 mins of in situ photo-cleavage.

A.3 Transport Mechanism Studies

A.3.1 CF Assay

The following data shows: the change in relative fluorescence intensity over time in the CF assay (POPC LUVs, internal: 10 mM NaCl, 10 mM HEPES and external: 50 mM CF buffered to pH 7.0 and external buffer of 107 mM NaCl, 10 mM HEPES, pH 7.0).

A.3.1.1 Chapter 2

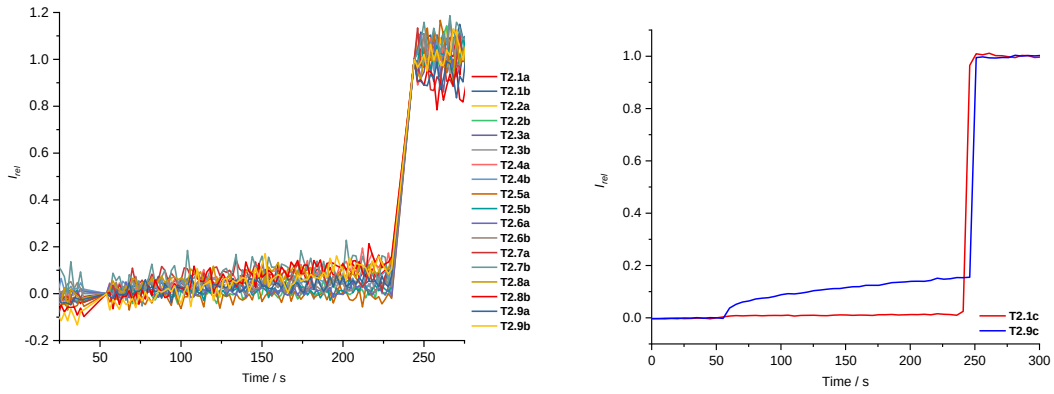


Figure A.53. CF assay data for carriers **T2.1-9a/b** and fluorotriazoles **T2.1c** and **T2.9c** (right).

A.3.1.2 Chapter 3

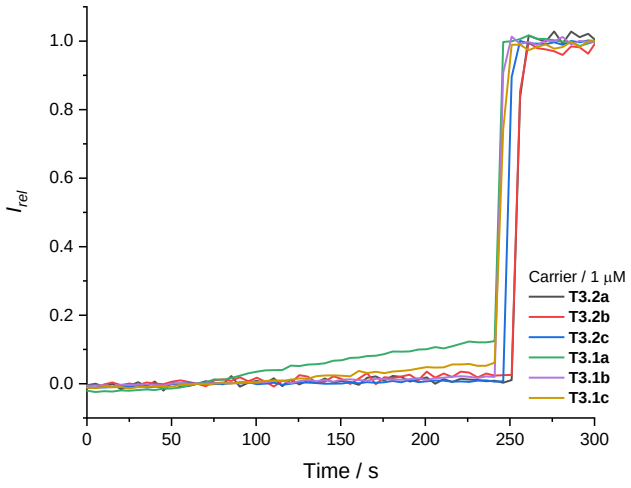


Figure A.54. CF assay data for carriers **T3.1a-c** and **T3.2a-c**.

A.3.1.3 Chapter 4

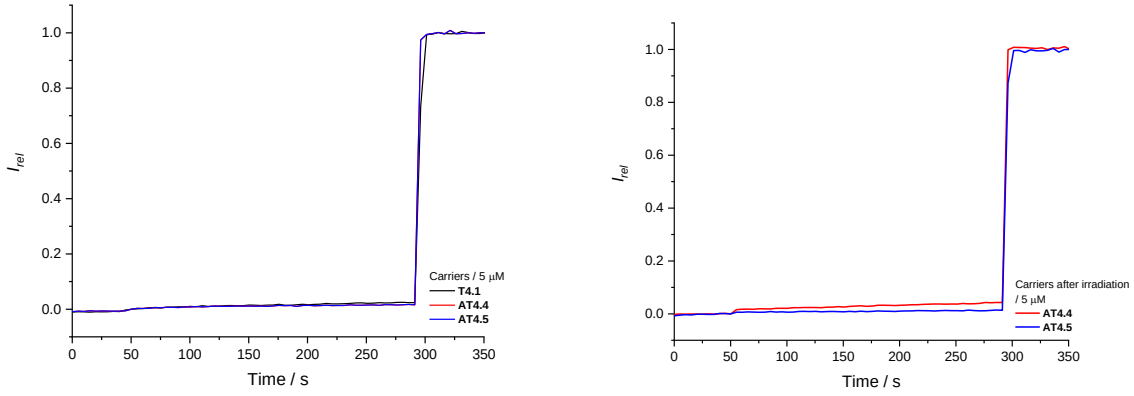


Figure A.55. CF assay data for carriers **T4.1, AT4.4** and **AT4.5** before (left) and after (right) 3 mins of in situ photo-cleavage.

A.3.2 DPPC Assay Data

In the following figures: The change in relative fluorescence intensity (I_{rel}) over time in the DPPC assay LUVs at 25°C and 45°C. The temperature of the sample was controlled using a Peltier temperature controller. (DPPC LUVs (31.25 μM vesicles); inside 100 mM NaCl, 10 mM HEPES, 1 mM HPTS, pH 7.0; outside: 100 mM NaCl, 10 mM HEPES, pH 7.0). The data reported is an average of at least two repeats. Lack of transport in the gel phase

at 25°C, and restoration above the phase transition temperature (41°C) at 45°C, is consistent with a mobile carrier transport mechanism.

A.3.2.1 Chapter 2

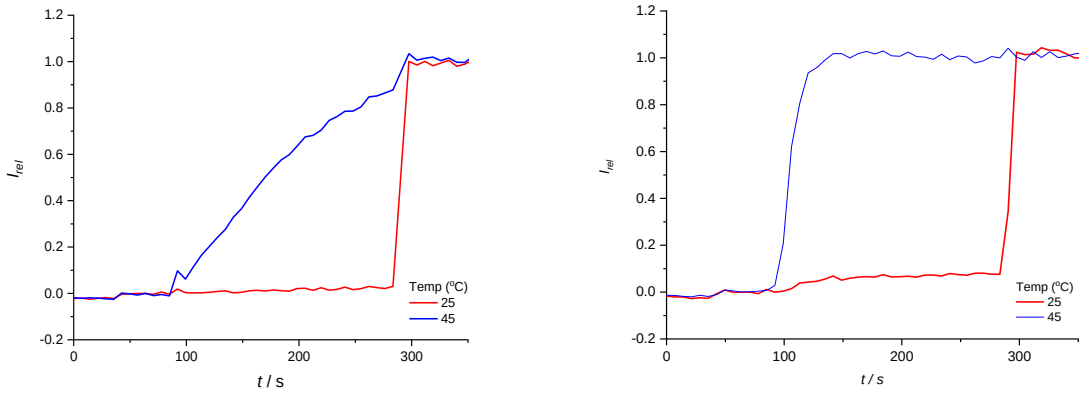


Figure A.56. DPPC assay data for: left, **T2.1a** (2 µM) and right, **T2.1b** (2 µM).

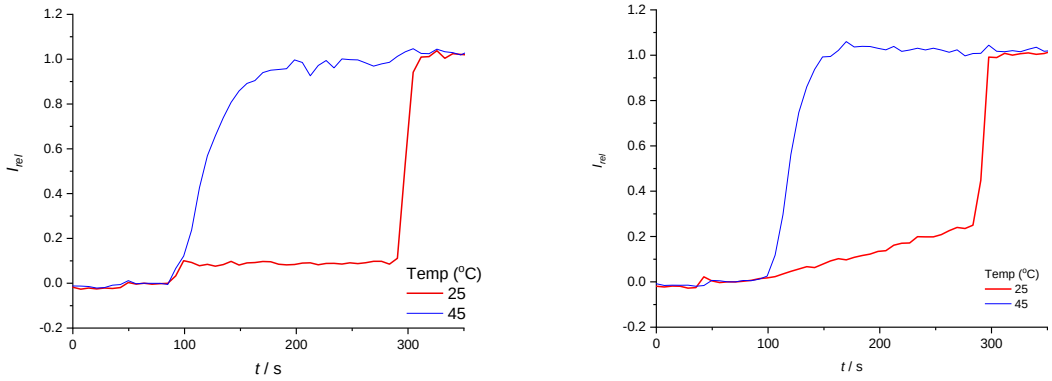


Figure A.57. DPPC assay data for: left, **T2.9a** (2 µM) and right, **T2.9b** (2 µM).

A.3.2.2 Chapter 3

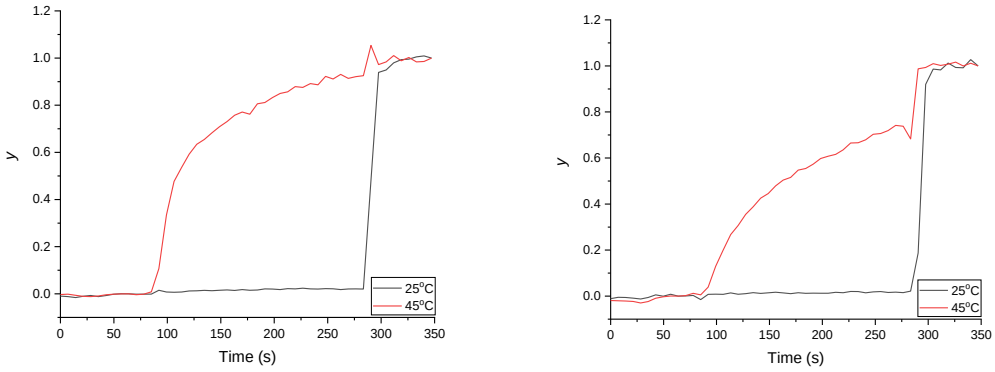


Figure A.58. DPPC assay data for: left, **T3.1a** (2.7 µM) and right, **T3.1b** (1 µM).

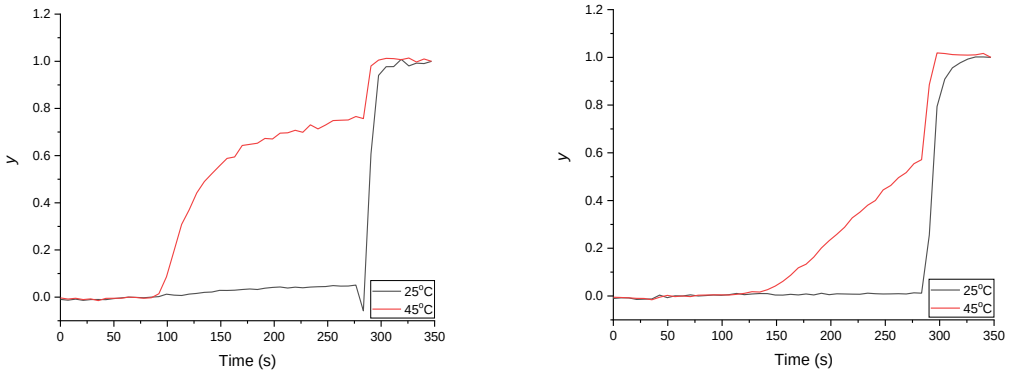


Figure A.59. DPPC assay data for: left, **T3.1c** (1.2 µM) and right, **T3.2a** (48 nM).

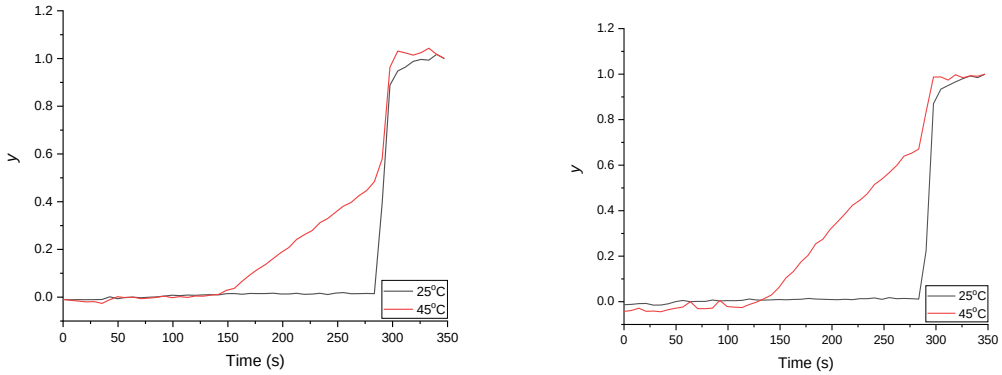


Figure A.60. DPPC assay data for: left, **T3.2b** (3 nM) and right, **T3.2c** (32 nM).

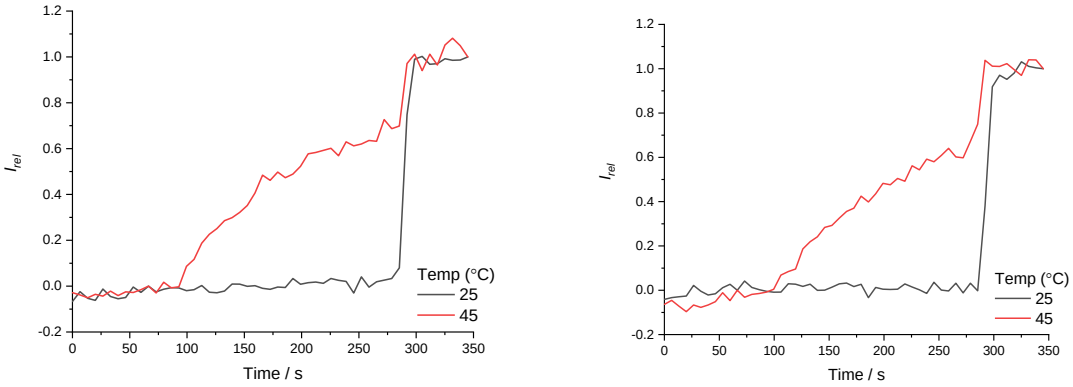


Figure A.61. DPPC assay data for: left, **T3.3a** (2 µM) and right, **T3.3b** (2 µM).

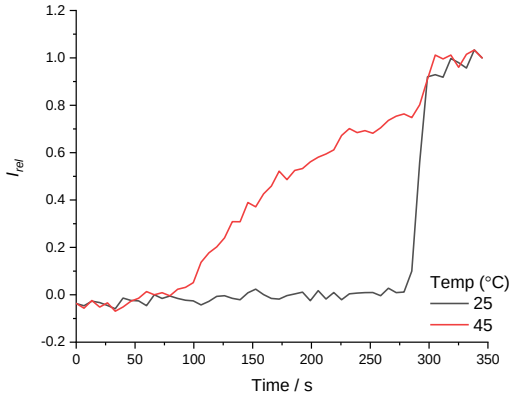


Figure A.62. DPPC assay data for **T3.4b** (2 µM).

A.3.2.3 Chapter 4

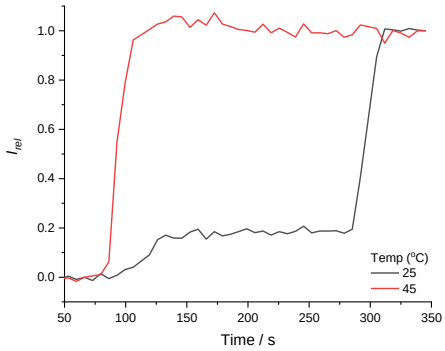


Figure A.63. DPPC assay data for **T4.1** (10 µM).

A.3.3 Anionic Lipid Assay

In the following figures: the change in relative fluorescence intensity over time in the EYPG assay (EYPG LUVs (2.5 mM lipid); inside 100 mM NaCl, 10 mM HEPES, 1 mM HPTS, pH 7.0; outside: 100 mM NaCl, 10 mM HEPES, pH 7.0). Reduction in transport when using negatively charged EYPG LUVs supports the conclusion of a Cl^-/OH^- antiporter mechanism. The data results from at least 2 repeats.

A.3.3.1 Chapter 2

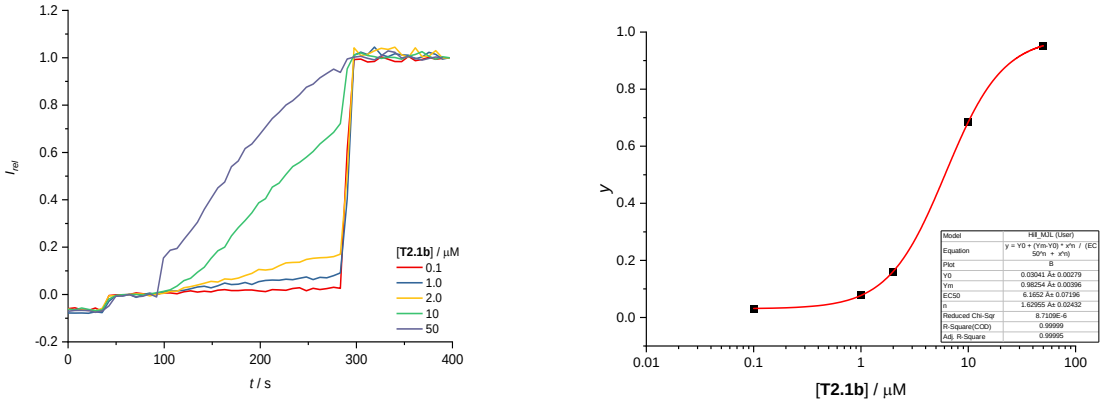


Figure A.64. EYPG assay data for **T2.1b**.

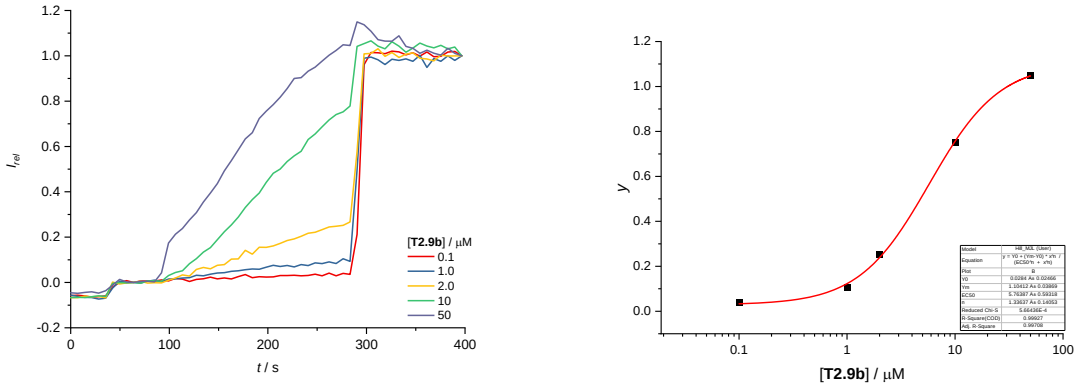


Figure A.65. EYPG assay data for **T2.9b**.

A.3.3.2 Chapter 3

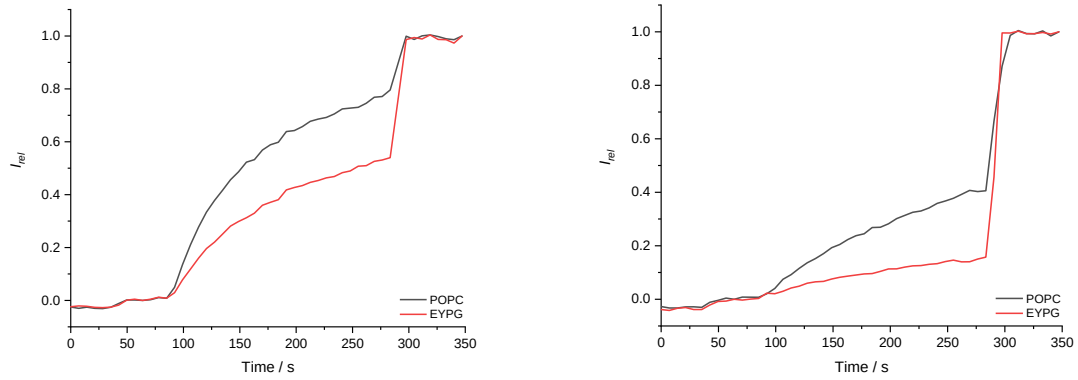


Figure A.66. EYPG assay data for: left, **T3.1a** (2.7 μM) and right, **T3.1b** (1 μM).

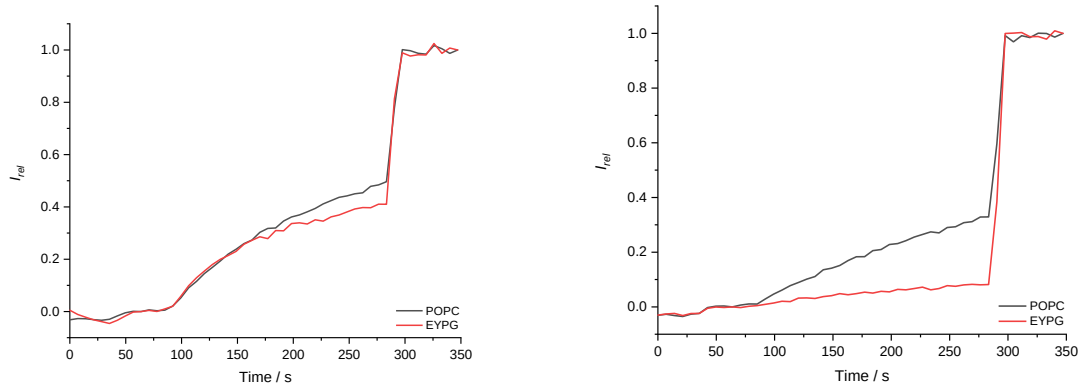


Figure A.67. EYPG assay data for: left, **T3.1c** (1.2 μM) and right, **T3.2a** (48 nM).

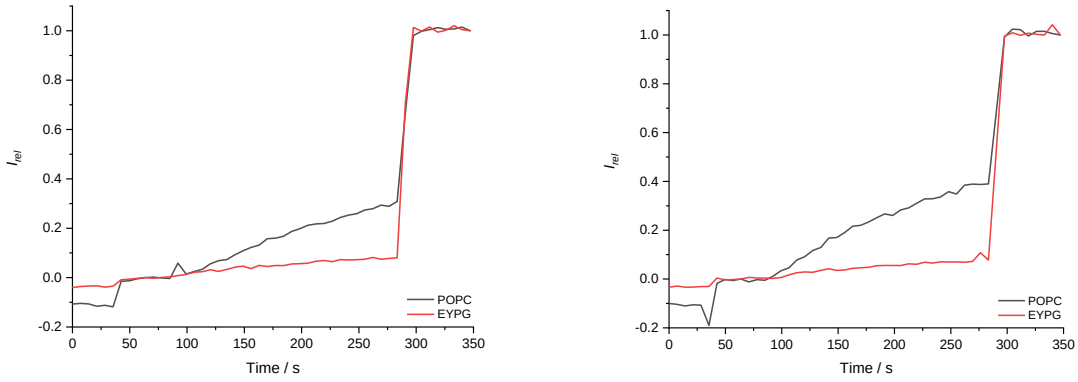


Figure A.68. EYPG assay data for: left, **T3.2b** (3 nM) and right, **T3.2c** (32 nM).

A.4 Transport Selectivity Experiments

A.4.1 Gluconate Assay Data

The following data shows: the change in relative fluorescence intensity over time in the gluconate variation of the HPTS assay (LUVs (2.5 mM lipid); inside 100 mM sodium gluconate, 10 mM HEPES, 1 mM HPTS, pH 7.0; outside: 100 mM sodium gluconate, 10 mM HEPES, pH 7.0). The decrease in transport with NaGlu for all carriers indicated they do not facilitate sodium cation transport (H^+/Na^+ antiport), and must therefore operate via an anion transport mechanism.

A.4.1.1 Chapter 2

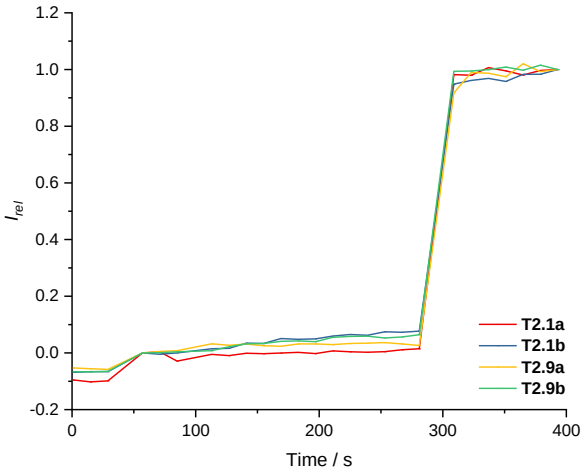


Figure A.69. Gluconate assay data for **T2.1a/b** (2 µM) and **T2.9a/b** (2 µM).

A.4.1.2 Chapter 3

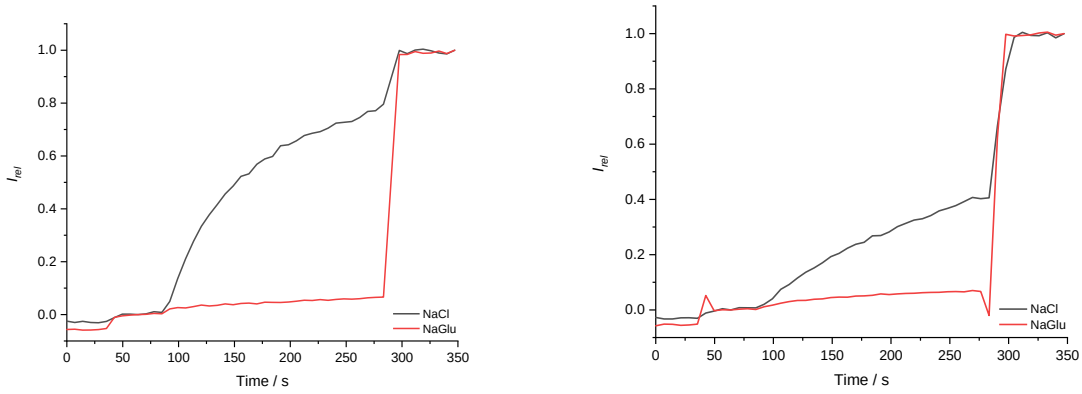


Figure A.70. Gluconate assay data for: left, **T3.1a** (2.7 µM) and right, **T3.1b** (1 µM).

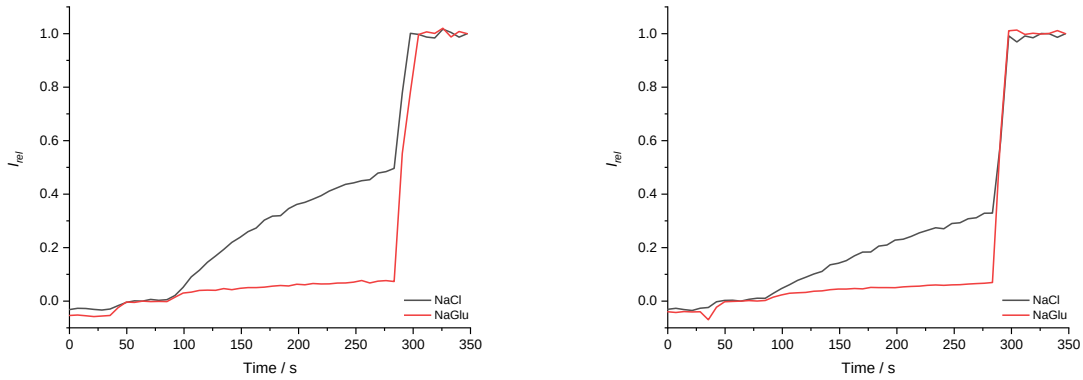


Figure A.71. Gluconate assay data for: left, **T3.1c** (1.2 µM) and right, **T3.2a** (48 nM).

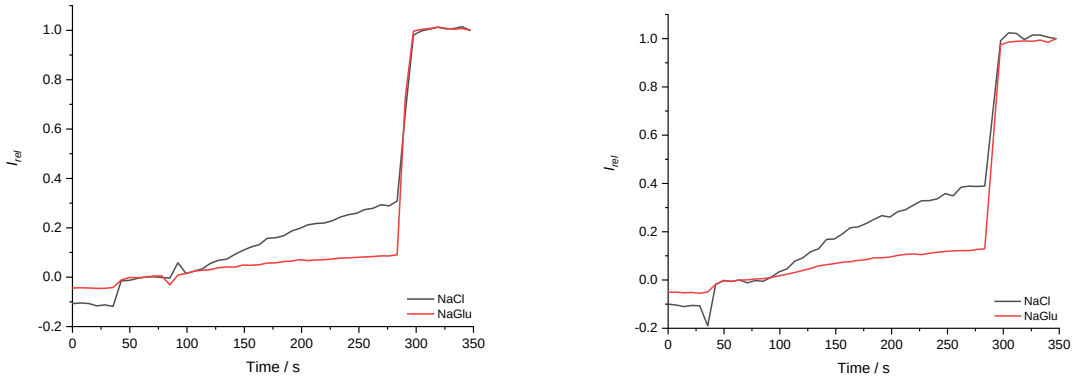


Figure A.72. Gluconate assay data for: left, **T3.2b** (3 nM) and right, **T3.2c** (32 nM).

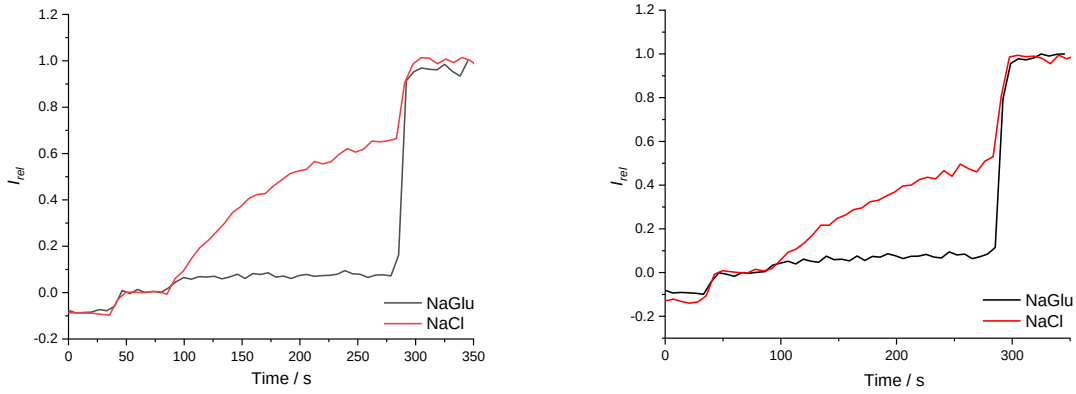


Figure A.73. Gluconate assay data for: left, **T3.3a** (2 µM) and right, **T3.3b** (2 µM).

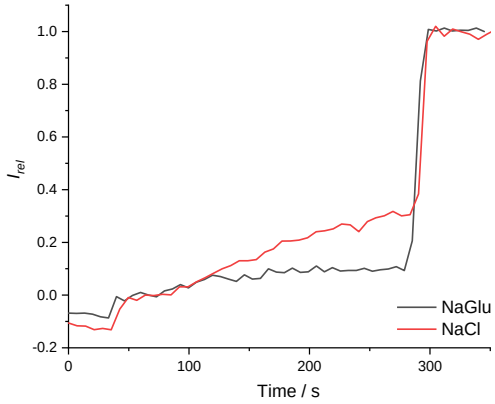


Figure A.74. Gluconate assay data for: left, **T3.4b** (2 µM).

A.4.1.3 Chapter 4

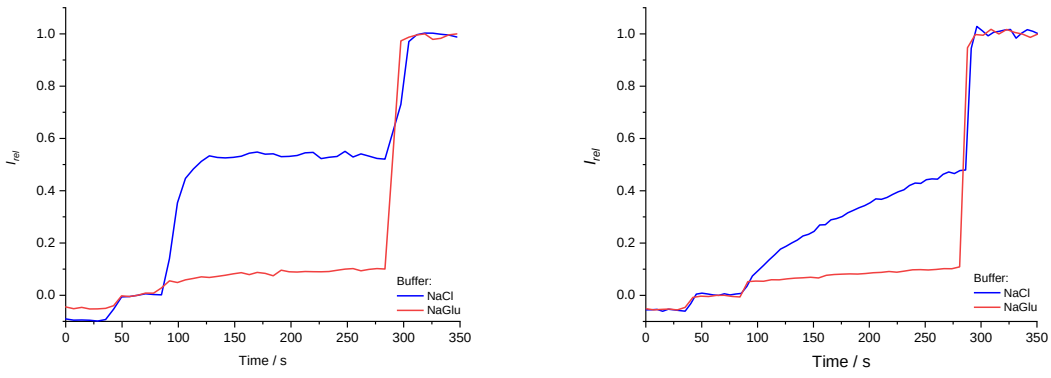


Figure A.75. Gluconate assay data for: left, **T4.1** (5 µM) and right, **T4.2** (5 µM).

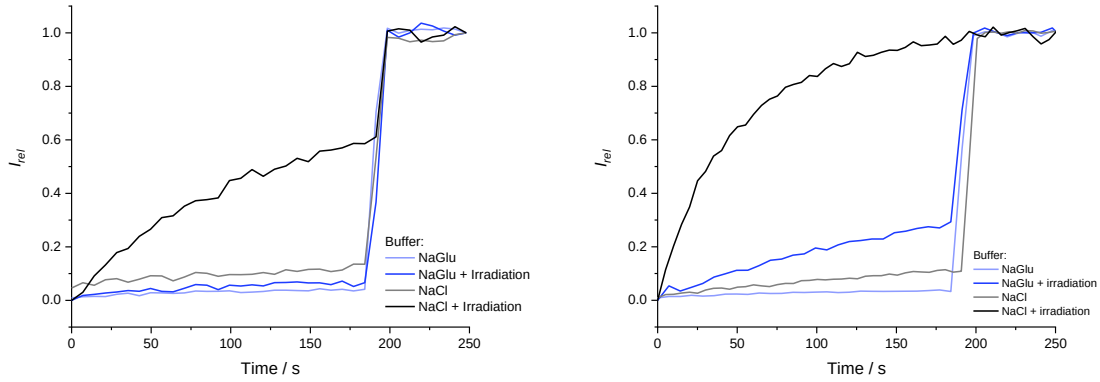


Figure A.76. Gluconate assay data for: left, **AT4.4** (5 µM) and right, **AT4.6** (5 µM) before and after 3 mins of in situ photo-cleavage.

A.4.2 Cation Selectivity HPTS Assay

The following data shows: the dependence of the fractional fluorescence intensity (I_{rel}) at 288 s on the external cation upon addition of the carrier to POPC vesicles containing 1 mM HPTS, 100 mM internal and external M^+Cl^- (M^+ = Li^+, Na^+, K^+, Rb^+), buffered with 10 mM HEPES at pH 7.0. A pH gradient is generated by addition of a M^+OH^- base pulse (0.5 M), followed by the carrier at t = 90 s. Vesicle lysis by Triton X-100 calibrates the assay.

A.4.2.1 Chapter 2

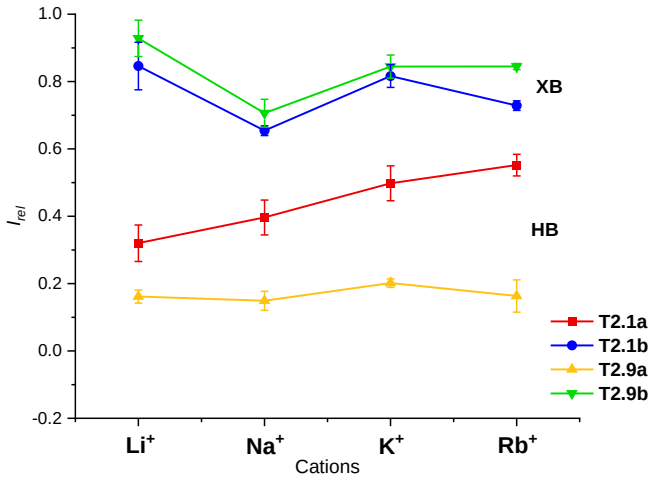


Figure A.77. Cation selectivity data for carriers **T2.1** (2 µM) and **T2.9** (2 µM).

A.4.2.2 Chapter 3

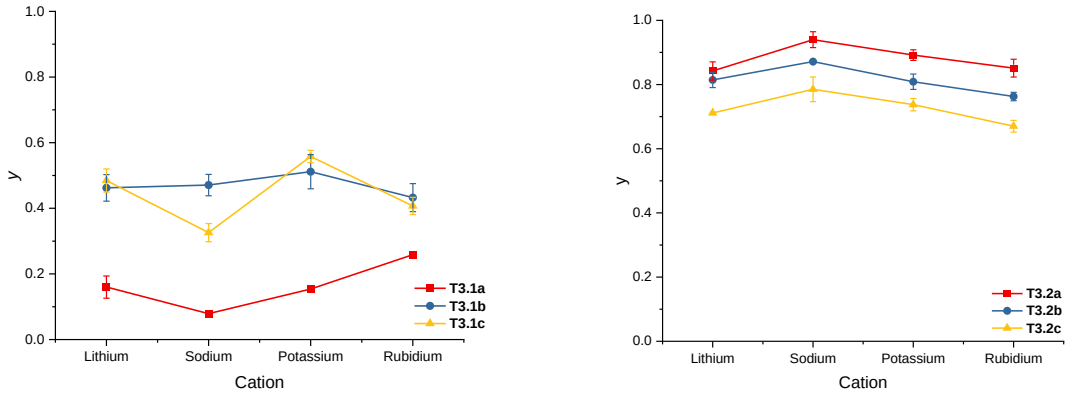


Figure A.78. Cation selectivity data for carriers **T3.1a-c** (1 µM) and **T3.2a-c** (1 µM).

A.4.3 Anion Selectivity and the FCCP Cl^- vs OH^- Selectivity HPTS Assay

A.4.3.1 Chapter 2

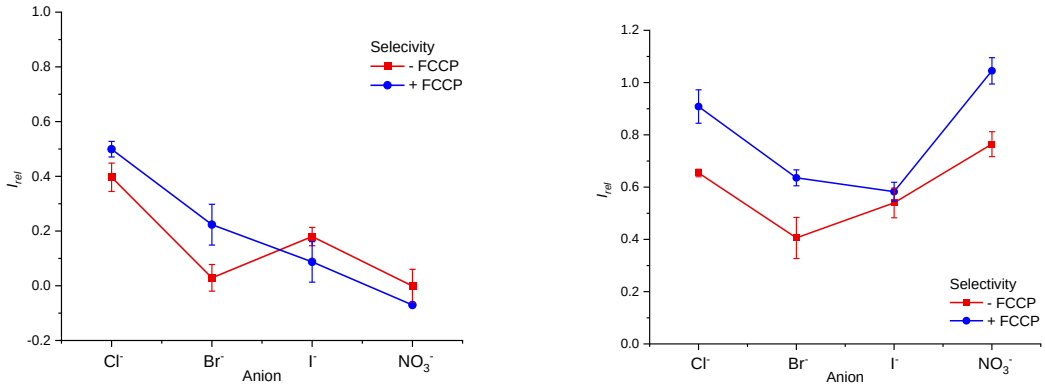


Figure A.79. Anion selectivity data for carriers **T2.1a** (left) and **T2.1b** (right) (2 µM). The dependence of the I_{rel} at 288 s on the external anion upon addition of the carrier to POPC vesicles containing 1 mM HPTS, 100 mM internal and external Na^+X^- (X^- = Cl^-, Br^-, I^-, NO_3^-), buffered with 10 mM HEPES at pH 7.0. A pH gradient was generated by NaOH (0.5 M), followed by the carrier at t = 90 s. Vesicle lysis by Triton X-100 calibrates the assay.

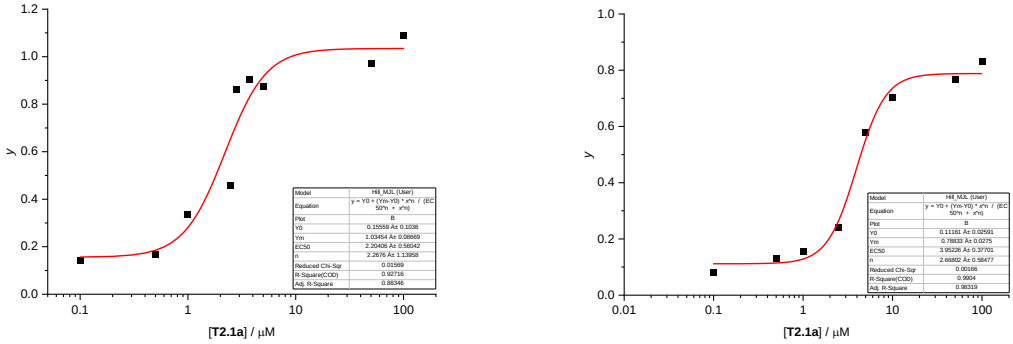


Figure A.80. Hill plots associated with transport mediated by **T2.1a** with the addition of FCCP (0.25 μM) in NaCl (left) and NaI (right) buffer.

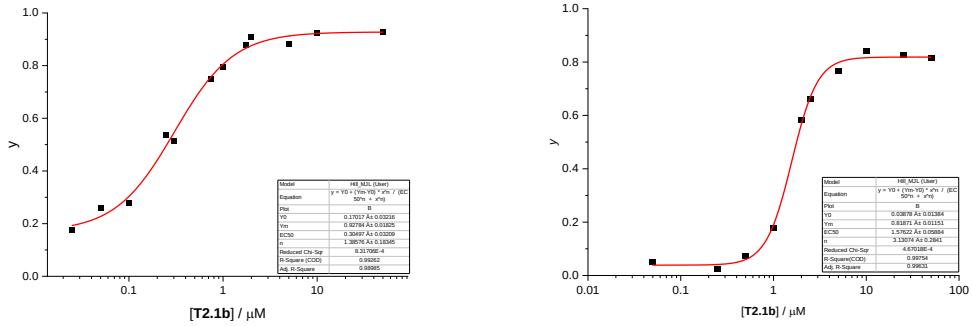


Figure A.81. Hill plots associated with transport mediated by **T2.1b** with the addition of FCCP (0.25 μM) in NaCl (left) and NaI (right) buffer.

A.4.3.2 Chapter 3

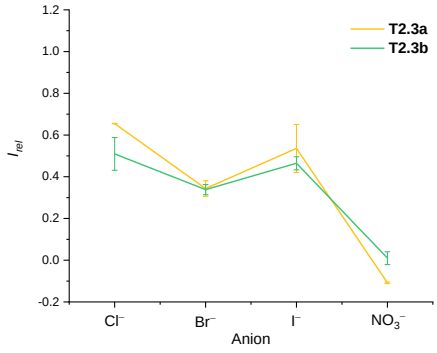


Figure A.82. Anion selectivity data for carriers **T2.1a** and **T2.1b** (2 μM). The dependence of the I_{rel} at 288 s on the external anion upon addition of the carrier to POPC vesicles containing 1 mM HPTS, 100 mM internal and external Na^+X^- (X^- = Cl^-, Br^-, I^-, NO_3^-), buffered with 10 mM HEPES at pH 7.0. A pH gradient was generated by NaOH (0.5 M), followed by the carrier at t = 90 s. Vesicle lysis by Triton X-100 calibrates the assay.

A.4.4 The NMDG Cl^- vs OH^- Selectivity HPTS Assay

In the following figures: Left: change in relative fluorescence intensity over time in the NMDG assay (LUVs (0.1 mM lipid); inside 100 mM NMDG-Cl, 10 mM HEPES, 1 mM HPTS, pH 7.0; outside: 100 mM NMDG-Cl, 10 mM HEPES, pH 7.0). Right: dependence of the fractional transport activity *y* in the HPTS assay on the concentration of transporter (black squares) and fitted to the Hill equation (red line). This assay was carried out with and without the addition of Gramicidin D (0.1 mol%, 4 µL DMSO solution) added after the NMDG base pulse (20 µL of 0.5 M) when used. Error bars represent 2 s.d.

A.4.4.1 Chapter 3

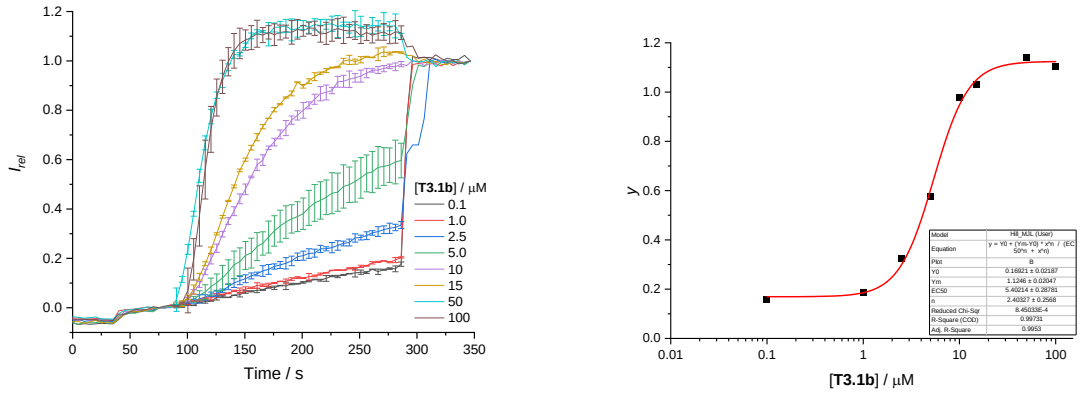


Figure A.83. NMDG assay data for carrier **T3.1b** without gramicidin.

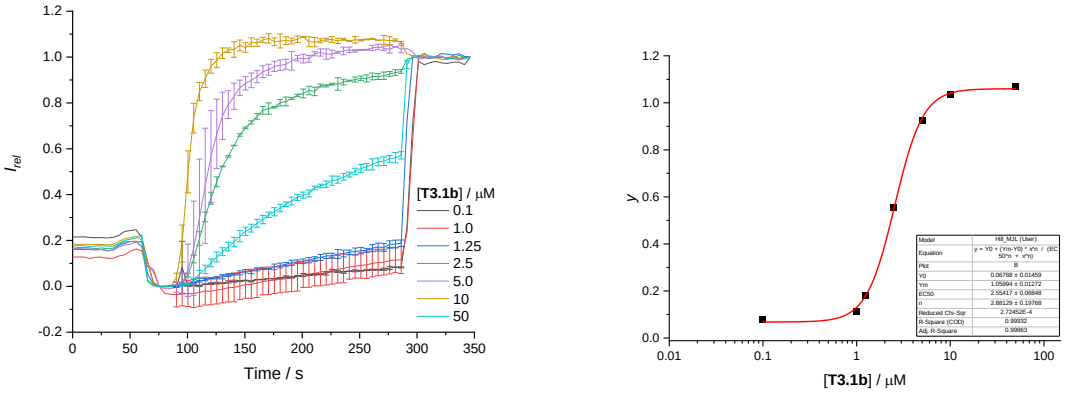


Figure A.84. NMDG assay data for carrier **T3.1b** with gramicidin.

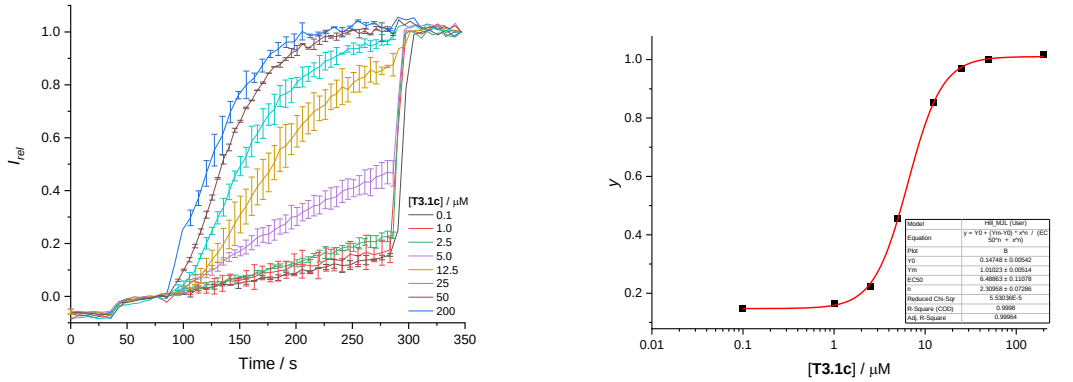


Figure A.85. NMDG assay data for carrier **T3.1c** without gramicidin.

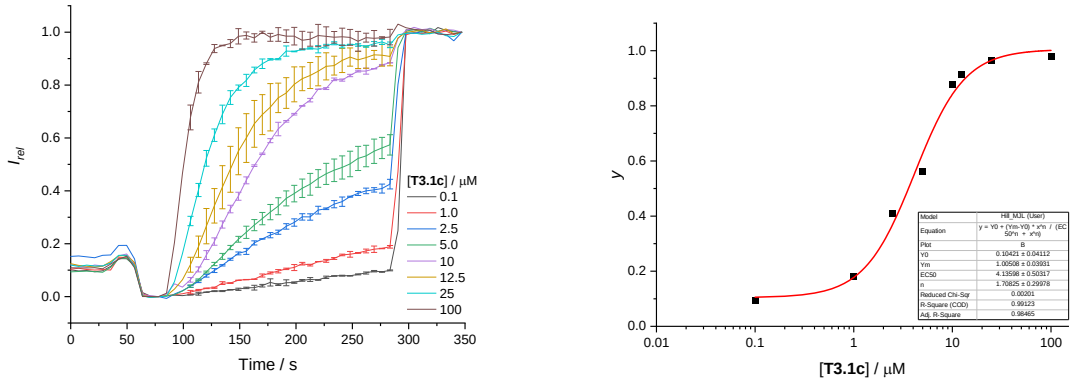


Figure A.86. NMDG assay data for carrier **T3.1c** with gramicidin.

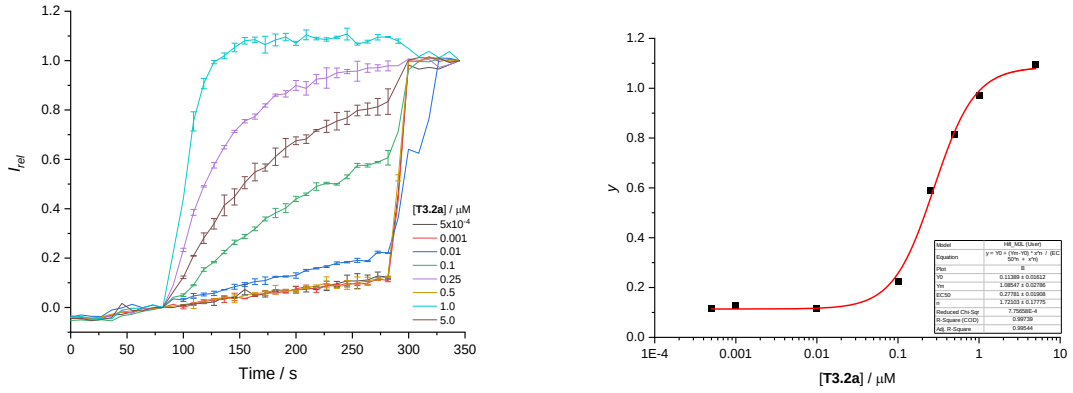


Figure A.87. NMDG assay data for carrier **T3.2a** without gramicidin.

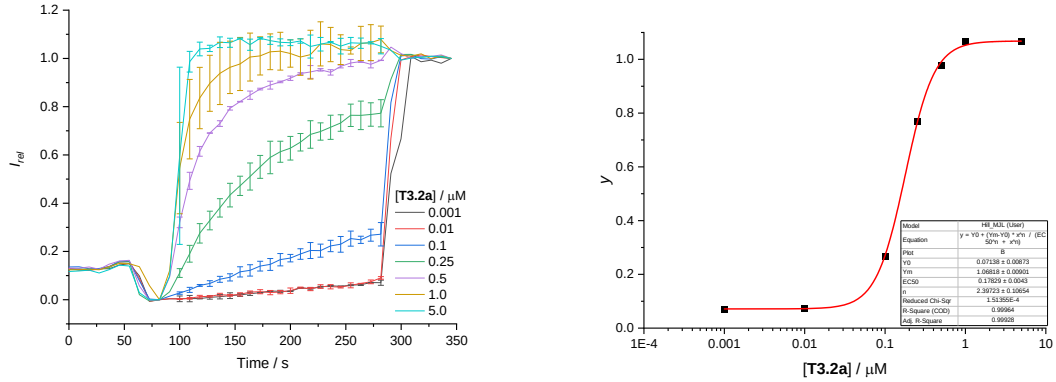


Figure A.88. NMDG assay data for carrier **T3.2a** with gramicidin.

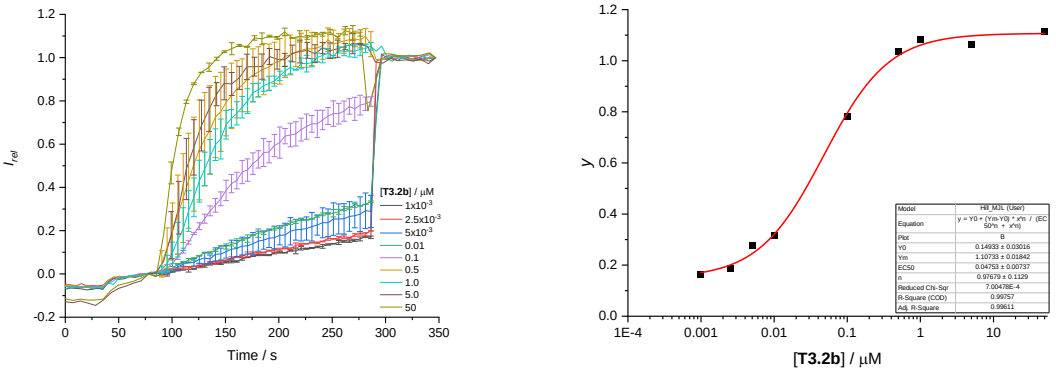


Figure A.89. NMDG assay data for carrier **T3.2b** without gramicidin.

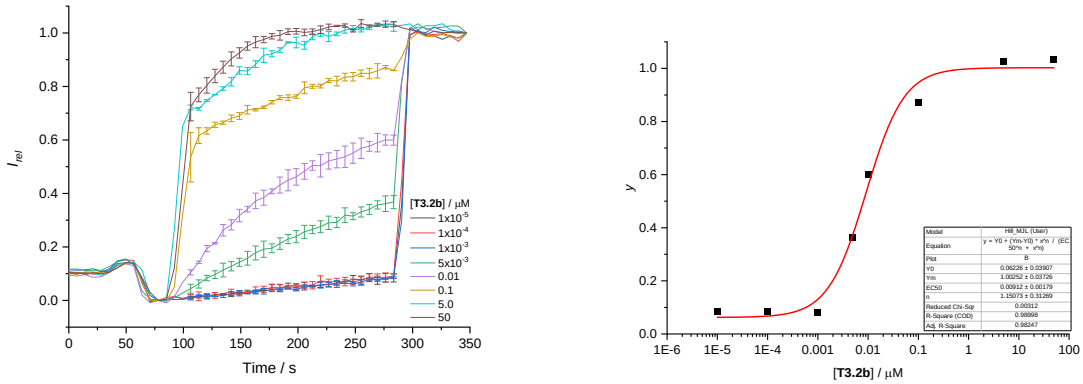


Figure A.90. NMDG assay data for carrier **T3.2b** with gramicidin.

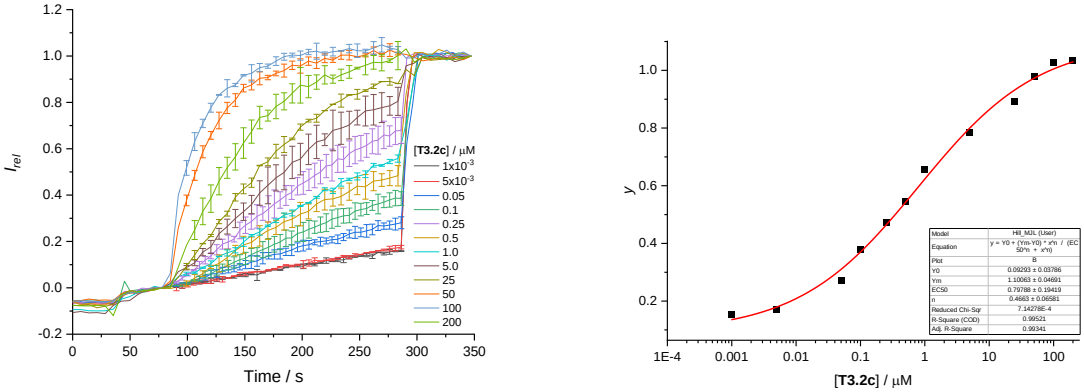


Figure A.91. NMDG assay data for carrier **T3.2c** without gramicidin.

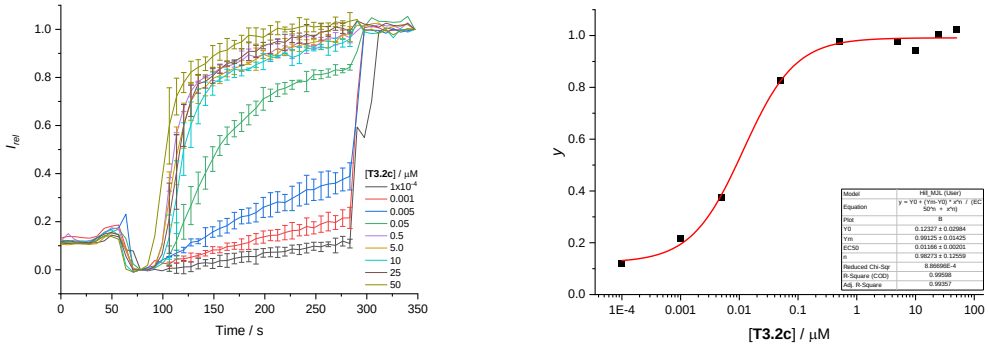


Figure A.92. NMDG assay data for carrier **T3.2c** with gramicidin.